GROUND MOTION PREDICTIONS FOR THE LOS ANGELES BASIN FROM A MAJOR SAN ANDREAS EARTHQUAKE (HA & HB)

R.J. Apsel
and
G.A. Frazier, A. Jurkevics and J.C. Fried

Del Mar Technical Associates
P.O. Box 1083
Del Mar, California 92014

USGS CONTRACT NO. 14-08-0001-17792
Supported by the EARTHQUAKE HAZARDS REDUCTION PROGRAM

OPEN-FILE NO.81-276

DELTA-R-80-044

GROUND MOTION PREDICTIONS FOR THE LOS ANGELES BASIN USING COMPUTER MODELING METHODS

FINAL REPORT

Prepared by

Del Mar Technical Associates
P. O. Box 1083
Del Mar, California 92014

Contract Number:	14-08-0001-17792
Contract Title:	Ground Motion Predictions for the Los Angeles Basin from a Major San Andreas Earthquake (HA and HB)
Principal Investigator:	R. J. Apsel
Other Authors:	G. A. Frazier, A. Jurkevics and J. C. Fried
Contract Technical Officer:	Dr. Gordon Green U. S. Geological Survey Office of Earthquake Studies 345 Middlefield Road Menlo Park, California 94025
Contract Period:	13 March 1979 to 30 September 1980
Amount of Contract:	$70,000
Date of Report:	10 October 1980

Sponsored by the
U. S. Geological Survey
Contract Number 14-08-0001-17792

TABLE OF CONTENTS

TABLE OF CONTENTS (continued)

CHAPTER 1

INTRODUCTION

1.1 EARTHQUAKE HAZARDS FOR THE LOS ANGELES BASIN

The Los Angeles basin is vulnerable to potential earthquake hazards from several nearby faults. The map of Southern California in Figure 1-1 shows the locations of the most prominent faults believed to be capable of supporting major earthquakes. There are many more faults in this region which may be capable of motion but have not experienced major earthquakes in recent times.

The east-west trending Transverse Ranges to the north of the Los Angeles basin are typified by east-west trending left-lateral, strike-slip faults and thrust faults (such as observed during the 1971 San Fernando and 1973 Point Mugu earthquakes). The faults located to the south and east of the Los Angeles basin trend northwest-southeast and can be expected to produce predominantly right-lateral, strike-slip motions (such as observed along the San Andreas and Newport-Inglewood fault systems).

The San Andreas Fault has a larger slip rate than all the other fault systems in California. The most recent major earthquake ruptures occurring along the San Andreas Fault near the Los Angeles basin were the Fort Tejon Earthquake in 1857 (magnitude approximately 8+) and the Banning Pass Earthquake in 1948 (magnitude approximately 6.5). The San Andreas Fault passes obliquely through the San Gabriel and the San Bernardino Mountain Ranges and is currently believed to be locked in this region of the bend. Simultaneously, shear strain is accumulating in the Southern California Uplift region centered near Palmdale (Prescott and Savage, 1976 and Castle, et al., 1977) and steady aseismic slippage is occurring north and south of this area (Thatcher, 1976).

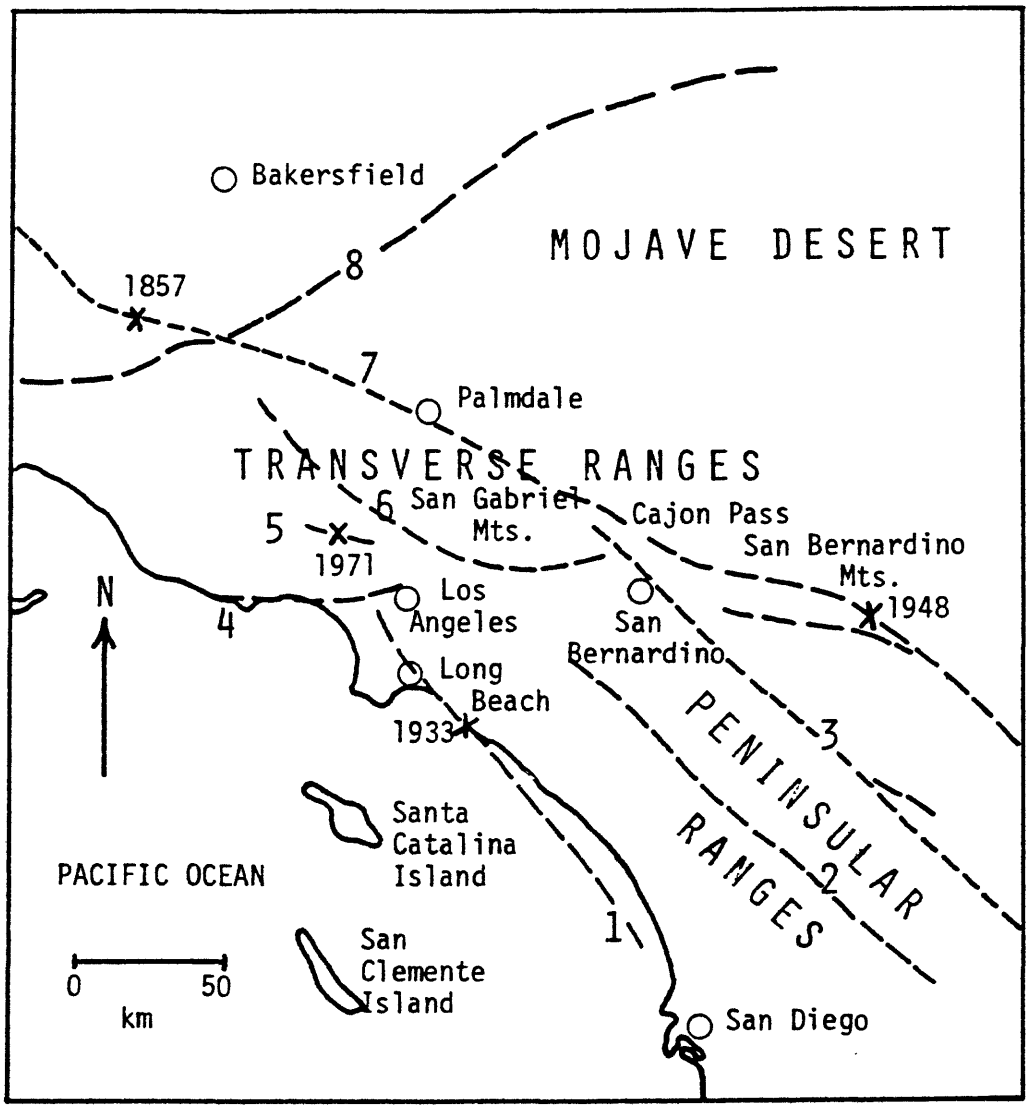

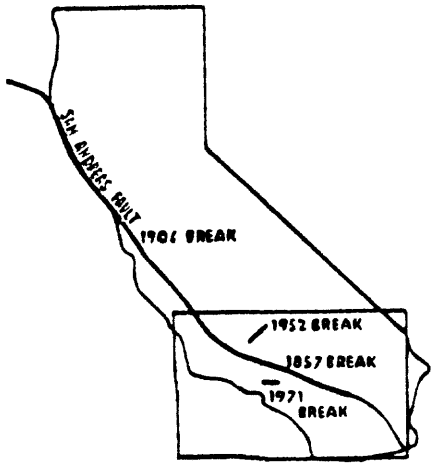

Faults Shown:

1 - Newport-Inglewood
2 - Elsinore
3 - San Jacinto
4 - Santa Monica-Malibu Coast
5 - San Fernando
6 - San Gabriel
7 - San Andreas
8 - Garlock
X - Important Recent Earthquakes

Figure 1-1. Map of selected important Southern California faults believed to be capable of supporting major earthquakes.

It has been postulated that a major earthquake along the San Andreas is likely to initiate somewhere between the locked region near Cajon Pass and the uplift region near Palmdale (personal communication or public statements by: Brune, 1980; Rawson, 1980; Bolt, 1980; and others). Such an earthquake could rupture several hundred kilometers along the San Andreas Fault causing catastrophic ground shaking over a substantial area of high population density. Therefore, major earthquake ruptures along the San Andreas in the vicinity of the Los Angeles basin are studied in this report in order to address the earthquake hazards for the Los Angeles basin.

The most recent major earthquake rupture to occur along the Newport-Inglewood Fault was the 1933 Long Beach Earthquake (magnitude approximately 6.3). This event killed about 100 people and caused widespread damage in Long Beach and other coastal communities. This event clearly establishes the Newport-Inglewood Fault as capable of supporting a major earthquake (Richter, 1958 and Allen, et al., 1965). If the 1933 earthquake had ruptured further to the north toward Beverly Hills, the fatalities and destruction could have been significantly greater. The western region of the Los Angeles basin is probably more vulnerable to a major earthquake along the Newport-Inglewood Fault than to a major earthquake along the San Andreas Fault due to the proximity to the rupture zone. Therefore, major earthquake ruptures along the Newport-Inglewood Fault are also studied in this report in order to address the earthquake hazards for the Los Angeles basin.

1.2 OBJECTIVES AND ORGANIZATION OF REPORT

The objective of this report is to quantify the potential earthquake shaking for the Los Angeles basin resulting from major earthquakes on nearby faults. The strategy is to use numerical modeling methods to represent the physics of earthquake rupture and wave propagation in order to compute synthetic ground motions. The computer model has been calibrated and validated against the strong motion recordings for five major Southern California earthquakes. This work has been discussed in detail in the following reports: DELTA, 1978; DELTA, 1979; DELTA, 1980a and DELTA 1980b.

The earthquake model is used to compute site-specific ground motions resulting from prescribed subsurface geologies, fault slippage, and rupture configurations. As discussed in the previous section, the Los Angeles basin is exposed to earthquake hazards from several nearby and active faults. The ground motions are calculated in the Los Angeles basin for several earthquakes on these faults using critical rupture configurations with respect to the receivers in the Los Angeles basin. The resulting ground motions are examined as a function of distance and orientation from several major earthquakes in Chapter 4 and as a function of model parameters such as rupture extent and fault type in Chapter 5.

The methodology and validation of the earthquake model is discussed in Sections 3.1 and 3.2, respectively. The methodology is based on integral representations over the rupture surface of the ground motions from elementary point-dislocations (Green's functions) convolved with a prescription of fault slippage at each integration node point. The Green's functions analytically account for the complete characterization of wave propagation from every point of rupture to every receiver of interest in a viscoelastic layered representation of the subsurface geology. The model parameters characterizing the rupture configuration and the fault slippage at each point of rupture are included when evaluating the spatial integrals over the rupture surface. Because the Green's functions account for such a

substantial portion of the numerical procedure for distributed ruptures, the methodology and validation of the associated numerical procedure used to evaluate the Green's functions is discussed in Sections 2.1 and 2.2, respectively.

Ground motion maps for the Los Angeles basin are presented in Chapter 4 for several possible earthquakes from nearby faults. In Section 4.1, a viscoelastic layered earth model of the subsurface geology is presented for the Los Angeles basin. This earth structure represents an average geologic structure as a function of depth for propagation paths between the various ruptures and all the receivers of interest in the Los Angeles basin. Values used for the seismic velocities in each layer are based on a composite of the geologic and seismic data available for the Los Angeles basin. Values used for the densities and material quality factors are based on generic formulae for Southern California geologic environments. Also discussed in Section 4.1 is the computation of the Green's functions for this Los Angeles basin geologic structure using the numerical procedure discussed in Chapter 2. The Green's functions include frequencies between 0 and 5 Hz and are calculated for a mesh of nodes representing horizontal distances between 1 and 200 km from the rupture surface and vertical depths along the rupture surface from 0 to 15 km.

Ground motions from major earthquakes along the San Andreas Fault for four critical rupture configurations are calculated using the numerical procedure discussed in Chapter 3. The results are presented in Section 4.2 in the form of maps describing values of peak acceleration, velocity and displacement at 22 receivers located throughout the Los Angeles basin. Two of the four rupture configurations represent two different incoherent rupture simulations (magnitude approximately 7.5) between the locked portion of the fault near Cajon Pass and the Southern California Uplift near Palmdale. The other two rupture configurations represent two different incoherent rupture simulations (magnitude approximately 7.5) centered around the locked portion of the fault. The same ground motion maps are

presented in Section 4.3 for two different incoherent rupture simulations (magnitude approximately 6.8) along the Newport-Inglewood Fault from a point offshore near Laguna Beach to a point northwest of Long Beach near Torrance. The magnitude of 6.8 corresponds to a hypothesized rupture length of 50 km and is not intended to illustrate the capability of the Newport-Inglewood Fault.

The sensitivity of the calculated ground motions to particular model parameters is investigated in Chapter 5. Ground motions at downtown Los Angeles are calculated for ten different earthquake ruptures along the San Andreas Fault using the numerical procedure discussed in Chapter 3. The resulting synthetic time histories and associated pseudo-velocity response spectra are compared in order to quantify the influences of a particular earthquake parameter. Each earthquake calculation is repeated four times using four different incoherent rupture simulations. Thereby, any bias introduced by the prescription of incoherent rupture (refer to Subsection 3.1.4) is suppressed by using the average results of the four simulations per earthquake (viz., mean response spectral values at each period and mean peak values of acceleration, velocity and displacement are compared for a given sensitivity study).

The ten different earthquake ruptures are grouped into five types of sensitivity studies corresponding to the five sections in Chapter 5. The first set of sensitivity studies in Section 5.1 ascertains the influences of rupture length on the computed results. The ground motions from unilateral strike-slip earthquakes along the San Andreas Fault are compared for four different rupture lengths. The four different rupture lengths of 50, 100, 175 and 250 km correspond to earthquake magnitudes of approximately 7.2, 7.5, 7.8 and 8.0, respectively. The sensitivity studies in Section 5.2 ascertain the influences of fault type on the computed results. The ground motions from a magnitude 7.5 unilateral earthquake along the San Andreas Fault are compared for strike-slip and 45 degree oblique motions. The sensitivity studies in Section 5.3 ascertain the influences of rupture direction on the computed results. The ground motions from a magnitude 7.5 strike-slip earthquake along the San Andreas Fault are compared for three different rupture directions

(viz., unilateral rupture from southeast to northwest; unilateral rupture from northwest to souteast; and bilateral rupture in both directions from the midpoint). Also, the ground motions from a magnitude 8.0 unilateral strike-slip earthquake along the San Andreas Fault are compared for two different rupture directions (i.e., southeast to northwest and northwest to southeast). The sensitivity studies in Section 5.4 ascertain the influences of rupture velocity on the computed results. The ground motions from a magnitude 7.5 unilateral strike-slip earthquake along the San Andreas Fault are compared for gross rupture velocities of 50 and 90 percent of the shear wave velocity in each subsurface layer. The sensitivity studies in Section 5.5 ascertain the influences of the deepest extent of rupture on the computed results. The ground motions from unilateral strike-slip earthquakes along the San Andreas Fault are compared for two different fault bottoms. The two fault bottoms extend to depths of 11.3 and 15 km and correspond to earthquake magnitudes of approximately 7.5 and 7.7, respectively.

A summary of the results is presented in Chapter 6. Conclusions regarding the applicability of the results are also discussed. In particular, the limited frequency content (5 Hz) and the uncertainties in the quality factors that characterize wave attenuation in the Los Angeles basin are discussed within the context of further work.

CHAPTER 2

GREEN'S FUNCTIONS FOR ELEMENTARY POINT DISLOCATIONS

2.1 METHODOLOGY

In this section, the methodology used to calculate the response of a layered viscoelastic half-space to a buried point source is described in considerable detail. The term Green's function will be used to represent the three components of ground motion observed at a particular distance and azimuth from the source, in which the source is an elementary point rupture located at a particular depth in the layered viscoelastic half-space. The formulation of the method and the calculation of the three-dimensional Green's functions are conducted in the frequency domain with the azimuthal dependence represented by a Fourier series expansion. The complete response at a particular frequency for any source-receiver geometry is expressed in terms of semi-infinite integrals with respect to wavenumber so as to automatically include all types of waves in a layered half-space (both near-field and far-field terms for body waves, head waves, multiple reverberations and interconversions, leaky modes, surface waves, etc.). Time domain results are then generated through use of a discrete Fast Fourier Transform algorithm.

In what follows is a summary of the formulation and methodology as presented by Apsel (1979) that is being used to solve this three-dimensional wave propagation problem. The formulation entails an analytic derivation of the three-dimensional dynamic displacement vector and stress tensor components resulting from concentrated point forces buried in a layered viscoelastic half-space. In order to obtain the Green's function displacements resulting from concentrated point dislocations, the Knopoff-deHoop (1958) representation theorem is readily used to reciprocally express the surface displacements due to a buried dislocation in terms of the stress tensor solution evaluated at the depth of the source due to a point force

acting at the free surface. The reader is referred to Appendix IV, Part I of Apsel (1979) for more details on this reciprocal representation of the results.

2.1.1 Integral Representations Over Wavenumber

The cylindrical components of the displacement and stress fields in the jth layer associated with a concentrated source located in the ℓth medium can by written as

$$4\pi\left(\bar{\mu}ru_r^j,\ r^2\sigma_{rz}^j,\ r^2\sigma_{rr}^j\right) = \sum_{n=0} P_n\left(r_o U_{rn}^j,\ r_o^2\,\Sigma_{rzn}^j,\ r_o^2\,\Sigma_{rrn}^j\right)\cos[n(\theta-\theta_o)]$$

$$4\pi\left(\bar{\mu}ru_\theta^j,\ r_\theta^2\sigma_{\theta z}^j,\ r^2\sigma_{\theta r}^j\right) = \sum_{n=0} P_n\left(r_o U_{\theta n}^j,\ r_o^2\,\Sigma_{\theta zn}^j,\ r_o^2\,\Sigma_{\theta rn}^j\right)\sin[n(\theta-\theta_o)]$$

$$4\pi\left(\bar{\mu}ru_z^j,\ r^2\sigma_{zz}^j,\ r^2\sigma_{\theta\theta}^j\right) = \sum_{n=0} P_n\left(r_o U_{zn}^j,\ r_o^2\,\Sigma_{zzn}^j,\ r_o^2\,\Sigma_{\theta\theta n}^j\right)\cos[n(\theta-\theta_o)] \qquad (2\text{-}1)$$

where $r_o = \omega r/\bar{\beta}$, $\bar{\beta}$ and $\bar{\mu}$ correspond to a shear wave velocity and a shear modulus of reference, P_o denotes the vertical component of the point load while P_1 represents the horizontal component of the point load along the $\theta = \theta_o$ azimuthal direction. The terms U_{rn}^j , ... , Σ_{rzn}^j , ... , are functions of the dimensionless variables r_o and $z_o = \omega z/\bar{\beta}$, and are obtained from the following Hankel transform-type integrals

$$\begin{Bmatrix} U^j_{rn} \pm U^j_{\theta n} \\ \Sigma^j_{rzn} \pm \Sigma^j_{\theta zn} \end{Bmatrix} = \int_0^\infty \begin{Bmatrix} \pm u^j_{1n} + u^j_{3n} \\ \pm \sigma^j_{21n} + \sigma^j_{23n} \end{Bmatrix} k\, J_{n\pm1}(kr_o)dk$$

$$\begin{Bmatrix} U^j_{zn} \\ \Sigma^j_{zzn} \\ \Sigma^j_{rrn} + \Sigma^j_{\theta\theta n} \\ \Sigma^j_{rrn} + \frac{2c_j}{d_j r_o}\left(U^j_{rn} + nU^j_{\theta n}\right) \\ \Sigma^j_{\theta rn} + \frac{2c_j}{d_j r_o}\left(nU^j_{rn} + U^j_{\theta n}\right) \end{Bmatrix} = \int_0^\infty \begin{Bmatrix} u^j_{2n} \\ \sigma^j_{22n} \\ \sigma^j_{33n} \\ \sigma^j_{11n} \\ \sigma^j_{31n} \end{Bmatrix} k\, J_n(kr_o)dk$$

(2-2)

in which $c_j = (\beta_j/\overline{\beta})^2$, $d_j = \overline{\rho}/\rho_j$, β_j and ρ_j correspond, respectively, to the shear wave velocity and density in the jth layer, and $\overline{\beta}$ and $\overline{\rho}$ are a shear wave velocity and density of reference ($\overline{\mu} = \overline{\beta^2\rho}$). The material quality factors Q_{β_j} and Q_{α_j} are accomodated by forming complex shear and compressional wave velocities, β_j and α_j, as discussed in Section 2.5, Part I of Apsel (1979).

The kernels u_{1n}, u_{2n}, σ_{21n}, σ_{22n}, σ_{33n} and σ_{11n} are associated with waves polarized in vertical planes (P, SV, Rayleigh), while the terms u_{3n}, σ_{23n} and σ_{31n} are associated with waves polarized in horizontal planes (SH, Love). All of these kernels are functions of the variables which describe the depth dependence of the problem; namely, the wavenumber (k), dimensionless receiver depth (z_o), dimensionless source depth (z^s_o) and viscoelastic layer properties (i.e., shear and compressional wave velocities, density, shear and compressional quality factors and layer thickness). The Bessel functions are functions of the variables k, r_o which describe the radial dependence of the problem and respectively denote wavenumber and dimensionless epicentral distance.

Again, the azimuthal dependence is represented by the Fourier series expansion in Eq. (2-1). Due to this Hankel transform-type formulation, it is expedient to numerically calculate the integrals for multiple epicentral distances and/or multiple depth variables simultaneously. In the near field, the terms U_{rn}, Σ_{rzn}, Σ_{rrn}, $\Sigma_{\theta\theta n}$ include some particle motion polarized in horizontal planes while the terms $U_{\theta n}$, $\Sigma_{\theta zn}$, $\Sigma_{\theta rn}$ include some particle motion polarized in vertical planes. For example, the azimuthal displacement may be isolated in Eq. (2-2) to read as

$$U^j_{\theta n} = \int_0^\infty \left\{ u^j_{1n} \left[\frac{n J_n(kr_o)}{(kr_o)} \right] - u^j_{3n} \left[\frac{\partial J_n(kr_o)}{\partial (kr_o)} \right] \right\} k \, dk \, . \tag{2-3}$$

The terms associated with waves polarized in vertical planes are obtained from

$$\left\{ \begin{array}{c} u^j_{1n} \\ u^j_{2n} \\ \hline \sigma^j_{21n} \\ \sigma^j_{22n} \\ \hline \sigma^j_{33n} \\ \sigma^j_{11n} \end{array} \right\} = \left[\begin{array}{c|c} I^j_{11} & I^j_{12} \\ \hline I^j_{21} & I^j_{22} \\ \hline I^j_{31} & I^j_{32} \end{array} \right] \left[\begin{array}{c|c} E^j_d(z_o) & 0 \\ \hline 0 & E^j_u(z_o) \end{array} \right] \left\{ \begin{array}{c} n^j_{dn}(z_o) \\ \hline n^j_{un}(z_o) \end{array} \right\} \tag{2-4}$$

where the 2 x 2 matrices I^j_{11}, I^j_{12} ... are defined by

$$\begin{bmatrix} I^j_{11} & I^j_{12} \\ I^j_{21} & I^j_{22} \\ I^j_{31} & I^j_{32} \end{bmatrix} = d_j^{-1} \left[\begin{array}{cc|cc} -kd_j & \nu_j' d_j & -kd_j & \nu_j' d_j \\ -\nu_j d_j & kd_j & \nu_j d_j & -kd_j \\ \hline 2k\nu_j c_j & -(2k^2c_j-1) & -2k\nu_j c_j & (2k^2c_j-1) \\ (2k^2c_j-1) & -2k\nu_j' c_j & (2k^2c_j-1) & -2k\nu_j' c_j \\ \hline 2(2\gamma_j^2-1) - 2k^2c_j & 2k\nu_j' c_j & 2(2\gamma_j^2-1) - 2k^2c_j & 2k\nu_j' c_j \\ (2\gamma_j^2-1) - 2k^2c_j & 2k\nu_j' c_j & (2\gamma_j^2-1) - 2k^2c_j & 2k\nu_j' c_j \end{array}\right] \tag{2-5}$$

while the 2 x 2 matrices $E^j_d(z_o)$ and $E^j_u(z_o)$ are given by

$$E^j_d(z_o) = \text{diag}\left(\exp\left[-\nu_j(z_o - z_o^{j-1})\right], \exp\left[-\nu_j'(z_o - z_o^{j-1})\right]\right) \tag{2-6}$$

$$E^j_u(z_o) = \text{diag}\left(\exp\left[\nu_j(z_o - z_o^{j})\right], \exp\left[\nu_j'(z_o - z_o^{j})\right]\right) \tag{2-7}$$

In the above equations, $\nu_j = [k^2 - \bar{\beta}/\alpha_j)^2]^{1/2}$, $\nu_j' = [k^2 - (\bar{\beta}/\beta_j)^2]^{1/2}$, $\gamma_j = \beta_j/\alpha_j$, and $z_o^j = \omega z_j/\bar{\beta}$ $(z_o^{N+1} = z_o^N)$ in which z_j defines the position of the lower interface of the jth layer $(z_o^0 = 0)$.

The 2 x 1 vectors $n^j_{dn}(z_o)$ and $n^j_{un}(z_o)$ correspond to the amplitudes of the downwardly and upwardly propagating P and SV waves in the jth layer. These amplitudes are independent of z_o in all layers with exception of the ℓth layer in which the source is located. The wave amplitudes n^j_{un} and n^j_{dn} in the jth layer are obtained from the following factorization

$$
\begin{cases} \eta^{j}_{un}(z_o) = \hat{T}^{u}_{j}\ \hat{T}^{u}_{j+1}\ \cdots\ \hat{T}^{u}_{\ell-1}\ \eta^{\ell}_{un}(z_o^{\ell-1}) & (j = 1,\ \ell-1) \\ \eta^{j}_{dn}(z_o) = \hat{R}^{u}_{j-1}\ \eta^{j}_{un}(z_o^{j-1}) & (j = 1,\ \ell-1) \end{cases}
$$

$$
\begin{cases} \eta^{j}_{dn}(z_o) = \hat{T}^{d}_{j-1}\ \hat{T}^{d}_{j-2}\ \cdots\ \hat{T}^{d}_{\ell}\ \eta^{\ell}_{dn}(z_o^{\ell}) & (j = \ell+1,\ N+1) \\ \eta^{j}_{un}(z_o) = \hat{R}^{d}_{j}\ \eta^{j}_{dn}(z_o^{j}) & (j = \ell+1,\ N+1) \end{cases}
$$

$$
\begin{cases} \eta^{\ell}_{un}(z_o) = \left(I - \hat{R}^{d}_{\ell}\ \hat{R}^{u}_{\ell-1}\right)^{-1}\left(S^{\ell}_{un} + \hat{R}^{d}_{\ell}\ S^{\ell}_{dn}\right) & (z_o^{\ell-1} \le z_o < z_o^{s}) \\ \eta^{\ell}_{dn}(z_o) = \hat{R}^{u}_{\ell-1}\ \eta^{\ell}_{un}(z_o^{\ell-1}) & (z_o^{\ell-1} \le z_o < z_o^{s}) \end{cases}
$$

$$
\begin{cases} \eta^{\ell}_{dn}(z_o) = \left(I - \hat{R}^{u}_{\ell-1}\ \hat{R}^{d}_{\ell}\right)^{-1}\left(S^{\ell}_{dn} + \hat{R}^{u}_{\ell-1}\ S^{\ell}_{un}\right) & (z_o^{s} < z_o \le z_o^{\ell}) \\ \eta^{\ell}_{un}(z_o) = \hat{R}^{d}_{\ell}\ \eta^{\ell}_{dn}(z_o^{\ell}) & (z_o^{s} < z_o \le z_o^{\ell}) \end{cases} \tag{2-8}
$$

in which I denotes the 2×2 identity matrix, $z_o^{s} = \omega z^{s}/\bar{\beta}$, z_s defines the location of the point source, and

$$
S^{\ell}_{d0} = d_{\ell}\begin{Bmatrix} \exp\left[\nu_{\ell}(z_o^{s} - z_o^{\ell-1})\right] \\ \dfrac{k}{\nu'_{\ell}}\exp\left[\nu'_{\ell}(z_o^{s} - z_o^{\ell-1})\right] \end{Bmatrix}, \quad S^{\ell}_{u0} = -d_{\ell}\begin{Bmatrix} \exp\left[-\nu_{\ell}(z_o^{s} - z_o^{\ell})\right] \\ \dfrac{k}{\nu'_{\ell}}\exp\left[-\nu'_{\ell}(z_o^{s} - z_o^{\ell})\right] \end{Bmatrix}
$$

$$
S^{\ell}_{d1} = d_{\ell}\begin{Bmatrix} \dfrac{k}{\nu_{\ell}}\exp\left[\nu_{\ell}(z_o^{s} - z_o^{\ell-1})\right] \\ \exp\left[\nu'_{\ell}(z_o^{s} - z_o^{\ell-1})\right] \end{Bmatrix}, \quad S^{\ell}_{u1} = d_{\ell}\begin{Bmatrix} \dfrac{k}{\nu_{\ell}}\exp\left[-\nu_{\ell}(z_o^{s} - z_o^{\ell})\right] \\ \exp\left[-\nu'_{\ell}(z_o^{s} - z_o^{\ell})\right] \end{Bmatrix}. \tag{2-9}
$$

The 2×2 matrices of generalized reflection and transmission coefficients $\hat{R}_j^u$, $\hat{R}_j^d$, $\hat{T}_j^u$ and $\hat{T}_j^d$ are obtained from the recurrence relations

$$\begin{cases} \hat{R}_o^u = R_o^u \\ \hat{T}_j^u = \left(I - R_j^d \hat{R}_{j-1}^u\right)^{-1} T_j^u & (j \geq 1) \\ \hat{R}_j^u = R_j^u + T_j^d \hat{R}_{j-1}^u \hat{T}_j^u & (j \geq 1) \end{cases}$$

$$\begin{cases} \hat{R}_{N+1}^d = 0 \\ \hat{T}_j^d = \left(I - R_j^u \hat{R}_{j+1}^d\right)^{-1} T_j^d & (j \leq N) \\ \hat{R}_j^d = R_j^d + T_j^u \hat{R}_{j+1}^d \hat{T}_j^d & (j \leq N) \end{cases}$$

(2-10)

in which the 2 x 2 matrices of modified reflection and transmission coefficients are given by

$$R_o^u = -\left(I_{21}^1\right)^{-1} I_{22}^1 E_u^1(0)$$

$$\left[\begin{array}{c|c} T_j^d & R_j^u \\ \hline R_j^d & T_j^u \end{array}\right] = \left[\begin{array}{c|c} -I_{11}^{j+1} & I_{12}^j \\ \hline -I_{21}^{j+1} & I_{22}^j \end{array}\right]^{-1} \left[\begin{array}{c|c} -I_{11}^j & I_{12}^{j+1} \\ \hline -I_{21}^j & I_{22}^{j+1} \end{array}\right] \left[\begin{array}{c|c} E_d^j(z_o^j) & 0 \\ \hline 0 & E_u^{j+1}(z_o^j) \end{array}\right].$$

(2-11)

$(1 \leq j \leq N)$

Explicit expression for the modified reflection and transmission coefficients are given in Appendix I, Part I, of Apsel (1979).

To insure the numerical convergence of the integral representation for large values of the dimensionless wavenumber k, it is necessary to introduce some modifications to the procedure just described. The general formalism remains intact except for the following changes:

(i) The matrices I^j_{pq} $(p = 1,2,3;\ q = 1,2)$ appearing in Eqs. (2-4) and (2-11) are replaced by

$$\bar{I}^j_{pq} = I^j_{pq}\, A_j^{-1} \qquad (p = 1,2,3;\ q = 1,2) \tag{2-12}$$

where A_j^{-1} is the inverse of the 2×2 matrix

$$A_j = -\frac{1}{\kappa_j}\begin{bmatrix} (k - \nu_j) & (k - \nu_j') \\ \nu_j + (\kappa_j - 1)k & -k - (\kappa_j - 1)\,\nu_j' \end{bmatrix} \tag{2-13}$$

in which $\kappa_j = (1 + \gamma_j^2)/(1 - \gamma_j^2)$.

(ii) The diagonal matrices $E^j_d(z_o)$ and $E^j_u(z_o)$ appearing in Eqs. (2-4) and (2-11) are replaced by

$$\bar{E}^j_d(z_o) = A_j\, E^j_d(z_o)\, A_j^{-1}$$

$$\bar{E}^j_u(z_o) = A_j\, E^j_u(z_o)\, A_j^{-1} \tag{2-14}$$

and,

(iii) The source terms S^{ℓ}_{dn} and S^{ℓ}_{un} appearing in Eqs. (2-8) are replaced by

$$\bar{S}^{\ell}_{dn} = A_{\ell}\, S^{\ell}_{dn}$$

$$\bar{S}^{\ell}_{un} = A_{\ell}\, S^{\ell}_{un} \quad . \tag{2-15}$$

Detailed expressions for I^{j}_{pq}, $\bar{E}^{j}_{d}$, $\bar{E}^{j}_{u}$, $\bar{S}^{\ell}_{dn}$ and $\bar{S}^{\ell}_{un}$ as well as for the resulting modified reflection and transmission coefficients are presented in Appendix II, Part I of Apsel (1979).

The terms u_{3n}, σ_{23n} and σ_{31n} associated with waves polarized in horizontal planes are obtained from

$$\begin{Bmatrix} u^{j}_{3n} \\ \sigma^{j}_{23n} \\ \sigma^{j}_{13n} \end{Bmatrix} = \begin{bmatrix} I^{j}_{11} & I^{j}_{12} \\ I^{j}_{21} & I^{j}_{22} \\ I^{j}_{31} & I^{j}_{32} \end{bmatrix} \begin{bmatrix} E^{j}_{d}(z_o) & 0 \\ 0 & E^{j}_{u}(z_o) \end{bmatrix} \begin{Bmatrix} n^{j}_{dn}(z_o) \\ n^{j}_{un}(z_o) \end{Bmatrix} \tag{2-16}$$

which has the same form as Eq. (2-4) except that in this case the quantities involved are scalars. The terms I^{j}_{11}, I^{j}_{12}, ... , are defined by

$$\begin{bmatrix} I^{j}_{11} & I^{j}_{12} \\ I^{j}_{21} & I^{j}_{22} \\ I^{j}_{31} & I^{j}_{32} \end{bmatrix} = \begin{bmatrix} k & k \\ -k\nu'_j c_j d_j^{-1} & k\nu'_j c_j d_j^{-1} \\ k^2 c_j d_j^{-1} & k^2 c_j d_j^{-1} \end{bmatrix} \tag{2-17}$$

while

$$E^{j}_{d}(z_o) = \exp\left[-\nu'_j (z_o - z_o^{j-1})\right] \tag{2-18}$$

$$E^{j}_{u}(z_o) = \exp\left[\nu'_j (z_o - z_o^{j})\right] \quad . \tag{2-19}$$

The terms $\eta^j_{dn}(z_o)$ and $\eta^j_{un}(z_o)$ correspond to the amplitudes of the downwardly and upwardly propagating SH waves in the jth layer. The wave amplitudes η^j_{dn} and η^j_{un} are also obtained from the factorization given in Eq. (2-8) except that the terms S^{ℓ}_{dn} and S^{ℓ}_{un} are now given by

$$
\begin{aligned}
S^{\ell}_{d0} &= 0 \ , \qquad S^{\ell}_{u0} = 0 \ , \\
S^{\ell}_{d1} &= \left(k\nu'_{\ell}c_{\ell}d_{\ell}^{-1}\right)^{-1} \exp\left[\nu'_{\ell}(z^s_o - z^{\ell-1}_o)\right] \ , \\
S^{\ell}_{u1} &= \left(k\nu'_{\ell}c_{\ell}d_{\ell}^{-1}\right)^{-1} \exp\left[-\nu'_{\ell}(z^s_o - z^{\ell}_o)\right] \ .
\end{aligned}
\tag{2-20}
$$

The generalized reflection and transmission coefficients for the case of horizontally polarized waves follow the same recurrence relations presented in Eq. (2-10). The modified reflection and transmission coefficients are also given in this case by Eq. (2-11) with the terms appearing in that equation defined as in Eqs. (2-17), (2-18) and (2-19). In particular, these coefficients are given by

$$
\begin{aligned}
R^u_o &= \exp(-\nu'_1 z^1_o) \\
\begin{bmatrix} T^d_j & R^u_j \\ R^d_j & T^u_j \end{bmatrix} &= \frac{1}{\Delta} \begin{bmatrix} 2\nu'_j c_j d_j^{-1} & -\left(\nu'_j c_j d_j^{-1} - \nu'_{j+1} c_{j+1} d_{j+1}^{-1}\right) \\ \left(\nu'_j c_j d_j^{-1} - \nu'_{j+1} c_{j+1} d_{j+1}^{-1}\right) & 2\nu'_{j+1} c_{j+1} d_{j+1}^{-1} \end{bmatrix} \\
&\quad \times \begin{bmatrix} \exp\left[-\nu'_j (z^j_o - z^{j-1}_o)\right] & 0 \\ 0 & \exp\left[\nu'_{j+1}(z^j_o - z^{j+1}_o)\right] \end{bmatrix} , \\
&\qquad\qquad (1 \le j \le N)
\end{aligned}
\tag{2-21}
$$

in which $\Delta = \nu'_j c_j d_j^{-1} + \nu'_{j+1} c_{j+1} d_{j+1}^{-1}$.

In the case of horizontally polarized waves the integral representation just described is valid for all values of the dimensionless wavenumber k and does not need to be modified for large values of k.

2.1.2 Method of Integration over Wavenumber

The Hankel transform-type integral representations of the displacement and stress components in the frequency domain are summarized in Eq. (2-2) and involve quantities of the form

$$I_n(r_o,z_o) = \int_0^\infty F(k,z_o)\, J_n(kr_o)\, dk\ , \qquad n = 0,1,2\ . \tag{2-22}$$

for the concentrated point loads. The kernel $F(k,z_o)$ depends upon wavenumber, frequency, receiver and source depth and layer properties; whereas the Bessel functions $J_n(kr_o)$ depend only upon the product of wavenumber times normalized epicentral observation distance ($r_o = \omega r/\bar{\beta}$). An effective procedure to evaluate the F integrands has been summarized in Section 2.1.1 based on highly efficient factorizations for the upgoing and downgoing wave amplitudes in each layer (refer to Eqs. (2-4) through (2-8)). All that remains then is to develop an efficient numerical integration scheme capable of handling the oscillatory nature of the Bessel functions in addition to the vigorous behavior of the pervasive F integrands (as a function of wavenumber).

The basic philosophy behind the method to integration is to sample the F integrands sufficiently fine to allow piecewise polynomials to interpolate the amplitudes of the F functions between the integration points. Thereby, the numerical integration over the Bessel functions can be performed analytically over each integration interval, thus avoiding the oscillation hazard of the Bessel functions. The integration out to infinite wavenumber is either handled analytically or truncated past some finite wavenumber due to the exponential decay of the F integrands (see Section 4.2.3, Part I of Apsel (1979) for more details).

After trying several types and orders of polynomials, quartic polynomial interpolation was found to be the most effective order scheme to employ in general. The five integration points on a given interval are defined as k_1, k_2, k_3, k_4, k_5 with the quartic polynomial determined by

$$F(k,z_o) = \sum_{m=1}^{5} A_m \left(\frac{k - k_2}{\Delta k} \right)^{m-1} , \qquad (2\text{-}23)$$

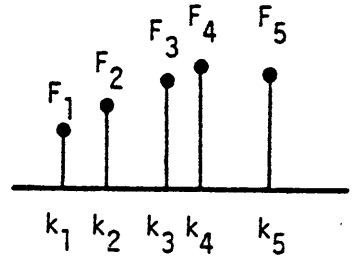

in which $\Delta k = k_4 - k_2$. The positions of the five integration points are chosen to assure a desired accuracy in the polynomial interpolation scheme. The normalization inherent in Eq. (2-23) is with the intention of integrating from k_2 to k_4 on each interval and overlapping k_1 and k_5 into the outer intervals in order to insure a smoother fit to $F(k, z_o)$ between k_2 and k_4.

Introducing matric notation, the coefficients $A_m (m = 1, 5)$ are uniquely determined by the five $F(k_m,z_o)$ according to

$$\underset{1x5}{(A_1, A_2, A_3, A_4, A_5)} = \underset{1x5}{(F_1, F_2, F_3, F_4, F_5)} \; \underset{5x5}{[C]^T} \qquad (2\text{-}24)$$

in which $F_m = F(k_m,z_o)$ and the individual elements of the interpolation matrix $[C]$ are listed in Section 4.2.4, Part I of Apsel (1979).

Rewriting the integral appearing in Eq. (2-22) as a summation of integrals over each interval (k_2,k_4), with $F(k, z_o)$ replaced by the quartic polynomial defined in Eqs. (2-23) and (2-24), leads to the following expression for $I_n(r_o,z_o)$:

$$I_n = \sum_{\text{intervals}} \left[\underset{1x5}{(F_1, F_2, F_3, F_4, F_5)} \quad \underset{5x5}{[C]^T} \int_{k_2}^{k_4} \underset{5x1}{\begin{Bmatrix} \left(\frac{k-k_2}{\Delta k}\right)^1 \\ \left(\frac{k-k_2}{\Delta k}\right)^2 \\ \left(\frac{k-k_2}{\Delta k}\right)^3 \\ \left(\frac{k-k_2}{\Delta k}\right)^4 \end{Bmatrix}} J_n(kr_o)\,dk \right] \tag{2-25}$$

in which superscript T denotes the transpose matrix. The summation in Eq. (2-25) is carried out over all the intervals of integration from k_2 to k_4, except for the first interval on which the integration is performed from k_1 to k_4 since no overlapping is possible from a previous interval. The overlapping into the outer integration intervals ensures a smooth fit to the F integrands over the integration interval (k_2, k_4), while at the same time provides desirable flexibility in sequentially sampling the F integrands over oscillatory wavenumber regions. For details on the error criteria used in sampling the F integrands, refer to Section 4.2.5, Part I of Apsel (1979).

It is important to notice in Eq. (4-25) that the product of the 5 x 5 matrix [C] times the 5 x 3 matrix of integrals (n = 0,1,2) is independent of source and receiver depth; hence needs to be formed only once for each epicentral range. Since the integrals in Eq. (2-25) can be evaluated analytically, the oscillation hazard of the Bessel functions is completely circumvented and the number of integration points is restricted to the tolerance desired in sampling the F integrands.

What remains to be discussed is the technique used to evaluate integrals of the type appearing in Eq. (2-25). Although formulae are available for these definite Bessel integrals, the following branch on the integration procedure for a given interval proves to be the more efficient

methodology. As depicted in Figure 2-1, the integration branch depends on the magnitude of the argument of the Bessel functions -- namely the product of dimensionless wavenumber k times dimensionless epicentral distance r_o.

In region 2 of Figure 2-1, the arguments of the Bessel functions are sufficiently large to allow Hankel's asymptotic expansions to replace the Bessel functions:

$$J_n(kr_o) = \sqrt{\frac{2}{\pi kr_o}}\left[P(n,kr_o)\cos(\chi) - Q(n,kr_o)\sin(\chi)\right] \tag{2-26}$$

where $\chi = kr_o - \left(\frac{n}{2} + \frac{1}{4}\right)\pi$ and, with $\delta = 4n^2$

$$P(n,kr_o) \sim 1 - \frac{(\delta-1)(\delta-9)}{2!(8kr_o)^2} + \frac{(\delta-1)(\delta-9)(\delta-25)(\delta-49)}{4!(8kr_o)^4} - \ldots$$

$$Q(n,kr_o) \sim \frac{(\delta-1)}{(8kr_o)} - \frac{(\delta-1)(\delta-9)\ (\delta-25)}{3!(8kr_o)^3} + \ldots \quad . \tag{2-27}$$

Using trigonometric identities, Eq. (2-26) can be rearranged into the more convenient form

$$J_n(kr_o) = \hat{P}(n,kr_o)\cos(kr_o) - \hat{Q}(n,kr_o)\sin(kr_o) \tag{2-28}$$

in which

$$\hat{P}(n,kr_o) = \sqrt{\frac{2}{\pi kr_o}}\left[P(n,kr_o)\cos\left(\frac{n}{2} + \frac{1}{4}\right)\pi + Q(n,kr_o)\sin\left(\frac{n}{2} + \frac{1}{4}\right)\pi\right]$$

$$\hat{Q}(n,kr_o) = \sqrt{\frac{2}{\pi kr_o}}\left[Q(n,kr_o)\cos\left(\frac{n}{2} + \frac{1}{4}\right)\pi - P(n,kr_o)\sin\left(\frac{n}{2} + \frac{1}{4}\right)\pi\right] .$$

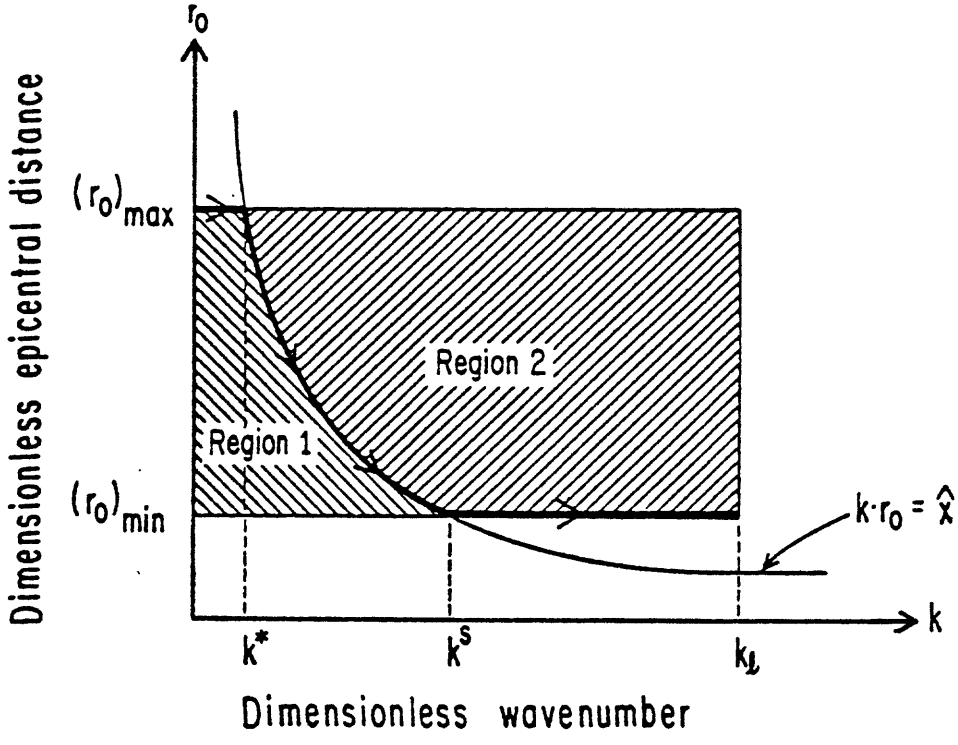

Figure 2-1. Regions for wavenumber integration separated by curve kr_0 = constant.

Now, for an interval contained within region 2 (i.e., $k_1 r_o > \hat{x}$), the Bessel functions are replaced by the expansions in Eq. (2-28), with the smoothly varying functions $\hat{P}(n,kr_o)$ and $\hat{Q}(n,kr_o)$ included in the polynomial interpolation of the F integrands. Therewith, the integral on the i^{th} interval may be written as follows if $k_1 r_o > \hat{x}$:

$$I_n^i(r_o,z_o) = \underset{1x5}{\{F\}^T} \underset{5x5}{[\hat{P}_n]} \underset{5x5}{[C]^T} \int_{k_2}^{k_4} \underset{5x1}{\{\kappa\}} \cos(kr_o)dk - \underset{1x5}{\{F\}^T} \underset{5x5}{[\hat{Q}_n]} \underset{5x5}{[C]^T} \int_{k_2}^{k_4} \underset{5x1}{\{\kappa\}} \sin(kr_o)dk \qquad (2\text{-}29)$$

in which

$$\text{diag}_m [\hat{P}_n] = \hat{P}(n,k_m r_o) \ , \quad \text{diag}_m [\hat{Q}_n] = \hat{Q}(n,k_m r_o)$$

and

$$\kappa_m = \left(\frac{k-k_2}{\Delta k}\right)^{m-1} \ , \quad m = 1,2,3,4,5 \ .$$

In region 1 of Figure 2-1, $k = k_4 - k_2$ is required to be small enough to insure that the Bessel functions oscillate slowly over the integration interval. Thereby, the entire Bessel function may be included in the polynomial interpolation of the F integrands, so that the integral on the i^{th} interval located in region 1 may be written by

$$I_n^i(r_o,z_o) = \underset{1x5}{\{F\}^T} \underset{5x5}{[J_n]} \underset{5x5}{[C]^T} \int_{k_2}^{k_4} \underset{5x1}{\{\kappa\}} dk \qquad (2\text{-}30)$$

in which

$$\text{diag}_m \left[\widetilde{J_n} \right] = J_n(k_m r_o)$$

and

$$\int_{k_2}^{k_4} \kappa_m dk = \Delta k/m \ , \quad m = 1,2,3,4,5.$$

The degree of smoothness necessary in the Bessel functions for Eq. (2-30) to be valid in region 1 depends on the accuracy desired in the numerical integration at a given frequency. For more details on the smoothness criteria, see section 4.2.6, Part I of Apsel (1979).

To complete the description of the method of integration, expressions for the integrals appearing in Eq. (2-29) are presented:

$$\int_{k_2}^{k_4} \begin{matrix}\cos\\ \sin\end{matrix}(kr_o)dk = \Delta k\left\{\begin{matrix}\cos\\ \sin\end{matrix}(\bar{x})S\right\}$$

$$\int_{k_2}^{k_4} \left(\frac{k-k_2}{\Delta k}\right)\begin{matrix}\cos\\ \sin\end{matrix}(kr_o)dk = \Delta k\left\{\frac{1}{2}\begin{matrix}\cos\\ \sin\end{matrix}(\bar{x})\,S \mp \frac{1}{\Delta x}\begin{matrix}\sin\\ \cos\end{matrix}(\bar{x})\left[S - \cos\left(\frac{\Delta x}{2}\right)\right]\right\}$$

$$\int_{k_2}^{k_4} \left(\frac{k-k_2}{\Delta k}\right)^2\begin{matrix}\cos\\ \sin\end{matrix}(kr_o)dk = \Delta k\left\{\frac{1}{2}\begin{matrix}\cos\\ \sin\end{matrix}(\bar{x})\left[S - \frac{4}{(\Delta x)^2}\left(S - \cos\frac{\Delta x}{2}\right)\right]\right.$$

$$\left. \mp \frac{1}{\Delta x}\begin{matrix}\sin\\ \cos\end{matrix}(\bar{x})\left[S - \cos\left(\frac{\Delta x}{2}\right)\right]\right\}$$

$$\int_{k_2}^{k_4} \left(\frac{k-k_2}{\Delta k}\right)^3\begin{matrix}\cos\\ \sin\end{matrix}(kr_o)dk = \Delta k\left\{\frac{1}{2}\begin{matrix}\cos\\ \sin\end{matrix}(\bar{x})\left[S - \frac{6}{(\Delta x)^2}\left(S - \cos\frac{\Delta x}{2}\right)\right]\right.$$

$$\left. \mp \frac{1}{\Delta x}\begin{matrix}\sin\\ \cos\end{matrix}(\bar{x})\left[\left(1.5\,S - \cos\frac{\Delta x}{2}\right) - \frac{6}{(\Delta x)^2}\left(S - \cos\frac{\Delta x}{2}\right)\right]\right\}$$

$$\int_{k_2}^{k_4} \left(\frac{k-k_2}{\Delta k}\right)^4\begin{matrix}\cos\\ \sin\end{matrix}(kr_o)\,dk = \Delta k\left\{\frac{1}{2}\begin{matrix}\cos\\ \sin\end{matrix}(\bar{x})\left[S - \frac{8}{(\Delta x)^2}\left(1.5\,S - \cos\frac{\Delta x}{2}\right)\right.\right.$$

$$\left. + \frac{48}{(\Delta x)^4}\left(S - \cos\frac{\Delta x}{2}\right)\right] \mp \frac{1}{\Delta x}\begin{matrix}\sin\\ \cos\end{matrix}(\bar{x})\left[\left(2.0\,S - \cos\frac{\Delta x}{2}\right)\right.$$

$$\left.\left. - \frac{12}{(\Delta x)^2}\left(S - \cos\frac{\Delta x}{2}\right)\right]\right\} \qquad (2\text{-}31)$$

in which

$$\bar{x} = \frac{1}{2}(k_2+k_4)r_o\ ,\quad \Delta x = \Delta k r_o\ ,\quad S = \frac{\sin(\Delta x/2)}{(\Delta x/2)}\ .$$

2.2 VALIDATION

The complexity of the numerical procedure used to evaluate the Green's functions suggests the need for an exhaustive set of validation calculations prior to employing the method in actual applications. Such a series of validation tests was successfully performed and presented in Chapter 5, Part I of Apsel (1979). Two of the validation studies are repeated here to demonstrate the reliability of the numerical procedure.

In the first validation study, the complete solution obtained using present method for a three-layered earth structure is compared to the results using the Finite Element approach of Day (1977) and to the hybrid Discrete Wavenumber/Finite Element Approach of Olson (1978). Although the alternate methods do not provide exact solutions, the particular problem chosen for comparison is expected to provide a rigorous validation over the limited (by cost) frequency band resolved by the alternate methods. The free-surface displacements resulting from the action of a buried point dislocation are tested for the earth structure shown in Figure 2-2, where individual parameters characterizing the layers are defined. The quality factors apply only to the present solution since the alternate solutions contain no material attenuation. The values of the quality factors are sufficiently large so as to insignificantly effect the amplitude of the results at the distances and highest frequencies of interest.

The source time dependence is represented by a ramp of one second duration and is equivalent to the vertical strike-slip dislocation depicted in Figure 2-2 with the receiver located at epicentral distances of 5, 15, 25 and 35 km at an azimuth of 22.5 degrees from the strike of the fault (in a dilatational quadrant). The ground motion is normalized by the ratio of the shear modulus (μ) in the source layer times 10^{10} cm^2 divided by the source moment (M_o). Comparisons for the surface displacements due to point dislocation at 5 km are shown in Figures 2-3 through 2-6 for the four epicentral distances, respectively. The alternate solutions have been low-pass filtered down to 0.5 Hz to remove spurious numerical ringing; the present results are computed to 5.0 Hz and passed through the same filter in order

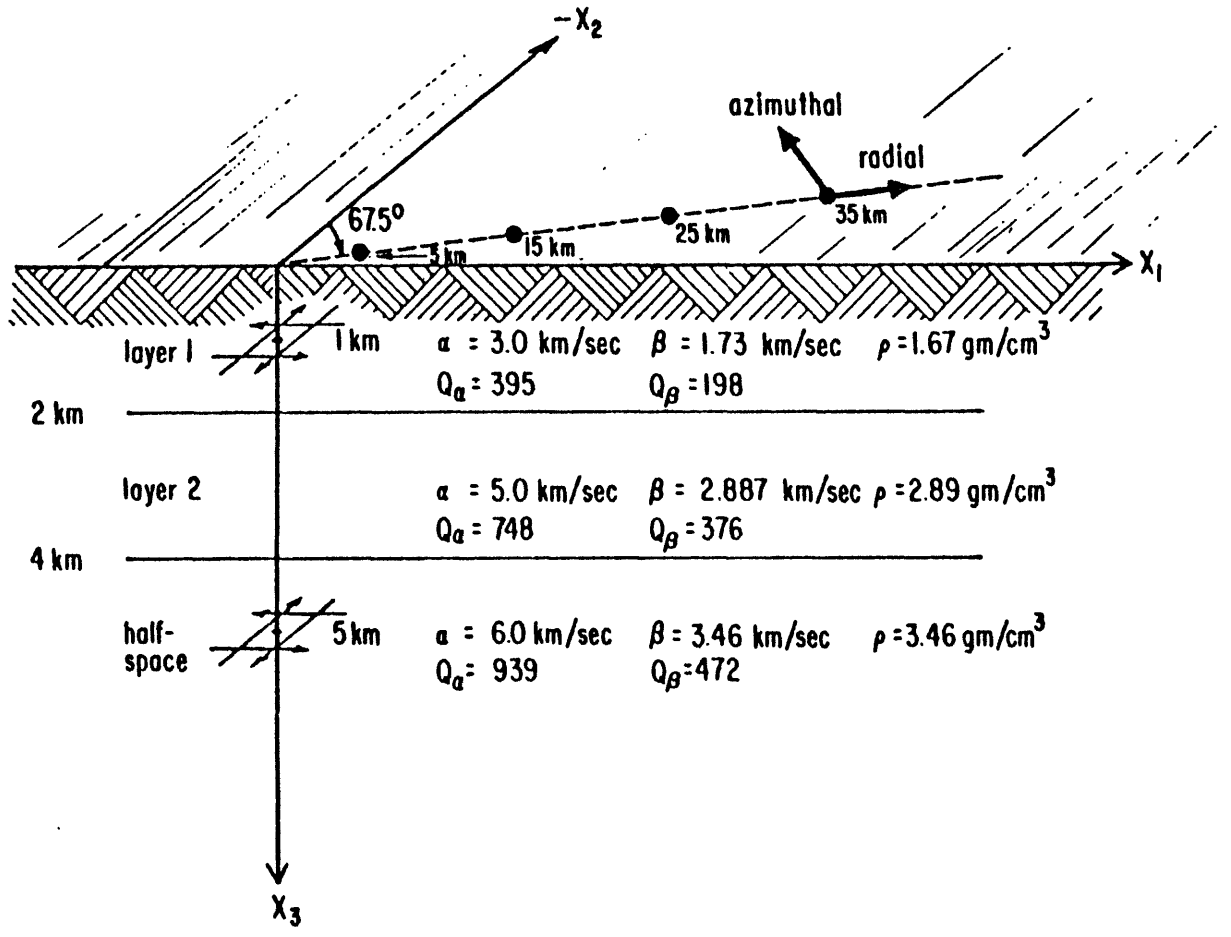

Figure 2-2. Source-receiver geometry and earth model, consisting of 2 layers overyling a half-space for use in comparison with the Finite Element (Day, 1977) and the Discrete Wavenumber/Finite Element (Olson, 1978) solutions.

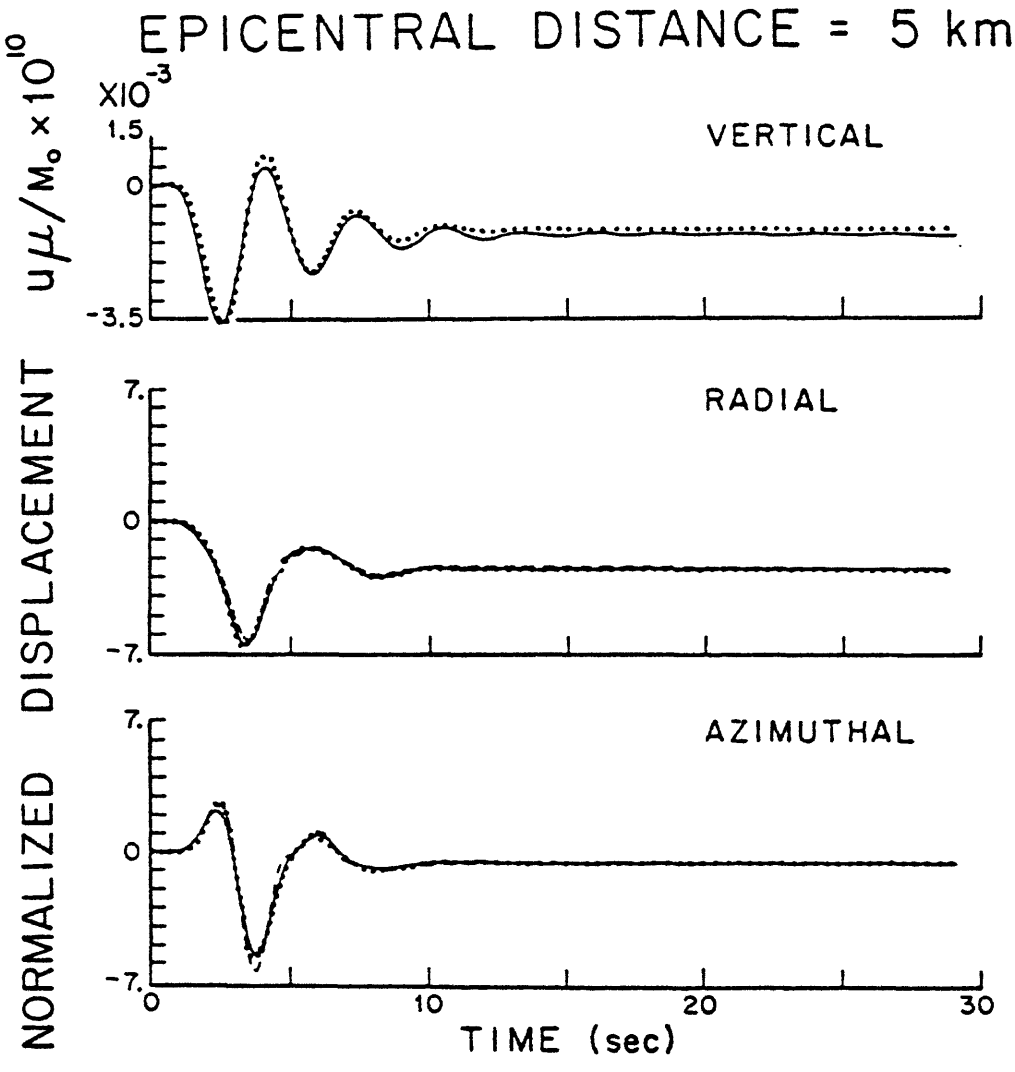

Figure 2-3. Comparison of the present solution with the Finite Element Solution (Day, 1977) and the Discrete Wavenumber/Finite Element solution (Olson, 1978) for the free surface displacement components at an epicentral distance of 5 km due to a vertical strike-slip dislocation buried at a depth of 5 km in the earth model depicted in Figure 2-2. Vertical component not calculated in the Finite Element method.

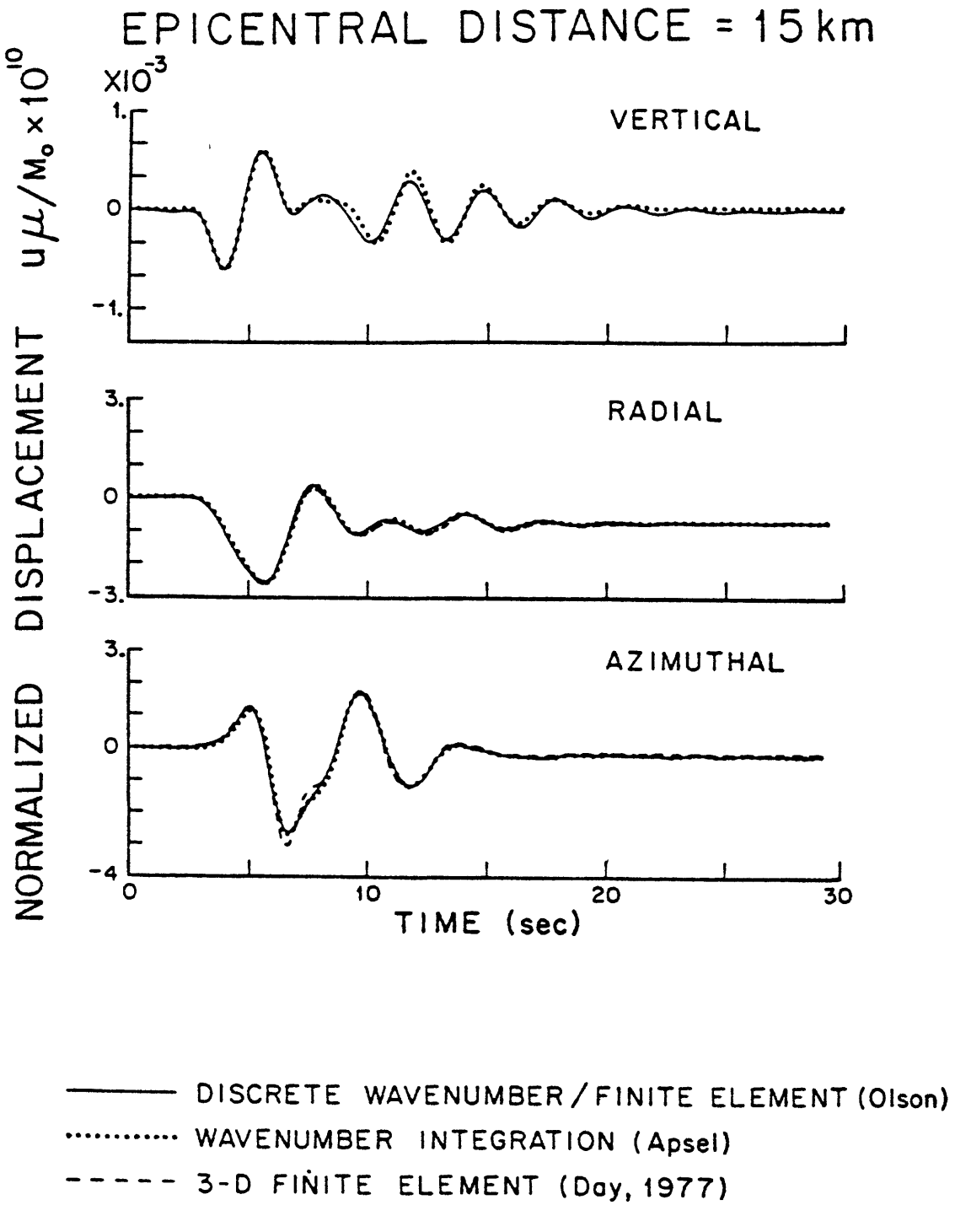

Figure 2-4. Corresponding comparison to Figure 2-3 for the free surface displacement components at an epicentral distance of 15 km.

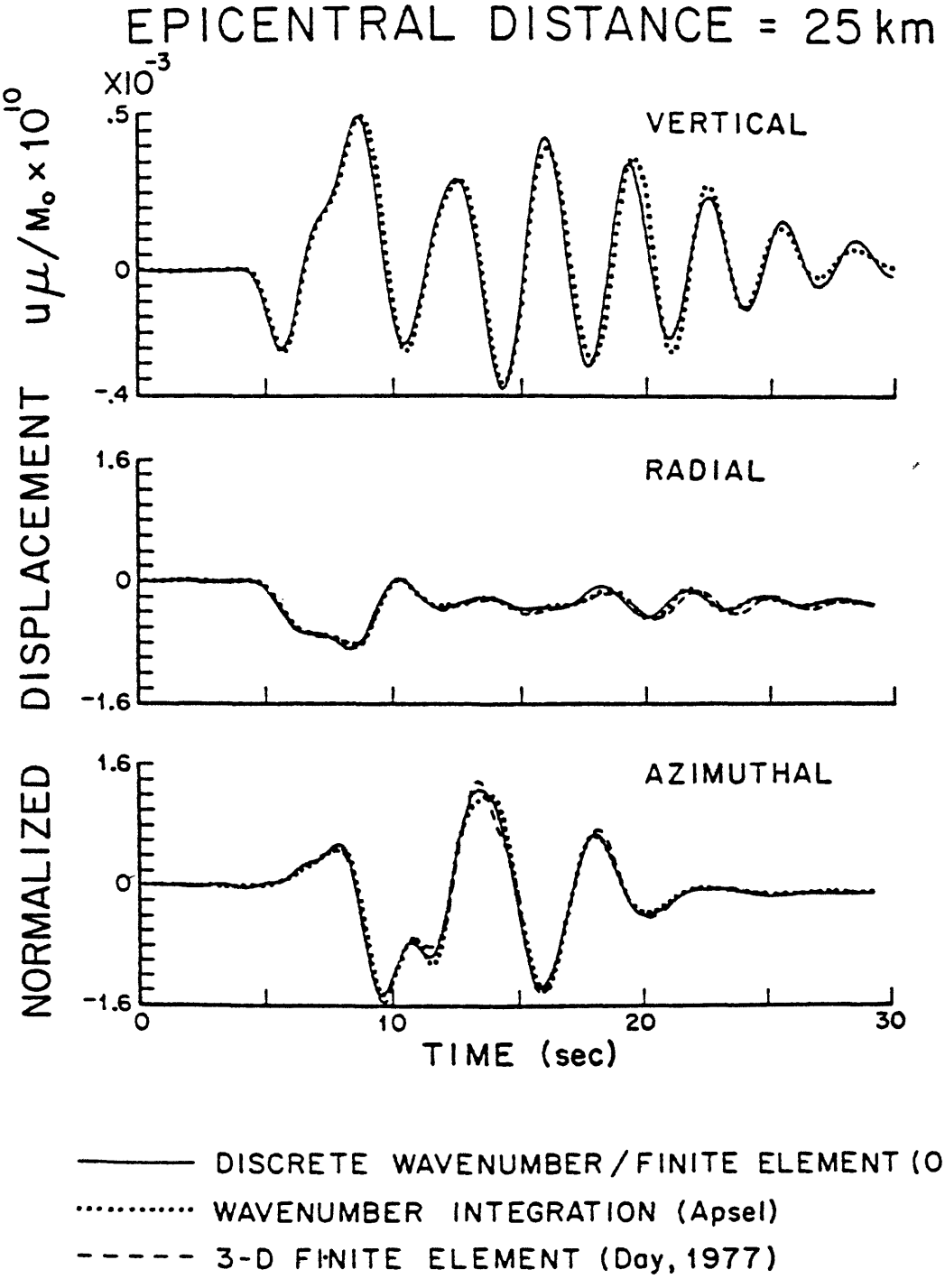

Figure 2-5. Corresponding comparison to Figure 2-3 for the free surface displacement components at an epicentral distance of 25 km.

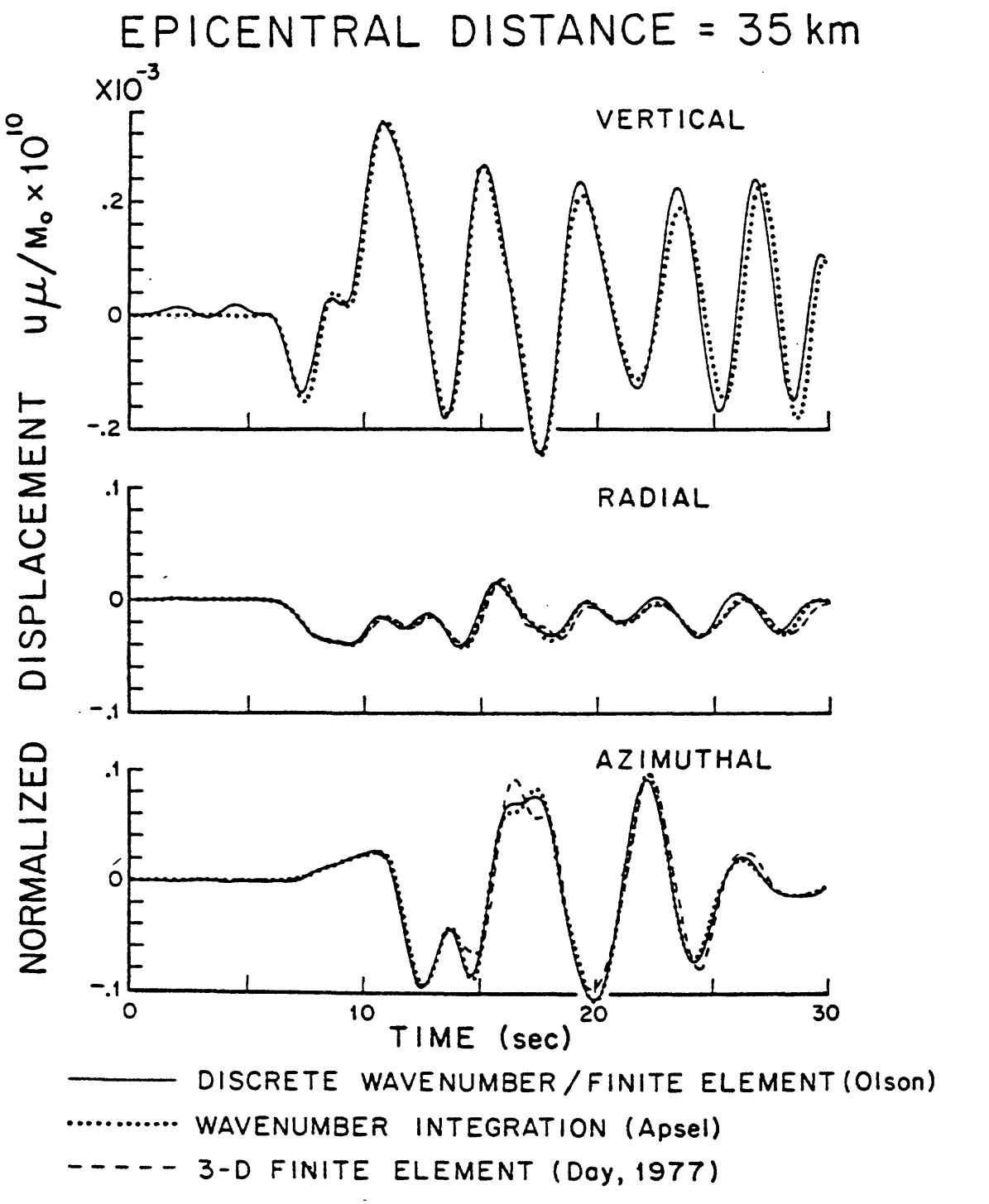

Figure 2-6. Corresponding comparison to Figure 2-3 for the free surface displacement components at an epicentral distance of 35 km.

to maintain consistency in the comparisons. The agreement is remarkable, especially in light of the vast differences between the solution techniques. The slight deviations in phase coherence have periods much longer than the expected resolution of two seconds (0.5 Hz).

In the second validation study, the complete solution obtained using the present technique is compared with the partial solutions obtained using the Generalized Ray approach of the Helmberger (1974) and the Normal Mode approach of Harkrider (1964, 1970). In this test, the frequencies resolved are an order of magnitude higher, but the comparisons are more difficult to interpret owing to the approximations and assumptions made in the alternate techniques.

In the generalized ray technique (Helmberger, 1974), the time-dependent wave field for a layered medium is decomposed into contributions attributed to an infinite set of rays travelling from the source to an individual receiver. Each ray contribution can be evaluated exactly by the Cagniard-deHoop technique (1939, 1960). However, the number of rays selected is invariably limited by the computational difficulties associated with finding the separate Cagniard paths for every point on the contour and for each kinematic group (rays with same travel time), for all source-receiver pairs. To reduce the cost for the comparisons, certain approximations are used in connection with the Bessel functions causing the generalized ray results to be least reliable at short distances and long periods. Also, differences can be expected in the decay of certain waves with distance since the generalized ray results include no material attenuation.

Similar to the present method, the normal mode technique operates first in the frequency domain so that the number of layers offers no limitations. However, the increase in number of contributing modes with frequency restricts the practicability of the normal mode technique to frequencies lower than about 1 or 2 Hz. Also, the inadequacies of the normal mode solution for epicentral distances less than a few source depths (or for any problem in which the ground motion is dominated by waves with relatively high horizontal phase velocities) are difficult to predict in general. For this problem,

however, the normal mode solution is expected to provide a closer match to the complete wavenumber integration solution than the generalized ray solution since the surface waves will tend to dominate the ground motion at periods greater than 1 or 2 seconds.

The soil model employed for the comparison consists of a single layer overlying a semi-infinite half-space as shown in Figure 2-7, where the individual parameters characterizeing the layers are delineated (the quality factors of Q_β = 10,000 and Q_α = 20,000 apply only to the present solution and are chosen high enough to eliminate any effects of material attenuations from the comparisons). It is hoped that by representing the 32 km thick crust by a single layer, the generalized ray technique will be able to include a sufficient number of multiple reflections and inter-conversions to converge to the complete solution generated by the present approach.

The source depth is 8 km and the source time-dependence is a quadratic ramp defined by the time integral of the function appearing at the top of Figure 2-7. The source is equivalent to a vertical strike-slip dislocation; receivers are located at epicentral distances between 100 and 1000 km. The azimuthal displacements are shown in Figure 2-8 for epicentral distances between 100 and 500 km and in Figure 2-9 for epicentral distances between 600 and 1000 km. The ground displacements for all three methods are normalized by the ratio of the shear modulus in the source layer times 10^{10} cm^2 divided by the scalar moment of the source. The maximum amplitudes obtained by the respective techniques are self-scaled to fit within the same height on each figure and are shown above each seismogram. The time scales are reduced by a time corresponding to the epicentral distance divided by the shear-wave velocity of the mantle, so as to align zero time with the first possible critically reflected arrival.

As in the first validation study, the phase coherence and amplitude agreement is superb. The somewhat larger time step in the normal mode calculations and the inadequate number of rays in the generalized ray calculation accounts for some of the amplitude discrepancies. Also, the modal superposition only includes the first five surface wave modes.

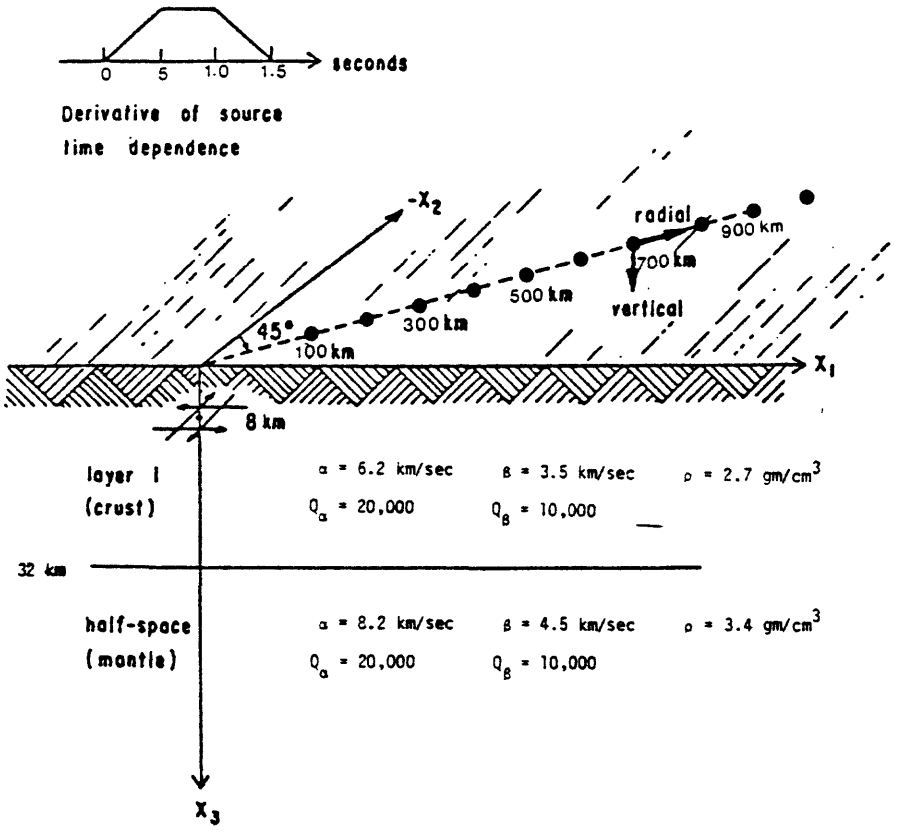

Figure 2-7. Source-receiver geometry and earth model, consisting of a 32 km thick crust overlying a half-space for use in comparison with the generalized ray and normal mode solutions.

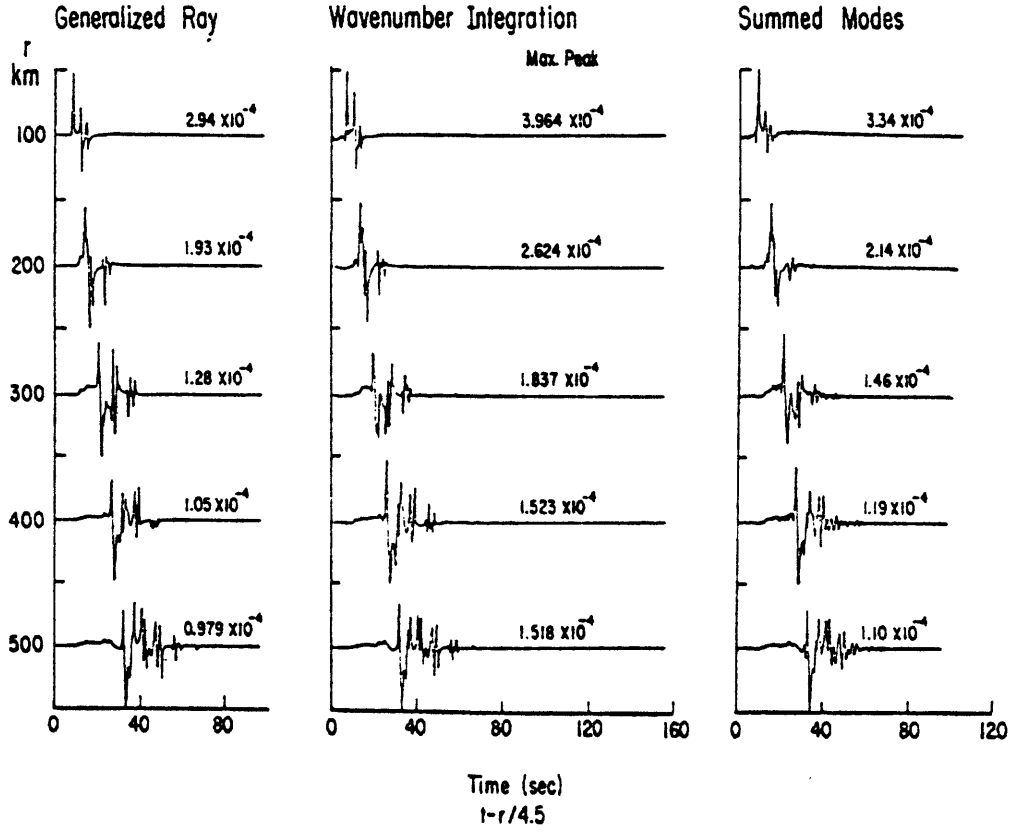

Figure 2-8. Comparison of the present solution with the summed normal mode solution (Harkrider, 1964) and the generalized ray solution (Helmberger, 1974) for the azimuthal displacement component at epicentral distances between 100 and 500 km due to a vertical strike-slip dislocation buried at a depth of 8 km in the earth model depicted in Figure 2-7.

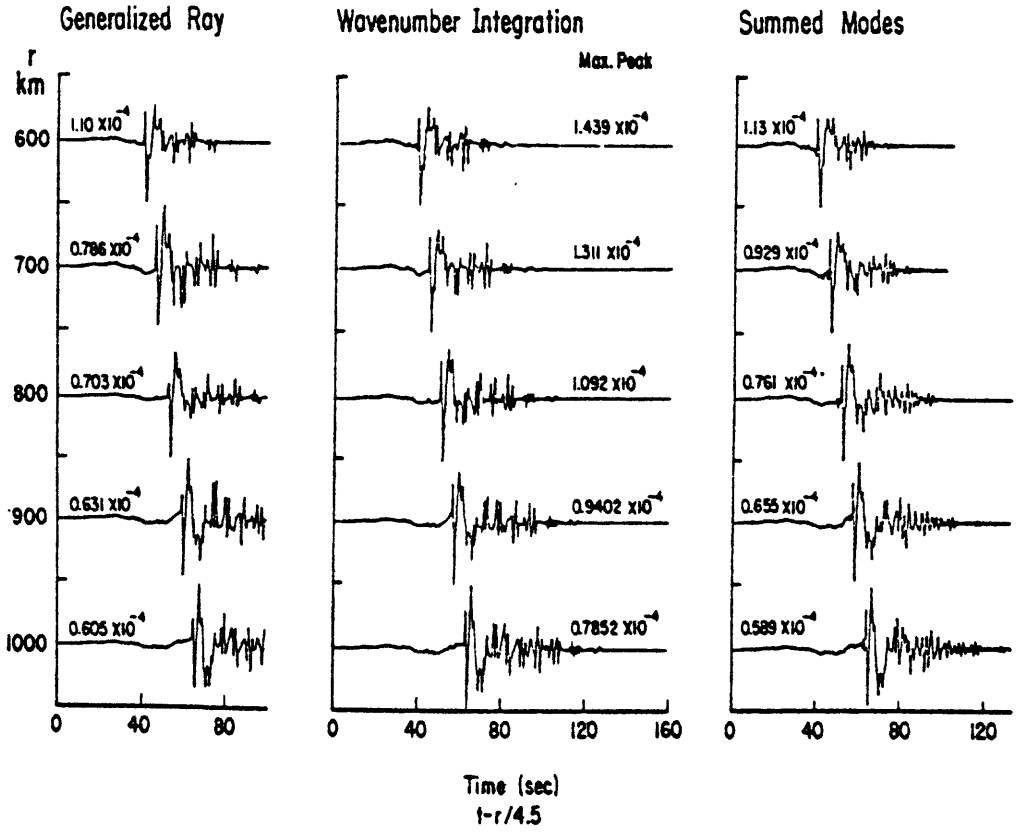

Figure 2-9. Corresponding comparison to Figure 2-8 for epicentral distances between 600 and 1000 km.

The results in Figure 2-10 portray the azimuthal displacements in response to the same source but with delta-function time dependence using the present method. The most important feature is the distinct set of pulses comprising the complete "elastic" (Q_β = 10,000) solution, so that the excellent match with the generalized ray results is not surprising for this simple problem.

Finally, the effects of using a nearly elastic (Q_β = 300) earth model versus an "elastic" (Q_β = 10,000) earth model in the present wave-number integration approach are investigated in Figure 2-11. Even withstanding the low-pass filtering effect of the source, much more high frequency energy is able to reach the receivers in the "elastic" model. The maximum peaks for the "elastic" model correspond to the surface waves which decay with distance according to a dependence of approximately $r^{-1/2}$. The nearly elastic model experiences an additional decay of $r^{-1/2}$ due to the small amount of damping. Otherwise, the wave forms are quite similar.

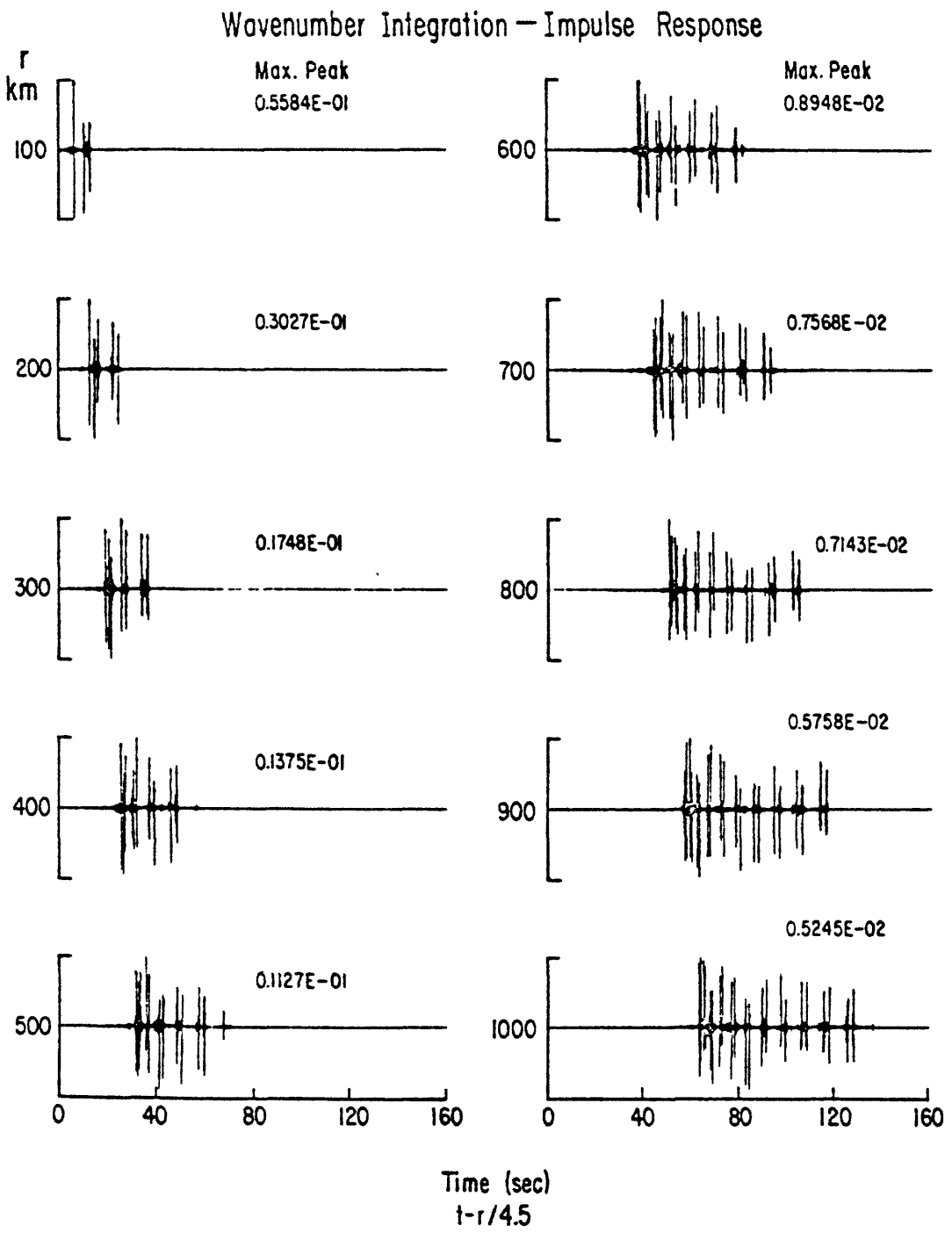

Figure 2-10. Present solution in response to the same source used in Figures 2-8 and 2-9 but with delta-function time dependence.

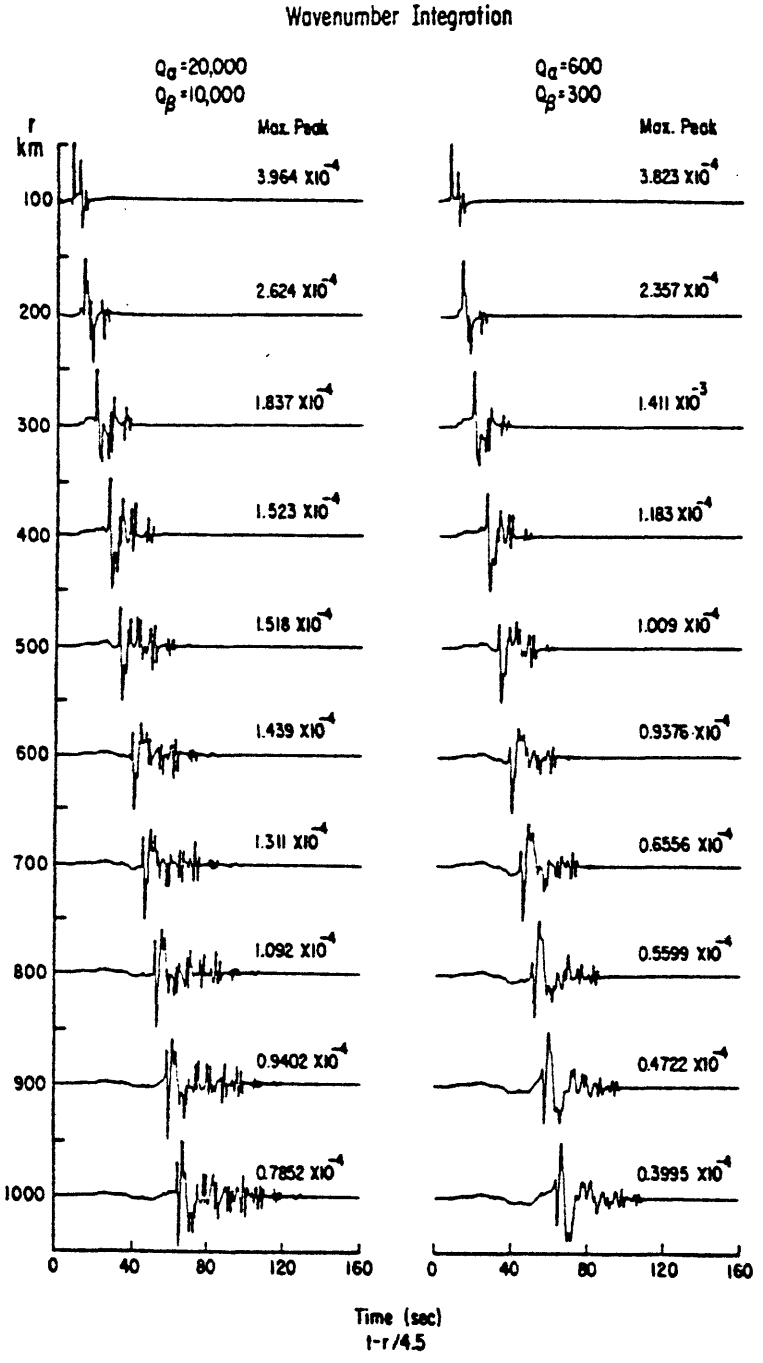

Figure 2-11. Effect on present solution of using a nearly elastic (Q_β = 300) earth model versus an "elastic" (Q_β = 10,000) earth model.

CHAPTER 3

NUMERICAL PROCEDURE FOR DISTRIBUTED RUPTURES

3.1 METHODOLOGY

3.1.1 Notation

Earthquake ground motion for a distributed source is formulated in terms of integral representations over the rupture surface of temporal convolutions of fault slippage with earthquake ground motion for point sources at each integration point. The ground displacements resulting from the action of each point dislocation on the rupture surface are the so-called Green's functions discussed in Chapter 2 and are obtained reciprocally in terms of the stress tensor solution evaluated at the depth of the point dislocation resulting from the action of a point force at the free surface. The widely known computer code PROSE (PROpagation Of Seismic Energy) is used to calculate the Green's functions and is described in considerable detail in Sections 2.1 and 2.2.

The mathematical characterization of fault slippage at each point $\vec{y}$ on the rupture surface S in Figure 3-1 must be prescribed as a function of time and orientation with respect to the surface receiver. The receiver is located at a point $\vec{x}$ on the free surface of volume V, which represents the viscoelastic layered half-space containing the rupture surface S. The local fault geometry at each point $\vec{y}$ is defined with respect to the unit vectors $\hat{e}_1$, $\hat{e}_2$, $\hat{e}_3$ in the Cartesian coordinate system x_1, x_2, x_3. The x_1 axis is aligned with the strike of the fault at point $\vec{y}$ (direction of $\hat{e}_1$, which is at an azimuth of β degrees from the receiver). The slip vector $\vec{\delta}(\vec{y}; t)$ is assumed to have a rake of γ degrees at point $\vec{y}$ in the plane defining surface S (see Figure 3-2):

$$\vec{\delta}(\vec{y}; t) = \delta_\infty(\vec{y};t)[(\cos\gamma)\hat{e}_1 + (\sin\gamma\cos\delta)\hat{e}_2 + (\sin\gamma\sin\delta)\hat{e}_3] \ . \qquad (3\text{-}1)$$

In Eq. (3-1), δ is the dip of the fault plane at point $\vec{y}$ measured counterclockwise from the x_2 axis, such that the projection of the unit normal

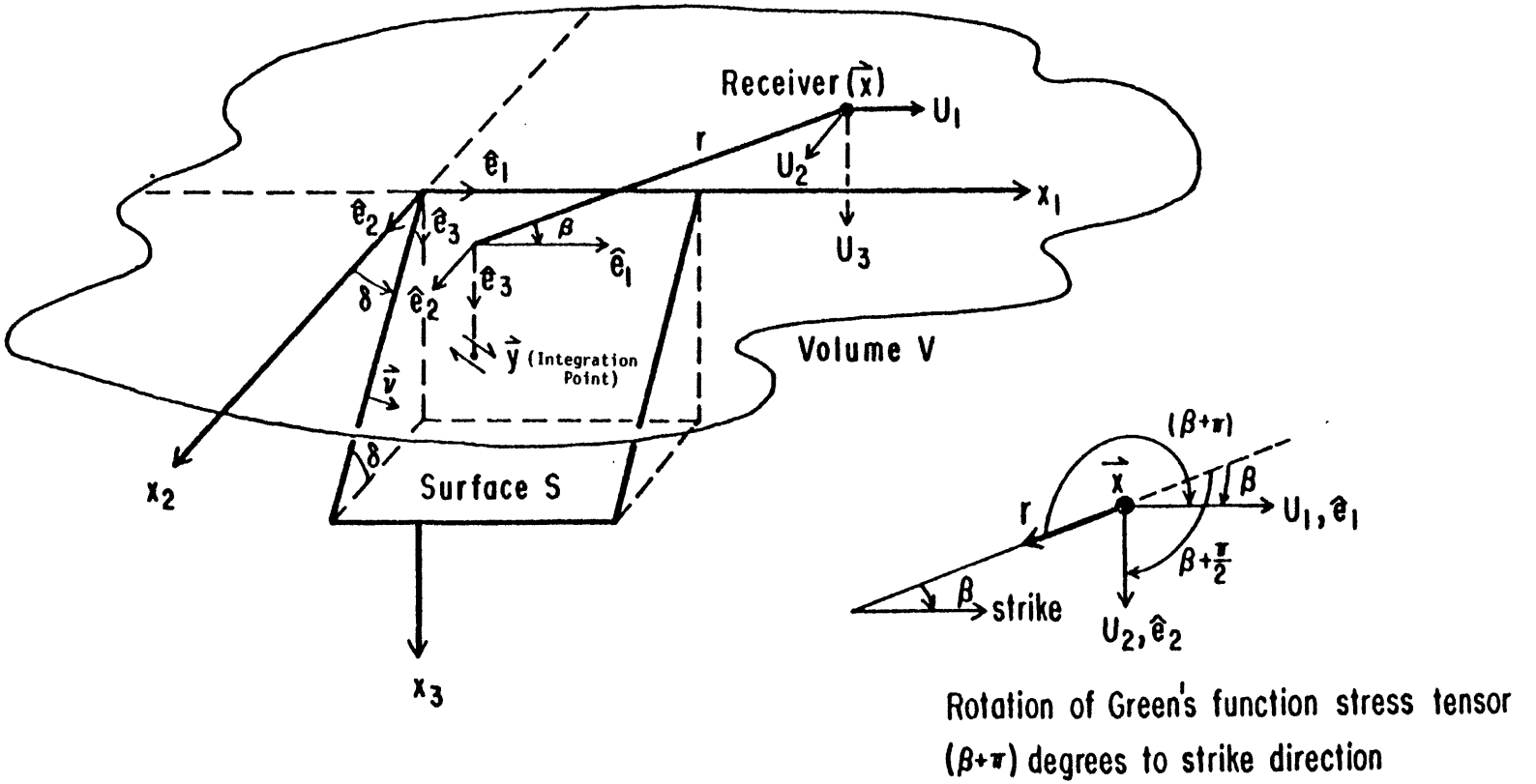

Figure 3-1. Coordinate system and source-receiver geometry for distributed source modeling.

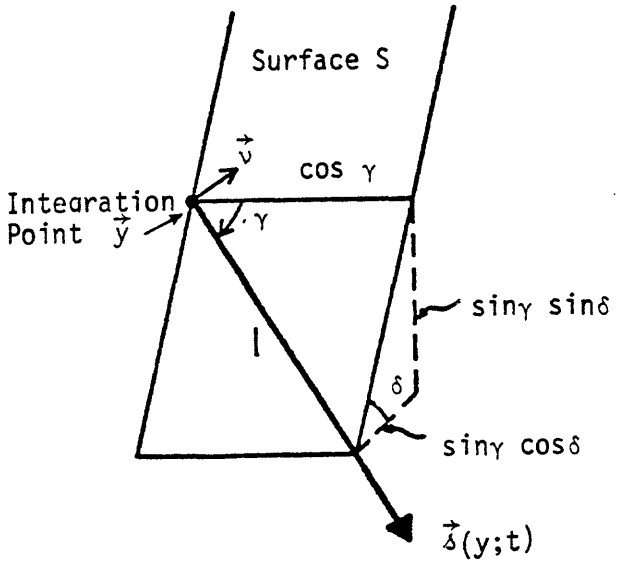

Figure 3-2. Slip vector orientation at point $\vec{y}$ on rupture surface S.

$$\vec{\delta}_{\infty}(\vec{y};t) = \vec{\delta}^{+}_{\infty}(y;t) - \vec{\delta}^{-}_{\infty}(\vec{y};t)$$

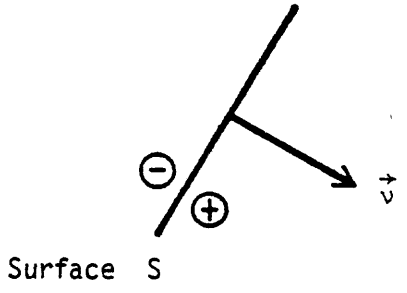

Figure 3-3. Sign convention for slip vector.

to surface S in the x_1, x_2, x_3 system is

$$\vec{\nu}(\vec{y}) = (-\sin\delta)\hat{e}_2 + (\cos\delta)\hat{e}_3 \quad , \tag{3-2}$$

and $\delta_\infty(\vec{y};\ t)$ is the amplitude of the dislocation at point $\vec{y}$ as a function of time t, i.e., the prescribed displacement discontinuity time history at point $\vec{y}$ of the positive side of the fault relative to the negative side, with the unit normal $\vec{\nu}(\vec{y})$ positive pointing from the negative side to the positive side (see Figure 3-3). The actual functional form for the slip amplitude $\delta_\infty(\vec{y};t)$ will be discussed in Subsection 3.1.3 after the formulation of the ground motion equation for distributed source modeling (Subsection 3.1.2). The numerical evaluation of the ground motion equation will be discussed in Subsection 3.1.4.

3.1.2 Formulation of the Ground Motion Equation

In the absence of body forces in the earth representation (volume V) and assuming continuity of tractions on the rupture surface S, the Knopoff-deHoop (1958) representation theorem may be applied to volume V in Cartesian coordinates to yield the ground motion equation as a function of frequency (ω):

$$U_i(\vec{x};\omega) = -\int_S \overset{\nu}{H}_{ji}(\vec{y},\vec{x};\omega)\, \delta_j(\vec{y};\omega) dS(\vec{y}), \qquad (i,j = 1,2,3) \tag{3-3}$$

in which the point $\vec{x}$ has been specialized to be on the free surface (defined by the plane $x_3 = 0$). $\overset{\nu}{H}_{ji}(\vec{y},\vec{x};\omega)$ denotes the j-component of the Green's function traction vector at $\vec{y} \in S$ due to a concentrated point load at $\vec{x}$ in the i-direction; $\delta_j(\vec{y};\omega)$ represents the j-component of the displacement vector prescribed at $\vec{y} \in S$. The summation convention over repeated indices is understood.

The time domain ground motion is obtained through Fourier synthesis after calculating the surface displacements on Eq. (3-3) at a discrete set of frequency points. The advantages of writing the ground motion equation in the frequency domain are twofold: (1) the Green's function tractions vectors are calculated directly in the frequency domain by PROSE, as discussed in the previous chapter; and (2) the temporal convolutions of the slip vector with the Green's function traction vector at each integration point $\vec{y}$ reduce to scalar products in the frequency domain.

The tractions $\overset{\nu}{H}_{ji}(y,x,;\omega)$ are expressed in terms of the stresses by

$$\overset{\nu}{H}_{ji}(\vec{y},\vec{x};\omega) = \tau_{kj_i}(\vec{y},\vec{x};\omega)\ \nu_k(\vec{y}) \tag{3-4}$$

in which $\tau_{kj_i}(\vec{y},\vec{x};\omega)$ denotes the kj-component of the stress tensor at $\vec{y} \in S$ due to a concentrated point load at $\vec{x}$ in the i-direction.

Equation (3-4) is introduced into Eq. (3-3) in conjunction with Eq. (3-2). Then substituting the Fourier transform of the slip vector, $\vec{\delta}(\vec{y};\omega)$, into the right-hand-side of Eq. (3-3) leads, after simplification, to an expanded version of the ground motion equation for distributed source modeling:

$$U_i(\vec{x};\omega) = \int_S \Big[(\cos\gamma\sin\delta)\ \tau_{12_i}(\vec{y},\vec{x};\omega) - (\cos\gamma\cos\delta)\ \tau_{13_i}(\vec{y},\vec{x};\omega) - (\sin\gamma\cos2\delta)\ \tau_{23_i}(\vec{y},\vec{x};\omega) + (1/2\ \sin\gamma\sin2\delta)\ \tau_{22_i}(\vec{y},\vec{x};\omega) - (1/2\ \sin\gamma\sin2\delta)\ \tau_{33_i}(\vec{y},\vec{x};\omega) \Big]\ \delta_\infty(\vec{y};\omega)\,dS(\vec{y}) \qquad (3\text{-}5)$$

The numerical evaluation of this equation will be discussed in Subsection 3.1.4.

All that remains is to relate the stresses $\tau_{kj_i}(\vec{y},\vec{x};\omega)$ in the x_1, x_2, x_3 system to the stresses in the system of cylindrical coordinates r, θ, z. Using the notation of Eq. (2-1), the clockwise rotation of $(\beta + \pi)$ degrees from the r, θ, z system to the x_1, x_2, x_3 system (as shown at the bottom of Figure 3-1) is delineated by

$$\tau_{11_i} = \frac{1}{2}\left(\sigma^j_{rr_i} + \sigma^i_{\theta\theta_i}\right) + \frac{1}{2}\left(\sigma^j_{rr_i} - \sigma^j_{\theta\theta_i}\right)\cos 2\beta + \sigma^j_{\theta r_i}\sin 2\beta$$

$$\tau_{22_i} = \frac{1}{2}\left(\sigma^j_{rr_i} + \sigma^j_{\theta\theta_i}\right) - \frac{1}{2}\left(\sigma^j_{rr_i} - \sigma^j_{\theta\theta_i}\right)\cos 2\beta - \sigma^j_{\theta r_i}\sin 2\beta$$

$$\tau_{12_i} = -\frac{1}{2}\left(\sigma^j_{rr_i} - \sigma^j_{\theta\theta_i}\right)\sin 2\beta + \sigma^j_{\theta r_i}\cos 2\beta$$

$$\tau_{13_i} = -\left(\sigma^j_{rz_i}\cos\beta + \sigma^j_{\theta z_i}\sin\beta\right)$$

$$\tau_{23_i} = -\left(-\sigma^j_{rz_i}\sin\beta + \sigma^j_{\theta z_i}\cos\beta\right)$$

$$\tau_{33_i} = \sigma^j_{zz_i} \qquad (3\text{-}6)$$

where the arguments $(\vec{y}, \vec{x}; \omega)$ have been omitted for brevity and the superscript j indicates the layer in which the stress tensor solution is monitored.

For completeness and consistency with the notation used in Chapter 2, the stresses appearing in the right-hand-side of Eq. (3-6) are presently listed. The stress components for the $i = 1, 2$ terms (concentrated point load at $\vec{x}$ in the $\hat{e}_1$, $\hat{e}_2$ directions, respectively) are given as follows:

$$\begin{Bmatrix} \sigma^j_{rz_i} \\ \sigma^j_{\theta z_i} \\ \sigma^j_{zz_i} \\ \sigma^j_{rr_i} \\ \sigma^j_{\theta\theta_i} \\ \sigma^j_{\theta r_i} \end{Bmatrix}_{(\vec{y},\vec{x};\omega)} = \frac{r_o^2 P_j}{4\pi r^2} \begin{Bmatrix} \Sigma^j_{rz_1}(r_o,z_o)\cos(\theta-\theta_{o_i}) \\ \Sigma^j_{\theta z_1}(r_o,z_o)\sin(\theta-\theta_{o_i}) \\ \Sigma^j_{zz_1}(r_o,z_o)\cos(\theta-\theta_{o_i}) \\ \Sigma^j_{rr_1}(r_o,z_o)\cos(\theta-\theta_{oi}) \\ \Sigma^j_{\theta\theta_1}(r_o,z_o)\cos(\theta-\theta_{o_i}) \\ \Sigma^j_{\theta r_1}(r_o,z_o)\sin(\theta-\theta_{o_i}) \end{Bmatrix}, \quad i = 1,2 \tag{3-7}$$

in which the reference angles $\theta-\theta_{o_i}$ for the direction of the concentrated point force at $\vec{x}$ are determined from Figure 3-1 to be

$$\theta-\theta_{o_i} = \begin{cases} \beta, & \text{for } i = 1 \\ \beta + \frac{\pi}{2}, & \text{for } i = 2 \end{cases} \tag{3-8}$$

The stress components for the $i = 3$ terms (concentrated point load at $\vec{x}$ in the $\hat{e}_3$ direction) are given as follows:

$$\begin{Bmatrix} \sigma^j_{rz_3} \\ \sigma^j_{\theta z_3} \\ \sigma^j_{zz_3} \\ \sigma^j_{rr_3} \\ \sigma^j_{\theta\theta_3} \\ \sigma^j_{\theta r_3} \end{Bmatrix}_{(\vec{y},\vec{x};\omega)} = \frac{r_o^2 P_0}{4\pi r^2} \begin{Bmatrix} \Sigma^j_{rz_0}(r_o,z_o) \\ 0 \\ \Sigma^j_{zz_0}(r_o,z_o) \\ \Sigma^j_{rr_0}(r_o,z_o) \\ \Sigma^j_{\theta\theta_0}(r_o,z_o) \\ 0 \end{Bmatrix} . \qquad (3\text{-}9)$$

The amplitudes P_1 and P_0, of the horizontal and vertical concentrated point loads respectively, in Eqs. (3-7) and (3-9), are determined by realizing in Eqs. (3-3) and (3-4) that H corresponds to stress if $P_0 = P_1 = 1$. Dimensionally, Eq. (3-3) reveals that

$$U \sim \tau\, \delta_\infty\, A = \frac{\tau}{\mu}\,(\mu\, \delta_\infty\, A) = \tau\, \frac{M_o}{\mu} \qquad (3\text{-}10)$$

so that if $U \sim \tau$ as in Eq. (3-5), then

$$P_0 = P_1 = \frac{M_o}{\mu} . \qquad (3\text{-}11)$$

In Eqs. (3-10), (3-11), A is the area of surface S over which the rupture occurs; δ_∞ is the maximum amplitude of the slip at a point $\vec{y} \in S$; M_o is the source moment; and μ is the shear modulus of the layer containing the point $\vec{y}$.

To summarize, the displacements at a point $\vec{x}$ on the i-direction on the free surface due to a distributed propagating rupture on surface S are given in Eq. (3-5). The displacements at point $\vec{x}$ in any direction may be obtained from Eq. (3-5) by appropriately adding vectorially the $U_i(\vec{x};\omega)$, $(i = 1, 2, 3)$. After evaluating the integral in Eq. (3-5) at a discrete set of frequency points, time histories of ground displacement may be obtained through use of a Fast Fourier Transform algorithm. Ground velocities and accelerations are readily obtained by time domain differentiation or by initially using slip velocity or slip acceleration in Eq. (3-5) instead of slip displacement.

The variables γ and δ represent the local (i.e., at each integration point $\vec{y} \in S$) rake and dip of the slip vector and β represents the local strike of the slip vector relative to the azimuth of the receiver. The stress tensor components appearing in Eq. (3-5) are defined in the local coordinates x_1, x_2, x_3 of the slip dislocation; Eq. (3-6) relates these local stress components to the stress components in the global cylindrical coordinates r, θ, z of the fault/receiver system. The individual global stress components are listed in Eqs. (3-7), (3-9) and are consistent with the notation used in Chapter 2 of this report and in Part I of Apsel (1979).

3.1.3 Functional Form of Slip Vector

The functional form of the slip displacement vector appearing in the ground motion equation (3-5) is mathematically deduced from three sources of evidence regarding the characterization of fault slippage: numerical and theoretical simulations of the rupture process; laboratory experiments; and recordings of earthquake ground motions. Due to the complexities associated with actual earthquakes, information more detailed than the size and location of the earthquake rupture zone and the average final offset is usually difficult to obtain. Under special circumstances, the duration of slippage on the fault surface and the rupture velocity may be obtained from the earthquake recordings.

Laboratory experiments and numerical simulations of fault rupture provide additional information that may be representative of actual earthquake behavior. For example, the finite element computer code SWIS (Stress Waves In Ssolids), developed by Frazier (1973), has been used to simulate spontaneous fracture in the earth's crust, as described by Archuleta and Frazier (1978). In Archuleta and Frazier's three-dimensional finite element model, fracture is initiated at a predetermined point (hypocenter) in a tectonically stressed medium. The crack spreads along a vertical, planar surface at a specified rupture velocity. Sliding occurs on the crack surface due to a reduction in the shear carrying capacity of the medium. The conditions on the crack surface consist of sliding friction vectorially opposing the slip velocity and continuity of particle velocity normal to the crack surface. Linear material response is assumed for all points not on the crack surface.

The crack tip continues to advance until it encounters prescribed barriers. Information from the rupture barriers propagates back into the active crack surface and retards sliding. Each point on the fracture surface heals at the instant sliding attempts to reverse directions. That is, the reduced shear carrying capacity of the fault, due to fracture, is sufficient to prevent further sliding at the instant the slip velocity attempts to reverse directions. Continuity of particle velocity and linear material response are enforced in the finite element calculations along healed portions of the fault.

Several calculations have been performed to test and validate Archuleta and Frazier's SWIS model of earthquake fracture. The accuracy of the numerical procedure for simulating the first stages of crack slip can be evaluated by comparing calculated results with results obtained analytically for the case of a circular crack in a homogeneous, unbounded medium as shown in Figure 3-4.

The solid curves in Figure 3-4 represent Kostrov's (1964) analytical solution for an idealized circular crack that nucleates from a point and spreads at a velocity equal to 90 percent of the shear wave velocity. The five curves correspond to time histories of particle displacement for five points on the crack surface, equally spaced along a radial line emanating from the hypocenter. The same conditions were simulated using Archuleta and Frazier's SWIS model, except that conditions were provided for terminating crack growth when the crack reached a radius equal to 10 grid dimensions. The results from the finite element calculations are also presented in Figure 3-4 at the same five points (every other grid point along the crack radius). The + symbols are plotted at the equally spaced time steps used in the SWIS calculations. The numerical results follow the analytical results very well until crack termination has an influence, at which time the analytical solution becomes inappropriate. The general behavior of a point on the idealized crack surface is as follows:

1. Slip is initiated at the time given by the quotient of hypocentral distance divided by rupture velocity.

2. The initial slip is abrupt; the slip velocity contains a square root singularity at the crack tip.

3. A short time after the crack tip passes, the slip velocity approaches a constant value.

4. Sliding is regarded by waves that return from barriers where the crack is terminated.

These same features are observed in three-dimensional finite difference simulations of fault dynamics (see Day, 1979), in which the sensitivity of earthquake slip functions to fault geometry, frictional strength, and prestress configuration is examined.

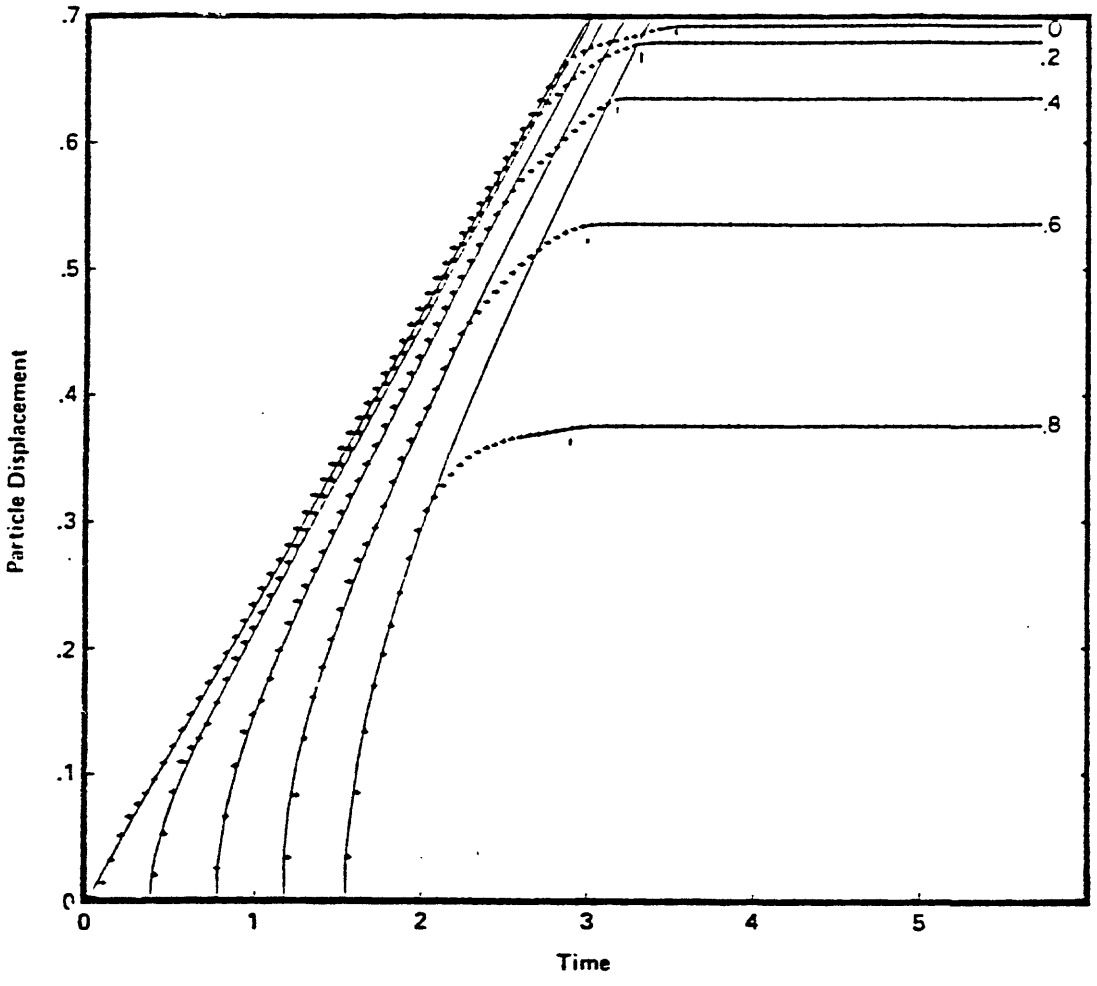

Kostrov's (1964) Self Similar Rupture

++++++++++++++++++ Archuleta and Frazier's (1978) Finite Element Results

Time histories of particle slip displacement for five points on a circular crack surface of radius r_o, equally spaced along a radial line emanating from the hypocenter.

Figure 3-4. Slip along a circular crack.

The idealized functional form of the slip vector is designed to contain the principal features illustrated in the numerical calculations discussed above. It is convenient to define such a function in terms of a minimal number of parameters due to the difficulties of uniquely tying down a large parameter set from a limiting number of earthquake modeling studies. Figure 3-5 presents the idealized three-parameter slip function that is used to simulate the earthquake rupture process. The three parameters are: initial slip velocity, v_0; final offset, δ_∞; and duration of slip (rise time), t_R. It should be pointed out that the more conventional ramped step two-parameter slip function (solid line in Figure 3-5) is obtained as a special case of the three-parameter slip function by taking the limit as the rise time approaches the final offset divided by the maximum slip velocity.

The final offset, δ_∞, is typically deduced from observations in the field or from distant seismic observations. The rise time, t_R, is determined by the time it takes for a shear wave to traverse the width of the fault. The time of rupture initiation, t_0, (which does not influence the functional form of the slip function) is determined by the time required for the rupture front to reach each point on the fault surface relative to the hypocenter time (zero time). The rupture front typically spreads at 90% of the shear wave velocity.

The third and final parameter that defines the functional form of the slip function is the maximum slip velocity, v_0, which is obtained by calibration from earthquake modeling studies. This is the slip function parameter that significantly influences the high frequency spectra obtained from the earthquake modeling procedure. Previous earthquake modeling studies (DELTA, 1979; DELTA, 1980a; DELTA, 1980b) indicate that the maximum slip velocity is constant from one earthquake to the next, independent of earthquake magnitude or stress drop. The constant value deduced for v_0 is 800 cm/sec and corresponds to a dynamic stress drop of about one kilobar. The results of the previous studies are summarized in Section 3.2. Since the maximum slip velocity at a point on the rupture front can be related to the failure strength of the gauge material, it is not surprising that this parameter would be similar from one earthquake to the next.

DELTA'S THREE-PARAMETER SLIP FUNCTION

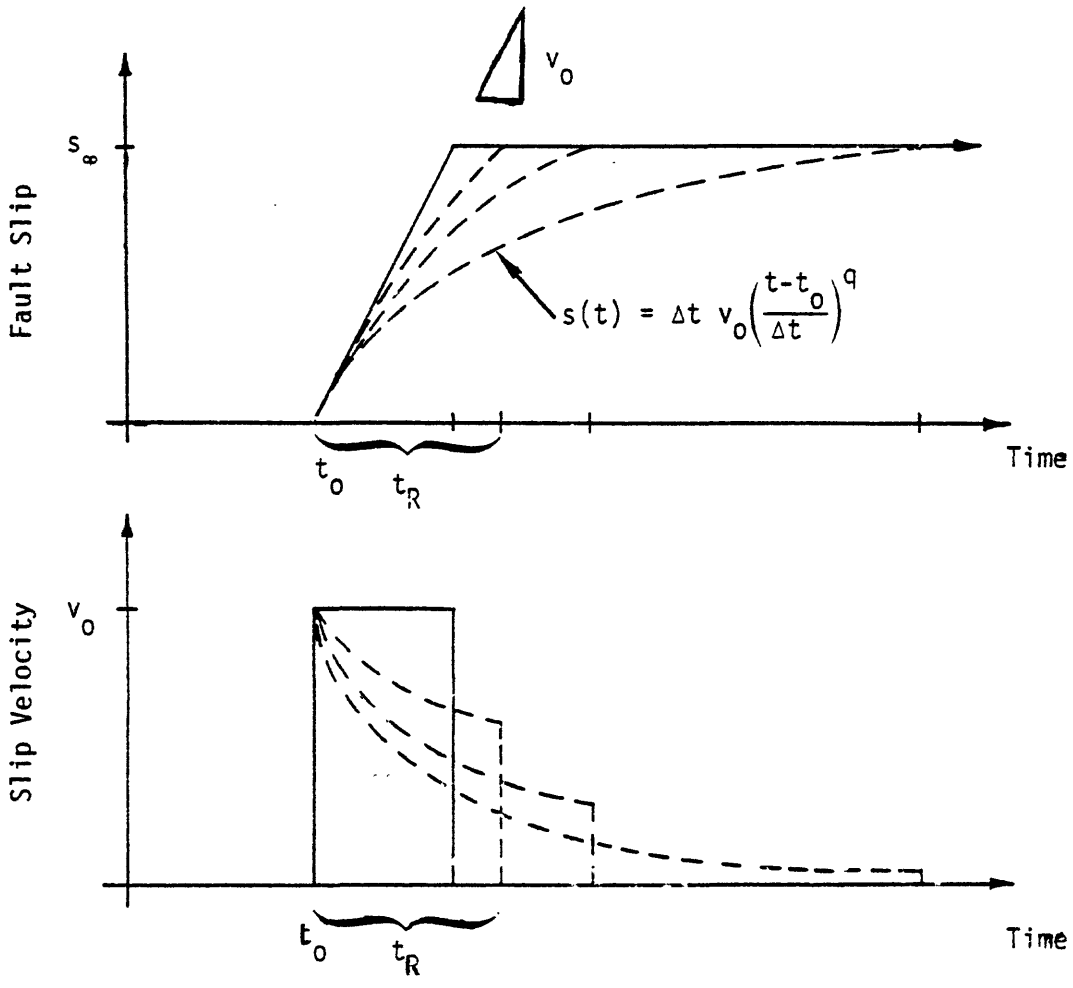

v_o = initial slip velocity ∿ dynamic stress drop

s_∞ = Final fault offset ∿ static stress drop

t_o = time of rupture initiation

t_R = rise time (duration of slip at a point)

$= \frac{s_\infty}{v_o}$ for a simplified two-parameter model.

Figure 3-5. Idealized slip function in which $q = [\ln(s_\infty/\Delta t\ v_o)]/\ln(t_R/\Delta t)$ is assigned to cause $s(t = t_o + t_R) = s_\infty$. Note that $q = 1$ for $t_R = s_\infty/v_o$, thus yielding a simplified two-parameter slip function.

To summarize, the digitized form of the displacement discontinuity time history (slip function) is given by

$$\delta_\infty(\vec{y};\ t) = \delta(t)\delta(t-t_o) \tag{3-12}$$

in which

$$\delta(t) = (\Delta t \cdot v_o)\left(\frac{t}{\Delta t}\right)^q \tag{3-13}$$

where

$$q = \frac{\ln\left(\frac{\delta_\infty}{\Delta t\ v_o}\right)}{\ln\left(\frac{t_R}{\Delta t}\right)}$$

insures that $\delta_\infty(\vec{y},\ t) = \delta_\infty$ for $t = t_o + t_R$. The Krönecker delta function in Eq. (3-12) insures that $\delta_\infty(\vec{y},\ t) = 0$ for $t < t_o$, in which the rupture initiation time (t_o) is related to the rupture velocity (V_R) and the distance of the point $\vec{y}$ from the hypocenter (i.e., $t_o \sim \frac{1}{V_R}\vec{y} \cdot \vec{v}$). The form of the slip function is typically invariant from point to point on a given fault plane (unless evidence exists for allowing any of the three shape-defining parameters v_o, δ_∞, T_R to vary over the fault plane). In fact, the parameter v_o has been found to be invariant from earthquake to earthquake using such a model (DELTA, 1979; DELTA, 1980a; DELTA, 1980b)

3.1.4 Evaluation of Ground Motion Equation Including Rupture Incoherence

Synthetic earthquake ground motions are calculated using computer code FALTUNG (German for the word convolution) by evaluating Eq. (3-5), in which the slip function vector is defined by Eq. (3-12). To evaluate the integral in Eq. (3-5), two important problems must be resolved. The first problem is how to discretize the rupture surface so as to accomodate a discrete mesh of Green's functions. This is a difficult problem because in order to preserve the highest frequencies of interest (e.g., 20 Hz), the required Green's function spacing would have to be on the order of decameters. However, for typical important earthquakes, the fault plane is at least 40 km long and 10 km wide, which would require a mesh of four million Green's functions (4,000 x 1,000) at each frequency. This is computationally infeasible, not to mention the computer storage requirements.

The second problem is that ground motion calculated for the ideally coherent rupture (as described in Subsection 3.1.3) exhibits behavior which is inconsistent with recorded motions, due primarily to incoherence in the rupture process of actual earthquakes. As suggested by several researchers, actual earthquake rupture stops, lurches ahead, changes direction and even ruptures several times at one point on the rupture surface. It is this non-regular rupture behavior that breaks up the emission of ideally coherent waves. In addition, as seismic energy leaves the rupture surface en route to the recording station, many paths are followed, not just those paths provided for in ideally horizontally layered structures. These non-coherent and irregular features of actual earthquake rupture are certainly more prevalent at high frequencies -- frequencies in the range of 5 to 20 Hz -- than for lower frequencies, where most of our theoretical understanding of earthquake waves has occurred. Some of these non-coherent or random processes must be incorporated into the evaluation of the ground motion equation in order to simulate realistic earthquake ground motion from distributed sources under all conditions, particularly when directly in the line of focus of the progressing rupture.

In light of the second problem, the dilemma of the mesh size spacing in the first problem is partially resolved, because utilizing a mesh size that will provide a perfectly coherent rupture defies the non-coherent behavior of actual earthquake ground motions. Therefore, in order to handle the mesh size problem, it is sufficient to device an interpolation scheme that prevents a relatively coarse mesh spacing from biasing the resulting ground motions.

Because of computing limitations, the Green's functions are typically spaced at one-km intervals over the surface of incipient rupture. The Green's functions at each integration point on the rupture surface are then approximated by the nearest Green's function computed in the same layer, but shifted in time to reflect the travel time delay of the direct shear wave from the source point to the receiver. The amplitude of the neighboring Green's function is also scaled to reflect change in amplitude with change in direction. Such an interpolation scheme is written in the time domain as

$$\overset{\nu}{H}_{ji}(\vec{y},\vec{x};t) \approx \overset{\nu}{H}_{ji}(\vec{y}_n,\vec{x};t)\delta(t - \Delta t_n)\left(\frac{r_n}{n}\right)^p \qquad (3\text{-}14)$$

in which $\Delta t_n \sim (r - r_n)\beta$ is the travel time delay from the receiver point $\vec{x}$ to Green's function node point $\vec{y}_n$ relative to the integration point $\vec{y}$. The amplitude scaling factor p is approximately 2.0 and is of considerably less consequence than the time shift, particularly at distances beyond 5 or 10 km (where the curvature of the rupture front is less influential).

Introduction of Eqs. (3-12) and (3-14) into Eq. (3-3) reduces the general ground motion equation to a form suitable for treating a discrete mesh of Green's functions:

$$U_i(\vec{x};\omega) = -\sum_n \mathcal{S}_n(\omega)\overset{\nu}{H}_{ji}(\vec{y}_n,\vec{x};\omega)\mathcal{F}\left\{\int_{S_n} \delta(t-\Delta t_n-t_{o_n})\left(\frac{r_n}{r}\right)^p dS_n(\vec{y})\right\} \qquad (3\text{-}15)$$

in which $\mathcal{F}\{\ \}$ defines the Fourier transform of the spatial integral of delay times over the nth mesh area. The summation over n represents the spatial summation of the contribution of rupture from individual mesh areas. The delay time integrals physically portray the passage of the rupture front through an individual rupture segment (typically one-km-square areas with the ground motion due a single point dislocation -- Green's function -- described at one point within the segment). It is straightforward to evaluate the delay time integral exactly over each rupture segment -- the result is a trapezoidal-shaped source distribution function (SDF), which, when convolved with a point-dislocation Green's function and a displacement discontinuity time history (slip function), yields coherent ground contributions from a 1-km-square distributed source that are mesh-size independent (see Chapter 2 of DELTA, 1979).

Therewith, utilizing Eq. (3-15) as the ground motion equation resolves the mesh size problem and what remains is to resolve the second problem -- namely, how to include physically realizable incoherence in the earthquake model. The prescription of rupture incoherence is implemented on two dimension scales. First, the ground motion calculated within each 1-km-square region is made more incoherent by modifying the analytical SDF for that region (referred to as micro-incoherence modifications). Second, the ground motion calculated from the summation of individual cell contributions over the entire rupture surface is made more incoherent by modifying certain rupture parameters through use of a Gaussian random number generator (referred to as macro-incoherence modifications).

The justification and implementation of the micro-incoherence is discussed first. Coherent ruptures expanding at 90 percent of the shear wave velocity over a one-km-square segment of rupture can, under ideal conditions, produce larger motions at stations directly in the line of focus from that rupture segment than the entire earthquake produces for stations not in line with the focus but much closer to the rupture surface. More simply stated, wavelengths on the order of 50 meters can strongly focus in a distance of one km under ideal conditions. To guard against unrealistically strong focussing from such small segments of rupture, a mathematical

limit is placed on the degree of focussing to be allowed from any single one-km-square segment of rupture. Specifically, the direct rays emanating from a one-km-square segment of rupture are not permitted to arrive at the receiver in a time frame narrower than one-tenth of a second, which is accomplished by limiting the narrowness of the delay time integrals (i.e., the SDF's).

The macro-incoherence is introduced to accomodate the previously mentioned non-regular rupture behavior (viz., actual earthquake rupture stops, lurches ahead and changes in direction; seismic energy propagates to the receiver from the rupture surface via paths that are not always provided for in an ideally horizontally layered viscoelastic medium). Four types of macro-incoherence are introduced into the earthquake model when considering distributed sources larger than a single one-km-square rupture segment. The purpose is to: (1) randomly delay the time of rupture initiation in each of the one-km-square rupture segments; (2) randomly alter the orientation of the rupture (strike, rake and dip of slip vector) in each segment; (3) randomly alter the direction in which the rupture progresses through each rupture segment; and (4) randomly alter the orientation of particle motions that arrive at the receiver from each rupture segment. Each of these sources of incoherence has been introduced through the use of a Gaussian random number generator, as summarized in Table 3-1.

The computer code FALTUNG utilizes this prescription of incoherence when evaluating the discretized ground motion equation in Eq. (3-15). The resulting calculated earthquake ground motions are found to be consistent with the amplitude, duration and frequency content of recorded motions (DELTA, 1979; DELTA, 1980a). Moreover, this prescription of incoherence allows for a systematic input to the earthquake modeling procedure of the uncertainties acknowledged to exist at this date in rupture physics. Variations that result from the stochastic properties introduced into the earthquake model by this prescription of incoherence are quantified by repeating a single earthquake simulation several times (i.e., different random number sequences) and considering a one-standard deviation variation around the mean of the FALTUNG results. As discussed in the next section, this earthquake model has been validated against four important earthquakes: 1940 El Centro and 1966 Parkfield Earthquake (DELTA, 1979); 1933 Long Beach and 1971 San Fernando (DELTA, 1980a).

Table 3-1. Prescription of Rupture Incoherence Used in DELTA's Earthquake Modeling Process

MICRO-INCOHERENCE:

The direct rays emanating from a 1-km-square rupture are not permitted to arrive at the receiver in a time frame narrower than 0.1 seconds.

MACRO-INCOHERENCE

(1) The time for rupture initiation in each segment is delayed beyond the arrival time of the gross crack by a random number with a two-thirds confidence of not exceeding one second;

(2) The orientation of rupture in each segment is modified by random numbers with a two-thirds confidence of not exceeding 20, 20 and 10 degrees for the strike, rake and dip, respectively, of the slip vector;

(3) The tip of the crack migrates through each segment in a direction that deviates from the gross direction of rupture propagation by a random number with a two-thirds confidence of not exceeding 30 degrees;

(4) The horizontal particle motion computed at the receiver station from each rupture segment is altered in direction by a random number with a two-thirds confidence of not exceeding 30 degrees.

It was recently determined that the prescription of micro-incoherence in Table 3-1 still allows more focussing from individual rupture segments than observed during actual earthquake rupture. The micro-incoherence has correspondingly been refined by introducing subcell randomness into the SDFs in order to simulate rupture irregularities on a scale of fifty meters in every one-km square rupture segment (DELTA, 1980b). The degree of randomness is inversely proportional to the rupture velocity through the rupture segment. This refined micro-incoherence is physically more realistic than the original 0.1-second minimum time width condition. The validation of the earthquake model including this refined prescription of micro-incoherence has been verified against the important and extensive coverage provided by the 1979 Imperial Valley Earthquake recordings (DELTA, 1980b).

3.2 VALIDATION

The computer code FALTUNG is used to calculate ground motion from distributed sources (refer to Section 3.1 for description of modeling methodology). The FALTUNG modeling procedure has been validated by matching the strong motion recordings of several important California earthquakes. The quality of the agreement between the calculated and recorded ground motions sufficiently confirms the validity of using FALTUNG to predict site specific strong ground motions resulting from hypothesized earthquake ruptures.

Model parameters describing the rupture configuration for the earthquake in each validation study are based on values obtained by independent studies (e.g., fault geometry, fault type, hypocentral location and rupture extent). Model parameters describing the earth structure in which the seismic waves propagate from the rupture surface to the receiver are also based on values obtained by other studies when available. It is assumed that the earth structure can be represented by a horizontally layered viscoelastic half-space. Typically, only the depth dependence of the velocities is given (from refraction studies, for example), in which case certain generic formulae are used to obtain the remainder of the viscoelastic layer parameters. Finally, model parameters describing the fault slippage at a point are obtained as follows: 1) the maximum slip velocity (related to dynamic stress drop) and the prescription of rupture incoherence are calibrated against the recorded data as part of the validation exercises -- these parameters affect the highest frequencies of interest; 2) the final slip displacement (related to static stress drop) is either the value observed or is obtained from generic formulae related to earthquake magnitude -- this parameter affects the lowest frequencies of interest; and 3) the rise time is typically related to the transit time for shear waves to traverse the widest dimension of the rupture surface. The maximum slip velocity was found to be a constant equal to 800 cm/sec for all earthquakes modeled in the validation studies.

Velocity response spectra and peak values of acceleration, velocity, and displacement are used as bases of comparison between the observed for computed ground motions. Wiggle-for-wiggle time domain matches are not

attempted, because an inversion of the displacement and/or velocity time histories would be required to sufficiently constrain the complex rupture sequences. Such an inversion procedure, although scientifically satisfying, is beyond the scope of the objectives set out in the site specific modeling procedure. The objective of the validation studies is merely to reproduce features of ground motion important for structural design using fairly simple rupture models as demonstrated in the following five subsections. The five subsections summarize, respectively, the validation studies for the following five California earthquakes (results of which have been extracted from referenced reports): 1940 Imperial Valley and 1966 Parkfield earthquakes (DELTA, 1979); 1933 Long Beach and 1971 San Fernando earthquakes (DELTA, 1980a); and 1979 Imperial Valley earthquake (DELTA, 1980b).

3.2.1 1940 Imperial Valley

The 1940 Imperial Valley Earthquake (M_L = 6.5, M_S = 7.1) is the largest strike-slip event recorded to date in Southern California. Strong motion recordings were obtained at a single station at El Centro, 6 km from the fault trace (see Figure 3-6). Trifunac and Brune (1970) suggest that this event is not a simple coherent rupture but rather a sequence of smaller events with varying amounts of offset. The geologic model used for Imperial Valley is delineated in Table 3-2. This earth structure is based on published data (Heaton and Helmberger, 1978) determined by matching travel times and amplitudes from recordings of small earthquakes in the Imperial Valley. The quality factors are related empirically to the shear and compressional wave velocities as a function of depth (refer to Section 2.3 for the generic formulae used to model western United States earthquakes).

The fault parameters used to model the 1940 Imperial Valley Earthquake are listed in Table 3-3. The rupture surface is divided into eight segments with varying amounts of offset, ranging from 500 cm near the south end of the fault to less than 50 cm at the north end.

As shown in Figure 3-7, the fit to the response spectra of the three recorded components of ground motion is quite good. Table 3-4 shows a comparison between the observed and calculated peak accelearations, velocities and displacements. The response spectra and peak values for the simulated ground motions presented here (and in the subsequent validation studies) are the mean values calculated for several rupture simulations of the same earthquake using different random number sequences to account for rupture incoherence. There is some discrepancy between the high frequency spectral components of the vertical motions, in that the calculated values are deficient. This issue will be addressed further when the 1979 Imperial Valley earthquake is discussed in subsection 3.2.5.

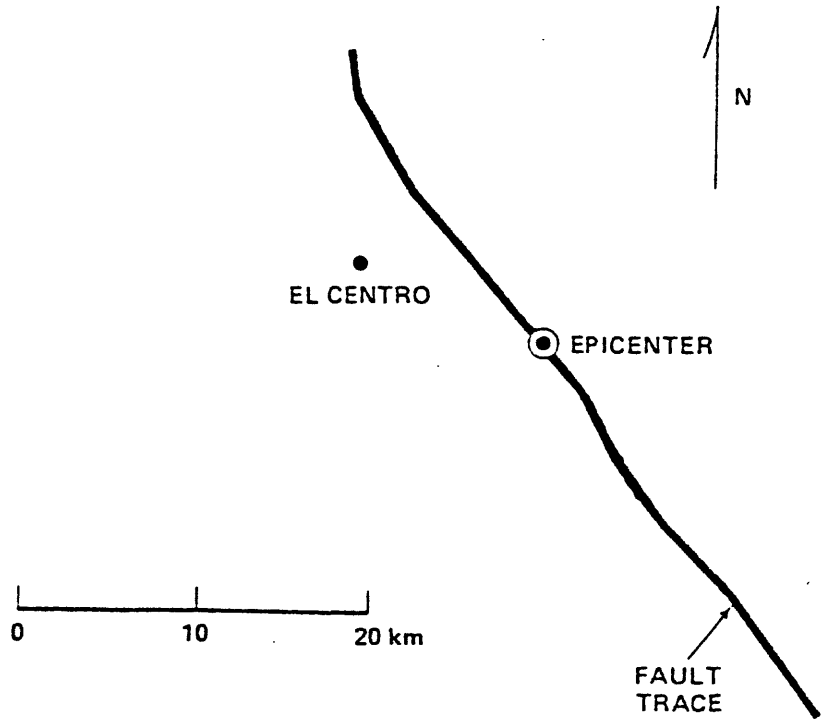

Figure 3-6. Map of the fault model for the 1940 Imperial Valley Earthquake.

Table 3-2. Viscoelastic parameters for the geologic structure for the 1940 Imperial Valley Earthquake.

Layer	β S-Wave Velocity (km/sec)	α P-Wave Velocity (km/sec)	ρ Density (gm/cm^3)	Q_β Shear Quality Factor	Q_α Compressional Quality Factor	h Layer Thickness (km)	Depth to Top of Layer (km)
1	0.75	1.70	1.50	21	81	0.45	0.
2	0.92	2.10	1.90	27	106	0.50	0.45
3	1.50	2.60	2.35	50	112	1.15	0.95
4	2.30	3.70	2.50	85	165	1.20	2.10
5	2.60	4.10	2.60	99	185	2.50	3.40
6	3.70	6.40	2.80	154	346	--	5.90

Table 3-3. Source parameters for the 1940 Imperial Valley Earthquake.

Fault Length	48 km
Fault Width	11 km
Shallowest Extent	1 km
Hypocenter Depth	12 km
Fault Strike	Approx. N35°W
Fault Dip	90°
Slip Direction	0° *
Slip Duration	3.8 sec
Fault Offset	50 to 500 cm
Seismic Moment	3.6×10^{26} dyne-cm

*Right lateral strike-slip faulting.

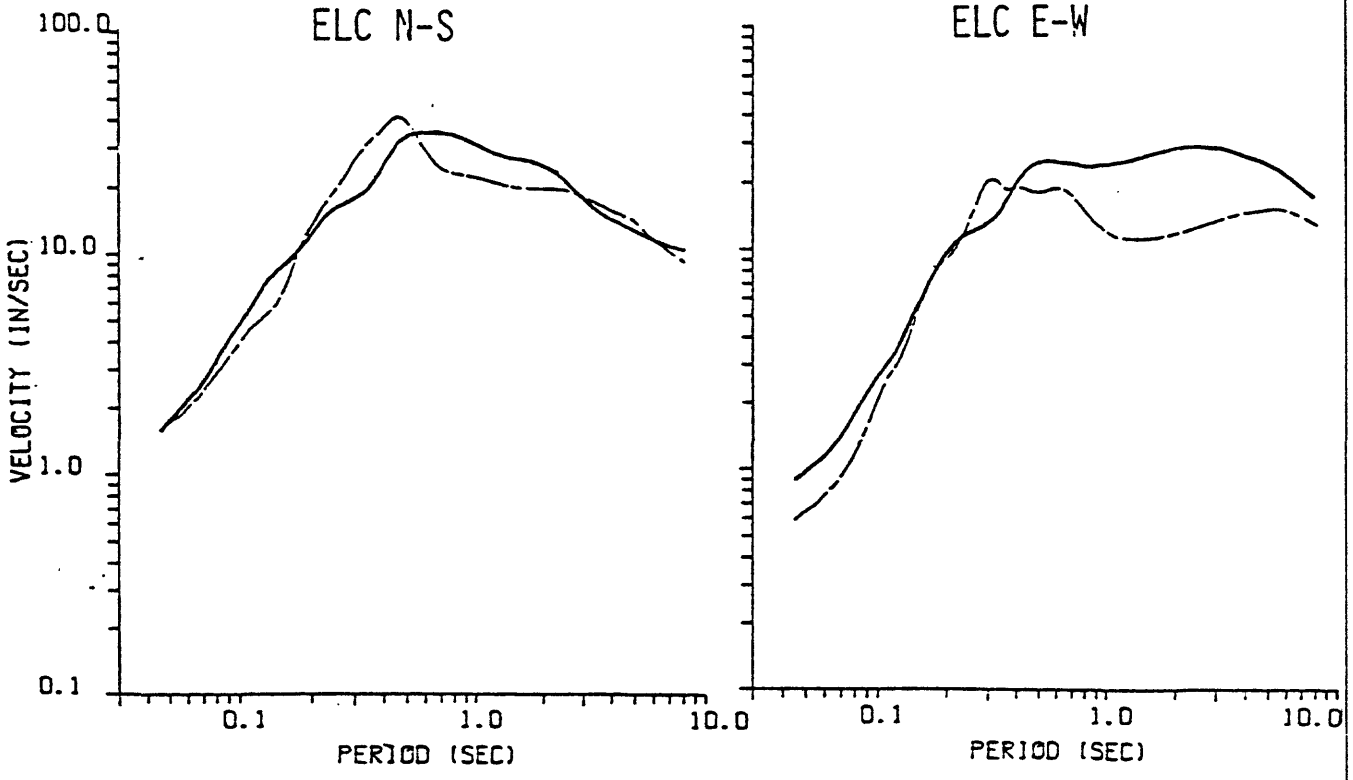

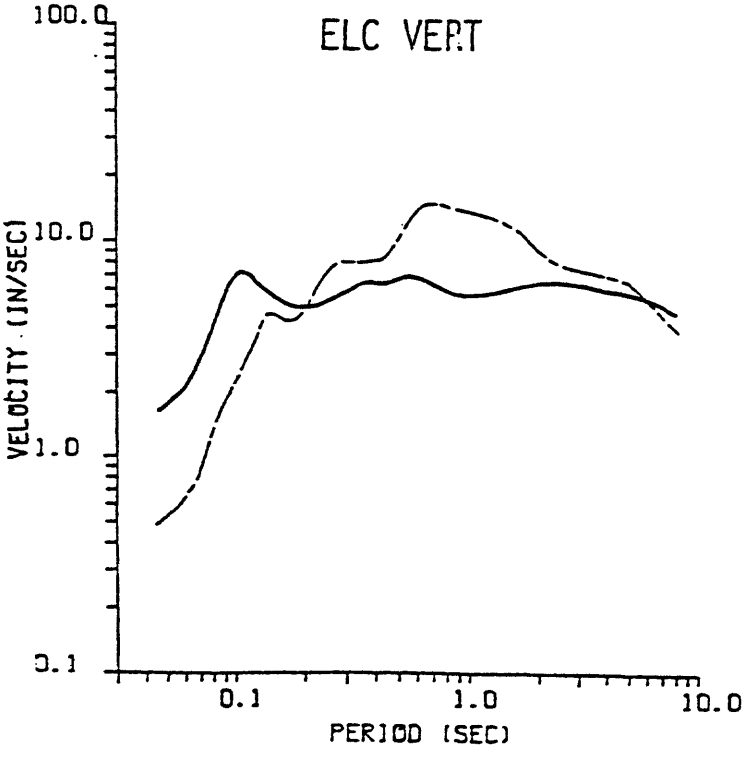

Calculated

Observed

Comparison of the smoothed 2% velocity response spectra for the 1940 Imperial Valley Earthquake, Station El Centro.

Figure 3-7.

Table 3-4. Maximum values of acceleration, velocity and displacement for the 1940 Imperial Valley Earthquake.

Station	Component	Acceleration (g) Obs.	Acceleration (g) Calc.	Velocity (cm/sec) Obs.	Velocity (cm/sec) Calc.	Displacement (cm) Obs.	Displacement (cm) Calc.
El Centro	Vertical	.2	.15	10	13	6	11
	South	.35	.49	30	33	10	20
	West	.25	.19	38	24	20	49

3.2.2 1966 Parkfield

The 1966 Parkfield Earthquake (M_L = 5.8, M_s = 6.4) was a strike-slip earthquake on the San Andreas fault in California. This well-studied event was recorded by six strong motion stations located within 15 km of the rupture trace (see Figure 3-8). Our understanding of this event indicates that Station 2 was located directly in the line of focussing as the rupture proceeded along the fault southeastward from the epicenter. The geologic model used for Parkfield is delineated in Table 3-5. The earth structure is based on published data by Eaton, ea al. (1970). The fault parameters used in the computer model are listed in Table 3-6. The rupture surface is divided into three segments, each having 60 cm final offset, but with different strike directions.

As summarized in Table 3-7, the agreement with the peak values of acceleration, velocity, and displacement is quite good. A comparison between the observed and calculated response spectra for Stations 2, 5 and 8 is provided in Figures 3-9, 3-10, and 3-11, respectively. The earthquake model yields a peak acceleration value for the horizontal component at Station 2 which is considerably larger than observed. Possible explanations are that either the recording at Station 2 is unreliable or that the distributed source model contains a degree of idealized focussing which is not observed in real earthquakes.

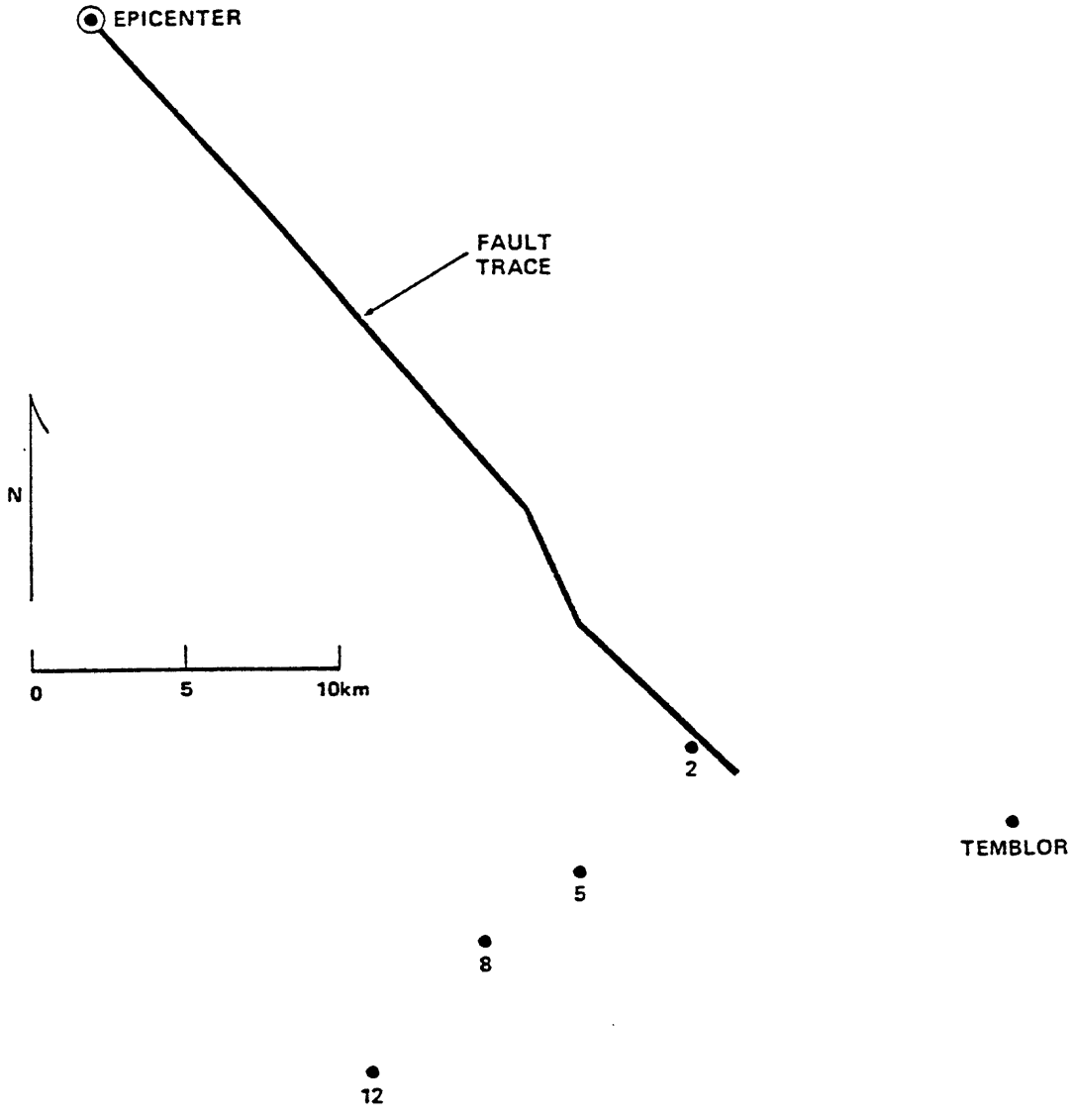

Figure 3-8. Map of the fault model for the 1966 Parkfield Earthquake.

Table 3-5. Viscoelastic parameters for the geologic structure for the 1966 Parkfield Earthquake.

Layer	β S-Wave Velocity (km/sec)	α P-Wave Velocity (km/sec)	ρ Density (gm/cm^3)	Q_β Shear Quality Factor	Q_α Compressional Quality Factor	h Layer Thickness (km)	Depth to Top of Layer (km)
1	0.57	0.99	1.50	15	34	0.116	0.
2	0.99	1.71	1.50	30	66	0.164	0.116
3	1.62	2.81	1.62	55	124	1.27	0.28
4	2.91	5.04	2.21	114	257	2.19	1.55
5	3.48	6.02	3.46	143	320	11.25	3.74
6	3.95	6.86	3.93	167	378	10.00	14.99
7	4.67	8.09	4.64	206	464	--	24.99

Table 3-6. Source Parameters for the 1966 Parkfield Earthquake

Fault Length	26 km
Fault Width	9 km
Shallowest Extent	1.5 km
Hypocenter Depth	10.5 km
Fault Strike	Variable
Fault Dip	90°
Slip Direction	0° *
Slip Duration	2.7 sec
Fault Offset	60 cm
Seismic Moment	5.1×10^{25} dyne-cm

*Right lateral strike-slip faulting.

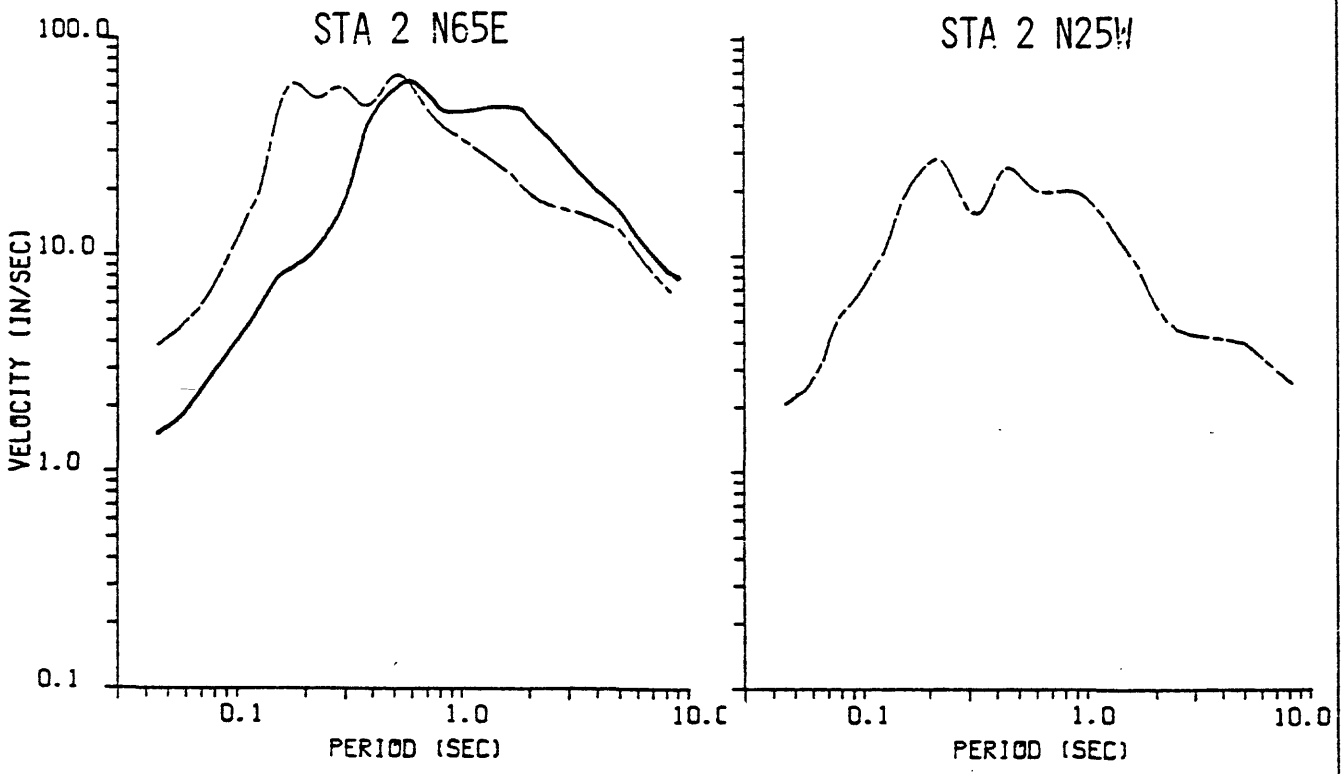

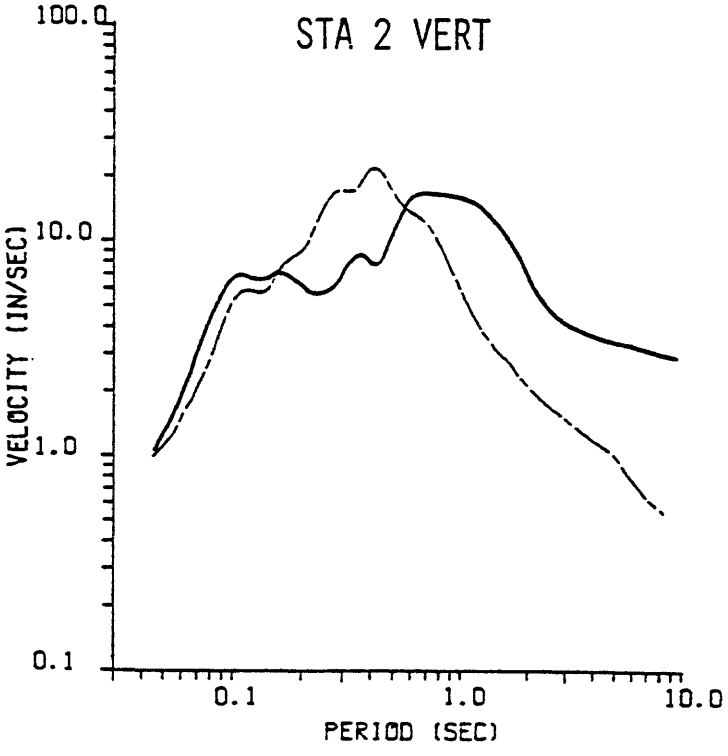

Calculated

Observed

Comparison of the smoothed 2% velocity response spectra for the 1966 Parkfield Earthquake, Station 2. Recording unavailable for horizontal component N25W.

Figure 3-9

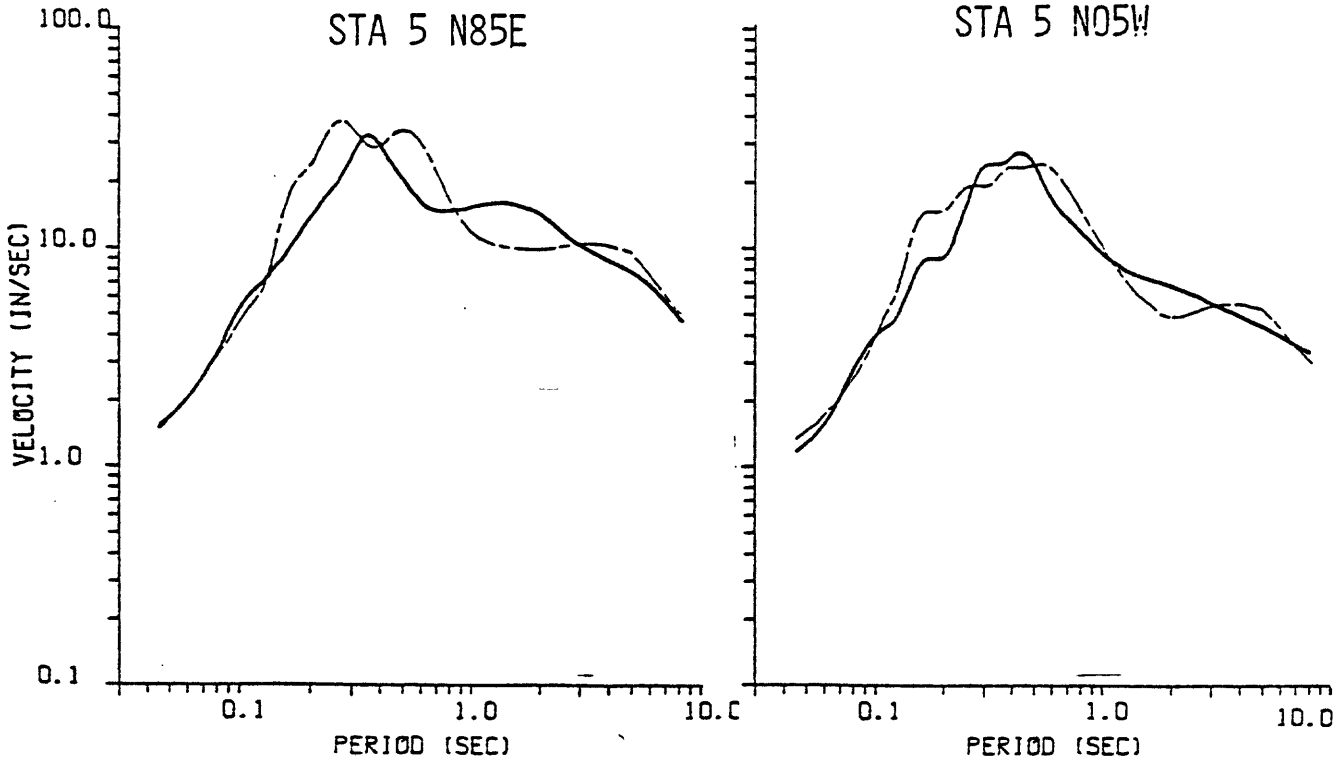

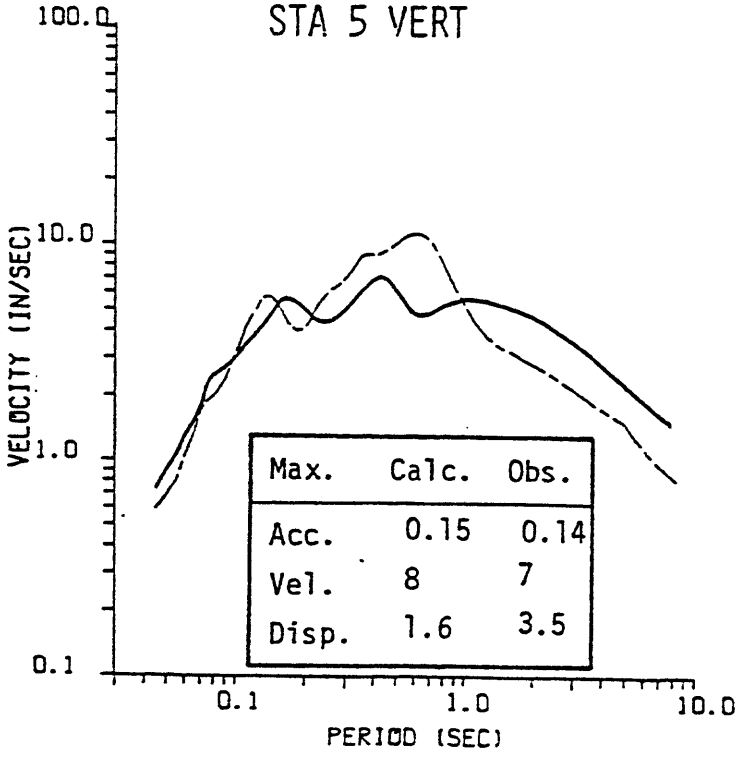

Calculated

Observed

Comparison of the smoothed 2% velocity response spectra for the 1966 Parkfield Earthquake, Station 5.

Figure 3-10

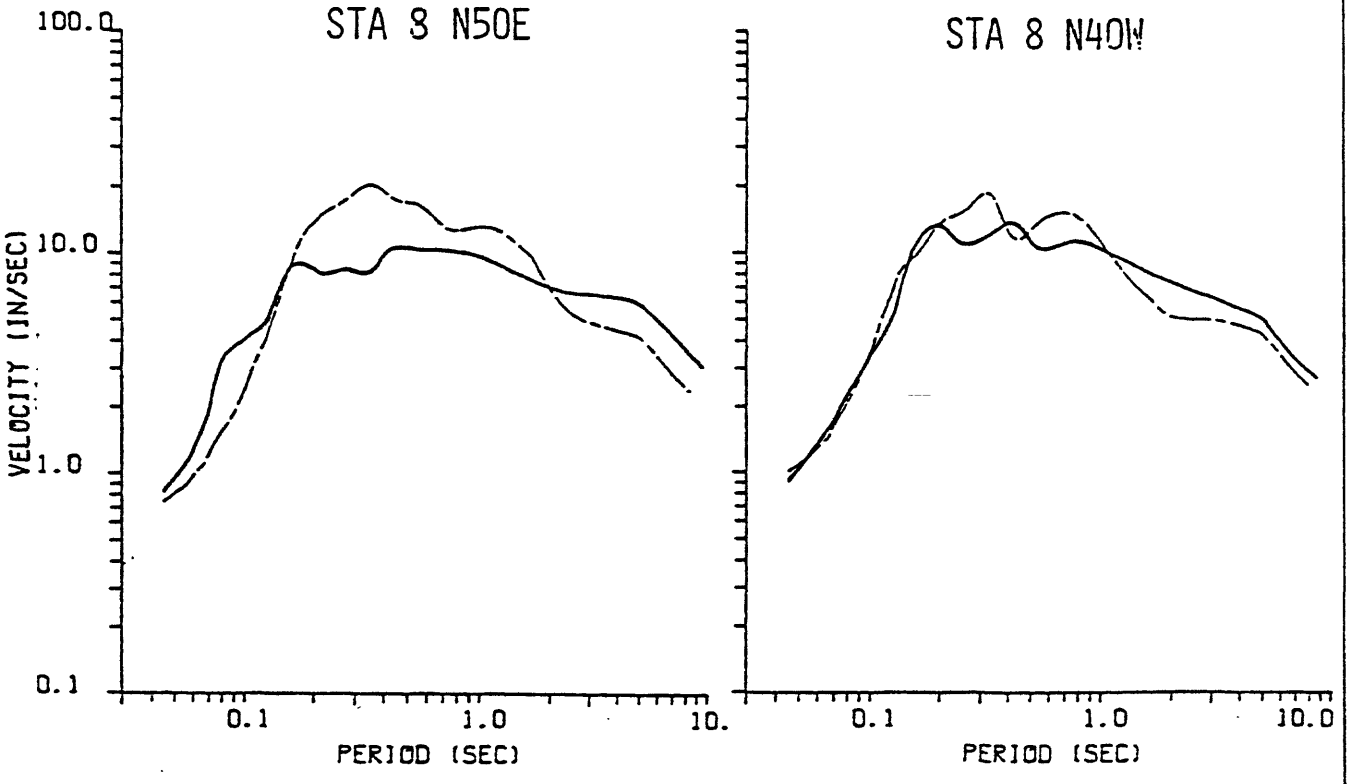

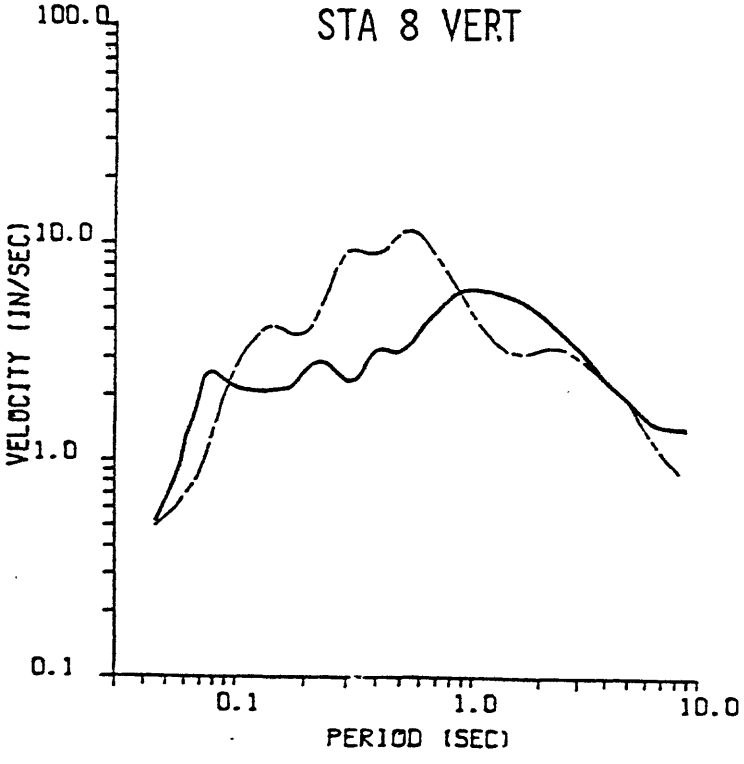

Calculated

Observed

Comparison of the smoothed 2% velocity response spectra for the 1966 Parkfield Earthquake, Station 8.

Figure 3-11

Table 3-7. Maximum values of acceleration, velocity and displacement for the 1966 Parkfield Earthquake

Station	Component	Acceleration (g) Obs.	Acceleration (g) Calc.	Velocity (cm/sec) Obs.	Velocity (cm/sec) Calc.	Displacement (cm) Obs.	Displacement (cm) Calc.
Sta. 2	Vertical	0.2	0.23	12	15	4	2
	N65E	0.5	1.20	80	77	26	20
	N25W	--	0.64	--	25	--	9
Sta. 5	Vertical	0.14	0.15	7	8	3.5	1.6
	N85E	0.45	0.47	28	26	7	11
	N05W	0.35	0.40	22	26	5	9
Sta. 8	Vertical	0.08	0.14	5	8	2	2
	N50E	0.25	0.23	10	19	5	6
	N40W	0.30	0.32	12	13	4	7
Sta. 12	Vertical	0.05	0.06	5	6	3	1
	N50E	0.06	0.14	7	6	4	5
	N40W	0.07	0.15	8	9	6	6
Temblor	Vertical	0.15	0.06	4.5	3.4	1.4	1.3
	N65W	0.30	0.14	15	10	4	4
	S25W	0.35	0.23	20	20	6	8

3.2.3 1933 Long Beach

The 1933 Long Beach Earthquake (M_S = 6.25) was a strike-slip earthquake on the Newport-Inglewood fault along the coast of Southern California. Due to poor constraints on epicenter location and extent of faulting for this event, the modeling study included determination of a rupture configuration which provided an optimal fit between the observed and computed strong ground motions. The strong motion recordings obtained during the 1933 Long Beach Earthquake were the first seismograms ever recorded. These data are less than ideal for several reasons: poor instrument amplification at long periods; late triggering of the instruments; and the burial of Station SBWY 19.5 meters beneath the ground surface.

The geologic structure for Long Beach is presented in Table 3-8 (provided by URS/John A. Blume and Associates, Engineers, 1978). The final fault model is shown relative to the recording stations in Figure 3-12, with source parameters listed in Table 3-9. The rupture surface is represented by a single fault plane striking N39°W. A comparison between the observed and computed response spectra is presented in Figures 3-13, 3-14 and 3-15. The peak ground motion values are shown in Table 3-10. The computed vertical components at Stations LNGB and VERN are deficient at high frequencies. Prior to the 1979 Imperial Valley Earthquake, the 1933 Long Beach event was unique in that the recorded vertical accelerations were substantially larger than the horizontals. The horizontal ground motions computed for station SBWY are excessive at high frequencies. The effects of instrument burial at station SBWY indicate that the recorded ground motions were considerably reduced for spectral periods lower than about 0.3 seconds (refer to Section 2.4 of DELTA, 1980a for verification calculations of such a deamplification).

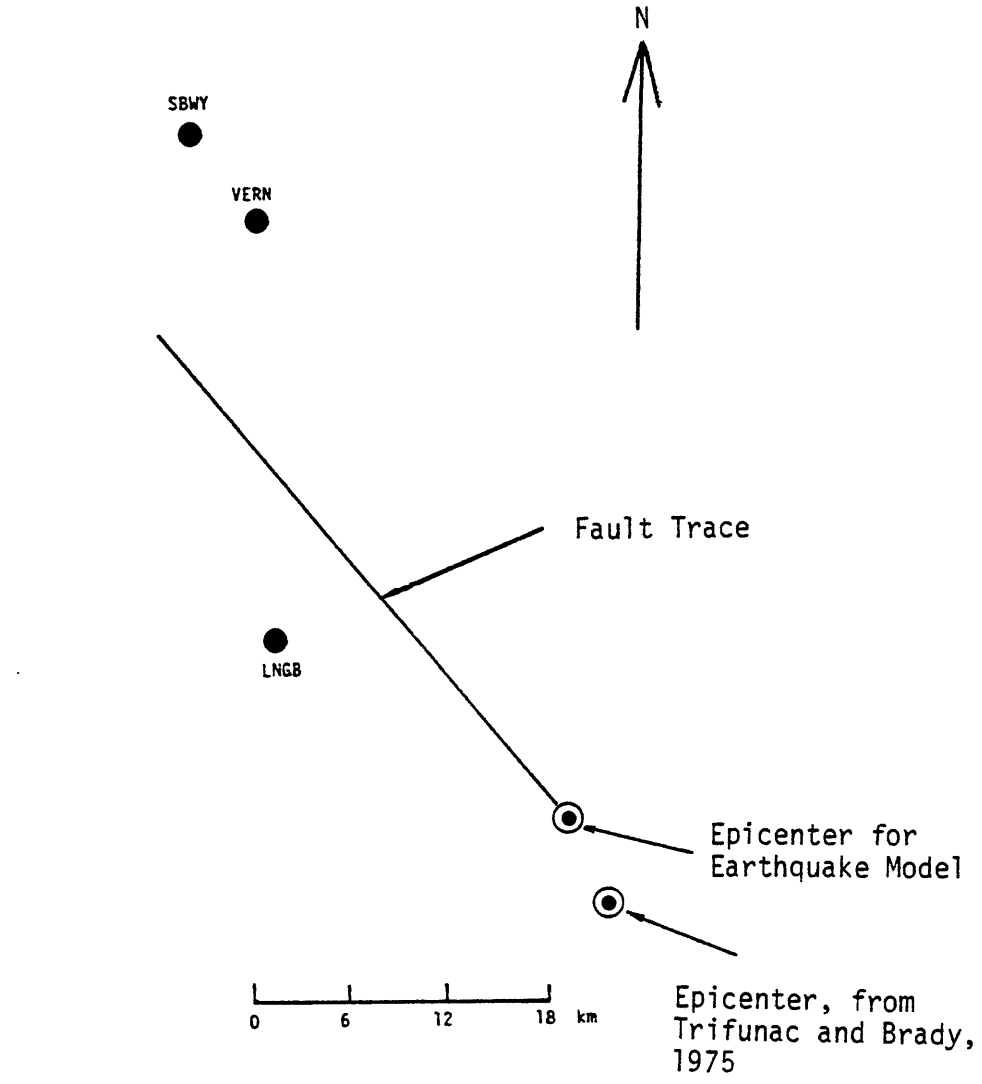

Figure 3-12. Map of the fault model for the 1933 Long Beach Earthquake.

Table 3-8. Viscoelastic parameters for the geologic structure for the 1933 Long Beach Earthquake.

Layer	β S-Wave Velocity (km/sec)	α P-Wave Velocity (km/sec)	ρ Density (gm/cm^3)	Q_β Shear Quality Factor	Q_α Compressional Quality Factor	h Layer Thickness (km)	Depth to Top of Layer (km)
1	.45	.85	1.9	15	30	.015	0.
2	.55	1.	2.1	15	35	.2	.015
3	.8	1.5	2.15	23	60	.4	.215
4	1.	1.9	2.2	30	81	.25	.615
5	1.2	2.3	2.25	38	104	.15	8.65
6	1.5	2.7	2.35	50	121	.6	1.105
7	1.7	3.1	2.5	58	145	.5	1.615
8	1.9	3.4	2.55	67	161	.3	2.115
9	2.2	3.9	2.6	80	189	.6	2.415
10	2.5	4.5	2.6	94	229	.3	3.015
11	3.4	6.1	2.7	139	334	∞	3.315

Table 3-9. Source Parameters for the 1933 Long Beach Earthquake.

Fault Length	40 km
Fault Width	12 km
Shallowest Extent	.5 km
Hypocenter Depth	12.5 km
Fault Strike	N39°W
Fault Dip	90°
Slip Direction	-15° *
Slip Duration	4.4 sec
Fault Offset	140 cm
Seismic Moment	1.7×10^{36} dyne-cm

*Predominantly right lateral strike-slip faulting. West block moves upwards relative to east block.

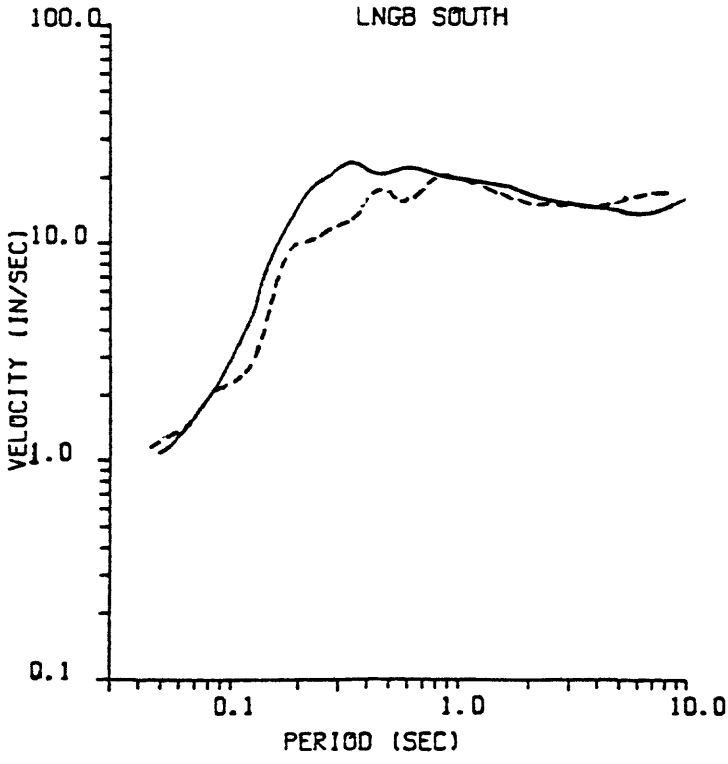

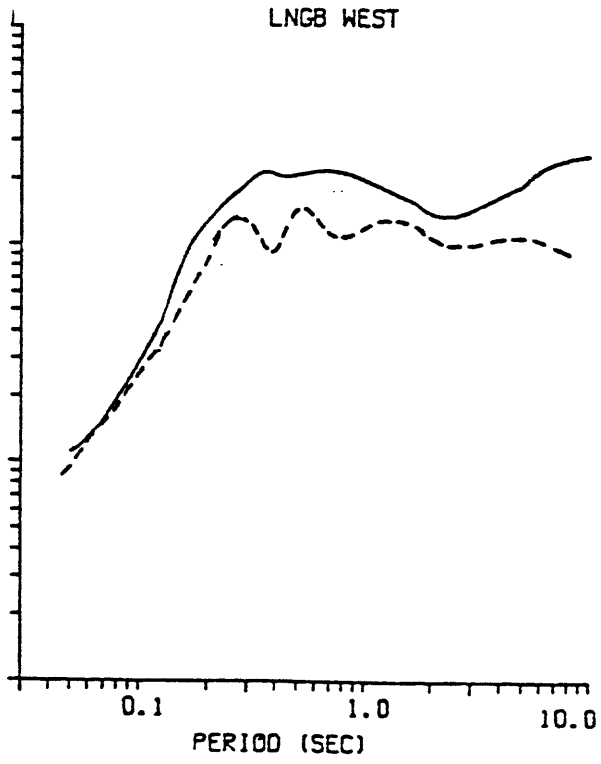

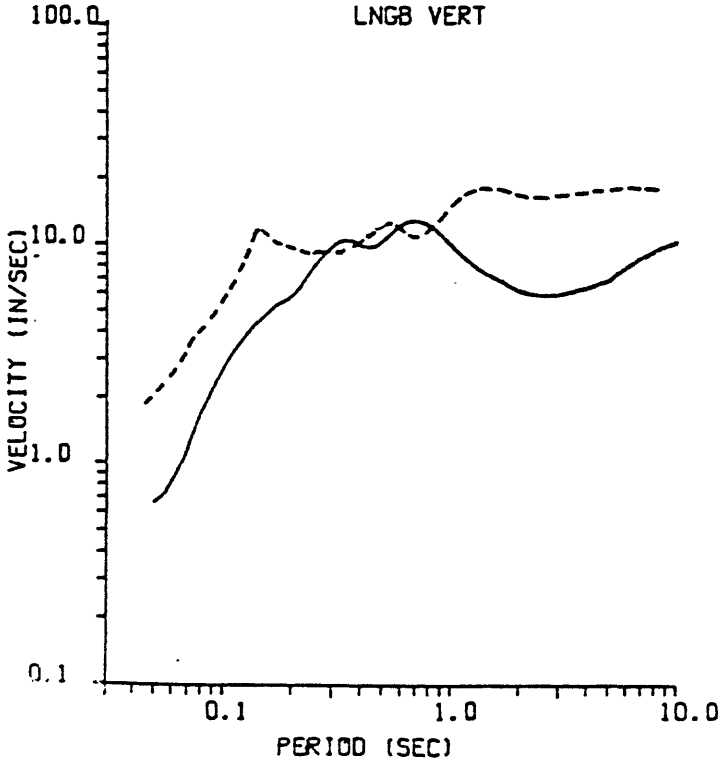

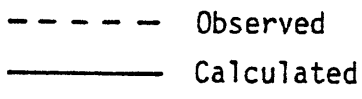

Comparison of the smoothed 2% velocity response spectra for the 1933 Long Beach Earthquake, Station LNGB.

Figure 3-13.

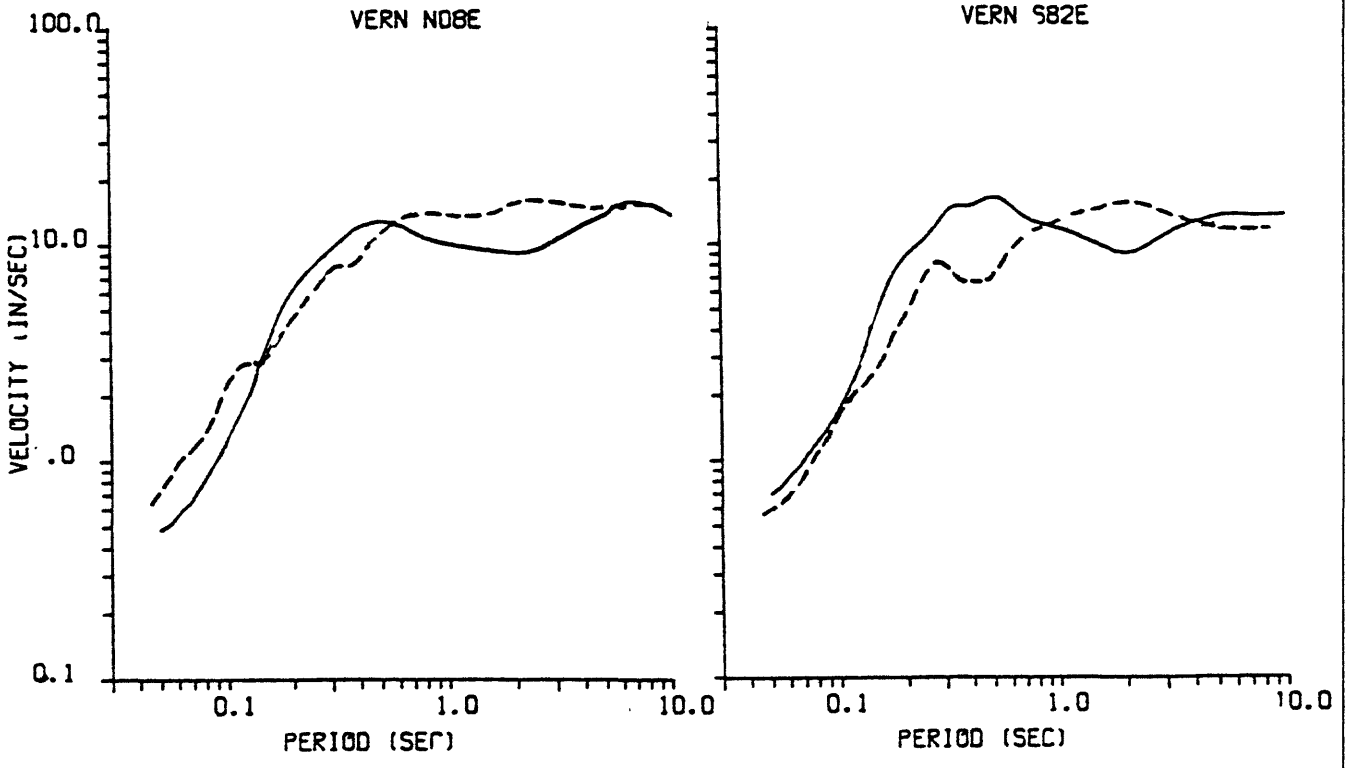

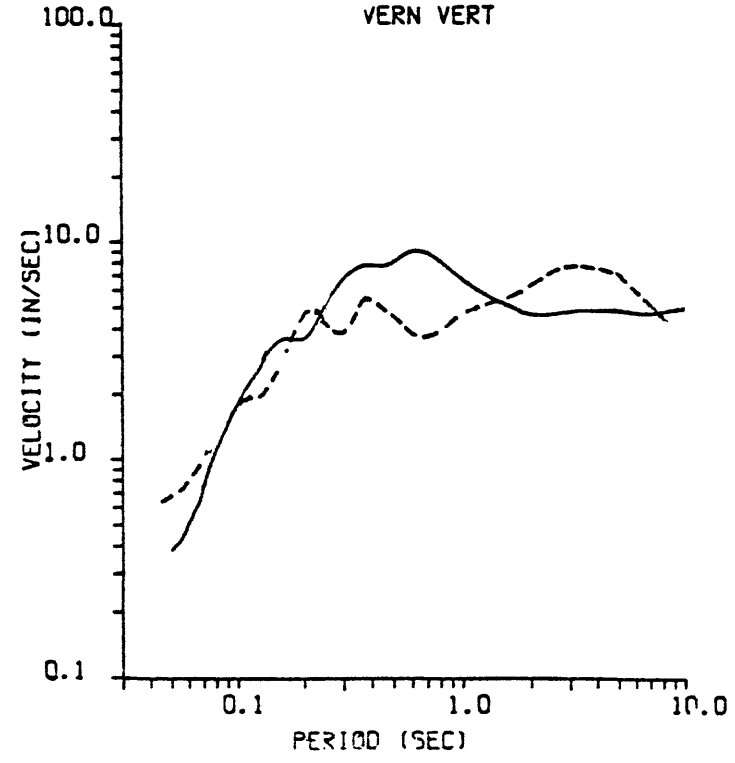

Observed

Calculated

Comparison of the smoothed 2% velocity response spectra for the 1933 Long Beach Earthquake, Station VERN.

Figure 3-14.

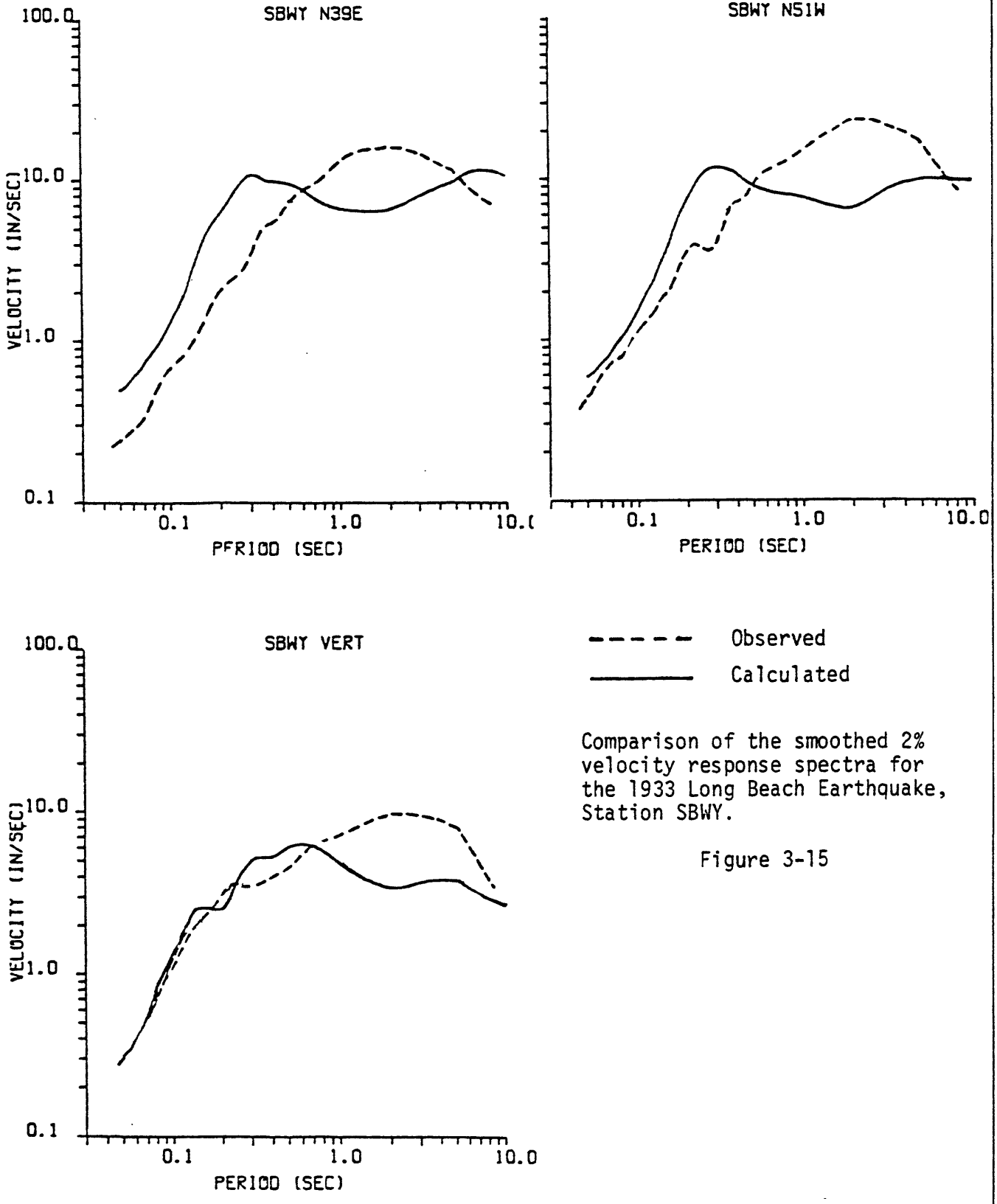

Comparison of the smoothed 2% velocity response spectra for the 1933 Long Beach Earthquake, Station SBWY.

Figure 3-15

Table 3-10. Maximum values of acceleration, velocity and displacement for the 1933 Long Beach Earthquake.

Station	Component	Acceleration (g) Obs.	Acceleration (g) Calc.	Velocity (cm/sec) Obs.	Velocity (cm/sec) Calc.	Displacement (cm) Obs.	Displacement (cm) Calc.
LNGB	Vertical	.29	.18	30	13	26	21
	South	.20	.35	29	32	23	34
	West	.16	.35	16	43	12	46
VERN	Vertical	.15	.1	12	9	7	13
	N08E	.13	.15	29	28	15	20
	S82E	.15	.22	17	21	18	25
SBWY	Vertical	.06	.09	9	6	6	8
	N39E	.06	.16	17	17	8	16
	N51W	.10	.19	24	15	16	15

3.2.4 1971 San Fernando

The 1971 San Fernando Earthquake (M_L = 6.4, M_S = 6.6) was a predominantly dip-slip (thrust) event occurring in the Transverse Ranges regime of California. Due to the proximity of the Pacoima Dam accelerograph to the rupture surface, these strong motion recordings present a unique opportunity to test the capabilities of the disbributed source model for simulating ground motions of a high stress-drop event.

Numerous studies of the faulting process for the 1971 San Fernando Earthquake indicate that the source mechanism was complex. Rupture initiated several kilometers north and east of Pacoima Dam at a depth of 9 to 14 km on a fault plane dipping about 50° NE. Rupture progressed upwards and toward the Southwest along a fault plane with dip which decreased with decreasing depth. The fault offset varied considerably over the rupture surface, with the largest offsets occurring near the ground surface and in the region of the hypocenter.

A half-space representation of the earth structure is used to model the San Fernando Earthquake, since the strong motion instrument and rupture surface were located within the crystaline basement complex of the San Gabriel Mountains. The viscoelastic parameters are presented in Table 3-11.

The Pacoima Dam accelerograph is located on a ridge in a region of large topographic relief. Several investigators have determined that the surface topography served to amplify the high frequency spectral component of ground motion by as much as 50 percent (Bouchon, 1973 and Boore, 1973). Figure 3-18 shows the amplification factor as a function of frequency which is used to compensate the response spectra of the Pacoima Dam data for the ridge effect.

The fault configuration for the San Fernando Earthquake model is shown in Figures 3-16 and 3-17. The source parameters of the computer model are listed in Table 3-12. A comparison between the observed and calculated response spectra in Figure 3-19 indicates that the distributed source model predicts the high frequency ground motions very well. The mismatch at low frequencies is attributed to the simplistic fault offset distribution used for the rupture surface in the computer model.

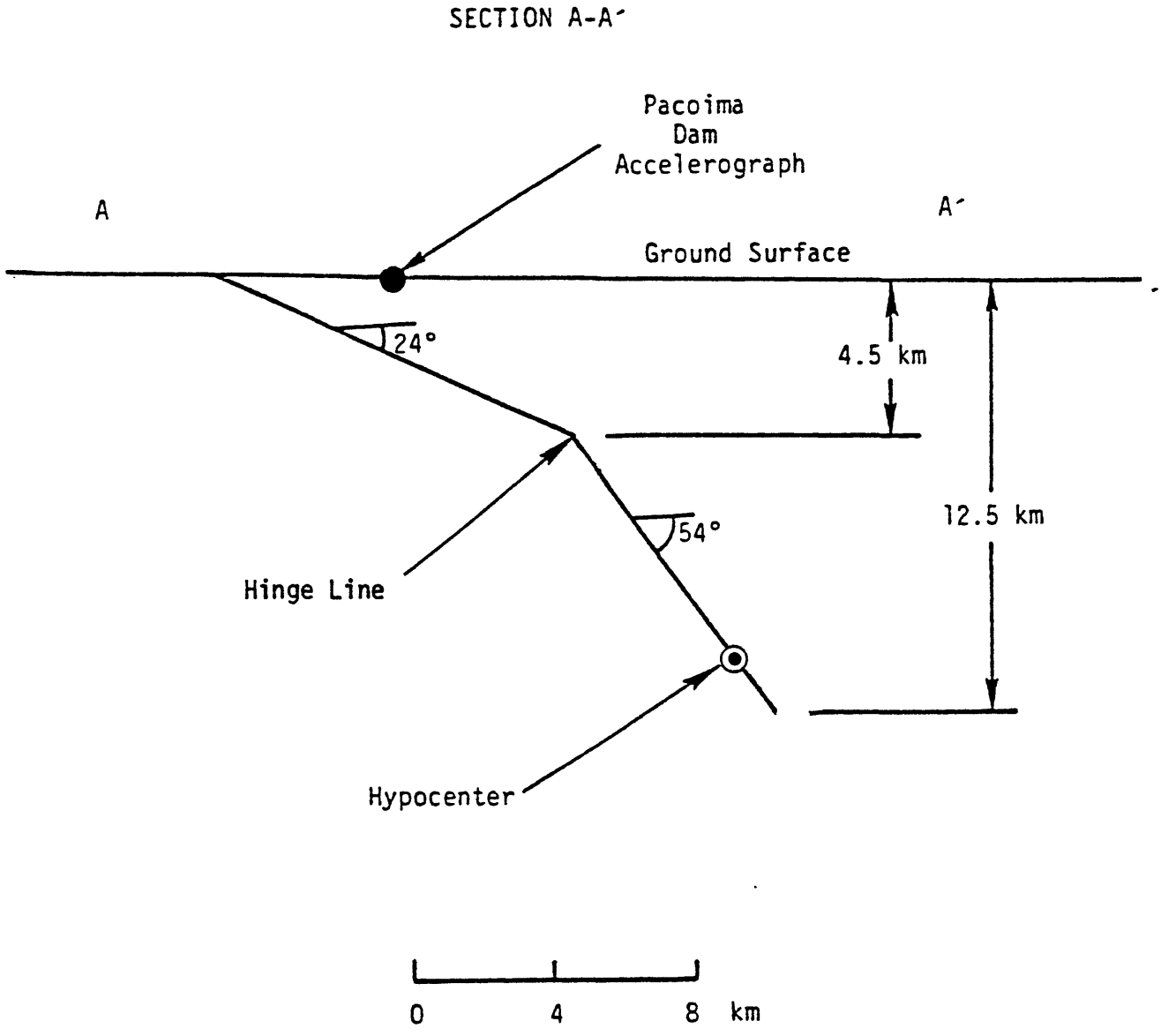

Figure 3-17. Sectional view of the fault model for the 1971 San Fernando Earthquake.

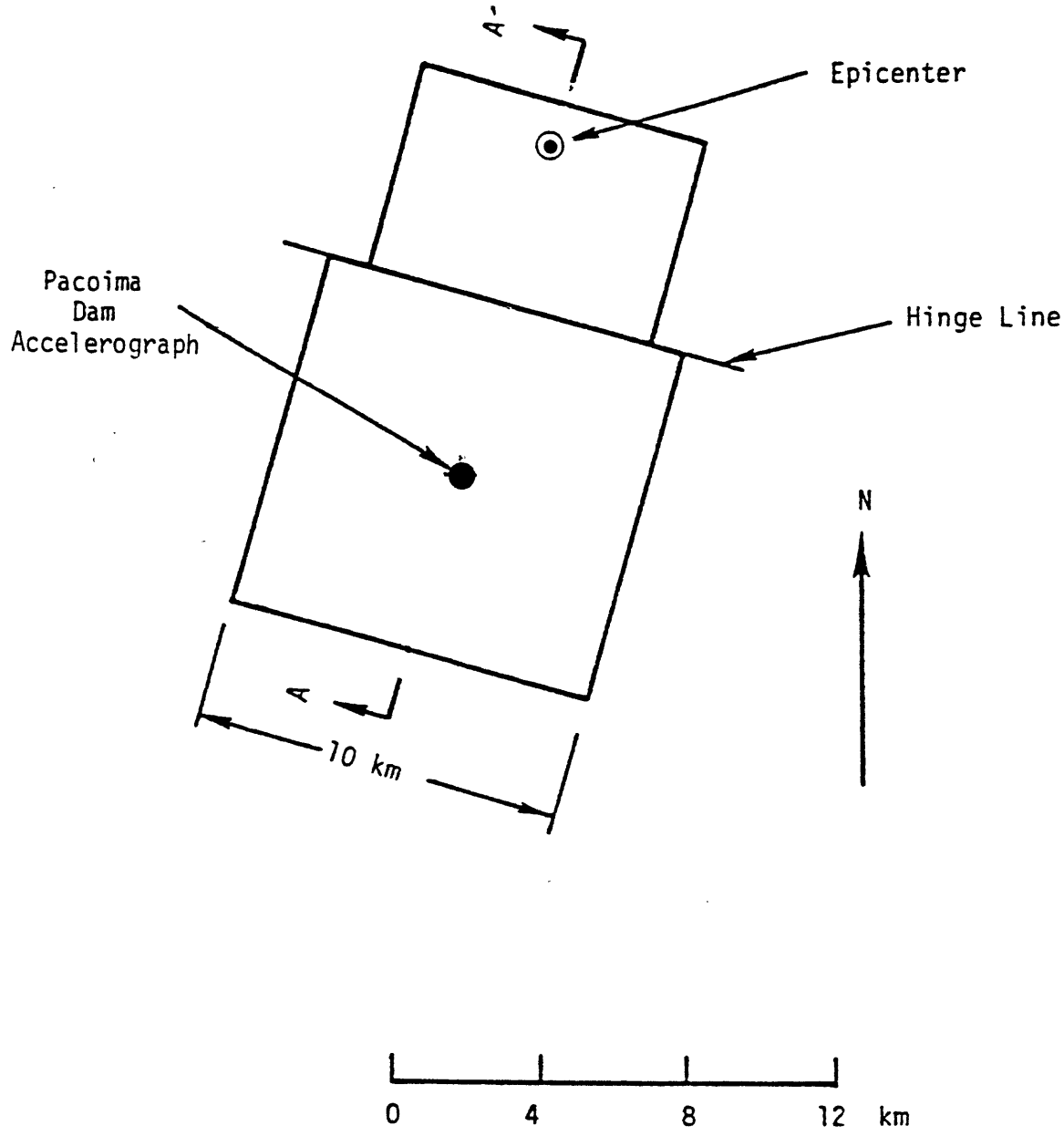

Figure 3-16. Plan view of the fault model for the 1971 San Fernando earthquake.

Table 3-11. Viscoelastic parameters for the geologic structure for the 1971 San Fernando Earthquake.

Layer	β S-Wave Velocity (km/sec)	α P-Wave Velocity (km/sec)	ρ Density (gm/cm^3)	Q_β Shear Quality Factor	Q_α Compressional Quality Factor	h Layer Thickness (km)
1	3.4	5.2	2.8	139	243	∞

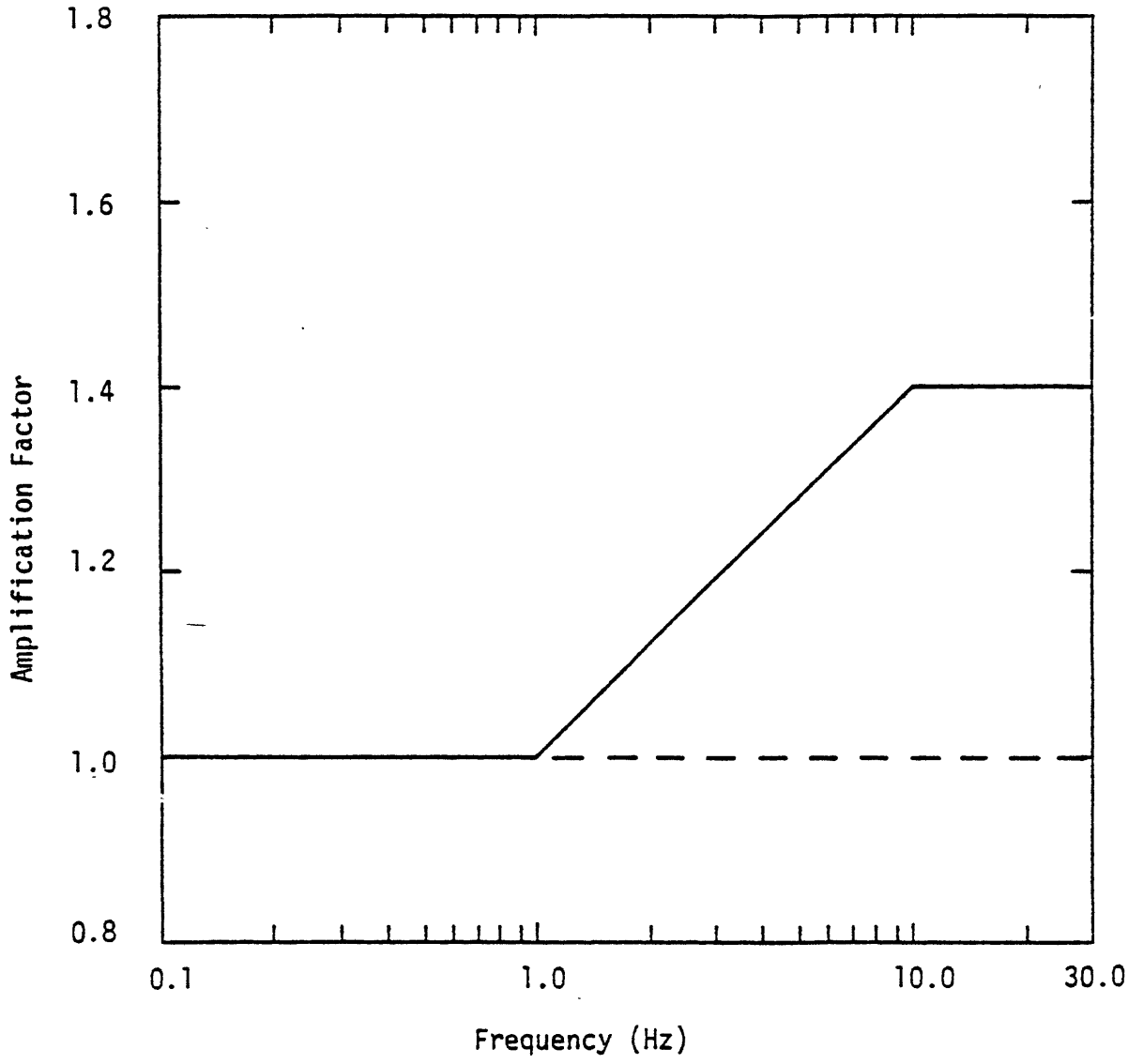

Figure 3-18. Topographic amplification factor used to compensate for ridge effect in recorded Pacoima Dam Response spectra. Adapted from Figures 4 and 5, Boore (1973).

Table 3-12. Source parameters for the 1971 San Fernando Earthquake.

	Upper Fault Plane	Lower Fault Plane
Fault Length	10 km	8 km
Fault Width	11 km	10 km
Shallowest Extent	0 km	4.5 km
Hypocenter Depth	11 km	11 km
Fault Strike	N75°W	N75°W
Fault Dip	24°N	54°N
Slip Direction	110° *	100° *
Slip Duration	2.9 sec	2.4 sec
Fault Offset	350 cm	200 cm
Seismic Moment	1.25×10^{26} dyne-cm	5.2×10^{25} dyne-cm

*Predominantly thrust faulting. Hanging block moves west relative to foot block.

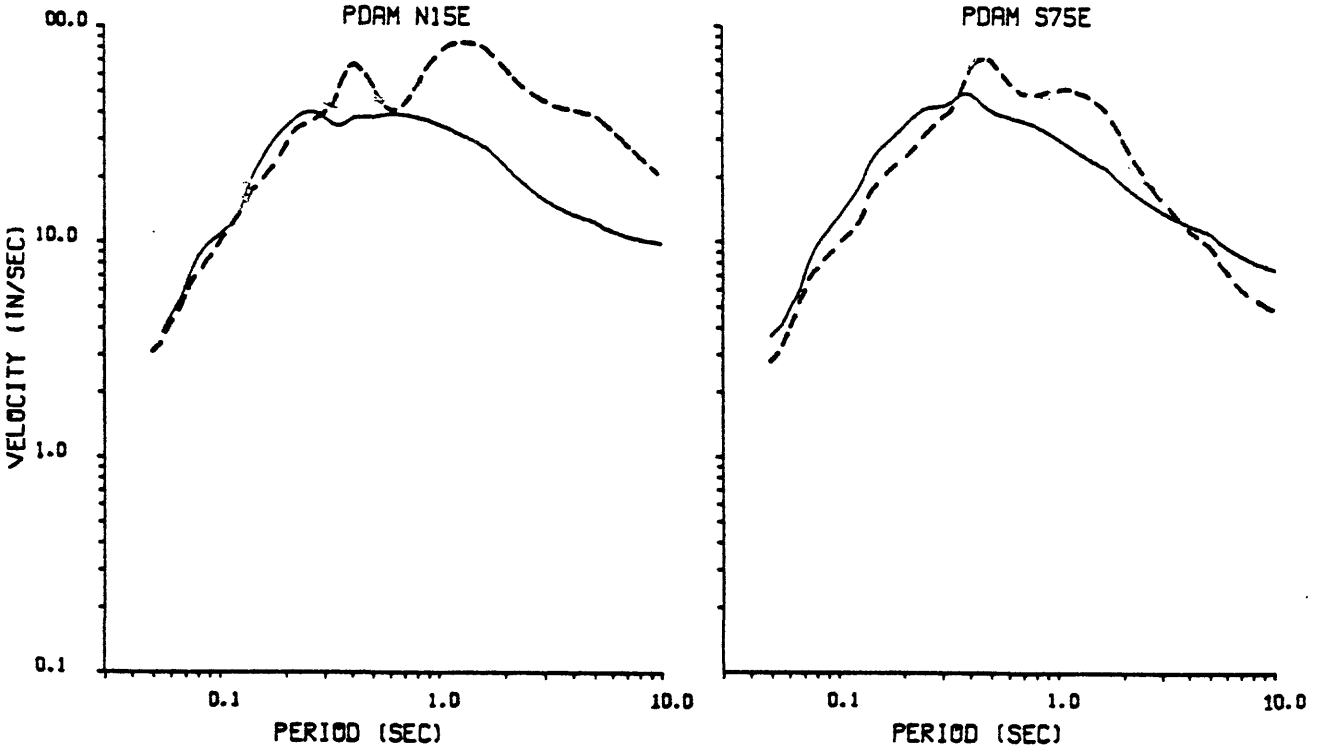

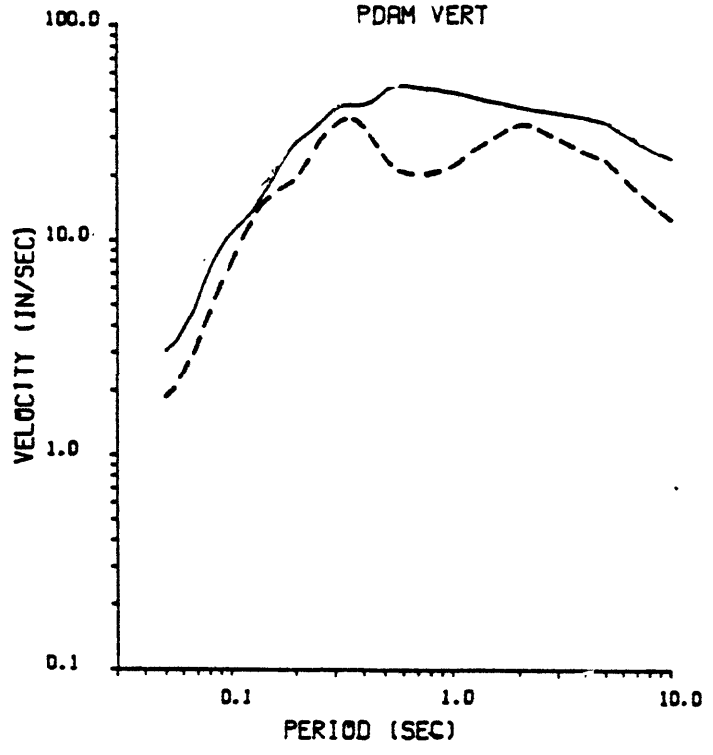

Observed

Calculated

Comparison of the smoothed 2% velocity response spectra for the 1971 San Fernando Earthquake, Station Pacoima Dam. Observed data have been compensated for the ridge effect.

Figure 3-19

Table 3-13. Maximum values of acceleation, velocity and displacement for the 1971 San Fernando Earthquake.

Station	Component	Acceleration (g) Obs.	Acceleration (g) Calc.*	Velocity (cm/sec) Obs.	Velocity (cm/sec) Calc.	Displacement (cm) Obs.	Displacement (cm) Calc.
Pacoima Dam	Vertical	.71	.81	58	110	19	49
	N15E	1.17	.84	113	56	38	18
	S75E	1.08	.94	58	58	11	14

*These observations include the effect of topographic amplification which is not present in the calculated accelerations. Bouchon (1973) concludes that the ridge at Pacoima Dam amplifies the high frequency observations by 30% to 50%. Boore (1973) finds ridge amplifications as large as 50% and concludes that the free-field peak acceleration, with ridge effects removed, is 0.73 g.

3.2.5 1979 Imperial Valley

The 1979 Imperial Valley Earthquake (M_L = 6.5, M_S = 6.7) was located on the Imperial Fault in approximately the same location as the 1940 Imperial Valley Earthquake. More than 30 strong motion recordings were obtained within 40 km of the fault for this event in the United States and Mexico (see Figure 3-20). Due to the quantity and distribution of near-field recordings, the 1979 Imperial Valley Earthquake presents a unique opportunity to increase our understanding about faulting processes and wave propagation effects for large earthquakes.

The geologic structure for the Imperial Valley has been determined from a detailed refraction survey recently carried out by the U.S.G.S. (Mooney and McMechan, 1979). The viscoelastic parameters used to model the 1979 earthquake are listed in Table 3-14.

When modeling studies were initially carried out for the 1979 Imperial Valley Earthquake, several deficiencies in the distributed source earthquake model became apparent. Ground motions computed for a wide distribution of source-receiver geometries and fault distances indicated that the effects of focussing were exaggerated at high frequencies and that the computed vertical accelerations were too low. In order to correct for these inadequacies, incoherence in the form of randomness was added to the rupture front as it progressed over the fault plane. The distributed source model, with these refinements added, yielded ground motions which compared very well with the recorded data.

The source parameters used in the 1979 earthquake computer model are listed in Table 3-15. The rupture surface consists of a single fault plane with a uniform offset and depth. The computed accelerations, velocities and displacements are compared with the observed data in Figures 3-21 through 3-26. Shown on these figures are calculated peak ground motions for Station 6 (1 km), Bond's Corner (3 km), Station 8 (4 km), Station 4 (7 km), Station 11 (13 km) and Station 1 (22 km). Curves of the form

$$\frac{A}{(R + C)^{1.75}} \qquad (3\text{-}16)$$

have been regressed in a least-squared-error sense against the observed peak ground motion values as a function of distance. The parameter A is a scaling factor determined by minimizing the squared error, R is the closest distance from each station to the fault trace and C is a constant, with C = 20 for horizontal data and C = 10 for vertical data. The $\pm$ one standard deviation curves are also shown. The calculated peak accelerations follow the trend of the mean of the data quite well. The peak horizontal velocities are somewhat defficient at all distances and the peak vertical displacements are too high. In general, the fit between the observed and computed ground motions is excellent (refer to Chapter 5 of DELTA, 1980b for the response spectral comparisons).

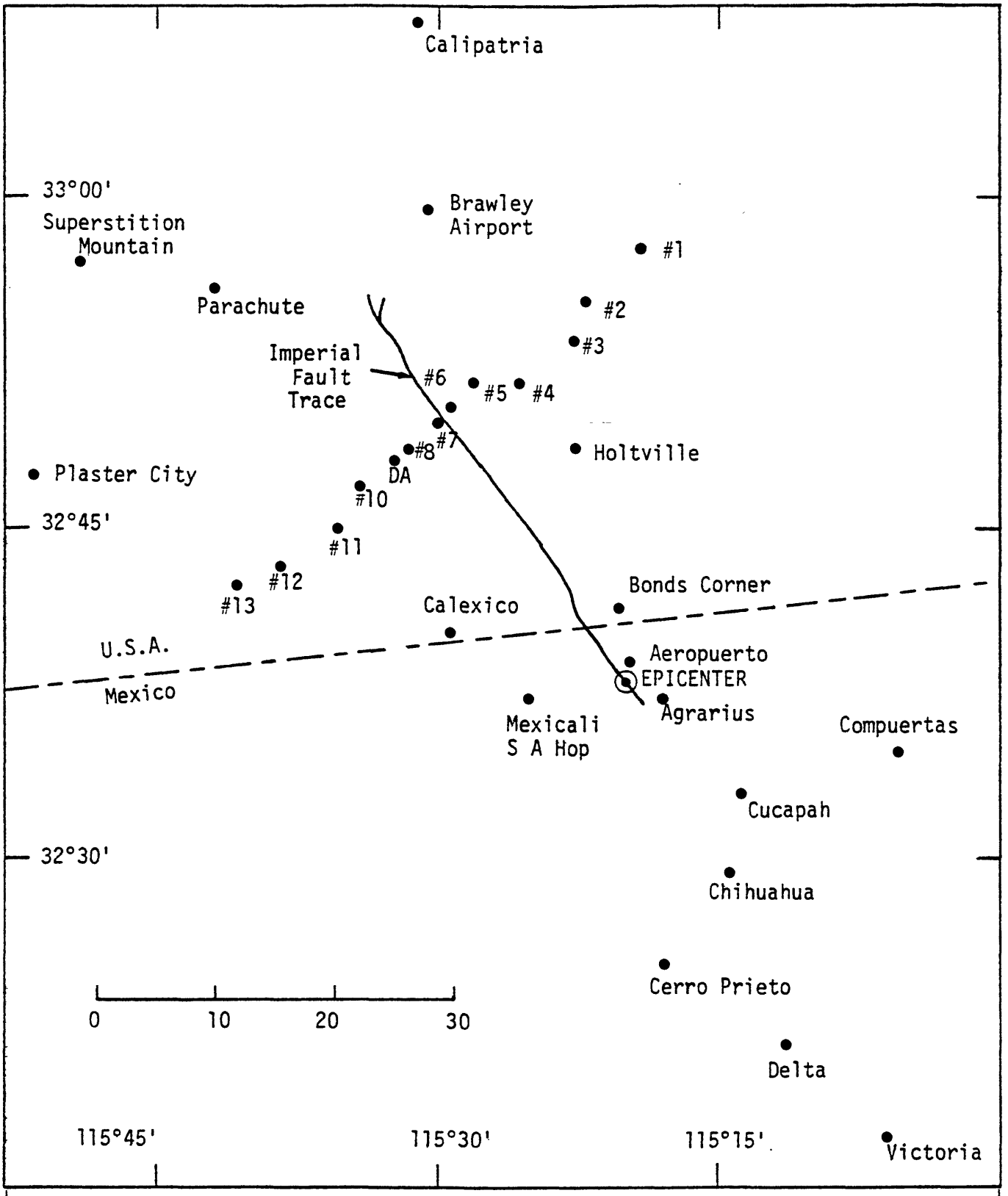

Figure 3-20. Strong motion stations for the 1979 Imperial Valley Earthquake. Fault trace is for the 1940 Imperial Valley Earthquake.

Table 3-14. Viscoelastic parameters for the geologic structure for the 1979 Imperial Valley earthquake.

Layer	β S-Wave Velocity (km/sec)	α P-Wave Velocity (km/sec)	ρ Density (gm/cm^3)	Q_β Shear Quality Factor	Q_α Compressional Quality Factor	h Layer Thickness (km)	Depth to Top of Layer (km)
1	0.818	1.790	2.06	23.	83.	0.25	0.0
2	1.010	2.167	2.13	30.	104.	0.50	0.25
3	1.200	2.533	2.21	38.	127.	0.50.	0.75
4	1.410	2.900	2.28	46.	146.	0.50	1.25
5	1.620	3.267	2.35	55.	168.	0.50	1.75
6	1.850	3.633	2.43	65.	188.	0.50	2.25
7	2.080	4.000	2.50	75.	208.	0.50	2.75
8	2.330	4.367	2.57	86.	227.	0.50	3.25
9	2.590	4.733	2.65	99.	248.	0.50	3.75
10	2.870	5.100	2.72	112.	265.	0.50	4.25
11	3.060	5.375	2.78	121.	280.	0.50	4.75
12	3.260	5.650	2.83	131.	295.	0.50	5.25
13	3.320	5.750	2.85	134.	301.	5.25	5.75
14	3.870	6.700	3.04	163.	366.	0.30	11.0
15	3.980	6.900	3.08	169.	381.	0.30	11.3
16	4.100	7.100	3.12	175.	394.	0.30	11.6
17	4.210	7.300	3.16	181.	408.	13.10	11.9
18	4.670	8.100	3.32	206.	465.	0.10	25.0

Table 3-15. Source parameters for the 1979 Imperial Valley Earthquake

Fault Length	37 km
Fault Width	11.4 km
Shallowest Extent	.5 km
Hypocenter Depth	11.9 km
Fault Strike	N34°W
Fault Dip	90°
Slip Direction	45° *
Slip Duration	2.4 sec
Fault Offset	100 cm
Seismic Moment	9.7×10^{25} dyne-cm

*Right lateral motion with west block moving upwards relative to east block.

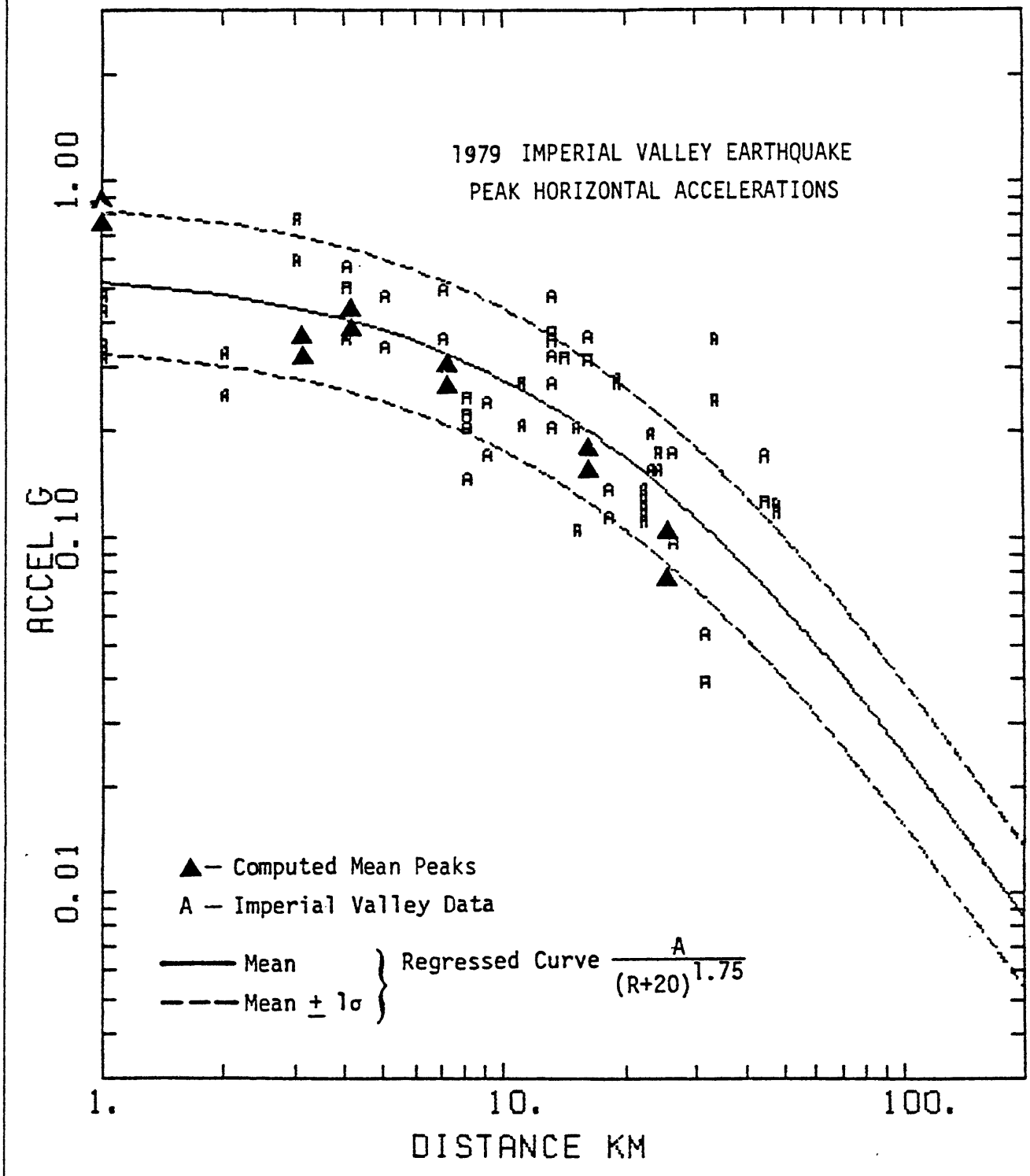

Figure 3-21. Computed peak horizontal accelerations plotted against the Imperial Valley data and regressed curves as a function of distance from the fault trace.

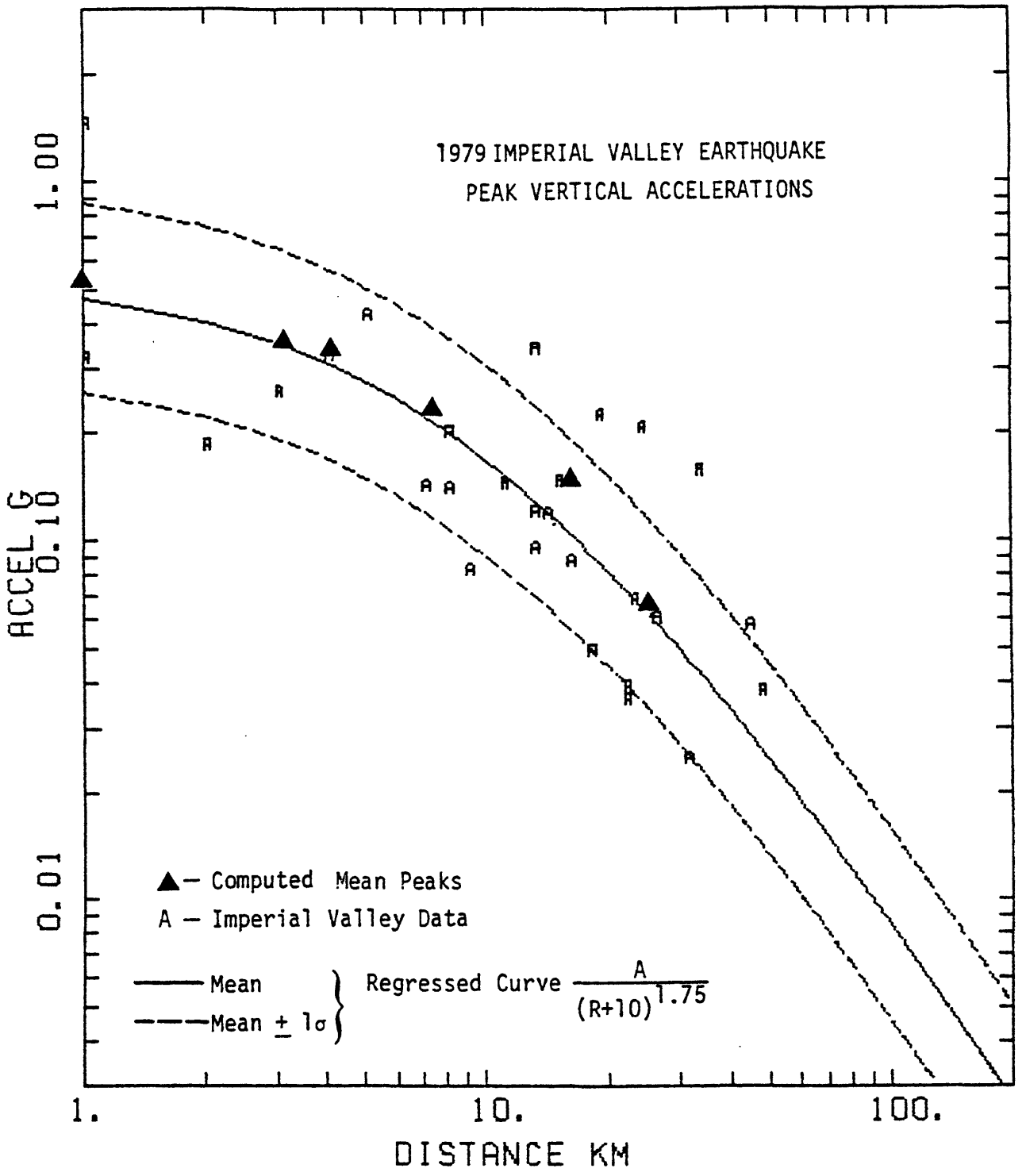

Figure 3-22. Computed peak vertical accelerations plotted against the Imperial Valley data and regressed curves as a function of distance from the fault trace.

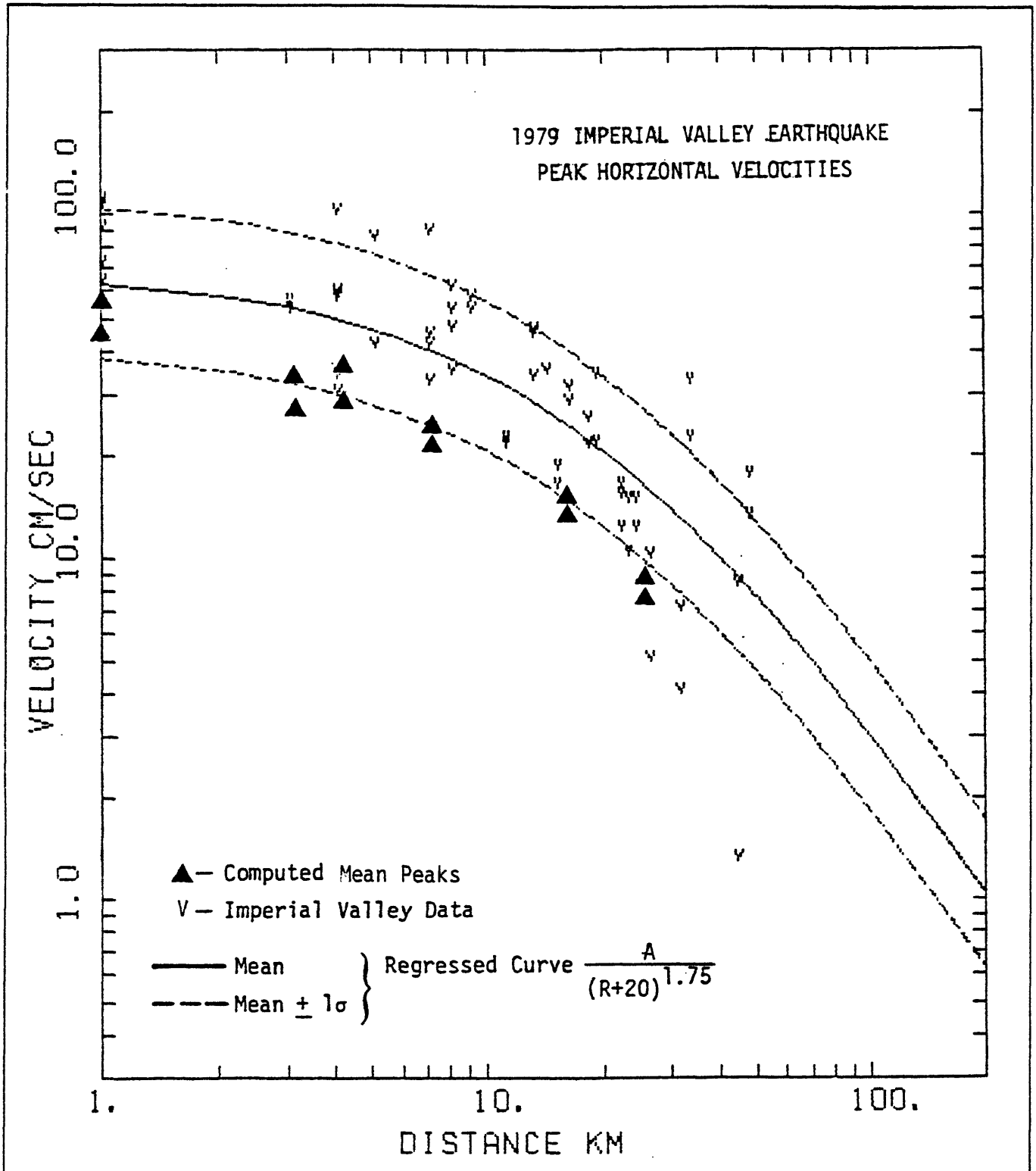

Figure 3-23. Computed peak horizontal velocities plotted against the Imperial Valley data and regressed curves as a function of distance from the fault trace.

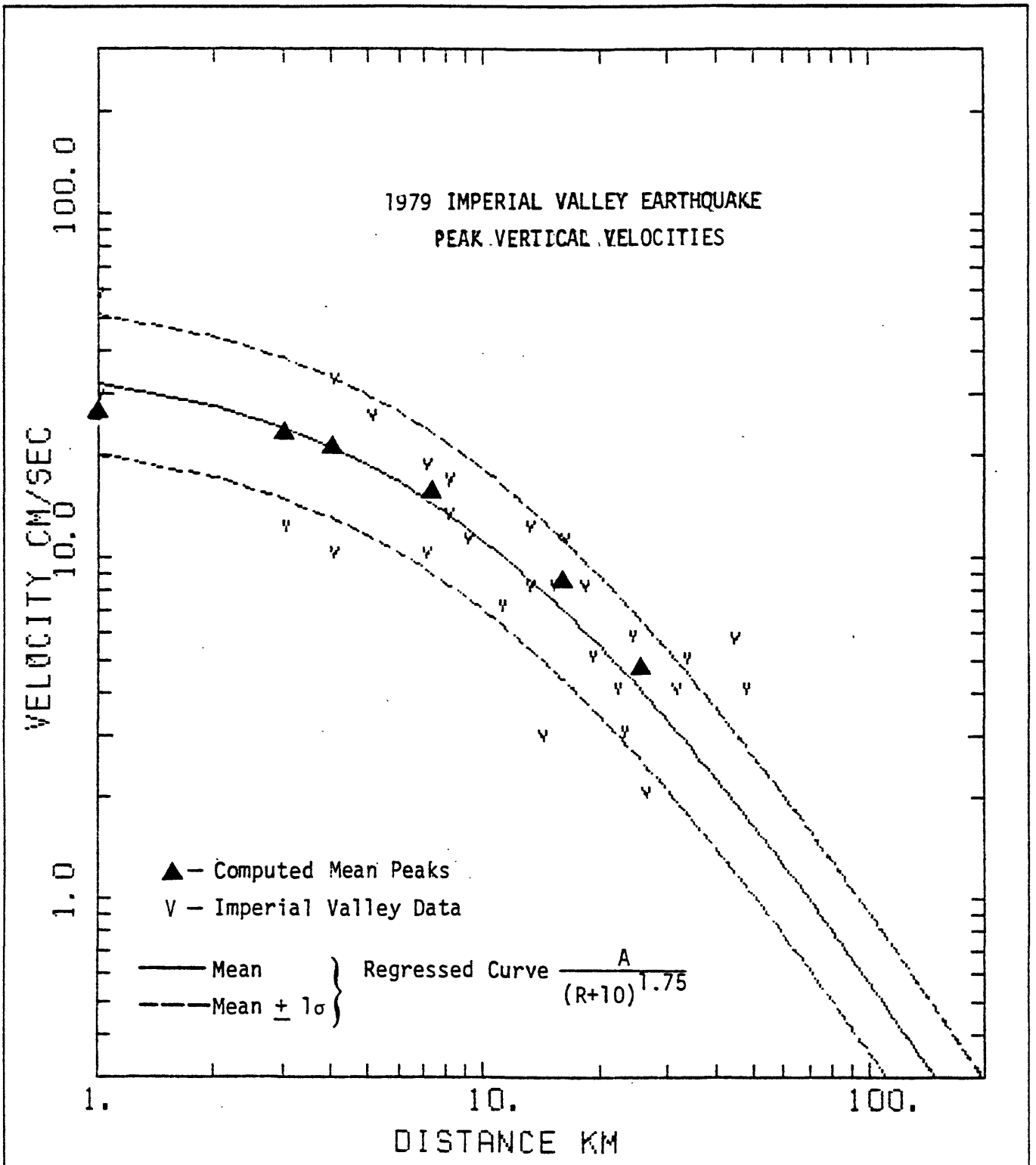

Figure 3-24. Computed peak vertical velocities plotted against the Imperial Valley data and regressed curves as a function of distance from the fault trace.

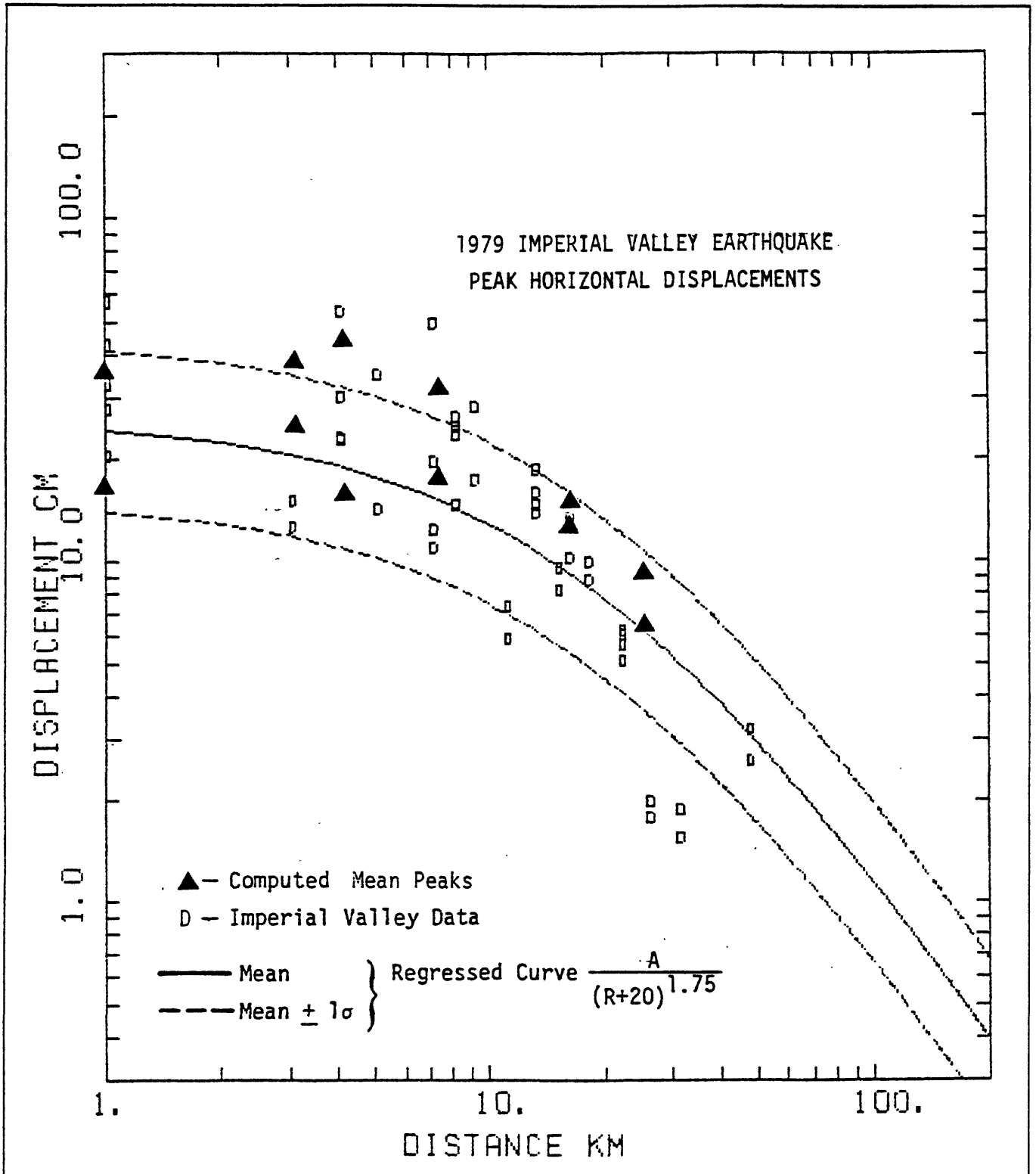

Figure 3-25. Computed peak horizontal displacements plotted against the Imperial Valley data and regressed curves as a function of distance from the fault trace.

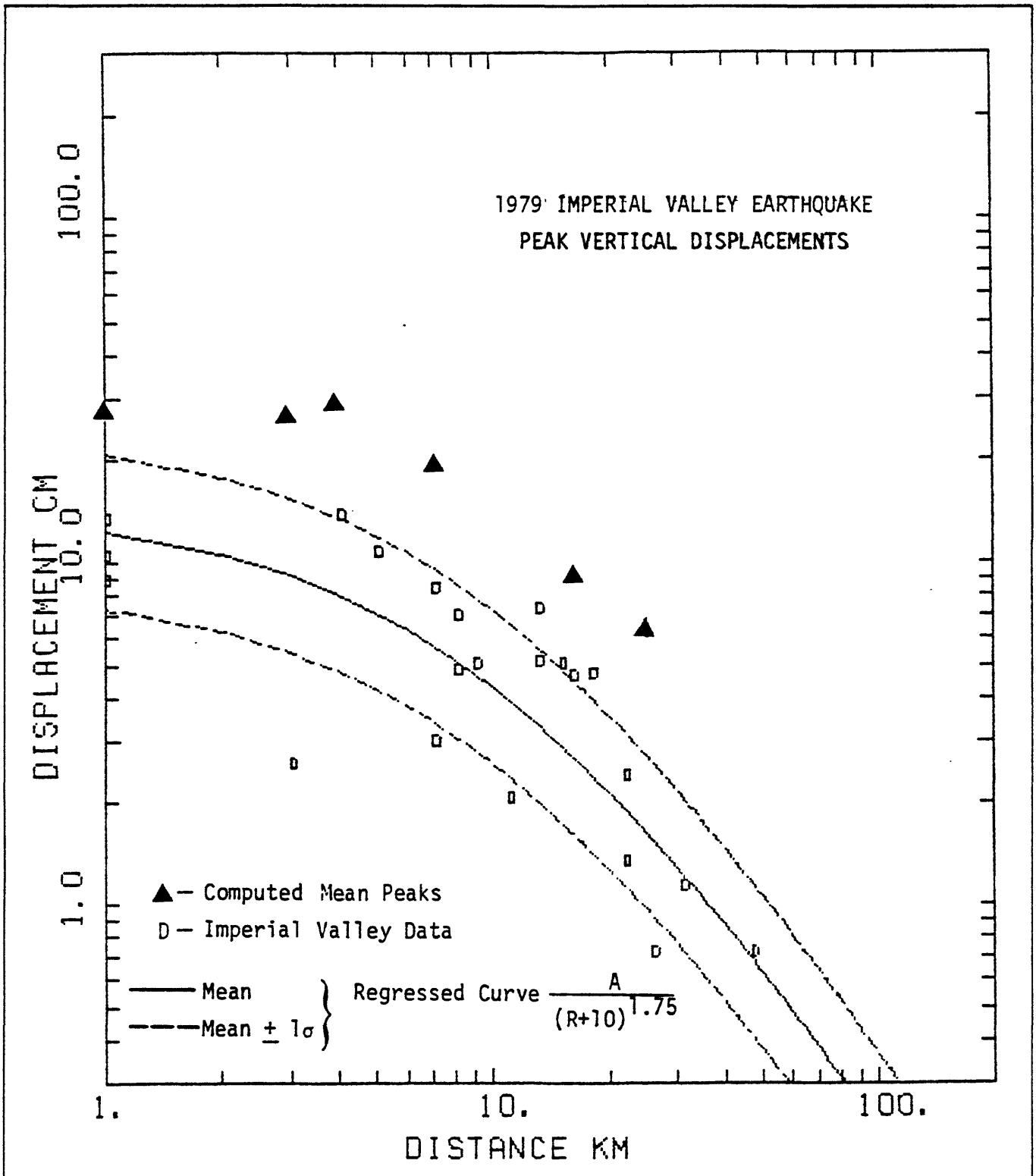

Figure 3-26. Computed peak vertical displacements plotted against the Imperial Valley data and regressed curves as a function of distance from the fault trace.

CHAPTER 4

GROUND MOTION MAPS FOR THE LOS ANGELES BASIN

4.1 EARTH STRUCTURE AND GREEN'S FUNCTION COMPUTATION

The Los Angeles basin is an extensive sediment-filled structural depression underlying much of the densely populated Los Angeles metropolitan area. The basin is characterized by rather flat surface topography and relatively low near-surface seismic velocities. The depth to the basement complex varies considerably throughout the basin, with the deepest point located about ten kilometers south of downtown Los Angeles. A gentle thinning of the sediments occurs northward toward the San Gabriel Mountains, southeastward toward the Peninsular Ranges and westward toward the Pacific Ocean coastline. The sedimentary basin structure extends eastward to San Bernardino with a similar basin structure eastward along the San Andreas Fault.

It is important to realize that the earth structure, for which the Green's functions are to be calculated, must be representative of the material behavior between the rupture surface and all the receivers of interest. The twenty-two receivers used in the calculation of the ground motion maps are located within the region bounded by the Transverse Ranges, the San Andreas Fault, the Peninsular Ranges and the Pacific Ocean coastline. Most of the rupture configurations that are considered along the San Andreas Fault in Section 4.2 and Chapter 5 extend through the Transverse Ranges north of the Los Angeles basin; the rupture configurations that are considered along the Newport-Inglewood Fault in Section 4.3 extend immediately through the southwestern part of the region bounding the receivers of interest. Because of computing limitations, the Green's functions can only be calculated for one earth structure. The earth structure is therefore chosen to represent a composite or average geologic section over the region just described.

The seismic velocities chosen for this geologic section are shown in Figure 4-1 as a function of depth. The layer thicknesses and seismic velocities are based on available geologic and seismic data. Investigators have used limited data from the past to describe generic velocity profiles for Southern California (Gutenberg, 1944, 1951, 1952, 1955; Richter, 1950; Shor, 1955; Press, 1956, 1960; Roller and Healy, 1963; Allen, et al., 1965; Healy, et al., 1968; and Kanamori and Hadley, 1975). Kovach (1974) has used surface wave dispersion data from subsidence events near Long Beach to estimate a velocity structure specific to the Long Beach area. Other investigators have more recently used extensive data sets obtained either by oil well logs, refraction studies, or microearthquakes to describe the velocity structure specific to the Los Angeles basin (Teng, et al., 1973 and Hadley and Kanamori, 1979).

The compressional-wave velocities for the top five layers down to a depth of 15 km have been extracted from the work by Teng, et al. (1973) and were determined from two-way transit time velocity logs taken from oil wells in the vicinity of Baldwin Hills by Chevron Research Corporation of California. The compressional-wave velocity for the uniform layer comprising the basement complex down to a depth of 28.4 km has also been extracted from the work by Teng, et al. (1978) and was determined indirectly from a refraction study by Roller and Healy (1963). In Roller and Healy's simplified model, the earth was represented by a single 27-km-thick layer with a compressional-wave velocity of 6.1 km/sec overlying a half-space with a compressional-wave velocity of 8.2 km/sec. The value of 6.3 km/sec for this sixth layer was assigned so that the vertical travel time through the top 28.4 km corresponds to a velocity of about 6.1 km/sec.

The compressional-wave velocities for the layers underlying the basement complex have been extracted primarily from the work by Hadley and Kanamori (1979). Travel-time data obtained from both natural and artificial events were used by Hadley and Kanamori to ascertain the compressional-wave velocities in the vicinity of the Transverse Ranges. They found an extensive layer with a velocity of about 6.8 km/sec just above the mantle as characterized by the seventh layer. The crustal thickness throughout the Los Angeles basin and the Transverse Ranges

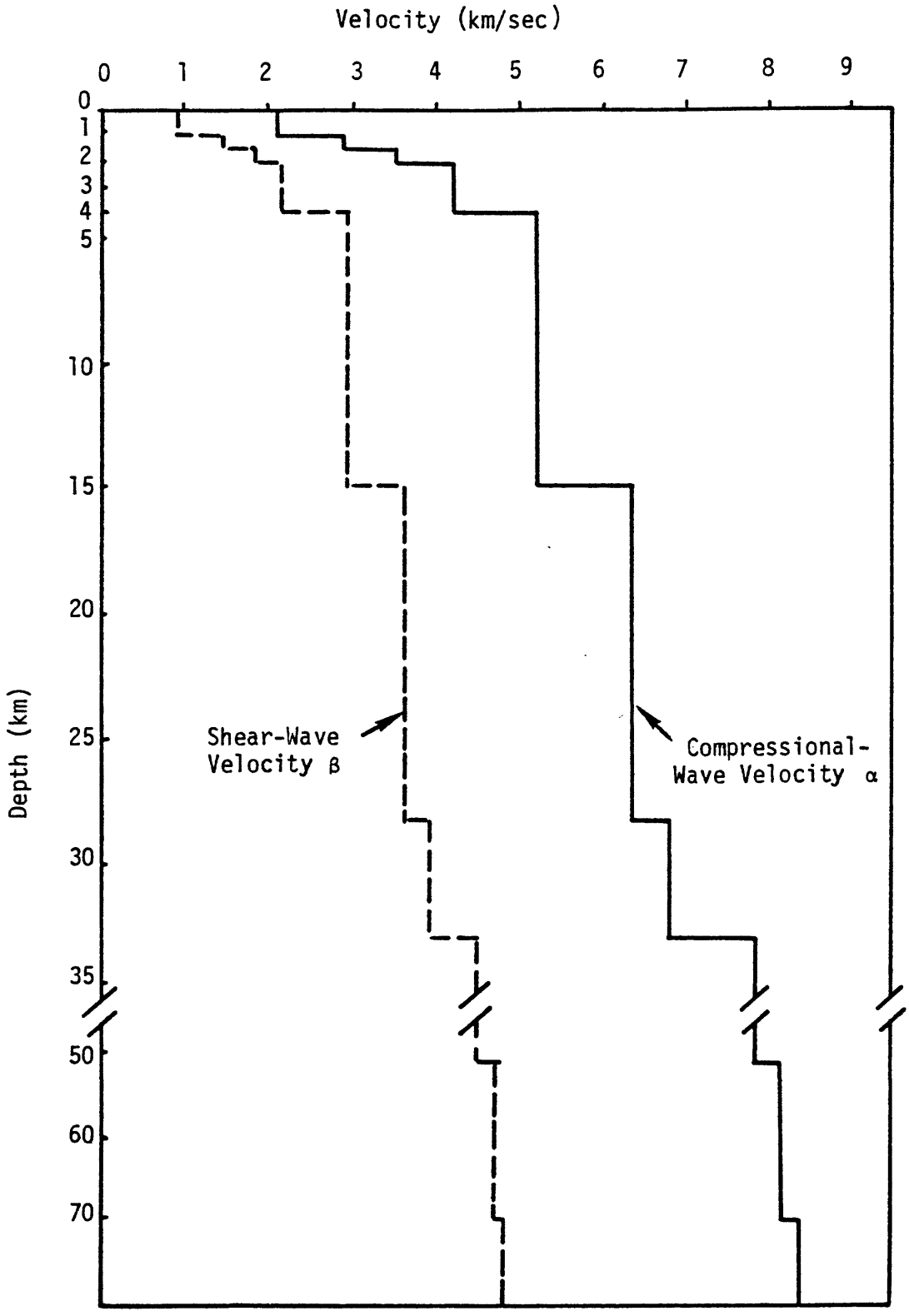

Figure 4-1. Velocity structure determined for an average section in the Los Angeles basin geologic environment.

varies between 30 to 35 km. The crust/mantle interface is characterized by a regionally observed 7.8 km/sec layer which is suggested by Hadley and Kanamori to be a zone of decoupling necessary to accomodate the horizontal shear resulting from the divergence of the crust and upper mantle plate boundaries. Therefore, the eighth layer beginning at a depth of 33.4 km with a compressional-wave velocity of 7.8 km/sec is chosen to represent the uppermost material of the mantle. Hadley and Kanamori also suggest that a high-velocity (8.3 km/sec) lens-shaped structure extends from 40 to 100 km in depth at the point of greatest thickness beneath the Transverse Ranges as shown in Figure 4-2 by the north-south cross section in the vicinity of Cajon Pass along the San Andreas Fault. At the same time, Press (1960) suggests a layer beginning at a depth of 51.0 km with a compressional-wave velocity of 8.1 km/sec. Using both of these pieces of information, the ninth layer with a velocity of 8.1 km/sec is chosen to extend from a depth of 51.0 km down to the mid-depth of 70 km in Hadley and Kanamori's high-velocity ridge. Then, the underlying half-space is assigned a compressional-wave velocity of 8.3 km/sec.

The shear wave velocities for this nine layer over a half-space representation of the earth are assigned values based on the ratios of shear to compressional wave velocities for the Los Angeles basin as published by Kovach (1974). The resulting shear velocity profile is also shown as a function of depth in Figure 4-1. The remainder of the parameters defining the material properties in each layer are based on generic formulae for Southern California geologic environments. In particular, the density ρ, in units of gm/cm^3, is related to the compressional-wave velocity α in a given layer by the formula $\rho = 1.7 + 0.2\alpha$ (DELTA, 1980b). The material quality factor for shear-wave propagation Q_β is related to the shear-wave velocity α in a given crustal layer by the formula $Q_\beta = 30\beta^{1.25}$ (DELTA, 1978 → present). Values of Q_β in the deeper layers are chosen to be representative of attenuation in the mantle. The material quality factor for compressional-wave propagation Q_α is related to the shear-wave quality factor in a given layer by the formula

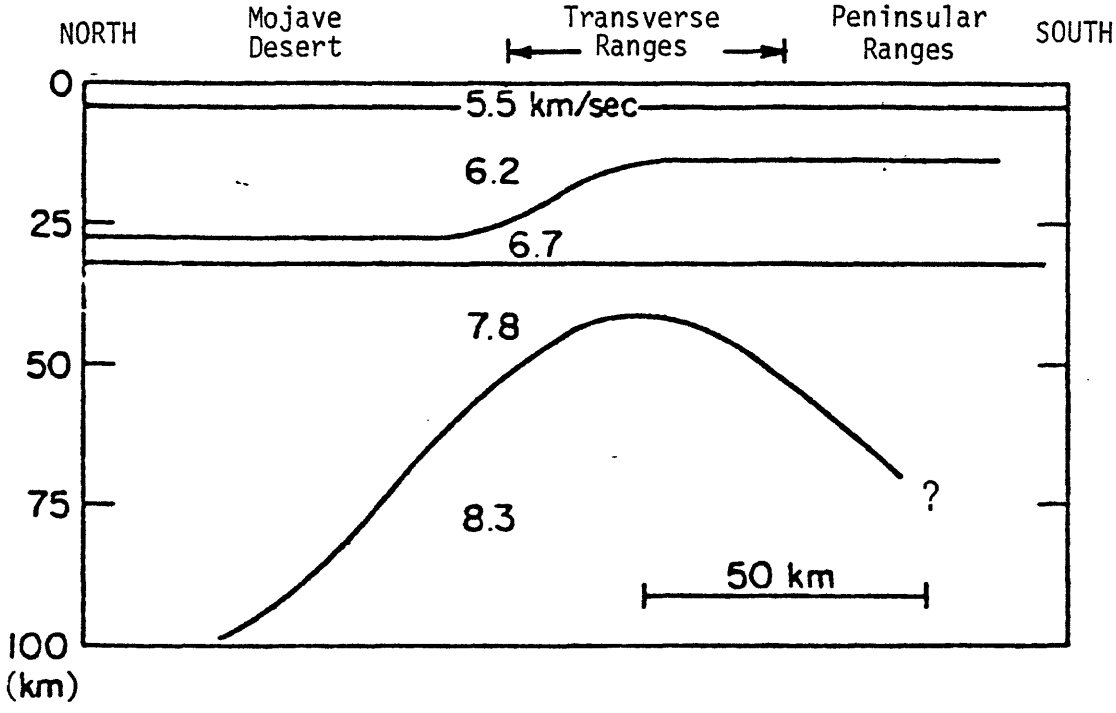

Figure 4-2. North-south cross section of compressional-wave velocities through the Transverse Ranges in the vicinity of Cajon Pass. Seismic sections for the crust from the Mojave Desert, Transverse Ranges and Peninsular Ranges have been smoothly connected. The thickness of the high-velocity ridge in the upper mantle is constrained by the vertical travel-time of a well-recorded PKP phase. The figure is courtesy of Hadley and Kanamori (1979).

$Q_\alpha = 0.75(\alpha/\beta)^2 Q_\beta$ which insures that no dissipation occurs in pure compression (DELTA, 1978 → present). The resulting viscoelastic parameters for each layer in the composite Los Angeles basin earth structure are tabulated in Table 4-1.

The Green's functions used to compute ground motions in the Los Angeles basin are calculated for this earth structure. The Green's functions represent the complete characterization of wave propagation from every point of rupture, through this earth structure, to every receiver point of interest. In order to accomodate every study considered in this report, the Green's functions are therefore calculated for 41 epicentral distances between 1 and 200 km (increments of 5 km) and 8 hypocentral depths (1.219, 1.829, 3.2, 5.0, 7.0, 9.0, 11.0 and 13.0 km). As discussed in Section 3.1, all ten independent stress tensor components are needed for the vertical and horizontal components of motion, so that a total of 3280 (41 x 8 x 10) complex Green's function components are calculated and stored for every frequency point of interest. The Green's functions are sampled at 1001 frequencies between 0 and 5 Hz, providing 200 seconds (1/0.005 Hz) of signal at every receiver of interest. When interpreting the high-frequency constitutents in the following computed ground motions (such as peak ground acceleration), one should always be aware that real earthquakes could easily produce ground motions with frequency content in excess of the Nyquist frequency used in the numerical calculations. Unfortunately, the Nyquist frequency was constrained to 5 Hz by the funds available under the existing contract. It would be interesting, in a future work, to continue the calculations out to a frequency of 20 Hz to give a more conservative appraisal of the highest frequency ground shaking hazards for the Los Angeles basin (cost would be about four times greater than the present effort).

Table 4-1. Viscoelastic parameters for the geologic structure underlying the Los Angeles Basin.

Layer	β S-Wave Velocity (km/sec)	α P-Wave Velocity (km/sec)	ρ Density (gm/cm^3)	Q_β Shear Quality Factor	Q_α Compressional Quality Factor	h Layer Thickness (km)	Depth to Bottom of Layer (km)
1	0.950	2.1	2.12	28.0	102.00	0.91400	0.91400
2	1.45	2.9	2.28	48.0	144.00	0.61000	1.5240
3	1.84	3.5	2.40	64.0	173.00	0.61000	2.1340
4	2.27	4.2	2.54	84.0	215.00	2.1330	4.2670
5	2.97	5.2	2.74	117.	269.00	10.733	15.000
6	3.64	6.3	2.96	150.	339.00	13.400	28.400
7	3.93	6.8	3.06	300.	675.00	5.0000	33.400
8	4.50	7.8	3.26	300.	675.00	17.600	51.000
9	4.68	8.1	3.32	300.	675.00	19.000	70.000
10	4.79	8.3	3.36	500.	1000.0	∞	∞

4.2 MAJOR EARTHQUAKES ALONG THE SAN ANDREAS FAULT

As discussed in Section 1.1, the Los Angeles basin is vulnerable to potentially catastrophic ground shaking from a major earthquake along the San Andreas Fault. Also discussed is the region of the San Andreas Fault along which such a devastating earthquake rupture is thought most likely to initiate. This region is located between the locked portion of the fault near the 1948 event and the Southern California Uplift near Palmdale (refer to Figure 1-1).

Ground motions from major earthquakes along this portion of the San Andreas Fault are calculated using the model discussed in Chapter 3 including the refined micro-incoherence. The results are presented in the form of maps describing the acceleration, velocity, and displacement values at 22 receivers located throughout the Los Angeles basin. The first pair of two pairs of critical rupture configurations represents two different incoherent rupture simulations (magnitude approximately 7.5) between the bend near Cajon Pass and the uplift region near Palmdale. The distributed source parameters for this rupture configuration are listed in Table 4-2. The earth structure is delineated in Table 4-1 of the previous section and the evaluation of the required mesh of Green's functions for this earth structure is also discussed in the previous section. The computed ground motion maps are presented in Figures 4-3 through 4-14 with a sketch of the rupture configuration (represented by arrows) and the Pacific Ocean coastline shown as points of reference.

The peak acceleration maps are shown in Figures 4-3 through 4-6. The first pair of maps in Figures 4-3 and 4-4 represents the peak horizontal accelerations for the two random rupture simulations, respectively. The peak value for the horizontal components in this chapter corresponds to the average of the peak values from the two horizontal components in the east and north directions. The second pair of maps in Figures 4-5 and 4-6 represents the peak vertical accelerations for the two random rupture simulations, respectively. When interpreting the results in terms of earthquake hazards for the Los Angeles

Table 4-2. Distributed source parameters for rupture simulations along the San Andreas Fault in Figures 4-3 through 4-14.

Epicenter Location*	Bend Near Cajon Pass
Fault Length, Strike Direction**	100 km, -150°
Fault Dip	90°
Depth to Fault Top	.914 km
Fault Width	10.4 km
Fault Slip-Offset	500 cm
Fault Slip-Rake	0°***
Fault Slip-Rise Time	3 sec
Gross Rupture Velocity	.9 β
Depth of Hypocenter	11.3 km

*Refer to ground motion map in Figure 4-3 for actual location.

**Measured clockwise from east direction.

***Predominantly right-lateral strike-slip motion.

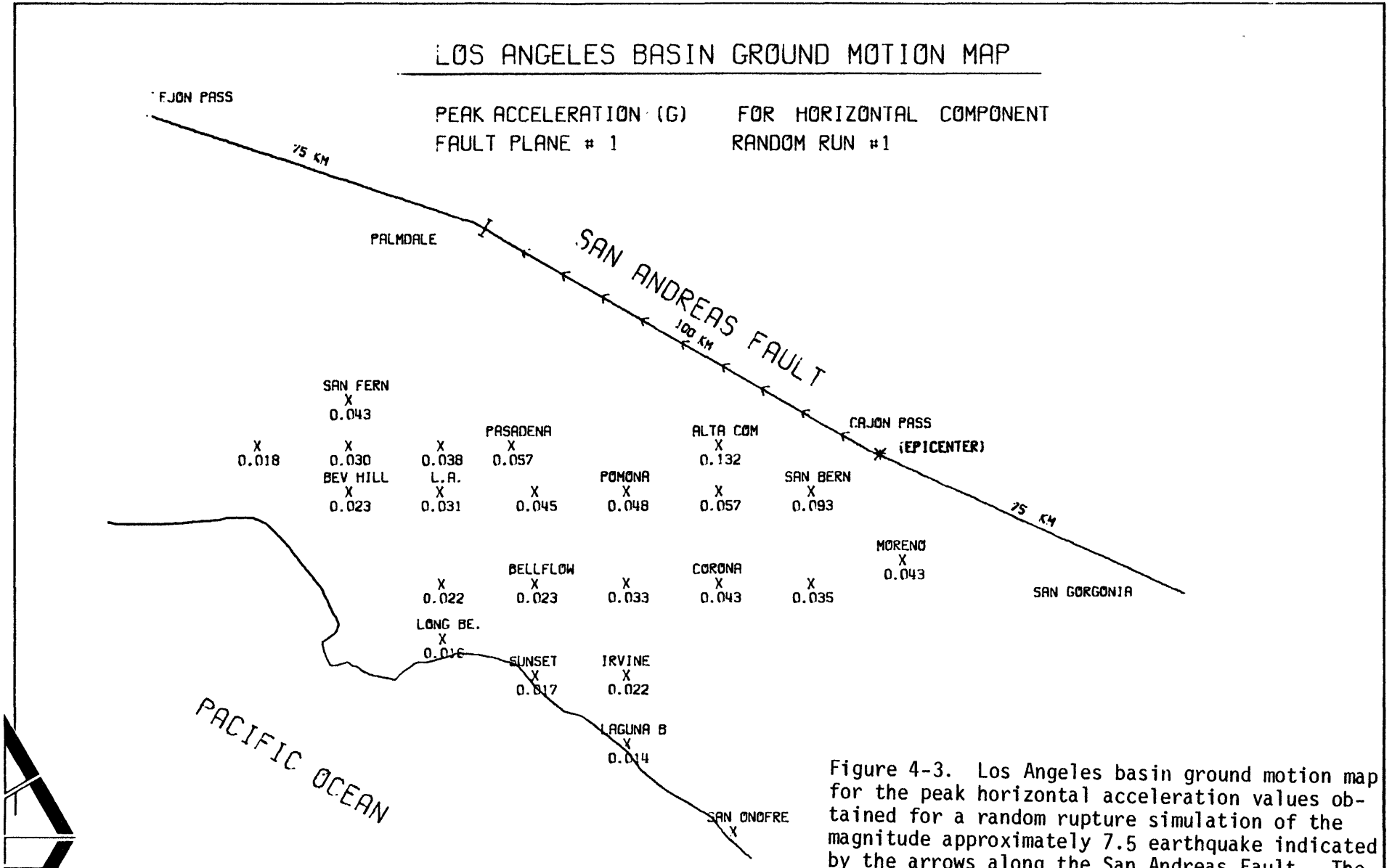

Figure 4-3. Los Angeles basin ground motion map for the peak horizontal acceleration values obtained for a random rupture simulation of the magnitude approximately 7.5 earthquake indicated by the arrows along the San Andreas Fault. The distributed source parameters are listed in Table 4-2 and the earth structure is delineated in Table 4-1.

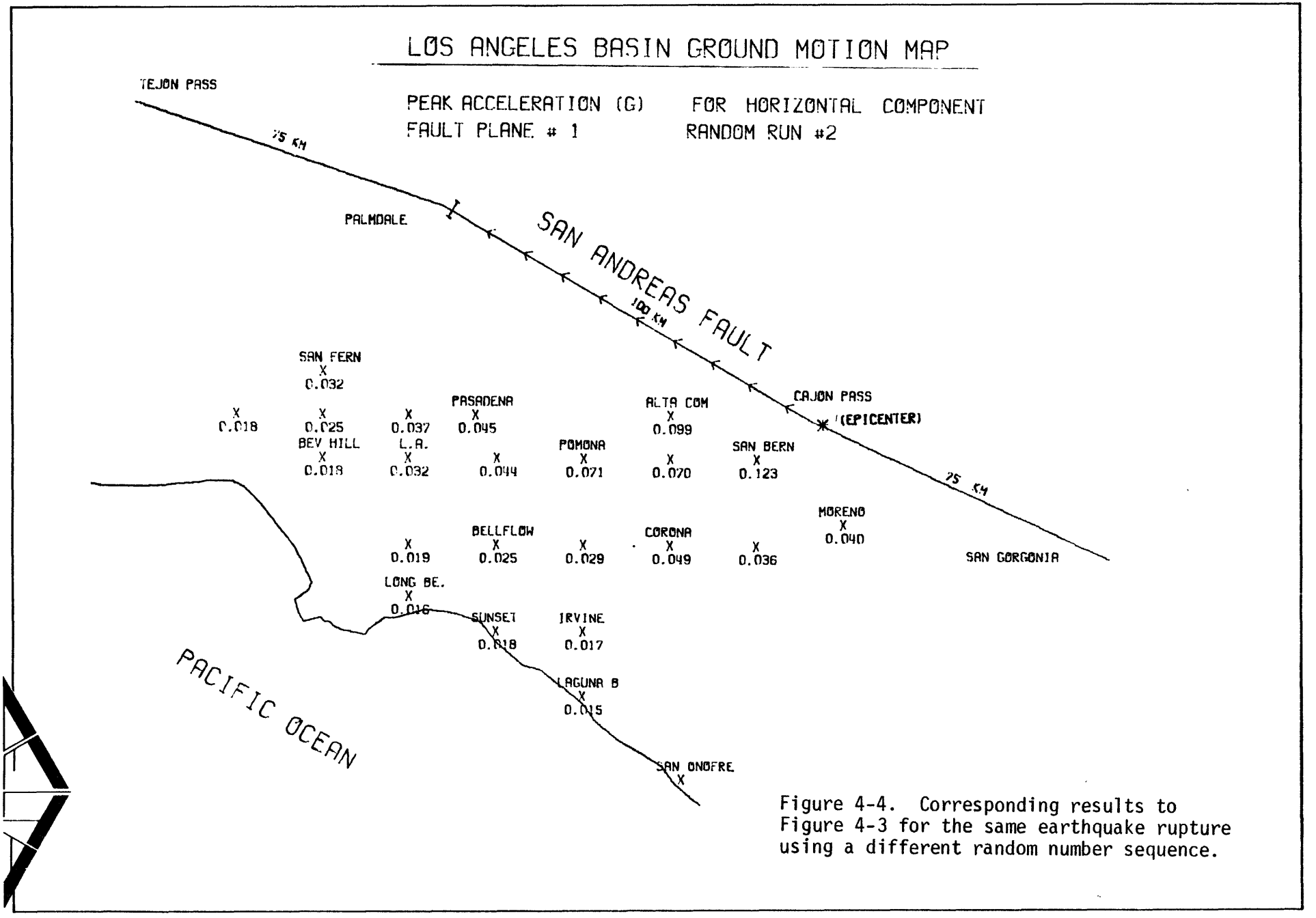

Figure 4-4. Corresponding results to Figure 4-3 for the same earthquake rupture using a different random number sequence.

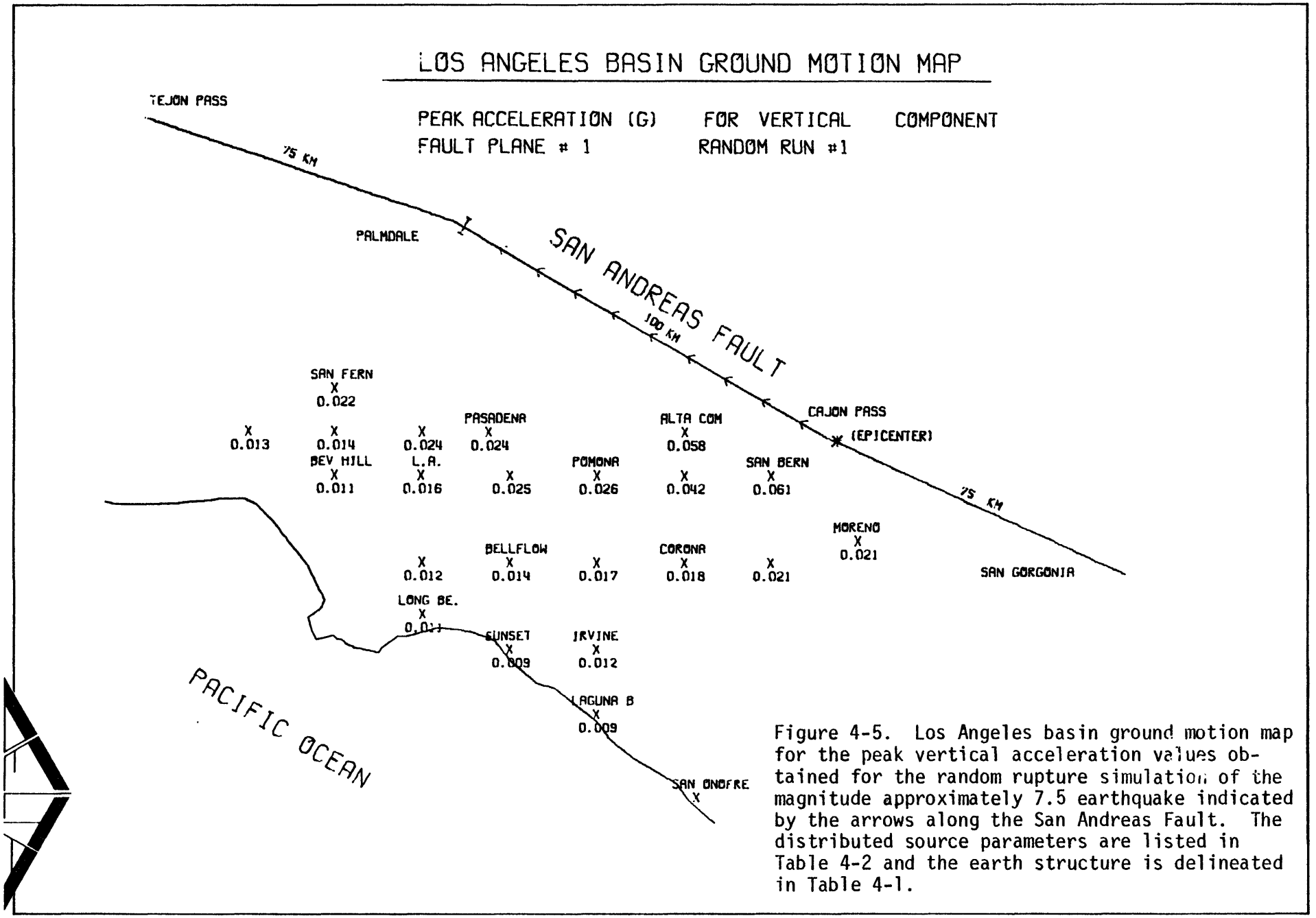

Figure 4-5. Los Angeles basin ground motion map for the peak vertical acceleration values obtained for the random rupture simulation of the magnitude approximately 7.5 earthquake indicated by the arrows along the San Andreas Fault. The distributed source parameters are listed in Table 4-2 and the earth structure is delineated in Table 4-1.

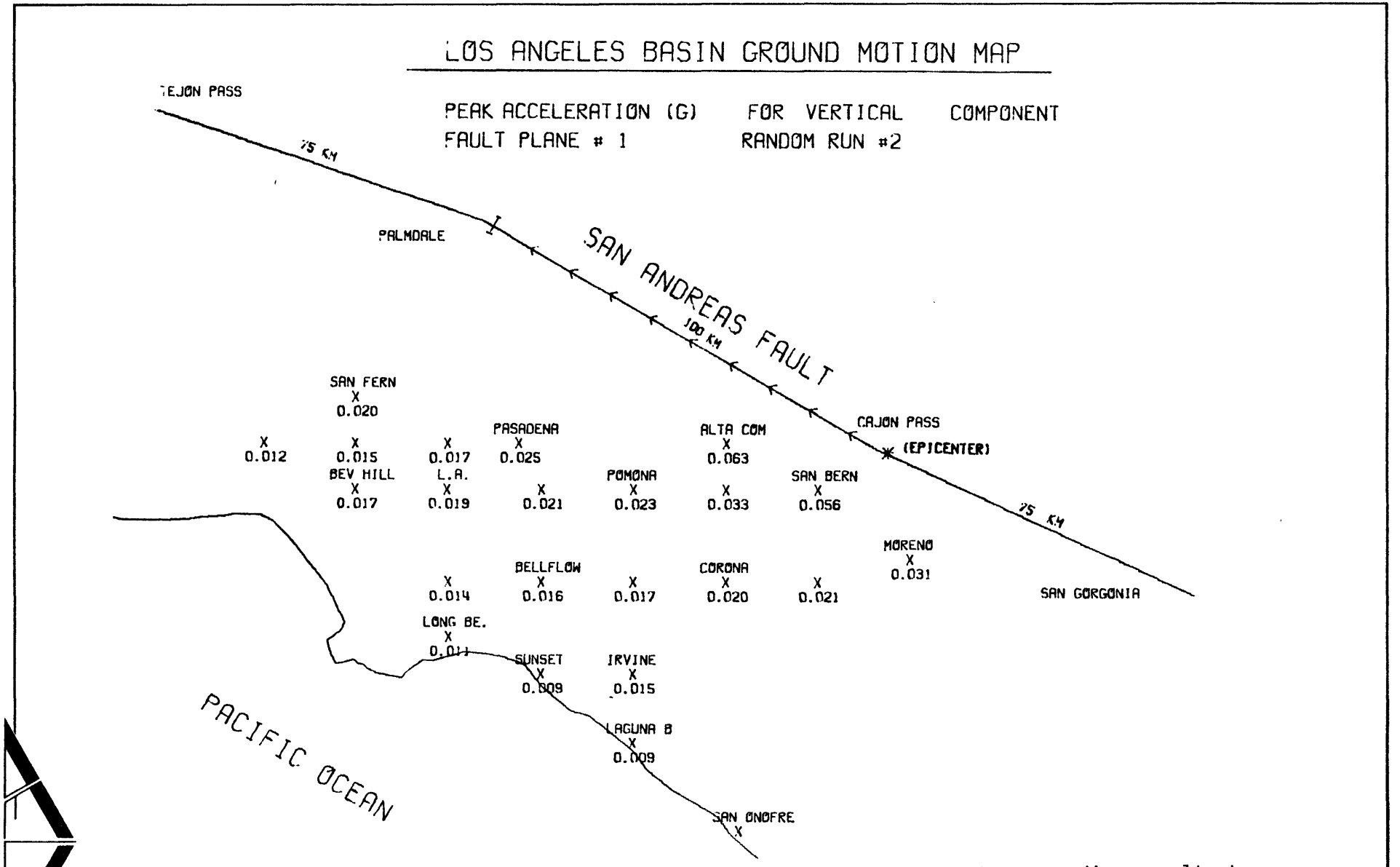

Figure 4-6. Corresponding results to Figure 4-5 for the same earthquake rupture using a different random number sequence.

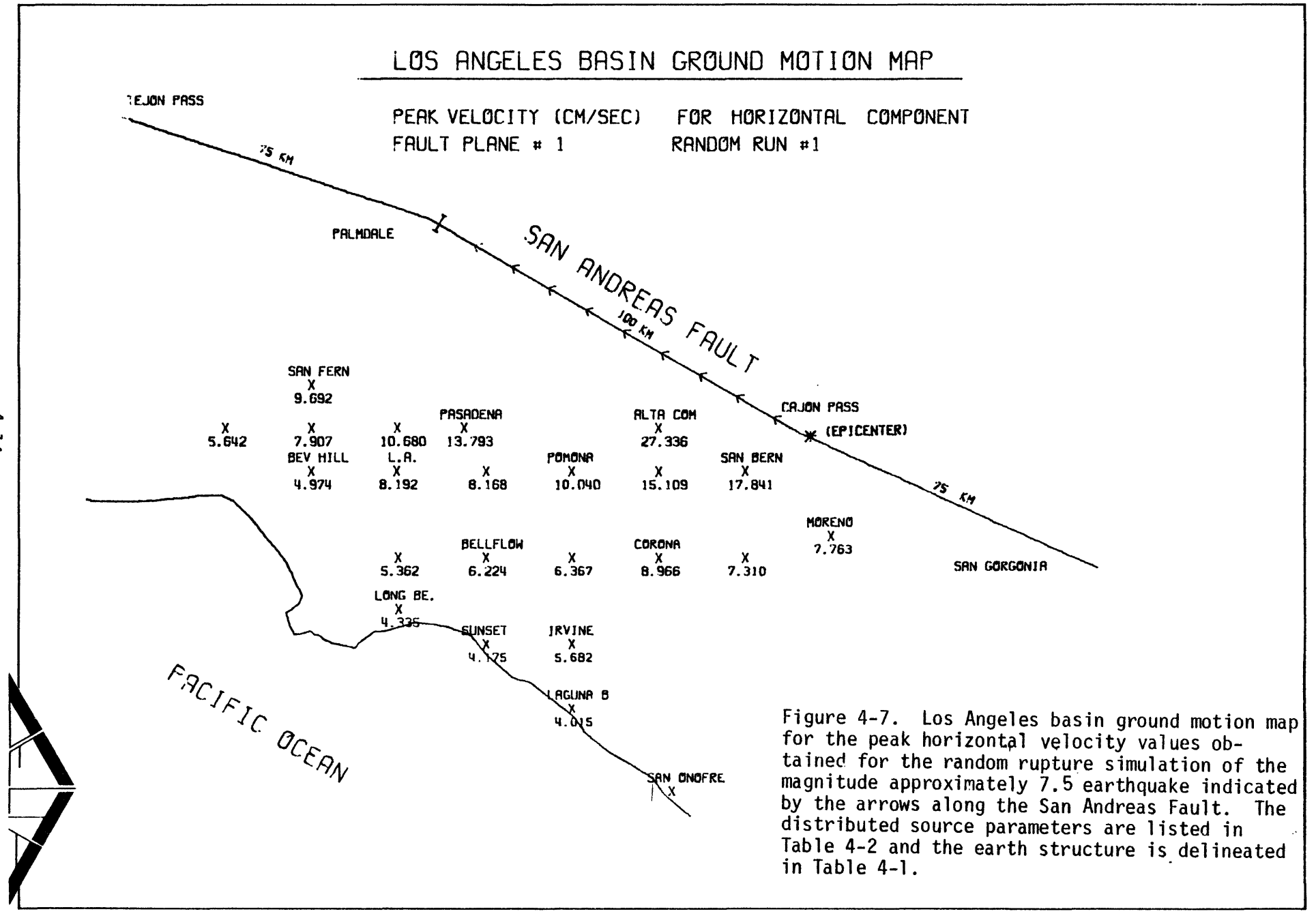

Figure 4-7. Los Angeles basin ground motion map for the peak horizontal velocity values obtained for the random rupture simulation of the magnitude approximately 7.5 earthquake indicated by the arrows along the San Andreas Fault. The distributed source parameters are listed in Table 4-2 and the earth structure is delineated in Table 4-1.

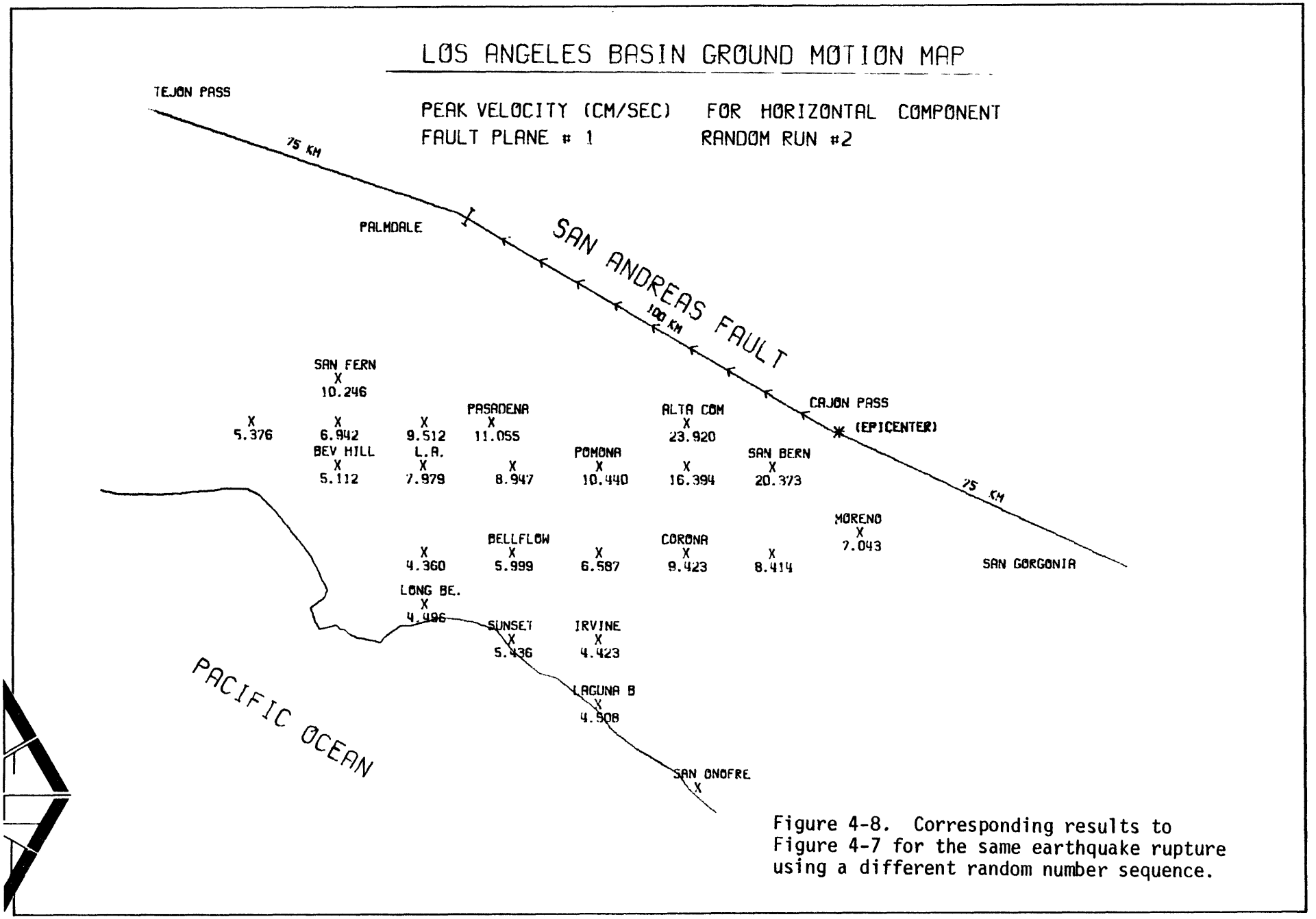

Figure 4-8. Corresponding results to Figure 4-7 for the same earthquake rupture using a different random number sequence.

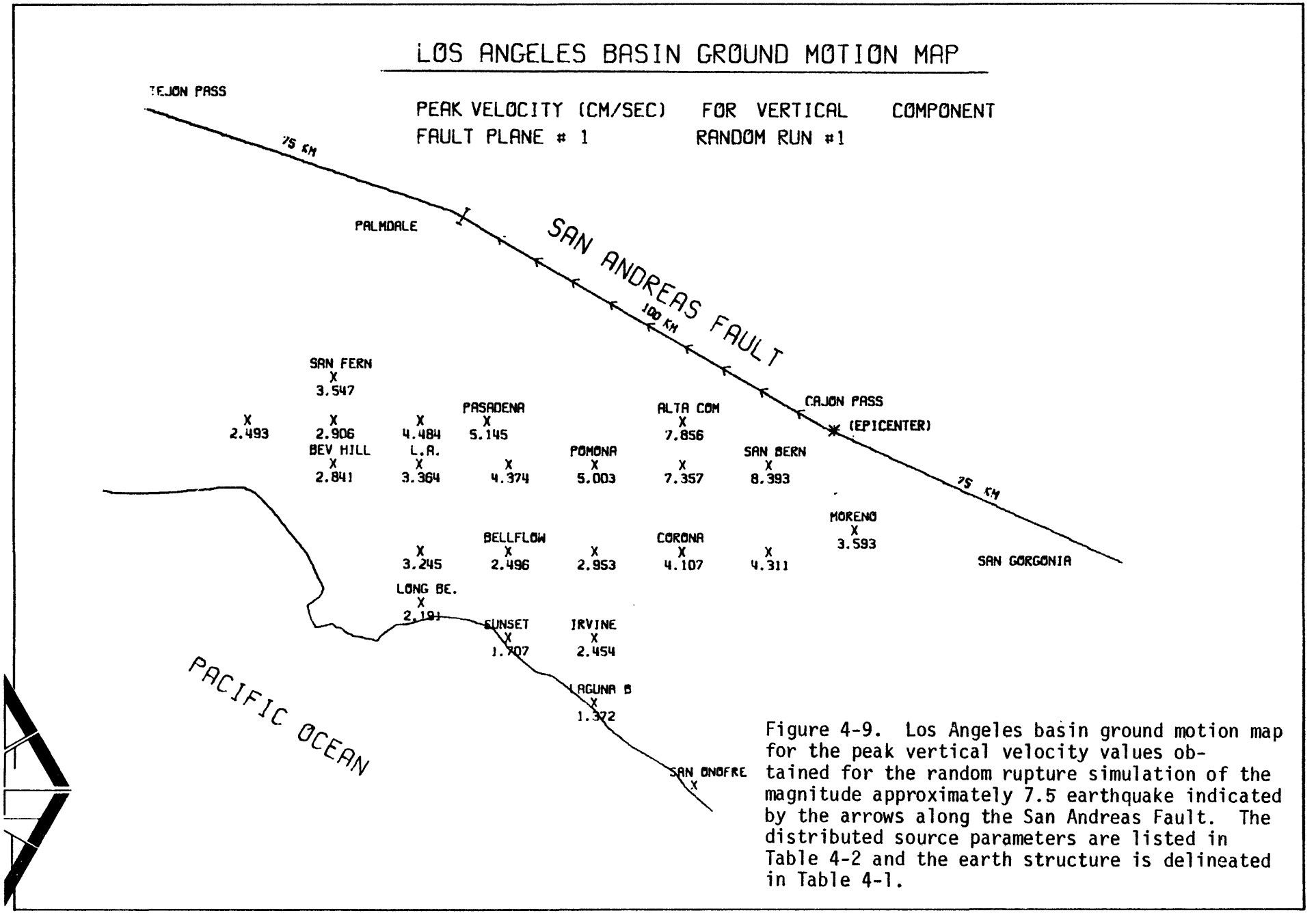

Figure 4-9. Los Angeles basin ground motion map for the peak vertical velocity values obtained for the random rupture simulation of the magnitude approximately 7.5 earthquake indicated by the arrows along the San Andreas Fault. The distributed source parameters are listed in Table 4-2 and the earth structure is delineated in Table 4-1.

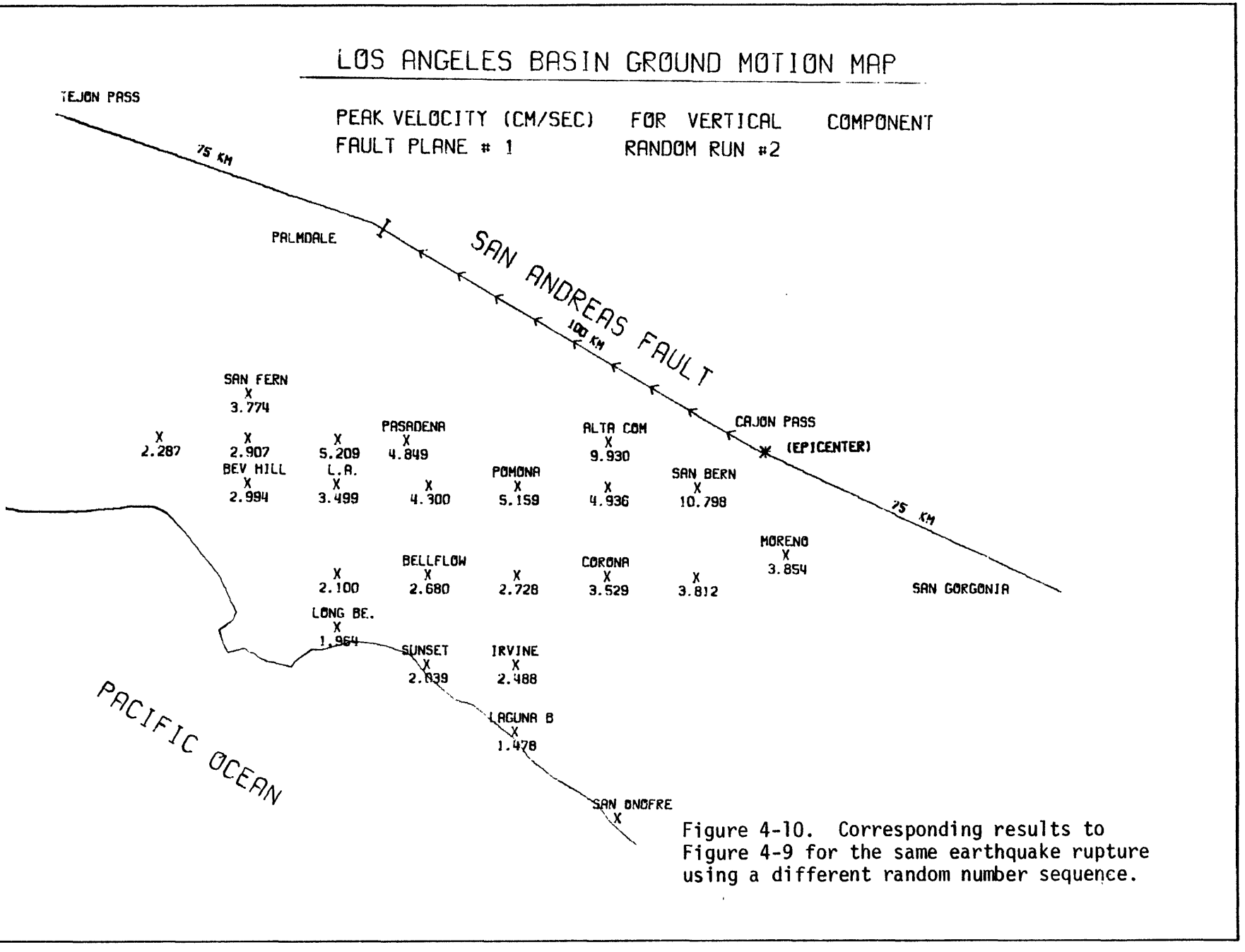

Figure 4-10. Corresponding results to Figure 4-9 for the same earthquake rupture using a different random number sequence.

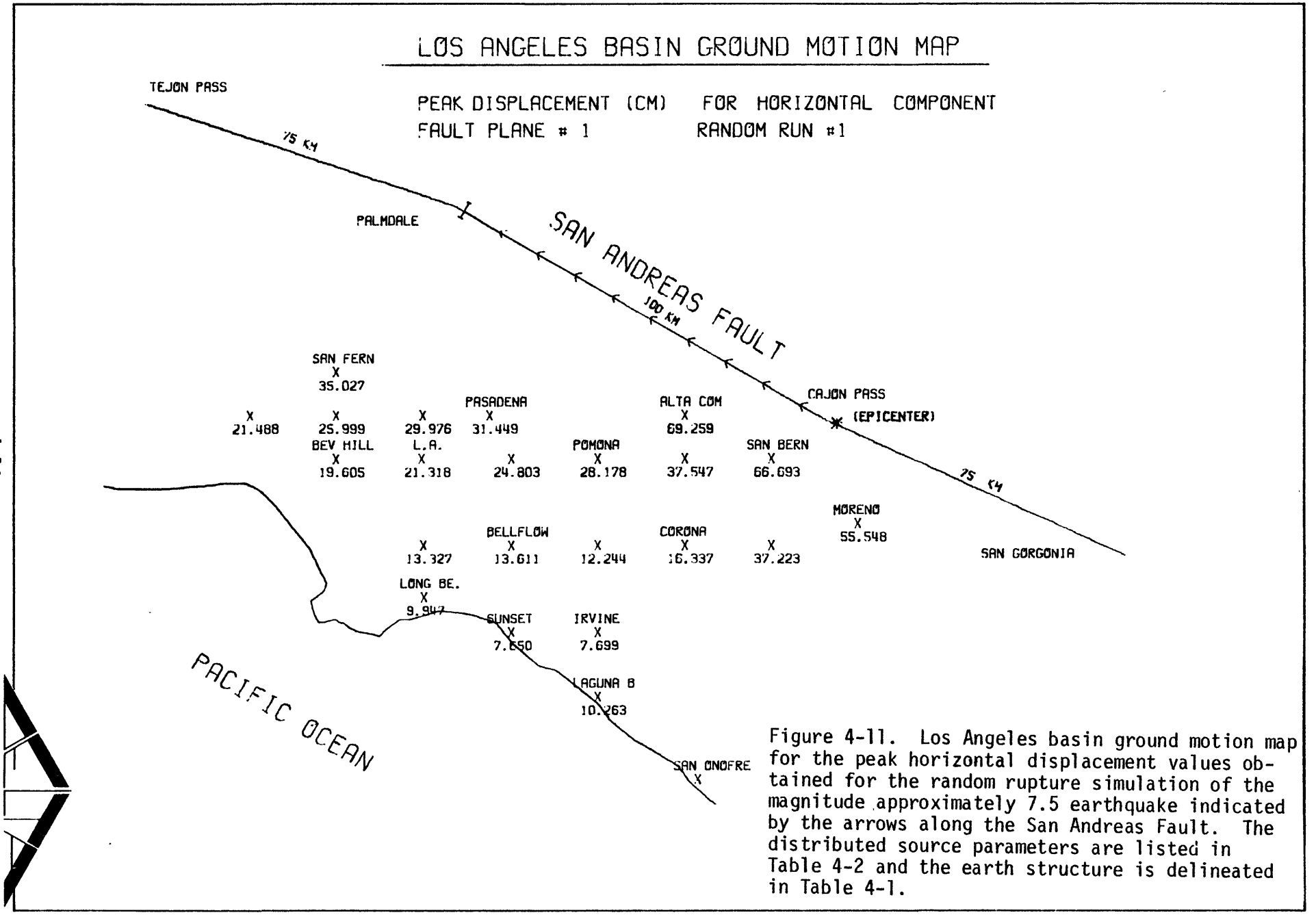

Figure 4-11. Los Angeles basin ground motion map for the peak horizontal displacement values obtained for the random rupture simulation of the magnitude approximately 7.5 earthquake indicated by the arrows along the San Andreas Fault. The distributed source parameters are listed in Table 4-2 and the earth structure is delineated in Table 4-1.

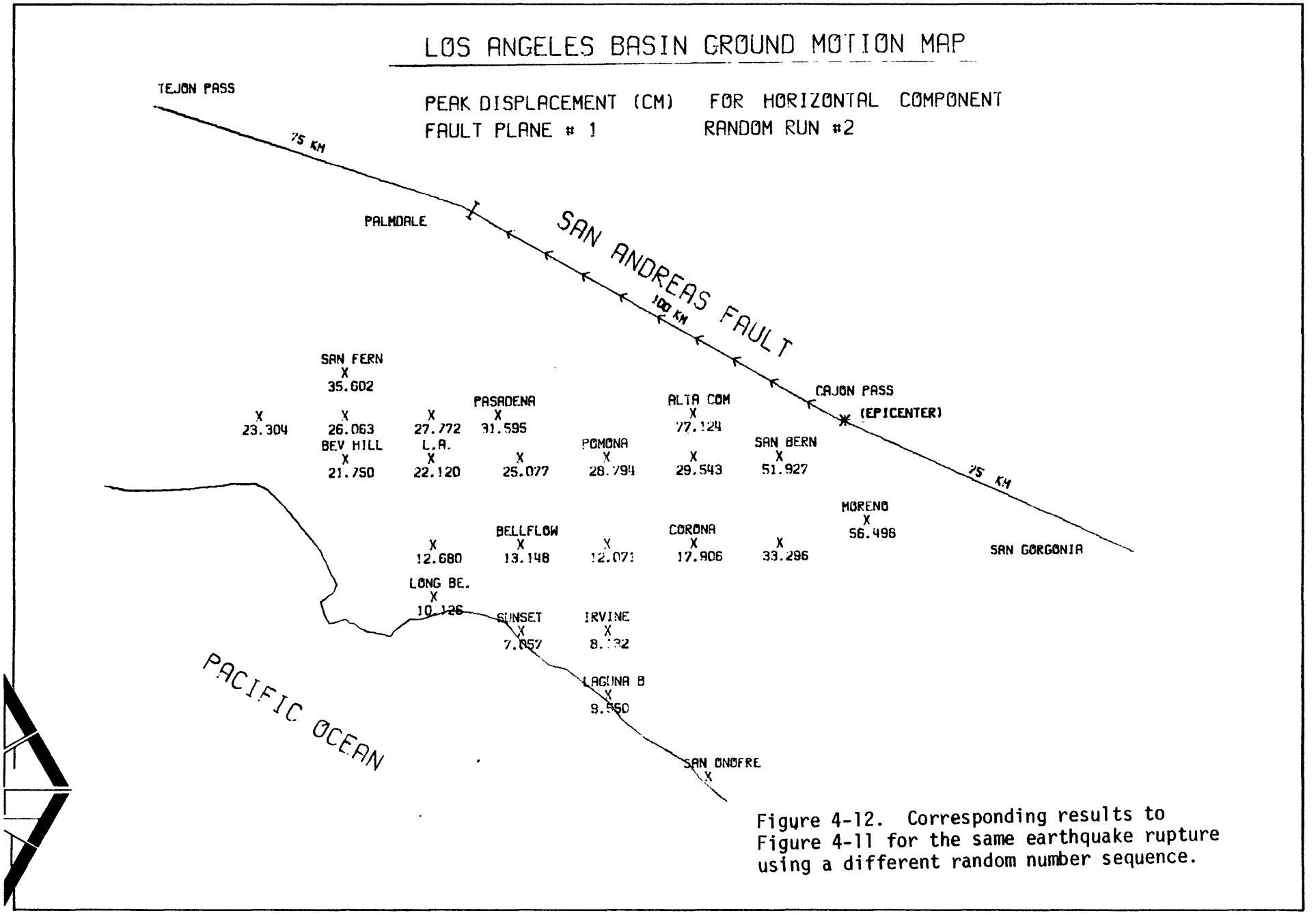

Figure 4-12. Corresponding results to Figure 4-11 for the same earthquake rupture using a different random number sequence.

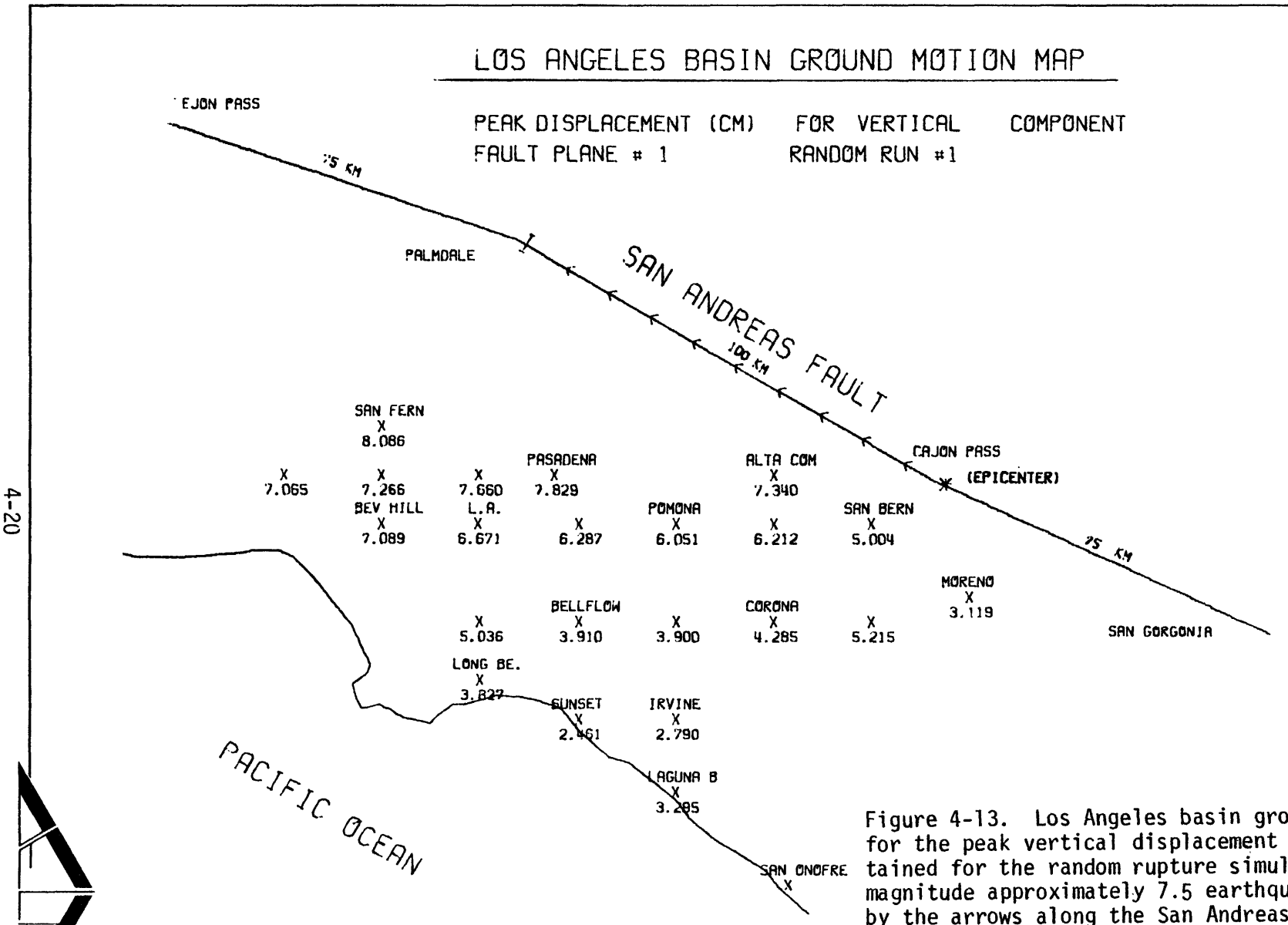

Figure 4-13. Los Angeles basin ground motion map for the peak vertical displacement values obtained for the random rupture simulation of the magnitude approximately 7.5 earthquake indicated by the arrows along the San Andreas Fault. The distributed source parameters are listed in Table 4-2 and the earth structure is delineated in Table 4-1.

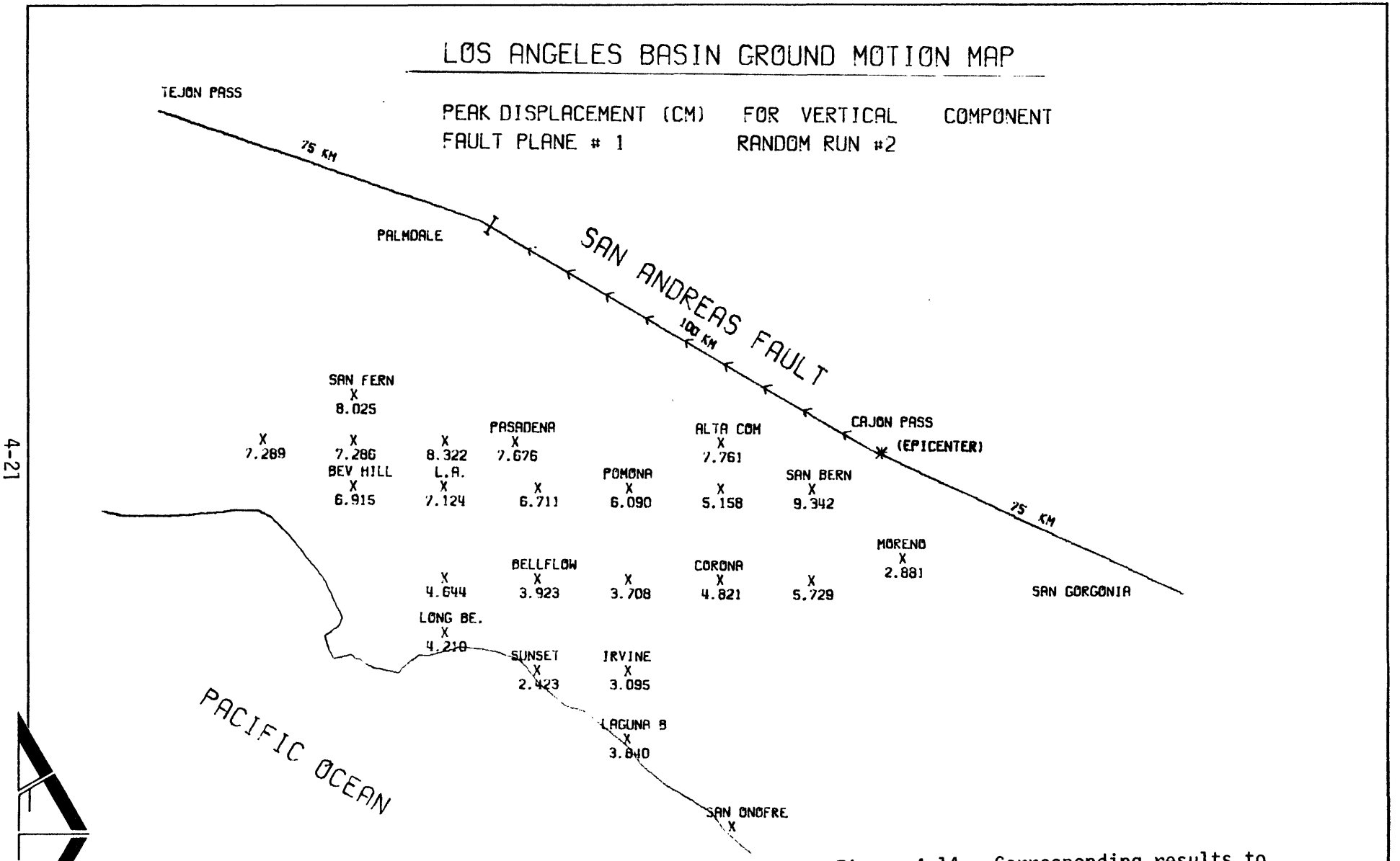

Figure 4-14. Corresponding results to Figure 4-13 for the same earthquake rupture using a different random number sequence.

basin , it is imperative to recall that the acceleration values are limited by the Nyquist frequency of 5 Hz chosen for the computation of the Green's functions. Furthermore, the peak acceleration values are strongly influenced by the material quality factors Q that characterize wave attenuation between source and receiver. Yet, the amplitude and to a lesser degree the frequency dependence of these quality factors is not well constrained (i.e., uncertainties in Q could translate into uncertainties in peak acceleration by factors in excess of two at these distances and frequencies of interest. Ignoring these cautions, the low peak acceleration values relative to those obtained in previous modeling studies (refer to Section 3.2) seem to indicate that most of the receivers in the Los Angeles basin are sufficiently far from this critical rupture along the San Andreas Fault to preclude catastrophic ground accelerations. For example, the peak acceleration values for metropolitan Los Angeles (about 56 km from the fault) are at least three times smaller than the corresponding values for cities closer to the fault; the peak acceleration values for the coastal communities (about 80 km from the fault) are an additional factor of two to three times smaller.

The peak velocity maps for this rupture configuration are shown in Figures 4-7 through 4-10 and are arranged in the same order as the peak acceleration maps in Figure 4-3 through 4-6, respectively. The attenuation of the peak velocities as a function of distance and orientation from the fault is similar to that observed for the peak accelerations. The frequency cut-off at 5 Hz is probably too high to significantly affect the velocity peaks, indicating that the material quality factors Q are primarily responsible for any decay rate higher than that for a non-dissipative earth model. Neither the Nyquist frequency nor the material quality factors affect the peak displacement maps which are shown in Figures 4-11 through 4-14. The peak displacements are controlled by the rise time of the slip function and by the seismic moment M_o for this rupture configuration given by the summation over the n discretized cells comprising the fault plane:

$$M_o = \sum_n \mu_n A_n \delta_{\infty_n}$$

in which μ_n is the shear modulus of the layer containing the n^{th} cell, A_n is the area of the n^{th} cell and $\delta_{\infty n}$ is the final offset of the slip function in the n^{th} cell. Using this formula in conjunction with Tables 4-2 and 4-1 give a seismic moment of 1.025×10^{27} dyne-cm for this 100 km long, 10.4 km wide rupture configuration.

The second pair of two pairs of critical rupture configurations represents two different incoherent rupture simulations (magnitude approximately 7.5) initiating along the locked portion of the San Andreas Fault near the 1948 event and centered around Cajon Pass. The distributed source parameters for this rupture configuration are listed in Table 4-3 and are identical to those in Table 4-2 except for the epicentral location. The computed ground motions are presented in Figure 4-15 through 4-26 in the identical format (except for sketch of rupture configuration) and arrangement as the first set of ground motion maps in Figures 4-3 through 4-14, respectively. The results are similar to those described for the previous rupture which initiated closer to the western Los Angeles basin. The differences in peak acceleration values are completely explainable in terms of the differences in distance from a given receiver to the most focussed regions of the respective earthquake ruptures. For example, the peak accelerations for the northwestern Los Angeles basin are about fifty percent lower while those in the southeastern Los Angeles basin increased by almost a factor of two; the peak accelerations for the coastal communities, being about the same distance from focussed ruptures, remained essentially the same.

Table 4-3. Distributed source paramaters for rupture simulations along the San Andreas Fault in Figures 4-15 through 4-26.

Epicenter Location*	50 km SE of Bend Near Cajon Pass
Fault Length, Strike Direction**	50 km, -156° +50 km, -150°
Fault Dip	90°
Depth to Fault Tip	.914 km
Fault Width	10.4 km
Fault Slip-Offset	500 cm
Fault Slip-Rake	0°***
Fault Slip-Rise Time	3 sec
Gross Rupture Velocity	.9 β
Depth of Hypocenter	11.3

*Refer to ground motion map in Figure 4-15 for actual location.

**Measured clockwise from east direction.

***Predominantly right-lateral strike-slip.

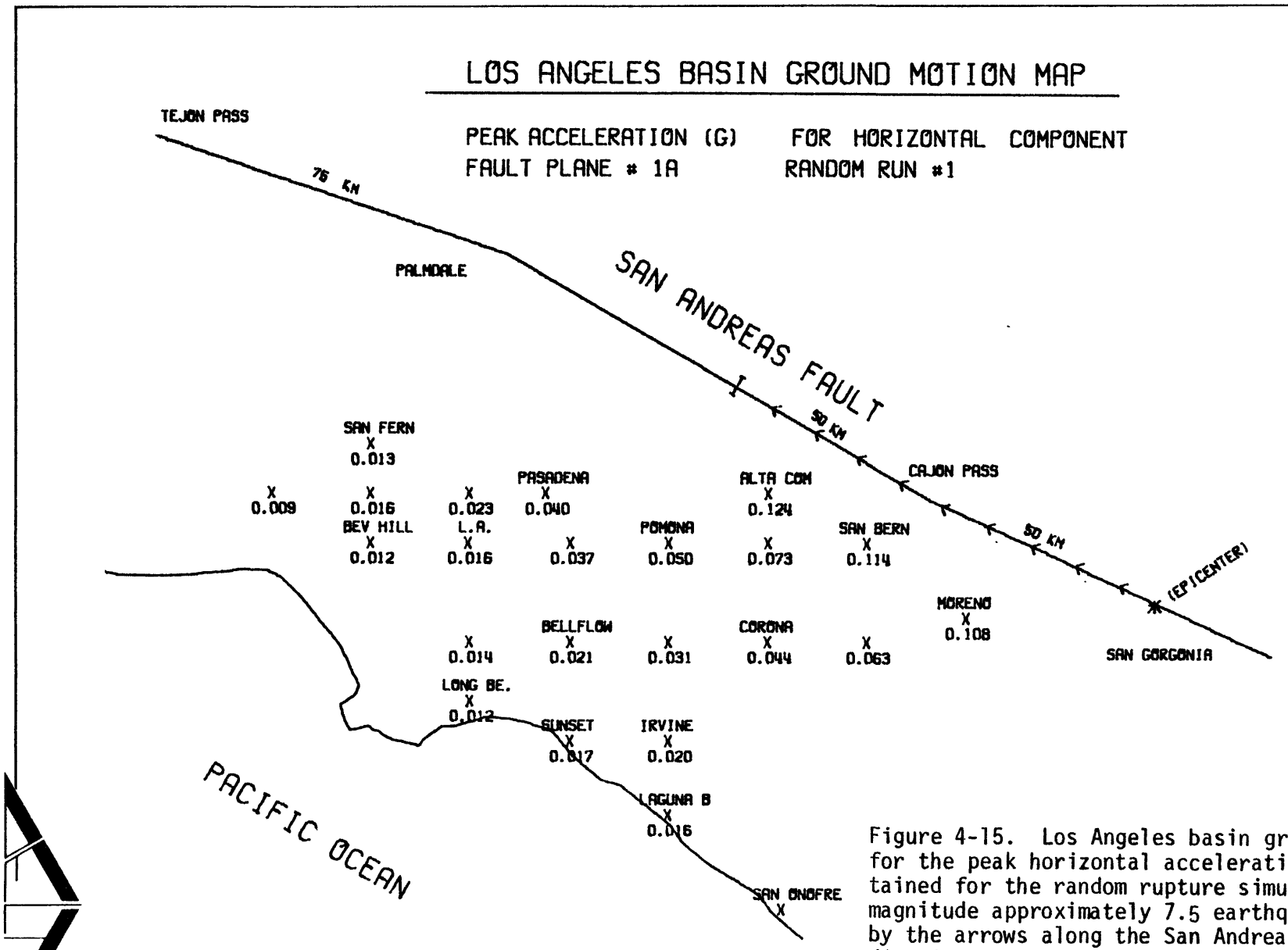

Figure 4-15. Los Angeles basin ground motion map for the peak horizontal acceleration values obtained for the random rupture simulation of the magnitude approximately 7.5 earthquake indicated by the arrows along the San Andreas Fault. The distributed source parameters are listed in Table 4-3 and the earth structure is delineated in Table 4-1.

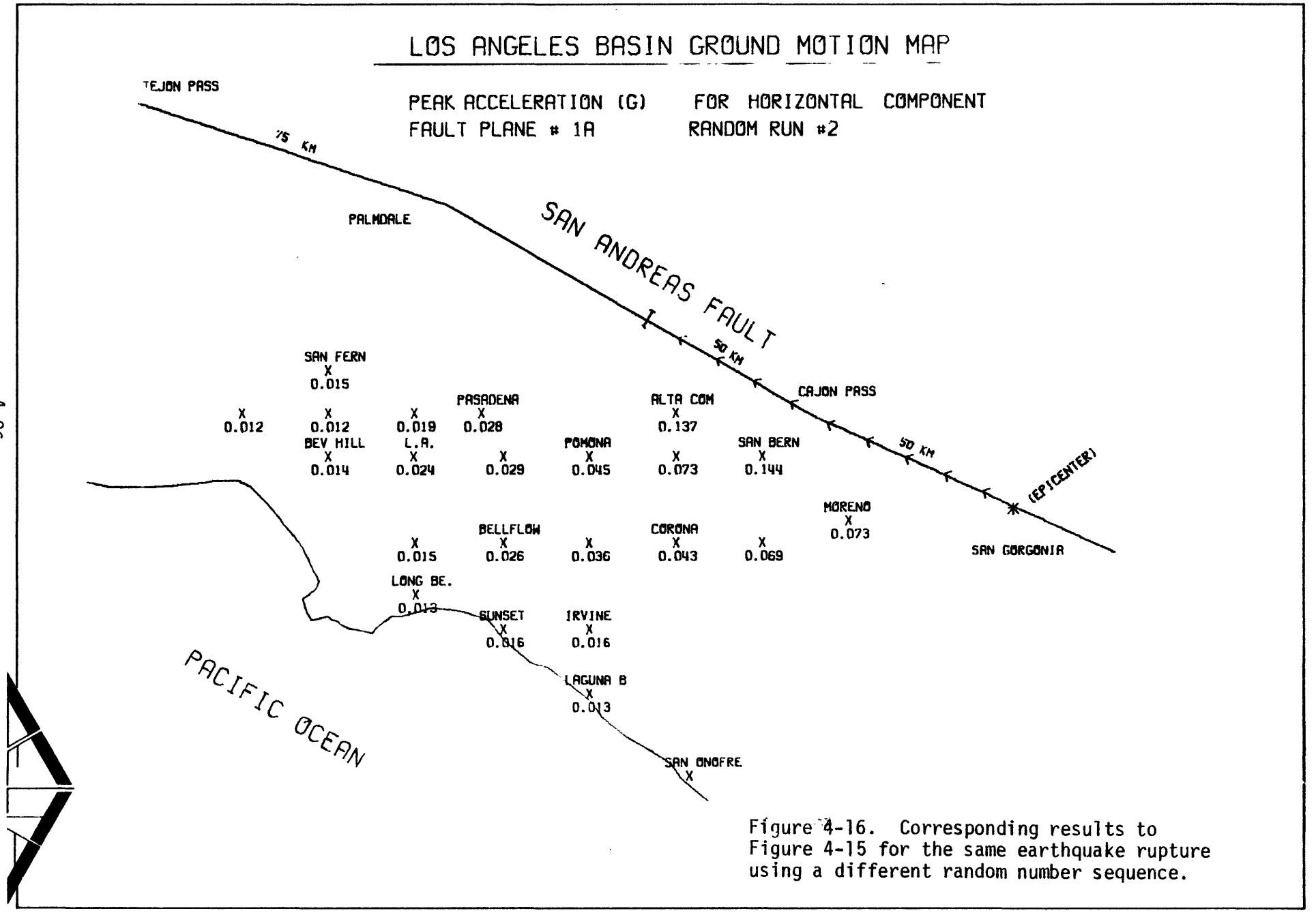

Figure 4-16. Corresponding results to Figure 4-15 for the same earthquake rupture using a different random number sequence.

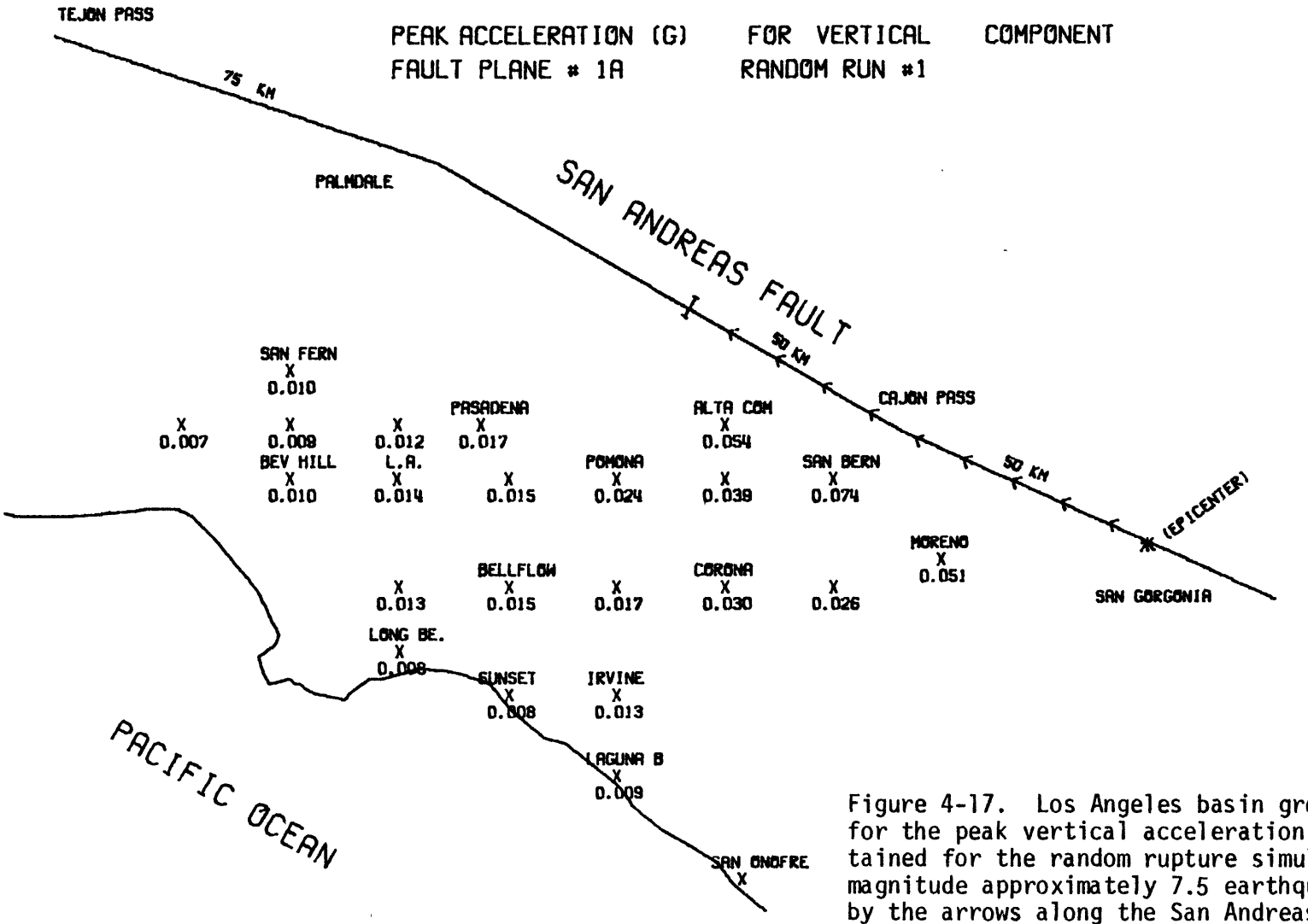

Figure 4-17. Los Angeles basin ground motion map for the peak vertical acceleration values obtained for the random rupture simulation of the magnitude approximately 7.5 earthquake indicated by the arrows along the San Andreas Fault. The distributed source parameters are listed in Table 4-3 and the earth structure is delineated in Table 4-1.

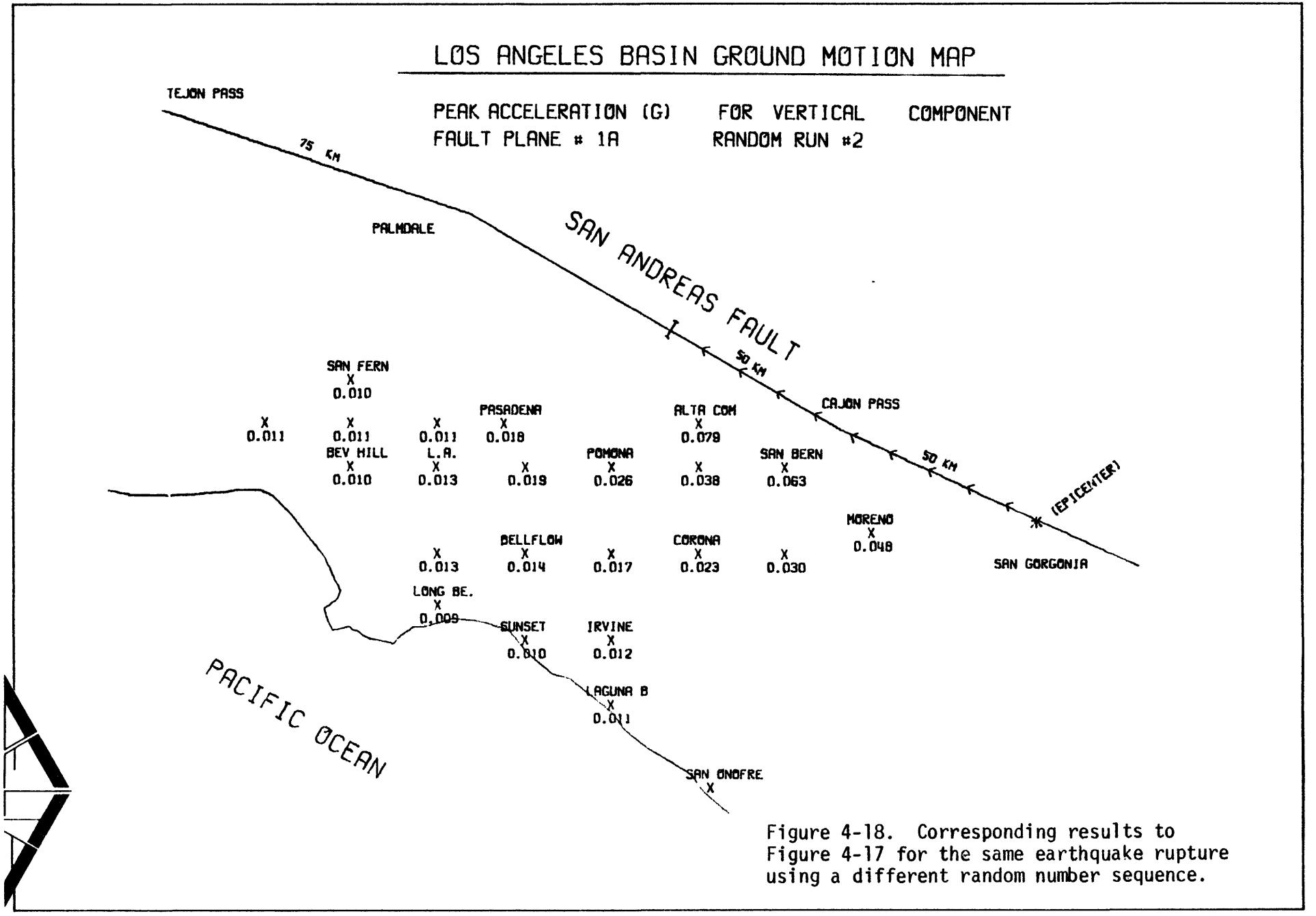

Figure 4-18. Corresponding results to Figure 4-17 for the same earthquake rupture using a different random number sequence.

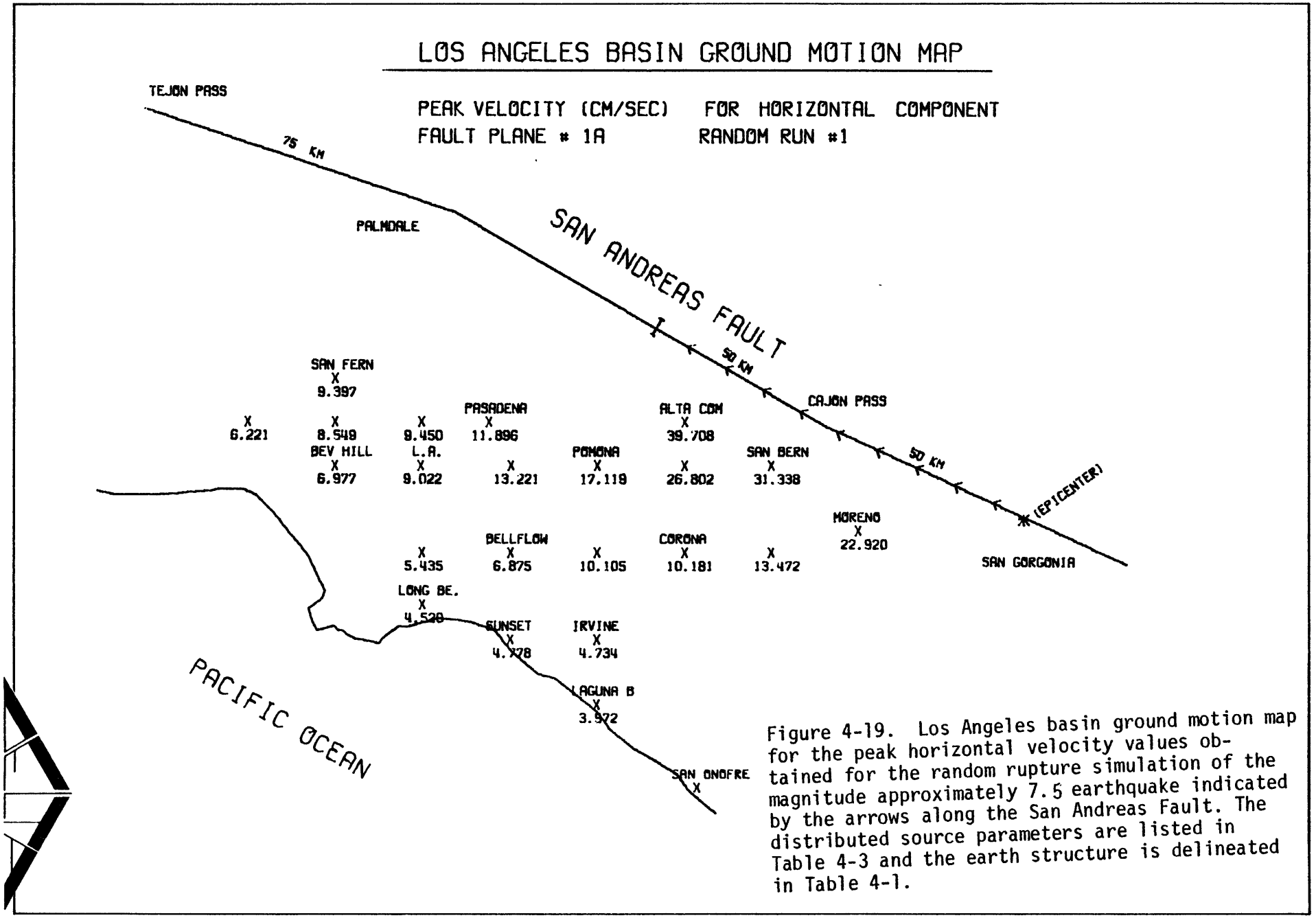

Figure 4-19. Los Angeles basin ground motion map for the peak horizontal velocity values obtained for the random rupture simulation of the magnitude approximately 7.5 earthquake indicated by the arrows along the San Andreas Fault. The distributed source parameters are listed in Table 4-3 and the earth structure is delineated in Table 4-1.

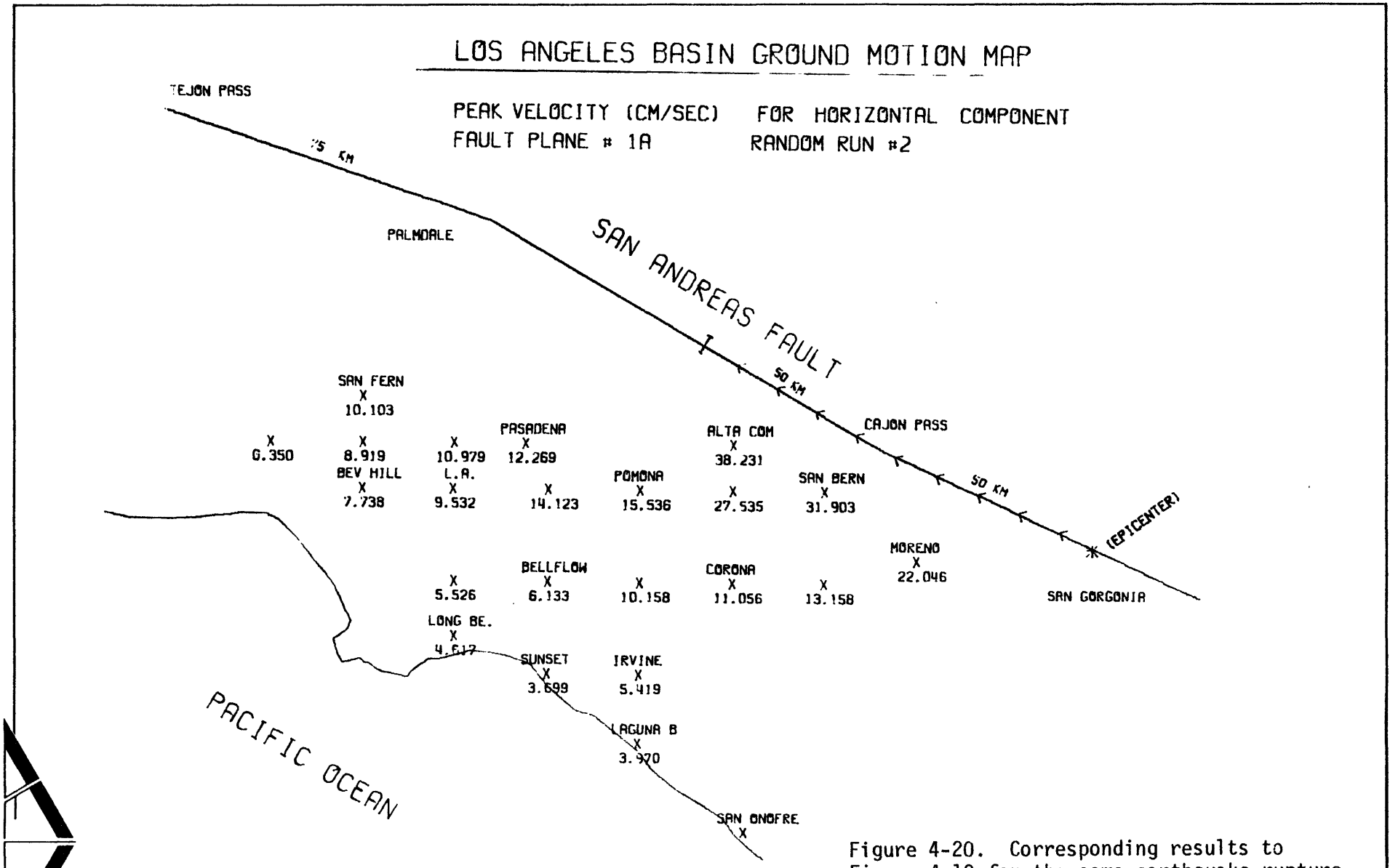

Figure 4-20. Corresponding results to Figure 4-19 for the same earthquake rupture using a different random number sequence.

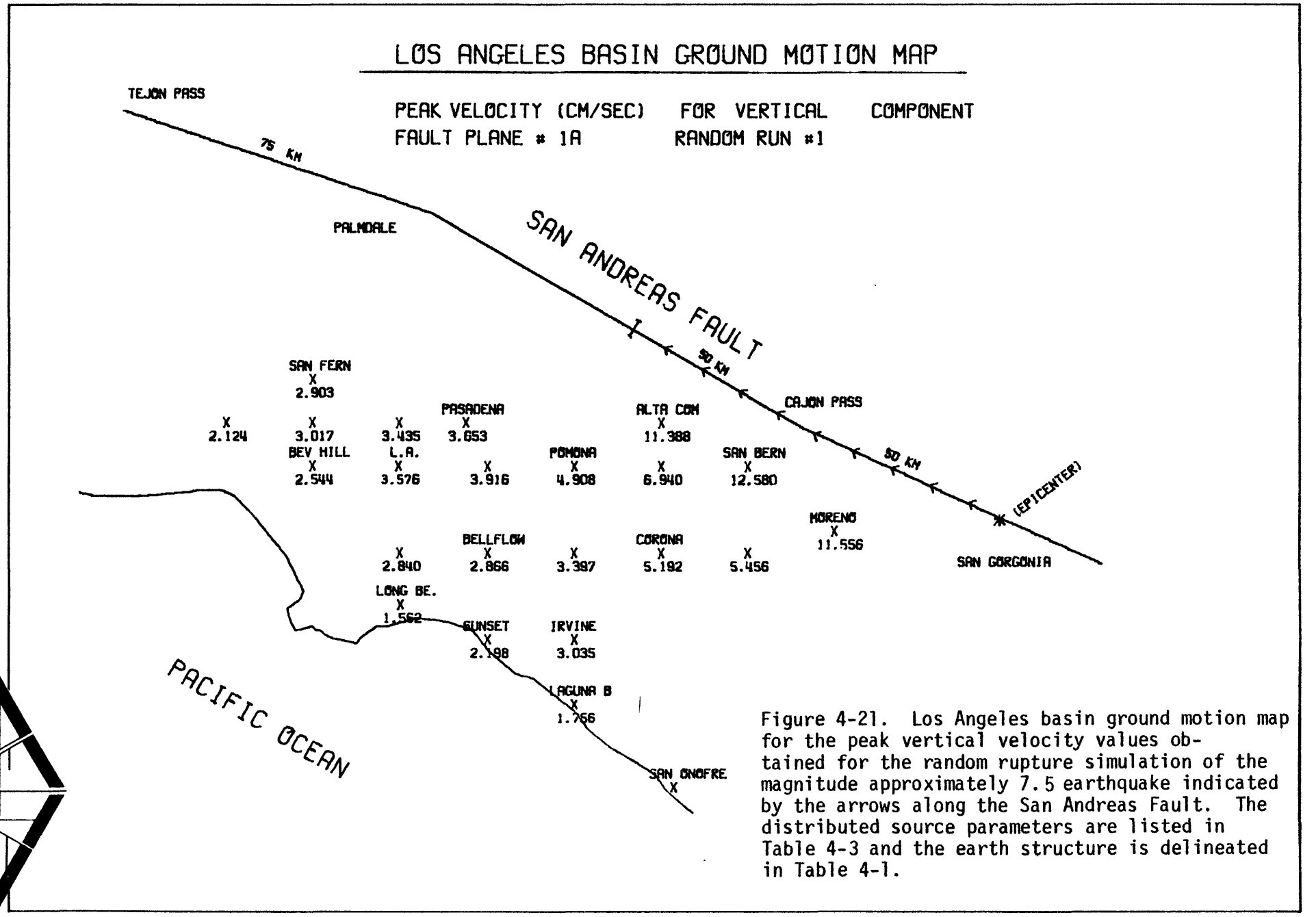

Figure 4-21. Los Angeles basin ground motion map for the peak vertical velocity values obtained for the random rupture simulation of the magnitude approximately 7.5 earthquake indicated by the arrows along the San Andreas Fault. The distributed source parameters are listed in Table 4-3 and the earth structure is delineated in Table 4-1.

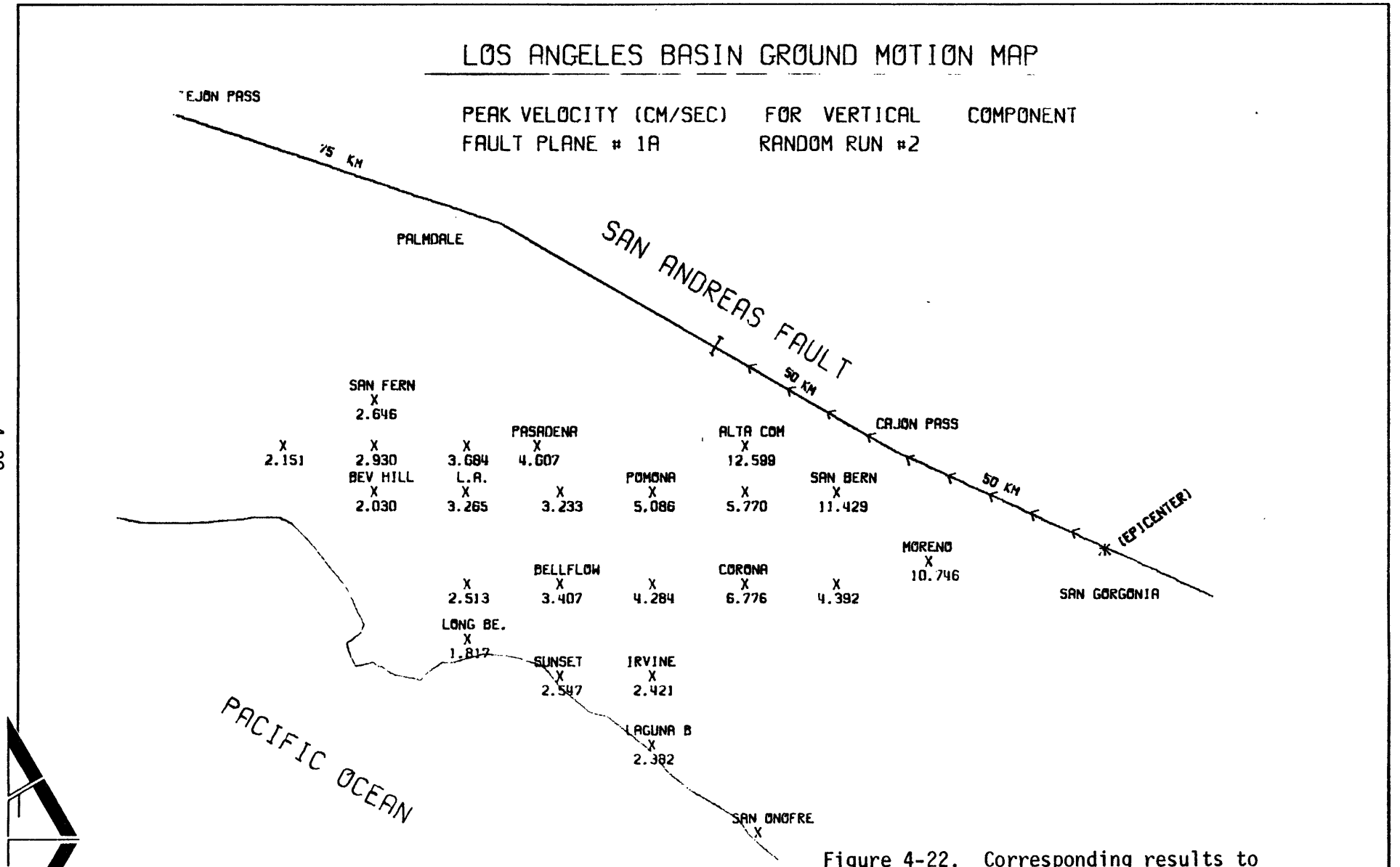

Figure 4-22. Corresponding results to Figure 4-21 for the same earthquake rupture using a different random number sequence.

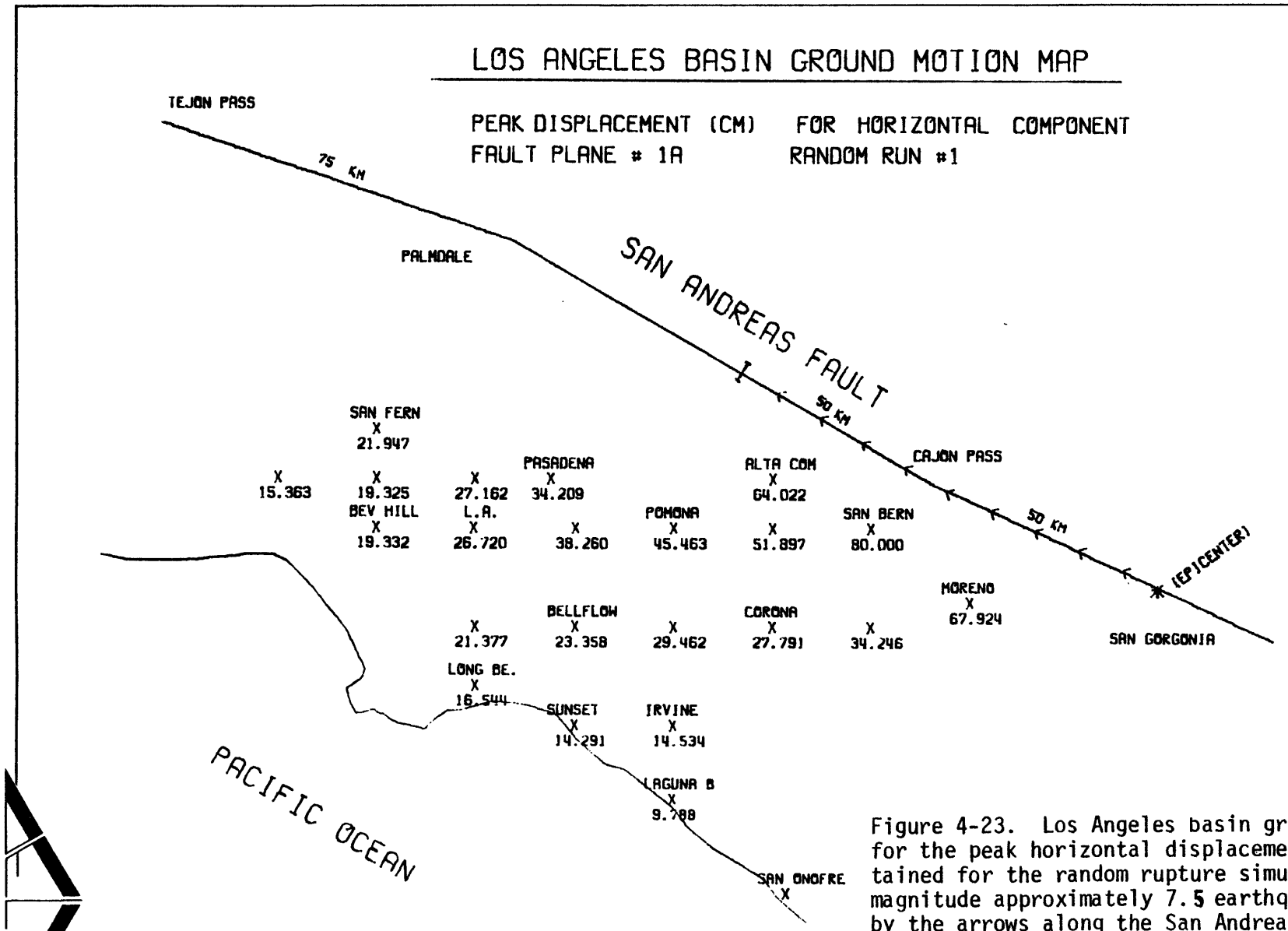

Figure 4-23. Los Angeles basin ground motion map for the peak horizontal displacement values obtained for the random rupture simulation of the magnitude approximately 7.5 earthquake indicated by the arrows along the San Andreas Fault. The distributed source parameters are listed in Table 4-3 and the earth structure is delineated in Table 4-1.

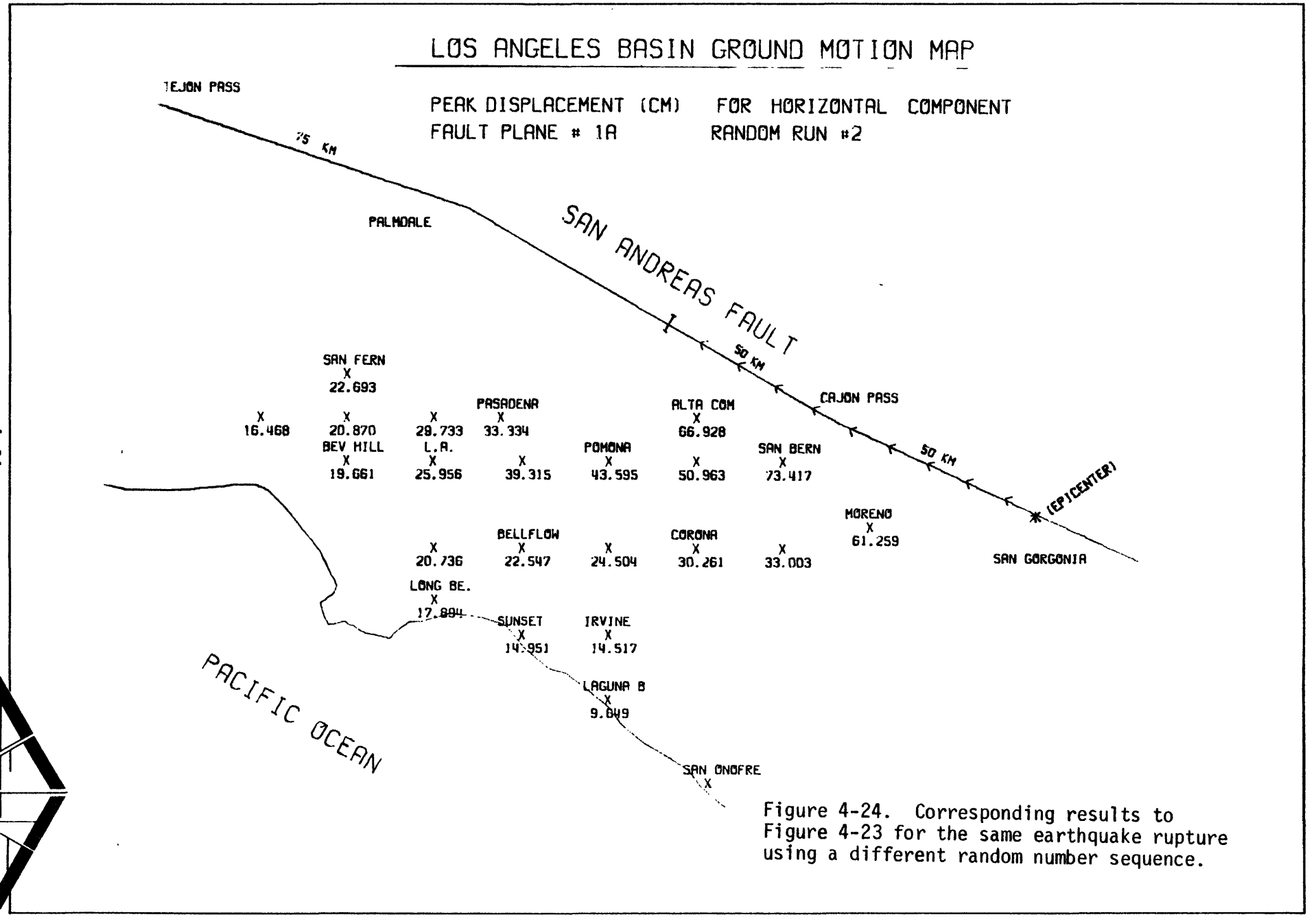

Figure 4-24. Corresponding results to Figure 4-23 for the same earthquake rupture using a different random number sequence.

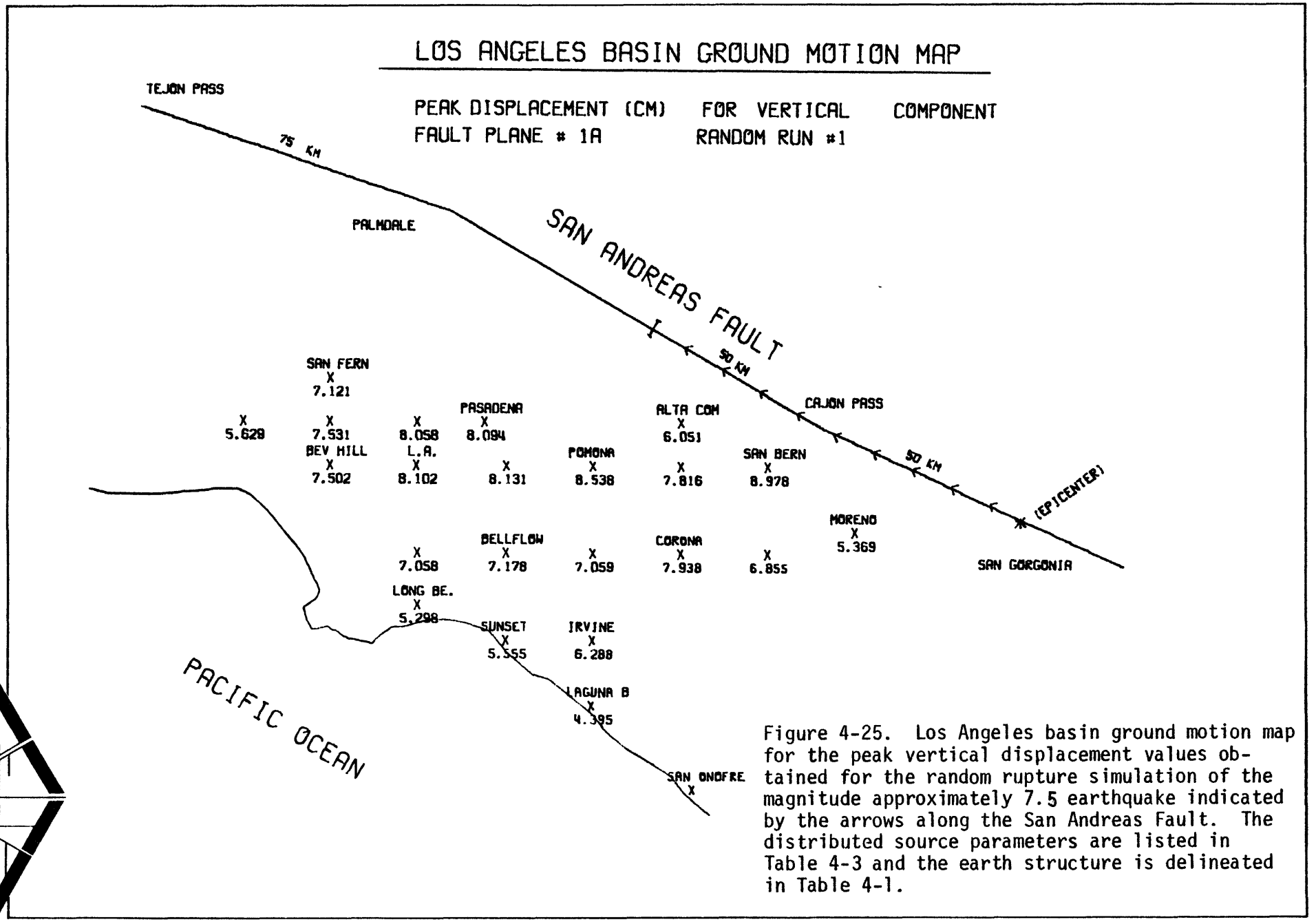

Figure 4-25. Los Angeles basin ground motion map for the peak vertical displacement values obtained for the random rupture simulation of the magnitude approximately 7.5 earthquake indicated by the arrows along the San Andreas Fault. The distributed source parameters are listed in Table 4-3 and the earth structure is delineated in Table 4-1.

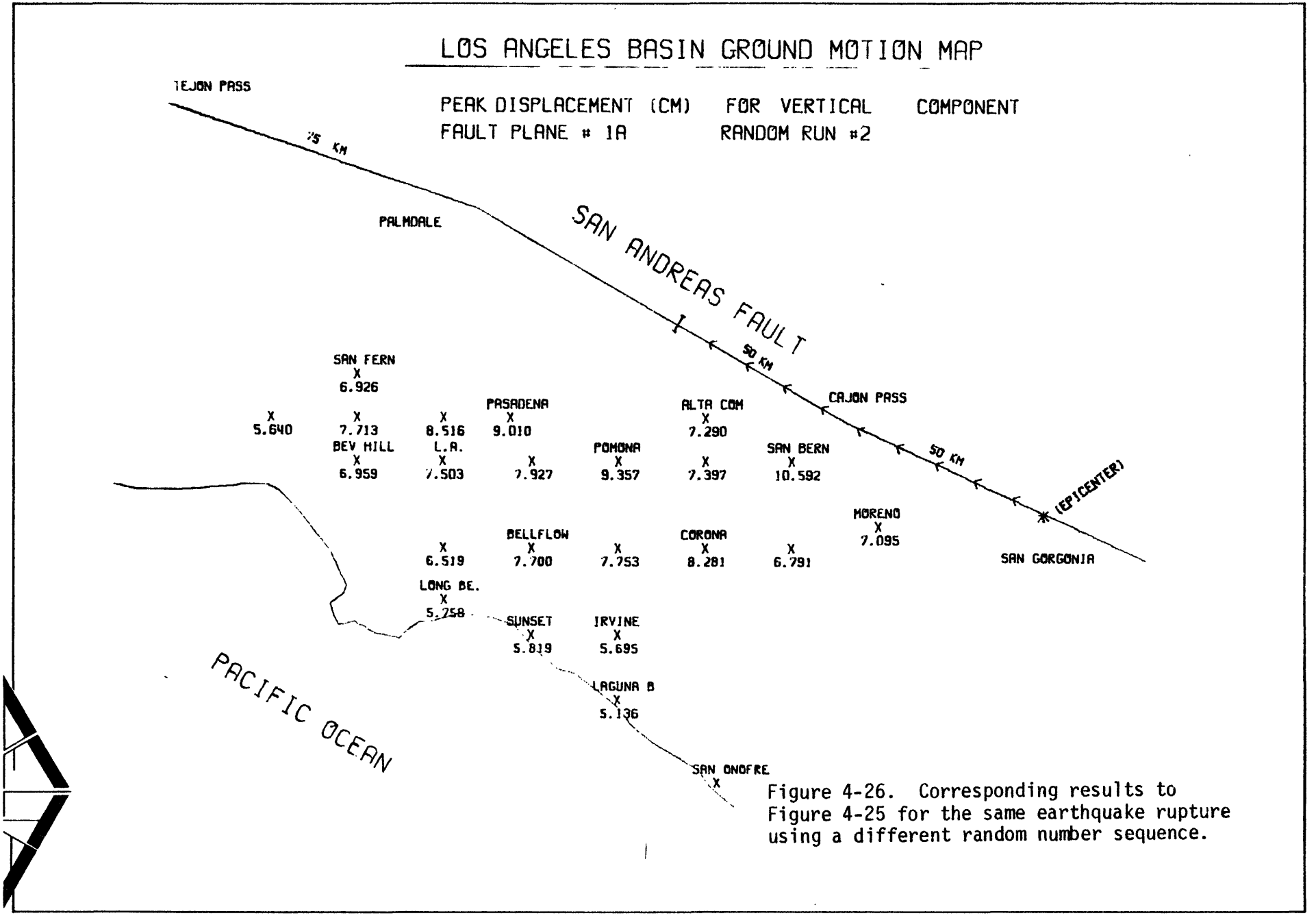

Figure 4-26. Corresponding results to Figure 4-25 for the same earthquake rupture using a different random number sequence.

4.3 MAJOR EARTHQUAKES ALONG THE NEWPORT-INGLEWOOD FAULT

The high-frequency constituents of recorded earthquake ground motions are observed to attenuate strongly as a function of the closest distance to the rupture zone, for receivers further than about 10 km distance from the rupture zone. This phenomena is also observed in the calculated earthquake ground motions as discussed in the previous section. Therefore, the western region of the Los Angeles basin is probably more vulnerable to potentially catastrophic ground shaking from a major earthquake along the Newport-Inglewood Fault than from a major earthquake along the San Andreas Fault (due to the closer proximity of the rupture zone). As discussed in Section 1.1, the 1933 Long Beach earthquake (magnitude approximately 6.3) ruptured along the Newport-Inglewood Fault, killing about 100 people and causing widespread damage in Long Beach and other coastal communities.

The western Los Angeles basin and adjacent coastal communities are clearly vulnerable to another earthquake along the Newport-Inglewood Fault. In fact, the fatalities and destruction could easily reach inconceivable proportions for a hypothetical major earthquake that ruptures further to the north toward Beverly Hills. Ground motions from such an earthquake rupture (magnitude approximately 6.8) are calculated using the numerical procedure discussed in Chapter 3. The distributed source parameters for this rupture configuration are listed in Table 4-3. The same earth structure (and hence the same Green's functions) as used in the previous section is assumed to be representative of the material properties between the Newport-Inglewood Fault and the receiver of interest in the Los Angeles basin (refer to Table 4-1 for the individual viscoelastic layer parameters).

The computed ground motions are presented in Figures 4-27 through 4-38 in the identical format and arrangement as the two sets of ground motion maps of the previous section (e.g., same as Figures 4-3 through 4-14 for rupture configuration between Cajon Pass and Palmdale along the San Andreas Fault). The only difference in format is, of course, the representation of the propagating rupture by the arrows on the

Table 4-4. Distributed source parameters for rupture simulations along the Newport-Inglewood Faults in Figures 4-27 through 4-38.

Epicenter Location*	6 km Offshore Near Laguna Beach
Fault Length, Strike Direction**	50 km, -133°
Fault Dip	90°
Depth to Fault Top	.914 km
Fault Width	10.4 km
Fault Slip-Offset	140 cm
Fault Slip-Rake	-15°***
Fault Slip-Rise Time	3 sec
Gross Rupture Velocity	.9 β
Depth of Hypocenter	11.3 km

*Refer to ground motion map in Figure 4-27 for actual location.

**Measured clockwise from east direction.

***Predominantly right-lateral strike slip motion. West block moves upwards relative to east block.

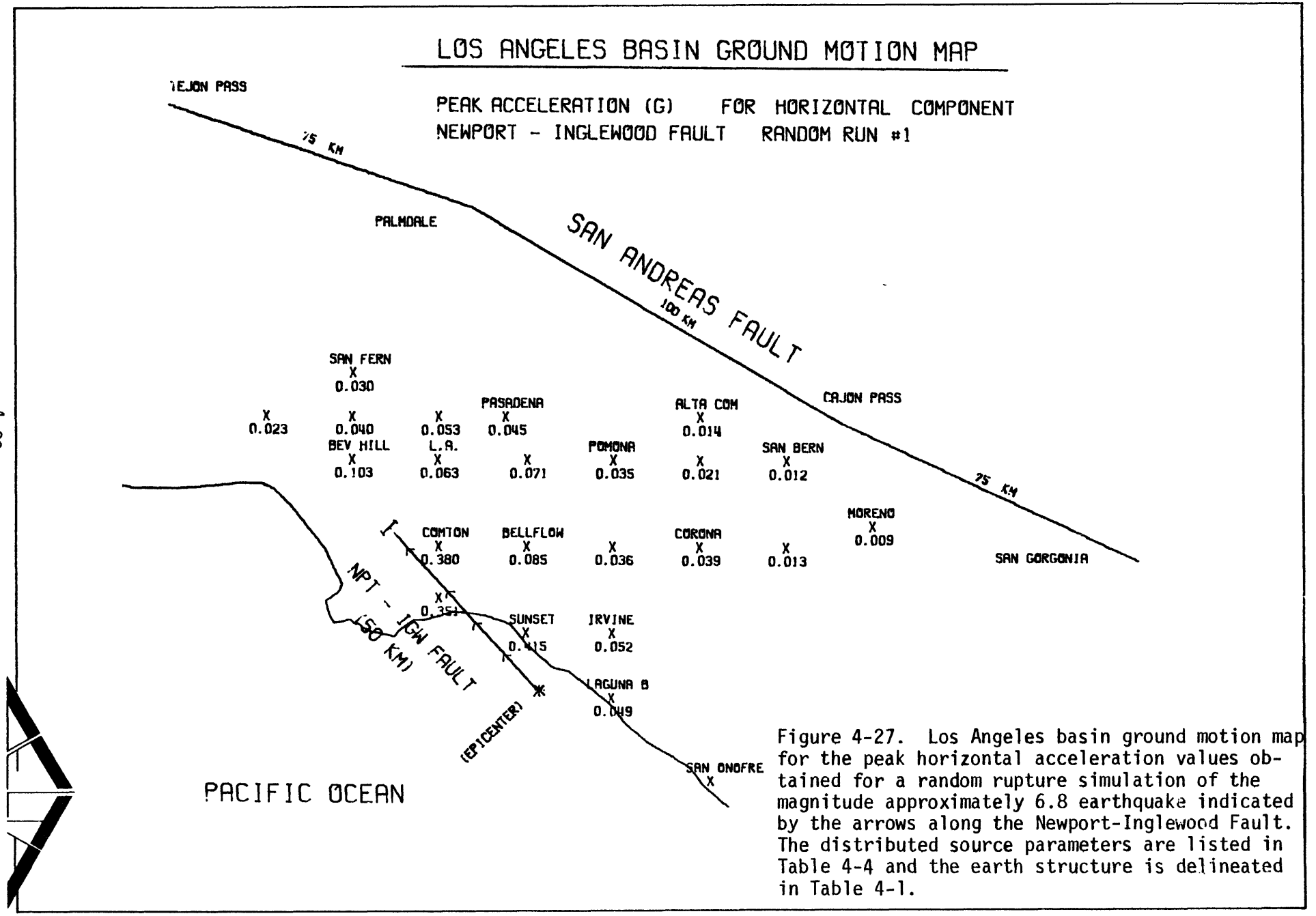

Figure 4-27. Los Angeles basin ground motion map for the peak horizontal acceleration values obtained for a random rupture simulation of the magnitude approximately 6.8 earthquake indicated by the arrows along the Newport-Inglewood Fault. The distributed source parameters are listed in Table 4-4 and the earth structure is delineated in Table 4-1.

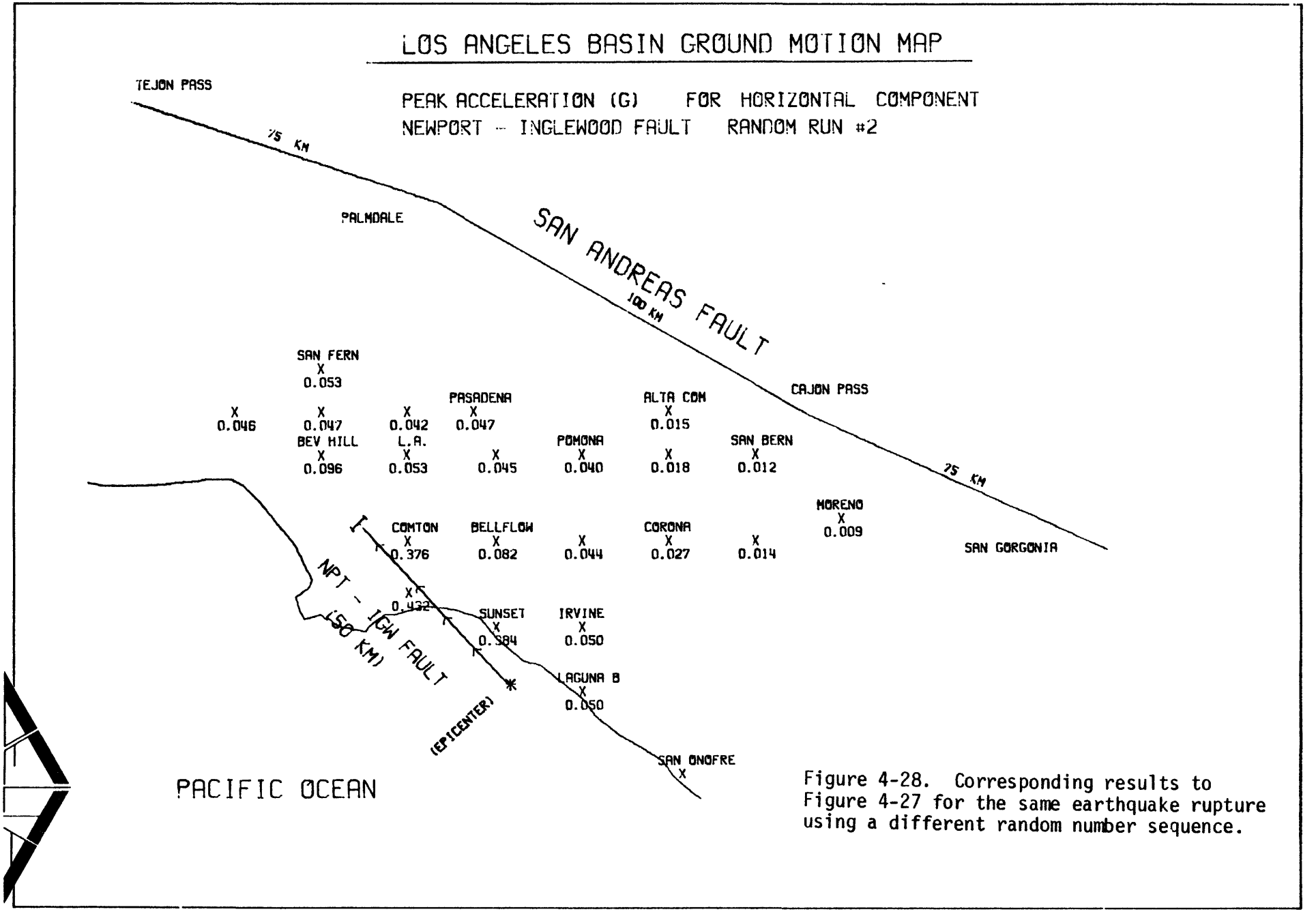

Figure 4-28. Corresponding results to Figure 4-27 for the same earthquake rupture using a different random number sequence.

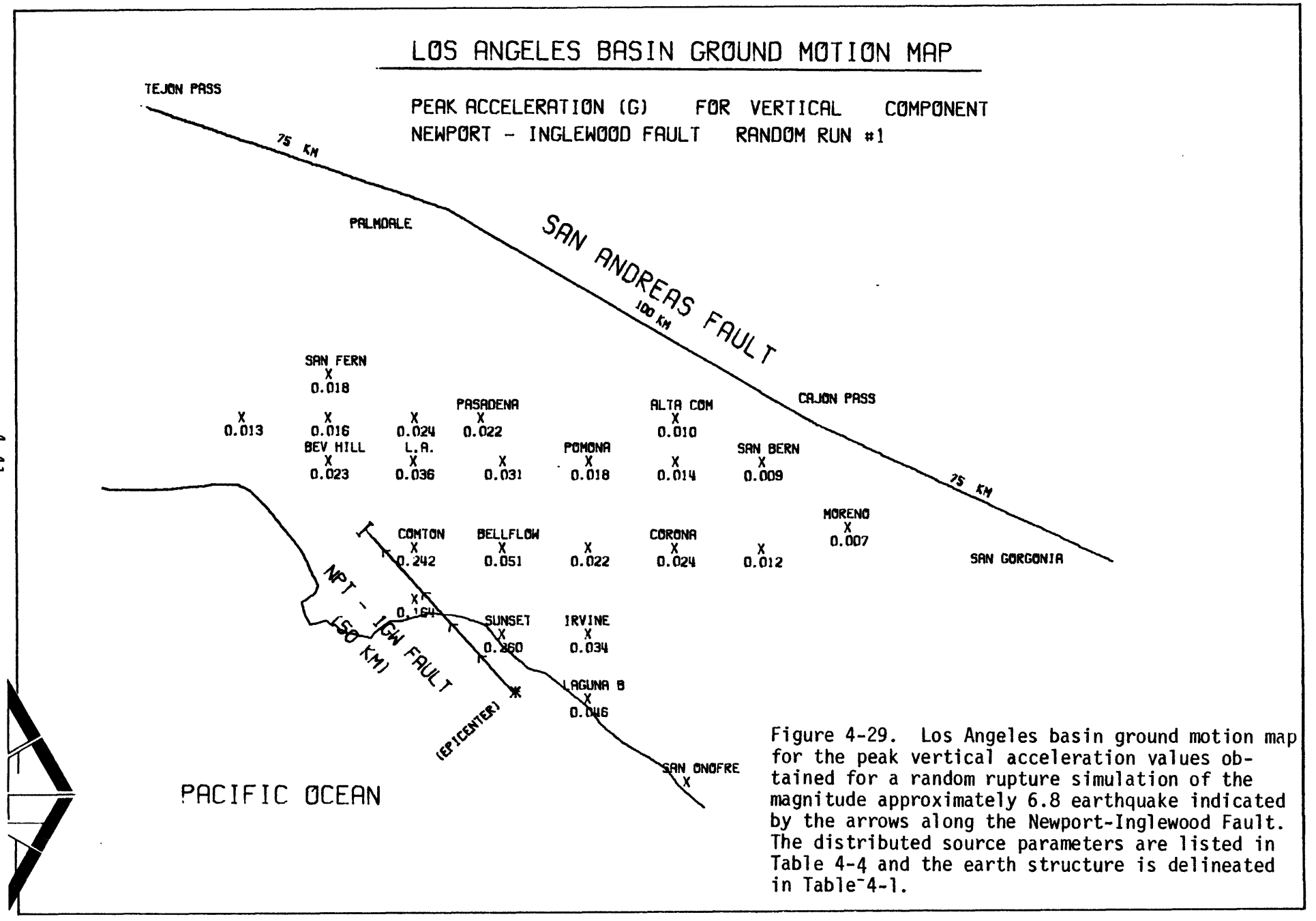

Figure 4-29. Los Angeles basin ground motion map for the peak vertical acceleration values obtained for a random rupture simulation of the magnitude approximately 6.8 earthquake indicated by the arrows along the Newport-Inglewood Fault. The distributed source parameters are listed in Table 4-4 and the earth structure is delineated in Table 4-1.

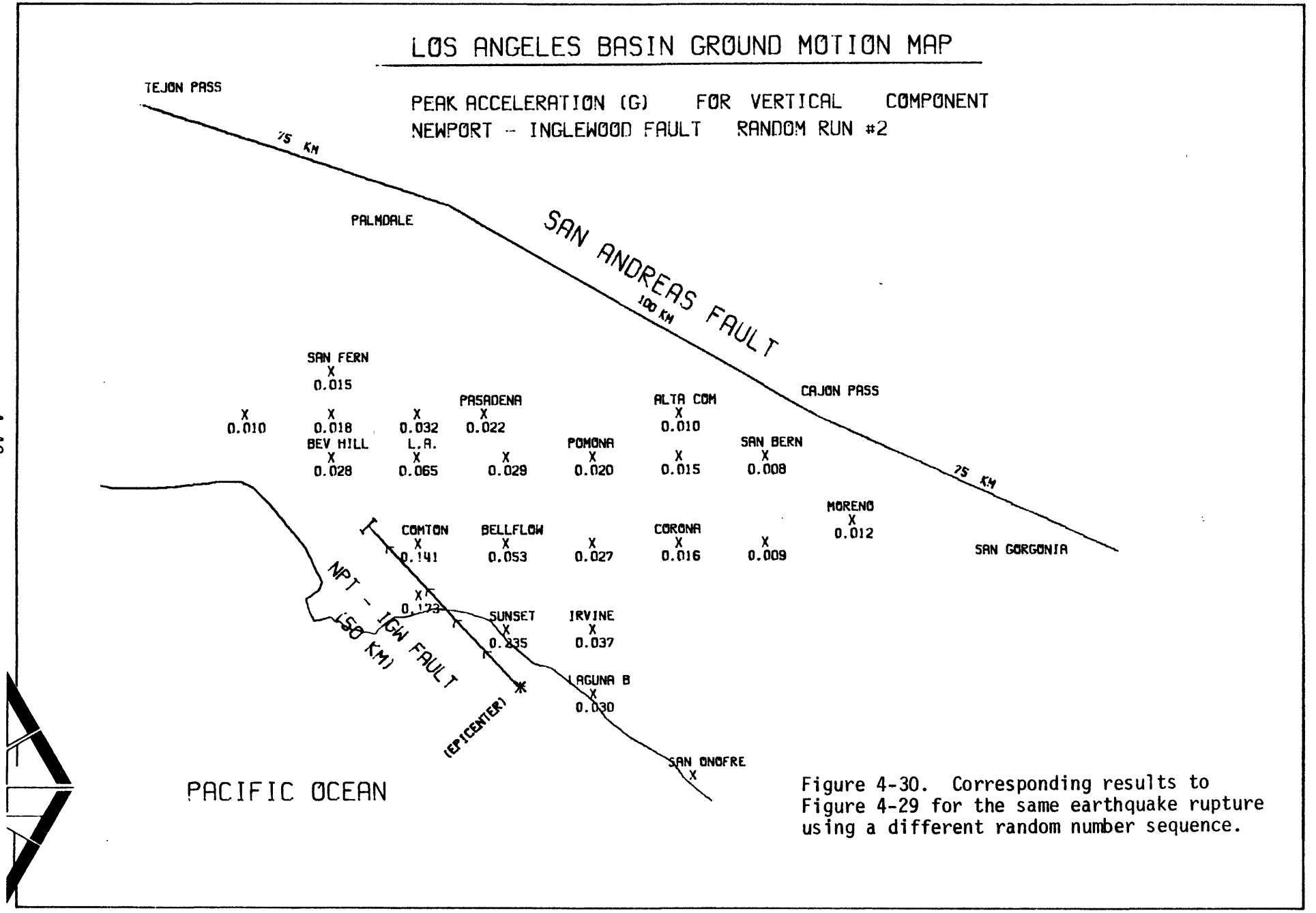

Figure 4-30. Corresponding results to Figure 4-29 for the same earthquake rupture using a different random number sequence.

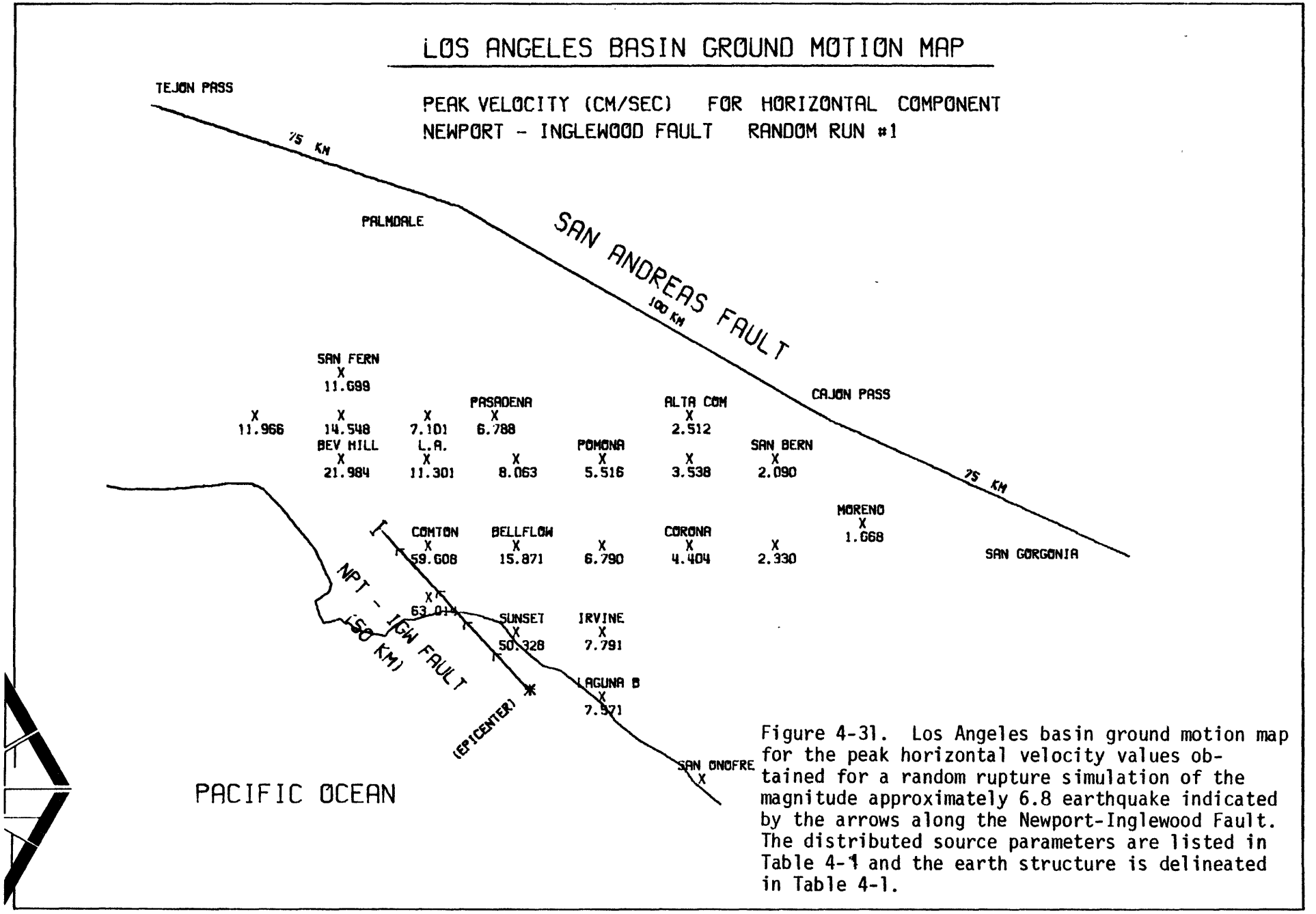

Figure 4-31. Los Angeles basin ground motion map for the peak horizontal velocity values obtained for a random rupture simulation of the magnitude approximately 6.8 earthquake indicated by the arrows along the Newport-Inglewood Fault. The distributed source parameters are listed in Table 4-1 and the earth structure is delineated in Table 4-1.

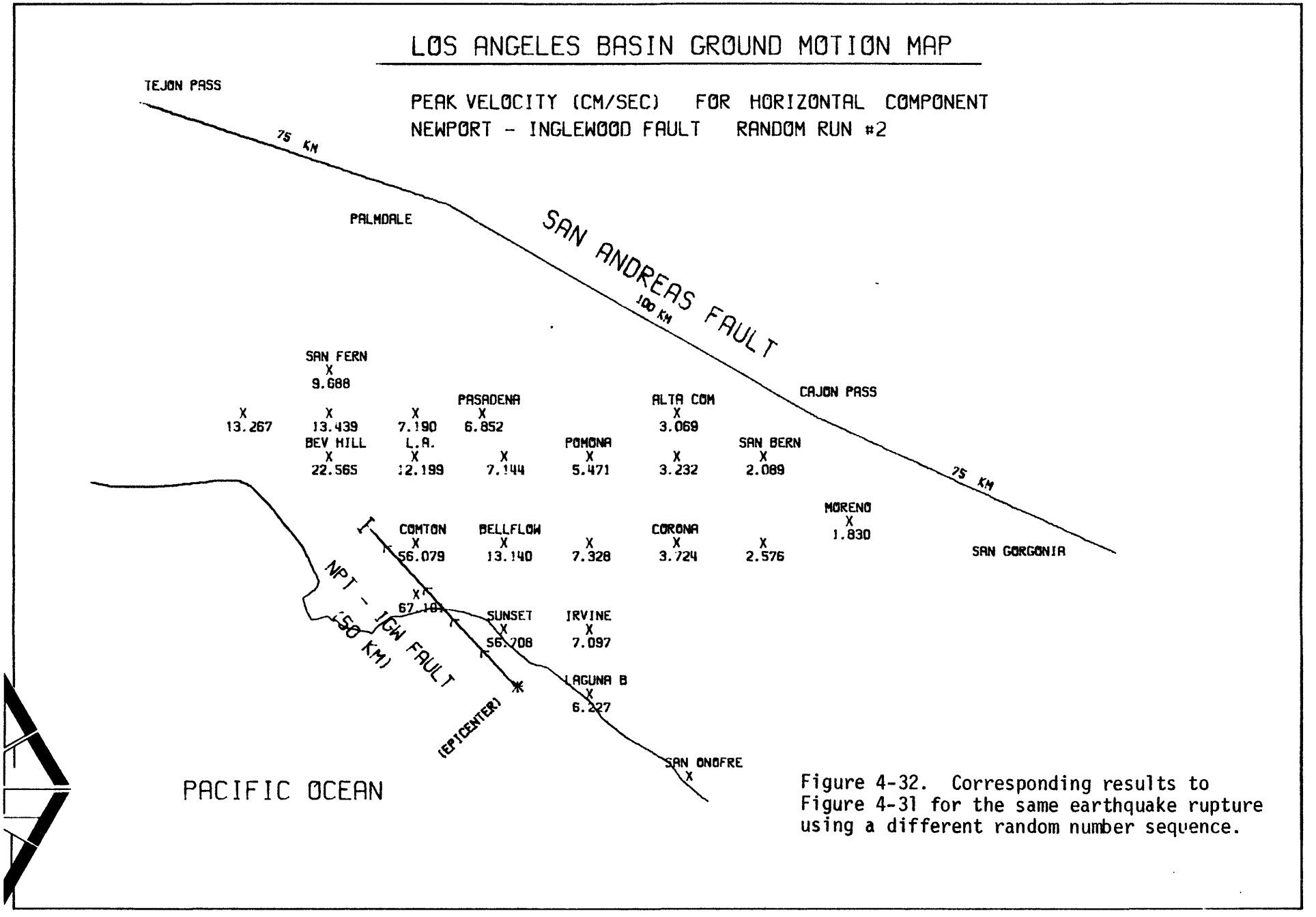

Figure 4-32. Corresponding results to Figure 4-31 for the same earthquake rupture using a different random number sequence.

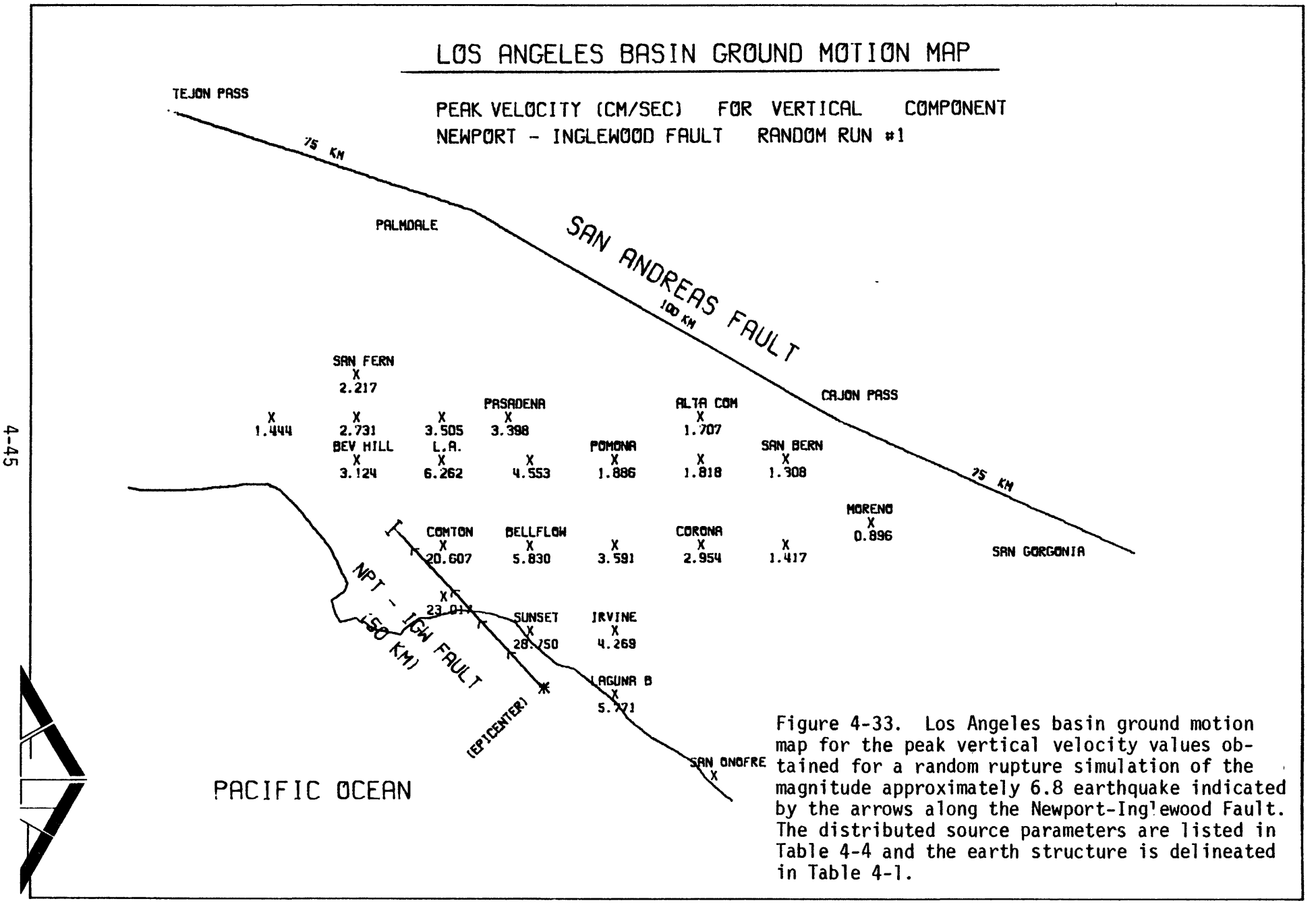

Figure 4-33. Los Angeles basin ground motion map for the peak vertical velocity values obtained for a random rupture simulation of the magnitude approximately 6.8 earthquake indicated by the arrows along the Newport-Inglewood Fault. The distributed source parameters are listed in Table 4-4 and the earth structure is delineated in Table 4-1.

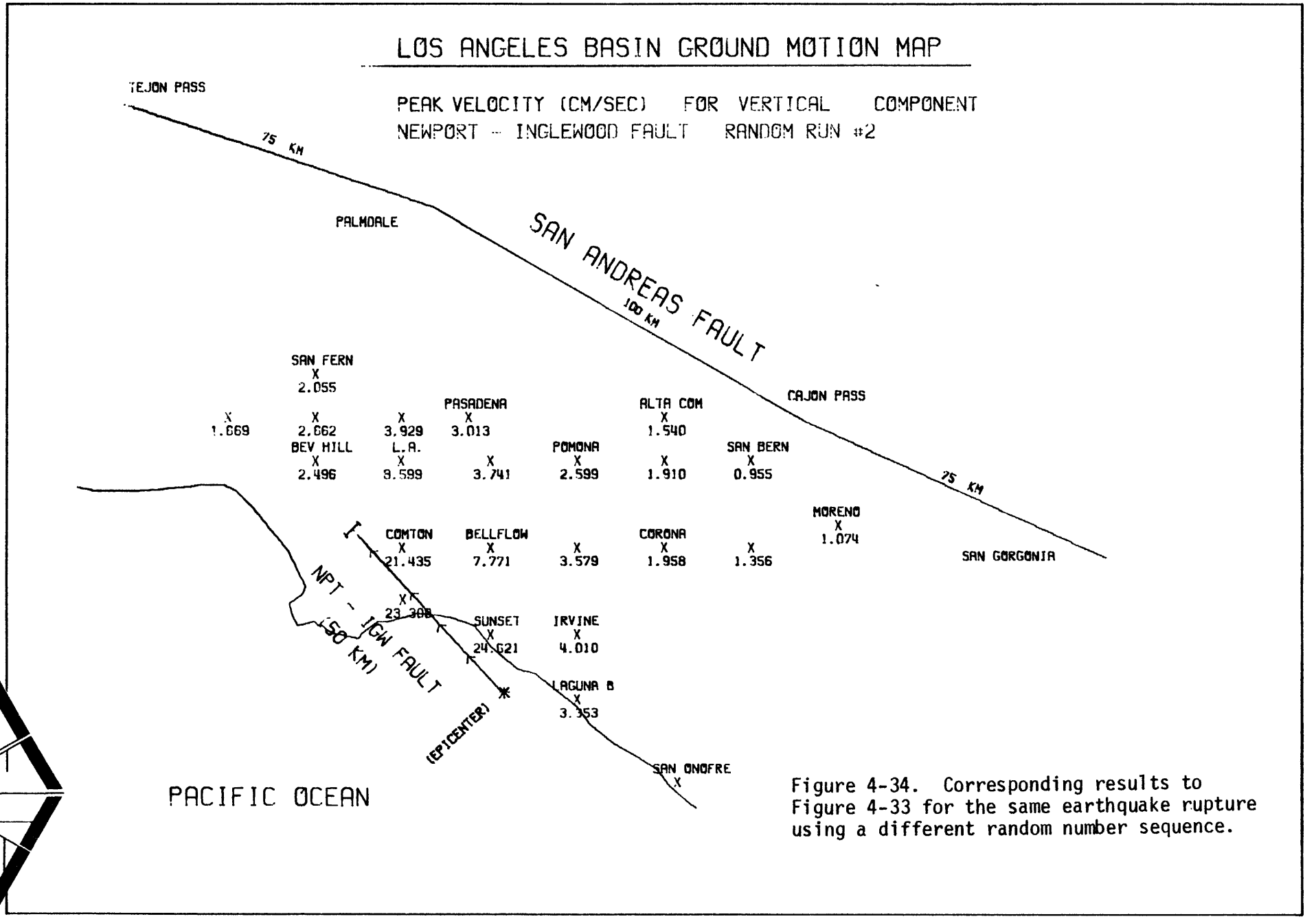

Figure 4-34. Corresponding results to Figure 4-33 for the same earthquake rupture using a different random number sequence.

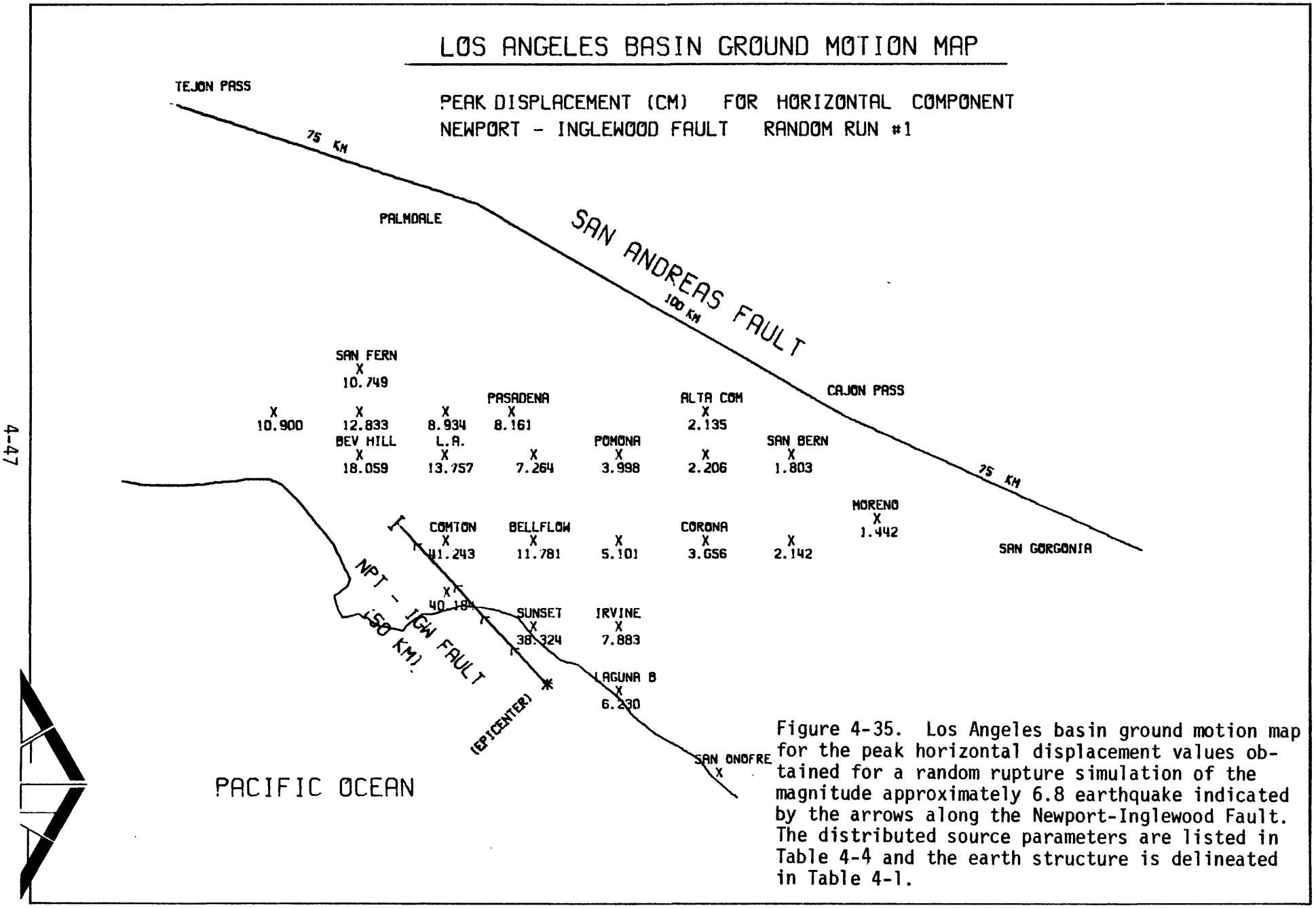

Figure 4-35. Los Angeles basin ground motion map for the peak horizontal displacement values obtained for a random rupture simulation of the magnitude approximately 6.8 earthquake indicated by the arrows along the Newport-Inglewood Fault. The distributed source parameters are listed in Table 4-4 and the earth structure is delineated in Table 4-1.

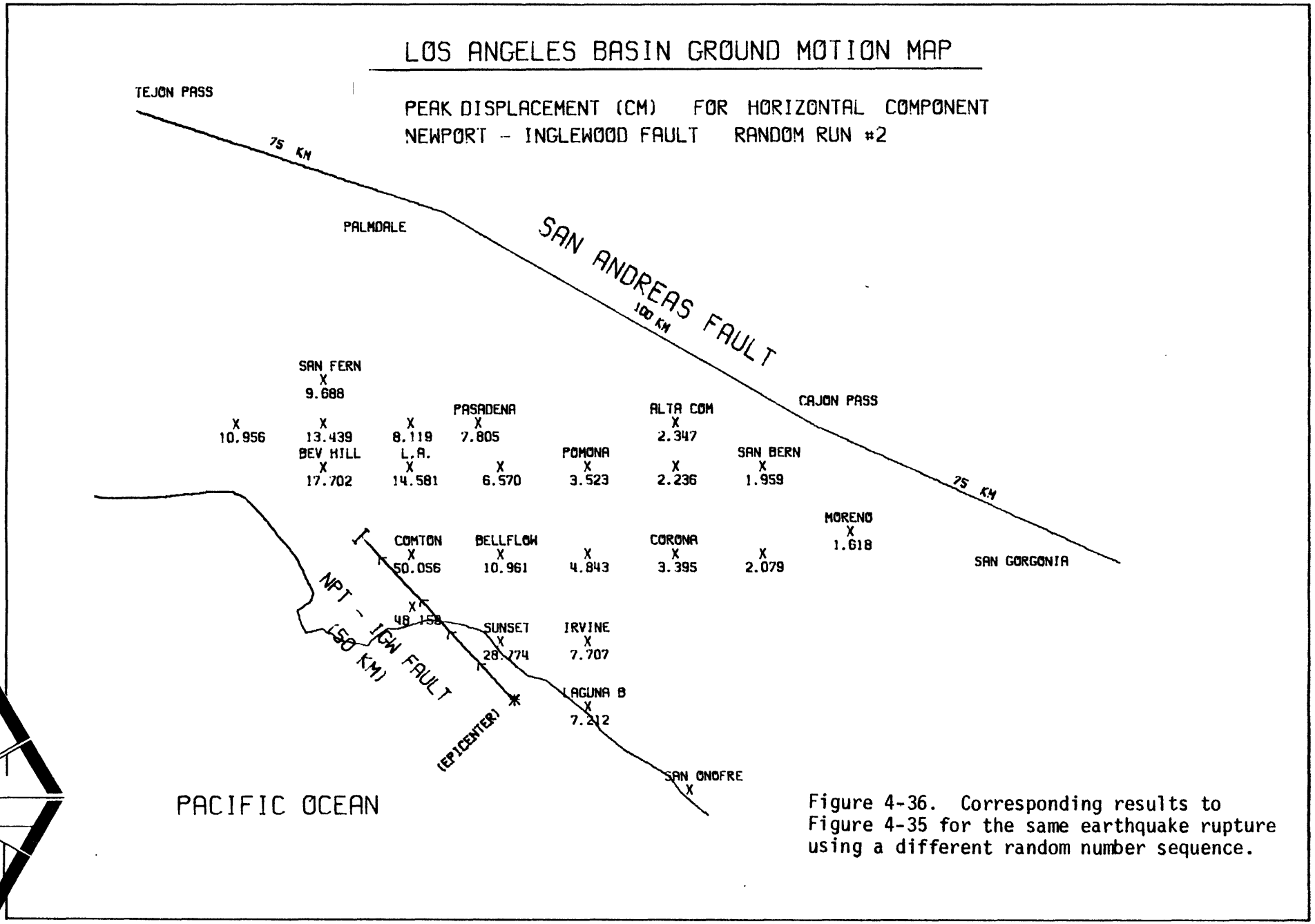

Figure 4-36. Corresponding results to Figure 4-35 for the same earthquake rupture using a different random number sequence.

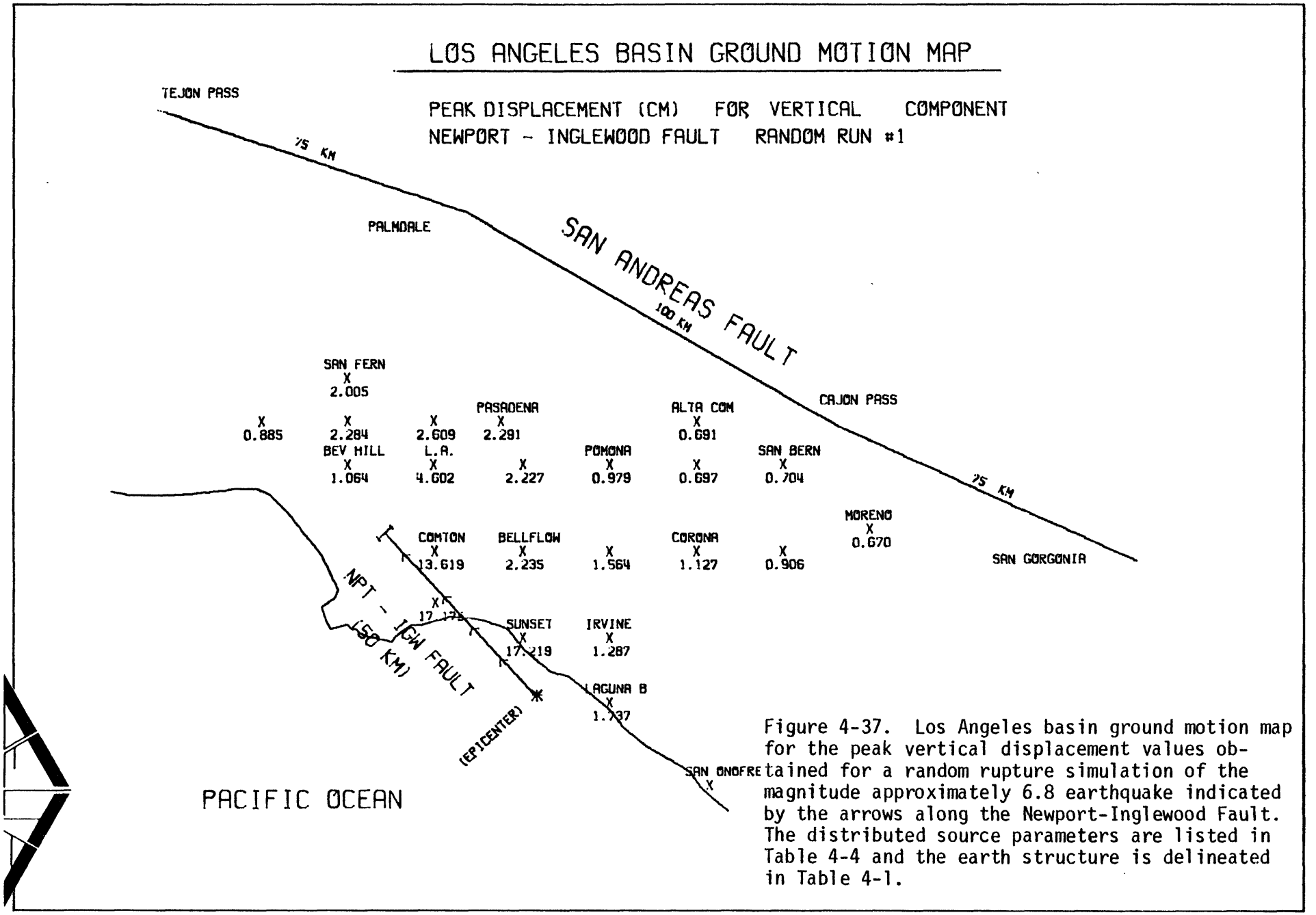

Figure 4-37. Los Angeles basin ground motion map for the peak vertical displacement values obtained for a random rupture simulation of the magnitude approximately 6.8 earthquake indicated by the arrows along the Newport-Inglewood Fault. The distributed source parameters are listed in Table 4-4 and the earth structure is delineated in Table 4-1.

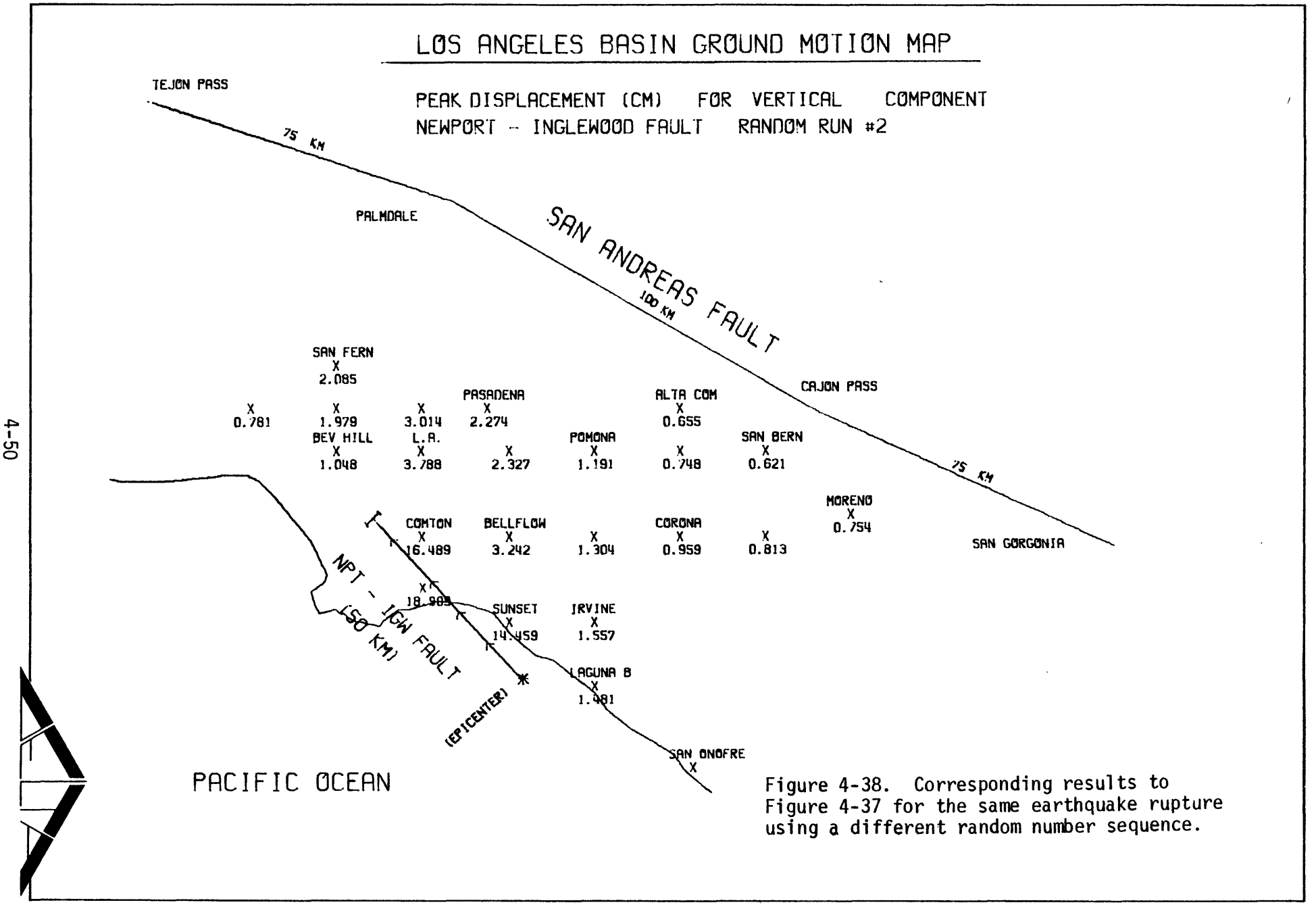

Figure 4-38. Corresponding results to Figure 4-37 for the same earthquake rupture using a different random number sequence.

Newport-Inglewood Fault. As expected, the peak acceleration values in Figures 4-27 through 4-30 reach hazardous levels for coastal communities near the line of rupture focussing; the values for the metropolitan areas around downtown Los Angeles are larger by factors of two or three. If the rupture were allowed to continue further to the north, then the peak acceleration values for the cities around downtown Los Angeles would also have reached extremely hazardous levels. The peak acceleration values far from the Newport-Inglewood rupture zone are similar to those obtained at equal distances from the San Andreas rupture zone in Figures 4-3 through 4-7. Again, as stressed in the previous section, it is imperative to recall that the acceleration values are limited by the Nyquist frequency of 5 Hz chosen for the computation of the Green's functions.

The peak velocity values in Figures 4-31 through 4-34 offer no surprises in light of the discussion on the peak acceleration values. The peak displacement values in Figures 4-25 through 4-38 are different in two respects than the corresponding values in Figures 4-12 through 4-15 for the San Andreas rupture. First, the values are smaller overall due to the smaller earthquake magnitude associated with a smaller slip function offset and half the rupture length. Second, the peak displacement values seem to attenuate more rapidly as a function of distance from the rupture zone due to the much shorter rupture length.

CHAPTER 5

SENSITIVITY STUDIES FOR DOWNTOWN LOS ANGELES

The computed ground motion maps in Chapter 4 illustrate the potential earthquake hazards for the Los Angeles basin as a function of distance and orientation from major earthquakes rupturing through critical regions with respect to the basin. The sensitivity studies in this chapter illustrate the behavior of the computed ground motions as a function of various earthquake parameters used in the numerical modeling procedure.

Ground motions at downtown Los Angeles are calculated for ten different earthquake configurations along the San Andreas Fault. Each earthquake calculation is repeated four times using four different incoherent rupture simulations. Thereby, any bias introduced by comparing the results from single incoherent rupture simulations is suppressed by comparing the average results of the four simulations per earthquake configuration. The results from the ten different sensitivity calculations are grouped into five types of sensitivity studies corresponding to the five sections that follow in this chapter. The distributed source parameters for each grouping of sensitivity calculations are compiled in Tables 5-1 through 5-6.

The first grouping of sensitivity calculations (numbers 1, 2, 3, 4) in Table 5-1 is used in Section 5.1 to investigate the influences of rupture length on the computed results. The second grouping of sensitivity calculations (numbers 1,5) in Table 5-2 is used in Section 5.2 to investigate the influences of fault type on the computed results. The third and fourth groupings of sensitivity calculations (numbers 1, 6, 7 and numbers 3, 8) in Tables 5-3 and 5-4, respectively, are used in Section 5.3 to investigate the influences of rupture direction on the computed results. The fifth grouping of sensitivity calculations (numbers 1, 9) in Table 5-5 is used in Section 5.4 to investigate the influences of gross rupture velocity on the computed results. The sixth and final grouping of sensitivity calculations (numbers 1, 10) in Table 5-6 is used in Section 5.5 to investigate the influences of fault bottom on the computed results.

Table 5-1. Distributed source parameters for the four sensitivity runs in Section 5.1 using different fault lengths corresponding in magnitude 7.5, 7.8, 8.0 and 7.2 earthquakes, respectively, along the San Andreas Fault.

Model Parameters \ Sensitivity Calculation Number	1	2	3	4
Epicenter Location*	Bend Near Cajon Pass	Point Near San Gorgonio	Point Near San Gorgonio	Bend Near Cajon Pass
Fault Length, Strike Direction**	100 km, -150°	75 km, -156° +100 km, -150°	75 km, -156° +100 km, -150° +75 km, -162°	50 km, -150°
Fault Dip	90°	90°	90°	90°
Depth to Fault Top	.914 km	.914 km	.914 km	.914 km
Fault Width	10.4 km	10.4 km	10.4 km	10.4 km
Fault Slip-Offset	500 cm	500 cm	500 cm	500 cm
Fault Slip-Rake	0°***	0°***	0°***	0°***
Fault Slip-Rise Time	3 sec	3 sec	3 sec	3 sec
Gross Rupture Velocity	.9β	.9β	.9β	.9β
Depth of Hypocenter	11.3 km	11.3 km	11.3 km	11.3 km

*Refer to map of San Andreas Fault in Figure 4-3.

**Measured clockwise from east direction.

***Right-lateral strike-slip.

Table 5-2. Distributed source parameters for the two sensitivity runs in Section 5.2 using different fault types for a magnitude approximately 7.5 earthquake along the San Andreas Fault.

Model Parameters \ Sensitivity Calculation Number	1	5
Epicenter Location*	Bend Near Cajon Pass	Bend Near Cajon Pass
Fault Length, Strike Direction**	100 km, -150°	100 km, -150°
Fault Dip	90°	90°
Depth to Fault Top	.9 km	.9 km
Fault Width	10.4 km	10.4 km
Fault Slip-Offset	500 cm	500 cm
Fault Slip-Rake	0°***	45°****
Fault Slip-Rise Time	3 sec	3 sec
Gross Rupture Velocity	.9β	.9β
Depth of Hypocenter	11.3 km	11.3 km

*Refer to map of San Andreas Fault in Figure 4-3.

**Measured clockwise from east.

***Right lateral strike-slip.

****Right lateral slip, north block moves downwards relative to south block.

Table 5-3. Distributed source parameters for the three sensitivity studies in Section 5.3 using different rupture directions for a magnitude approximately 7.5 earthquake along the San Andreas Fault.

Model Parameters \ Sensitivity Calculation Number	1	6	7
Epicenter Location*	Bend Near Cajon Pass	Bend Near Palmdale	Midway Between Bends near Cajon Pass and Palmdale
Fault Length, Strike Direction**	100 km, -150° (NW)	100 km, 30° (SE)	50 km, -150° / +50 km, 30° (bilateral)
Fault Dip	90°	90°	90°
Depth to Fault Top	.9 km	.9 km	.9 km
Fault Width	10.4 km	10.4 km	10.4 km
Fault Slip-Offset	500 cm	500 cm	500 cm
Fault Slip-Rake	0°***	0°***	0°***
Fault Slip-Rise Time	3 sec	3 sec	3 sec
Gross Rupture Velocity	.9β	.9β	.9β
Depth of Hypocenter	11.3 km	11.3 km	11.3 km

*Refer to map of San Andreas Fault in Figure 4-3.

**Measured clockwise from east.

***Right lateral strike-slip.

Table 5-4. Distributed source parameters for the two sensitivity studies in Section 5.3 using two different rupture directions for a magnitude approximately 8.0 earthquake along the San Andreas Fault.

Model Parameters \ Sensitivity Calculation Number	3	8
Epicenter Location*	Point Near San Gorgonio	Bend Near Cajon Pass
Fault Length, Strike Direction**	75 km, -156° +100 km, -150° (NW) +75 km, -162°	75 km, 18° +100 km, 30° (SE) +75 km, 24°
Fault Dip	90°	90°
Depth to Fault Top	.9 km	.9 km
Fault Width	10.4 km	10.4 km
Fault Slip-Offset	500 cm	500 cm
Fault Slip-Rake	0°***	0°***
Fault Slip-Rise Time	3 sec	3 sec
Gross Rupture Velocity	.9β	.9β
Depth of Hypocenter	11.3 km	11.3 km

*Refer to map of San Andreas Fault in Figure 4-3.

**Measured clockwise from east.

***Right lateral strike-slip.

Table 5-5. Distributed source parameters for the two sensitivity studies in Section 5.4 using different rupture velocities for a magnitude approximately 7.5 earthquake along the San Andreas Fault.

Model Parameters \ Sensitivity Calculation Number	1	9
Epicenter Location*	Bend Near Cajon Pass	Bend Near Cajon Pass
Fault Length, Strike Direction**	100 km, -150°	100 km, -150°
Fault Dip	90°	90°
Depth to Fault Top	.9 km	.9 km
Fault Width	10.4 km	10.4 km
Fault Slip-Offset	500 cm	500 cm
Fault Slip-Rake	0°***	0°***
Fault Slip-Rise Time	3 sec	3 sec
Gross Rupture Velocity	.9β	.5β
Depth of Hypocenter	11.3 km	11.3 km

*Refer to map of San Andreas Fault in Figure 4-3

**Measured clockwise from east.

***Right lateral strike-slip.

Table 5-6. Distributed source parameters for the two sensitivity studies in Section 5.5 using different fault bottoms corresponding to magnitude 7.5 and 7.7 earthquakes, respectively, along the San Andreas Fault.

Model Parameters \ Sensitivity Calculation Number	1	10
Epicenter Location*	Bend Near Cajon Pass	Bend Near Cajon Pass
Fault Length, Strike Direction**	100 km, -150°	100 km, -150°
Fault Dip	90°	90°
Depth to Fault Top	.9 km	.9 km
Fault Width	10.4 km	14.1 km
Fault Slip-Offset	500 cm	500 cm
Fault Slip-Rake Direction	0°***	0°***
Fault Slip-Rise Time	3 sec	3 sec
Gross Rupture Velocity	.9β	.9β
Depth of Hypocenter	11.3 km	15 km

*Refer to map of San Andreas Fault in Figure 4-3.

**Measured clockwise from east.

***Right-lateral strike-slip.

The computed acceleration time histories for the ten sensitivity calculations are shown in Figures 5-1 through 5-10, respectively. The four computed accelerograms associated with using different Gaussian random number sequences in the four incoherent rupture simulations per sensitivity calculation are shown for all three components of ground motion in each figure. The time histories are all self-scaled to fit on the same size plot with the scaling factor (i.e., the peak acceleration value) shown to the left of each accelerogram. In all cases, 200 seconds of signal are shown with zero time corresponding to the time of rupture initiation at the hypocenter for that rupture configuration.

These computed acceleration time histories and their associated response spectra will be used in the next five sections to quantify the influences of all the earthquake parameters that were varied in the ten sensitivity calculations. The relative changes in ground motion characteristics for the various sensitivity calculations in a given grouping will be stressed in an attempt to reduce the impact of the limited frequency content and the poor constraint of the material quality factors for the Los Angeles basin earth structure on the computed ground motions.

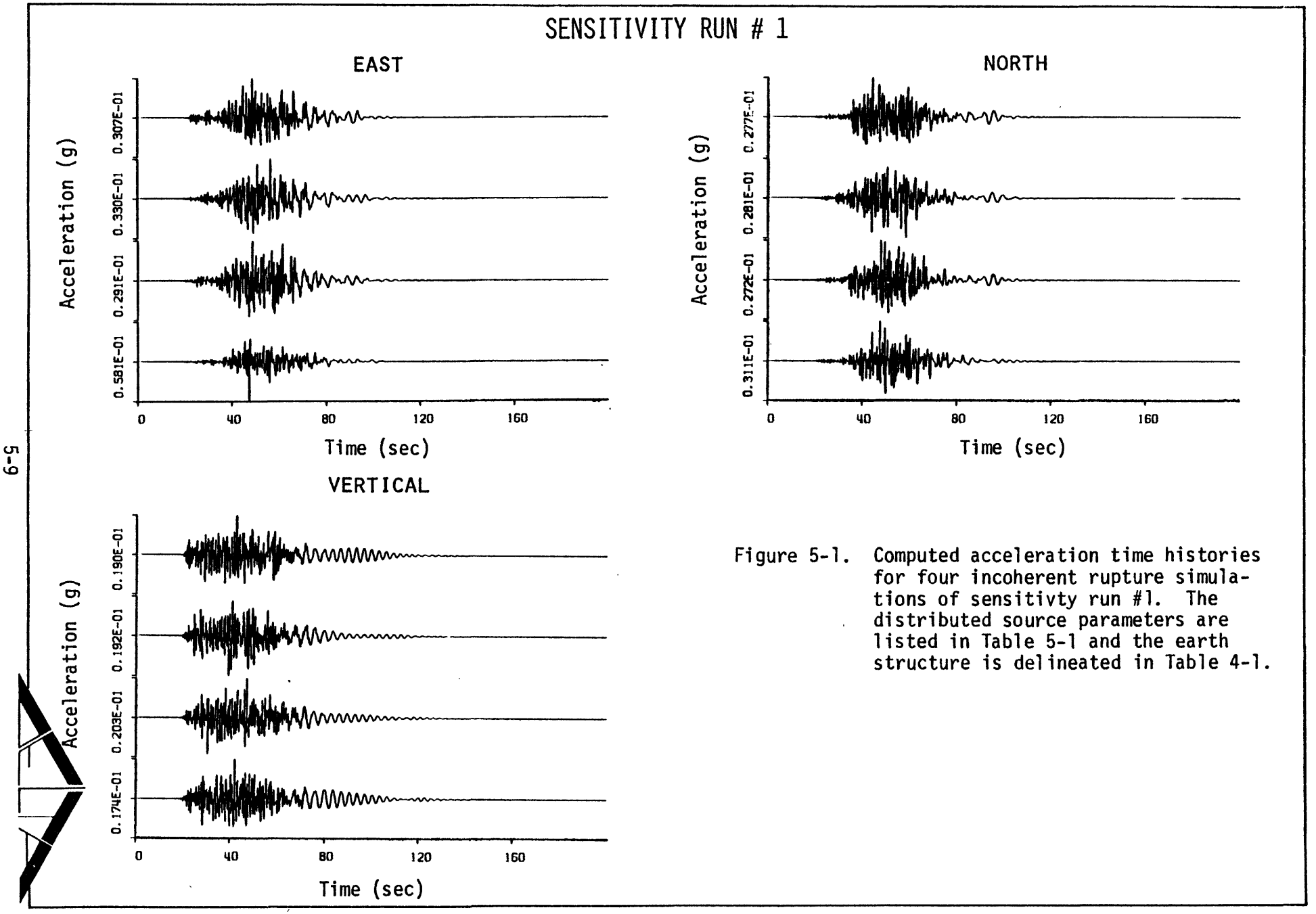

Figure 5-1. Computed acceleration time histories for four incoherent rupture simulations of sensitivty run #1. The distributed source parameters are listed in Table 5-1 and the earth structure is delineated in Table 4-1.

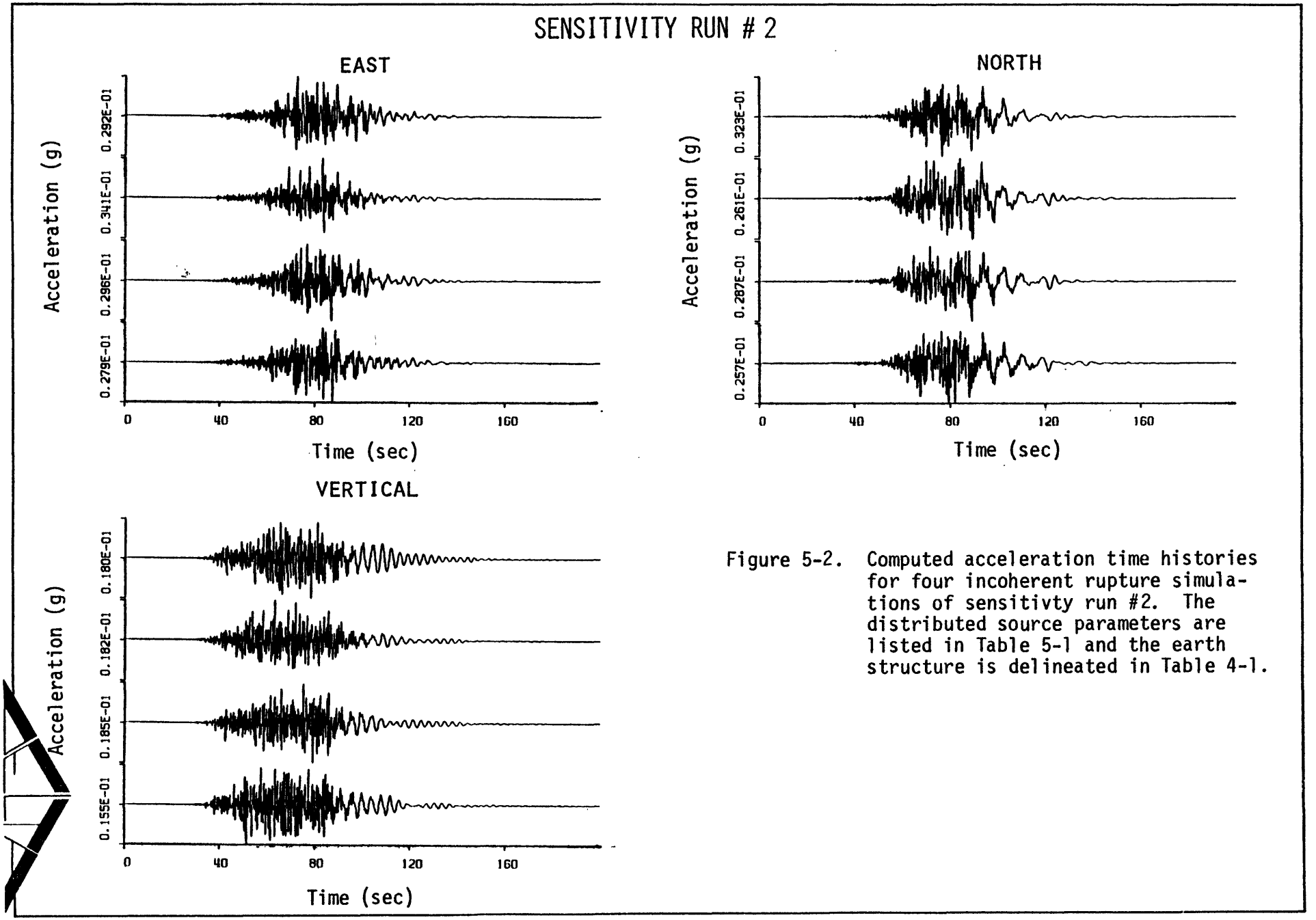

Figure 5-2. Computed acceleration time histories for four incoherent rupture simulations of sensitivty run #2. The distributed source parameters are listed in Table 5-1 and the earth structure is delineated in Table 4-1.

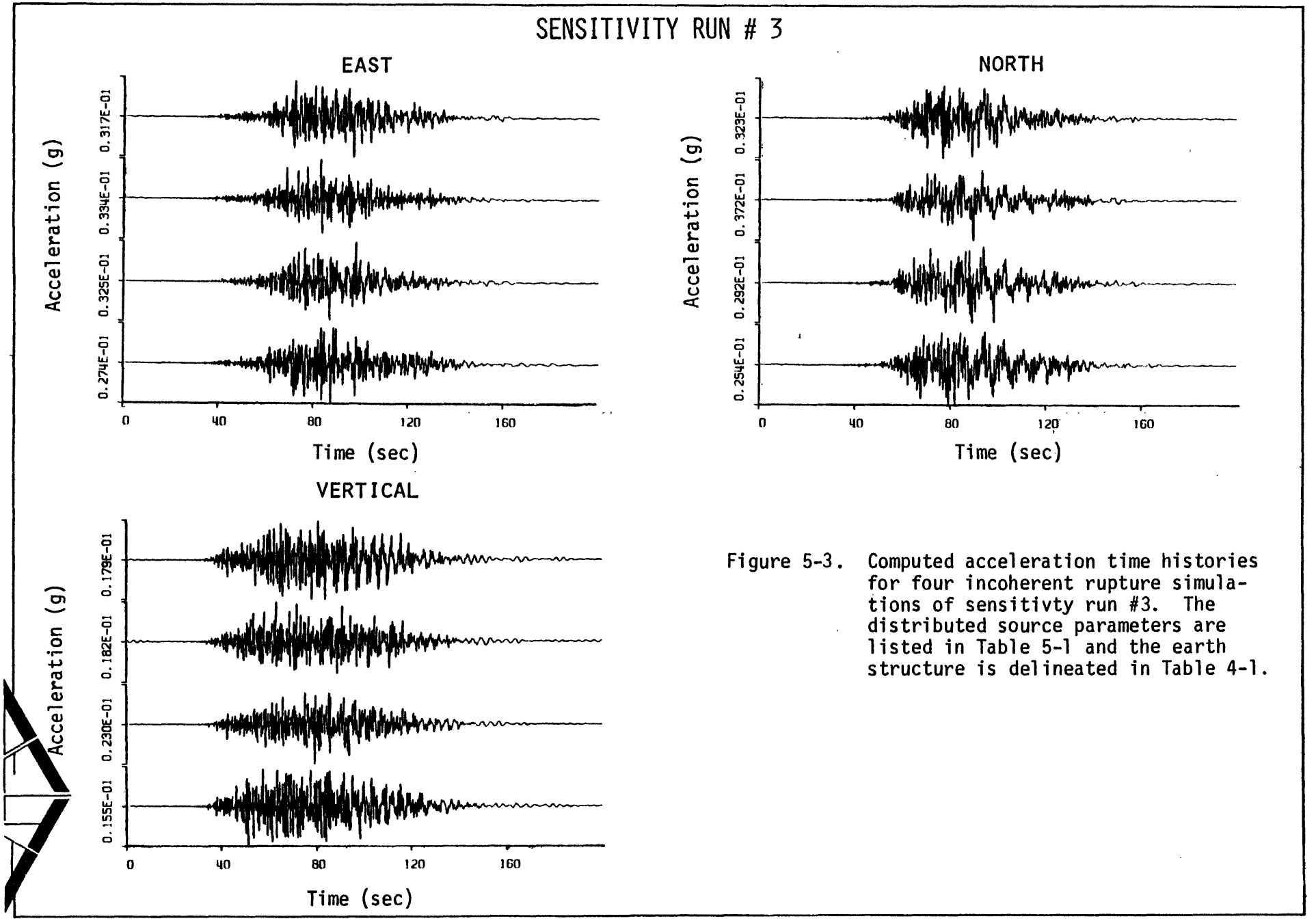

Figure 5-3. Computed acceleration time histories for four incoherent rupture simulations of sensitivty run #3. The distributed source parameters are listed in Table 5-1 and the earth structure is delineated in Table 4-1.

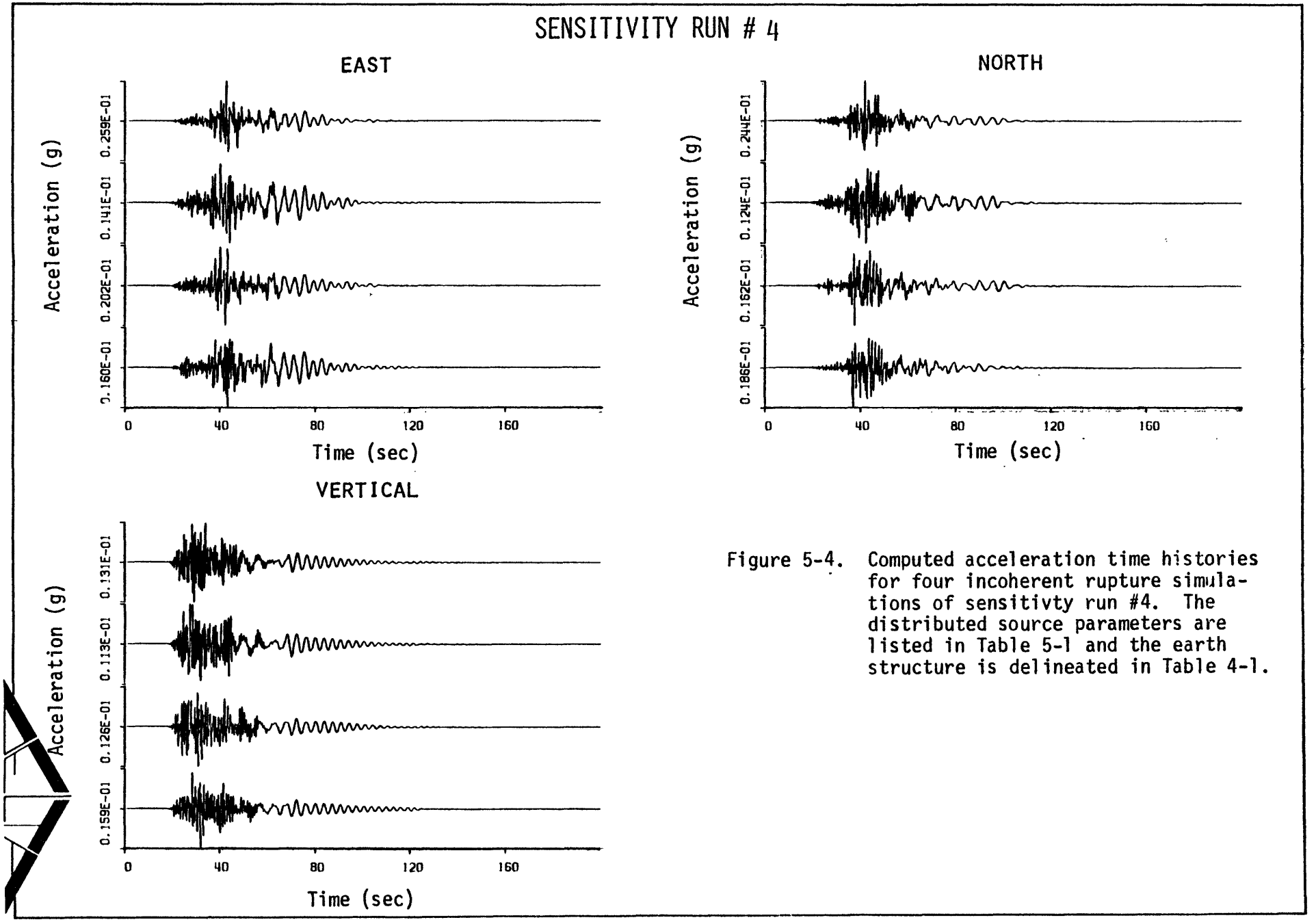

Figure 5-4. Computed acceleration time histories for four incoherent rupture simulations of sensitivty run #4. The distributed source parameters are listed in Table 5-1 and the earth structure is delineated in Table 4-1.

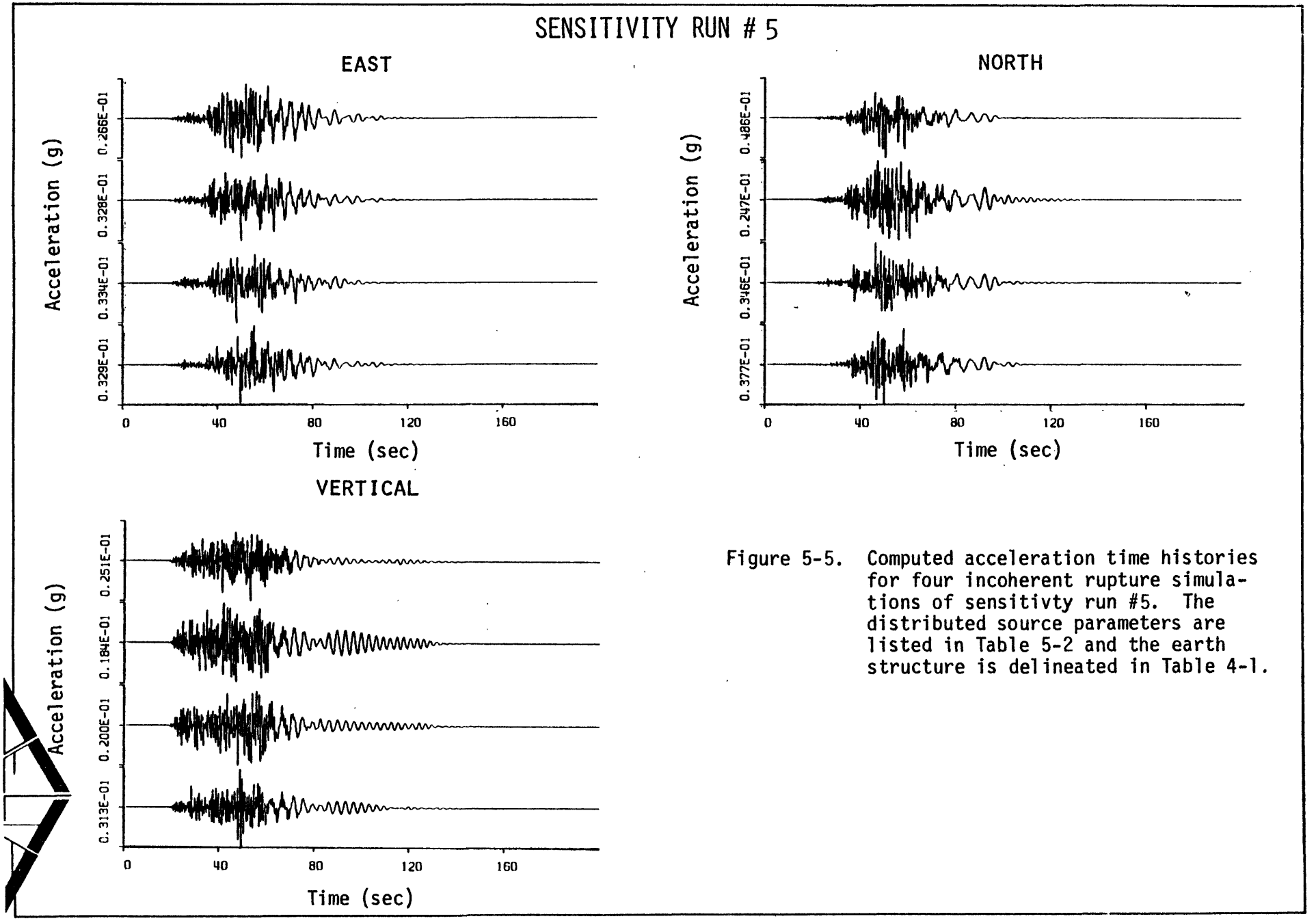

Figure 5-5. Computed acceleration time histories for four incoherent rupture simulations of sensitivty run #5. The distributed source parameters are listed in Table 5-2 and the earth structure is delineated in Table 4-1.

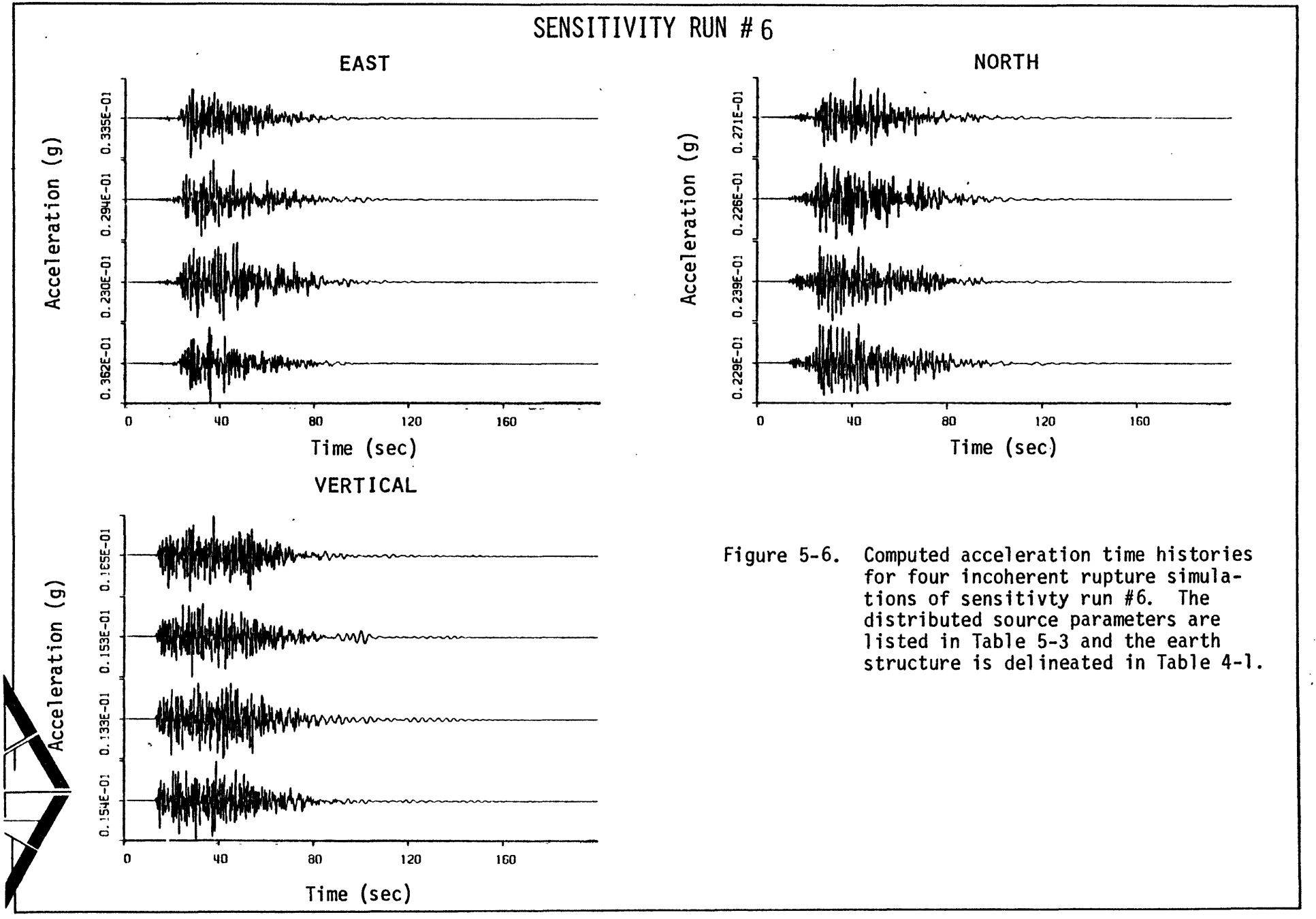

Figure 5-6. Computed acceleration time histories for four incoherent rupture simulations of sensitivty run #6. The distributed source parameters are listed in Table 5-3 and the earth structure is delineated in Table 4-1.

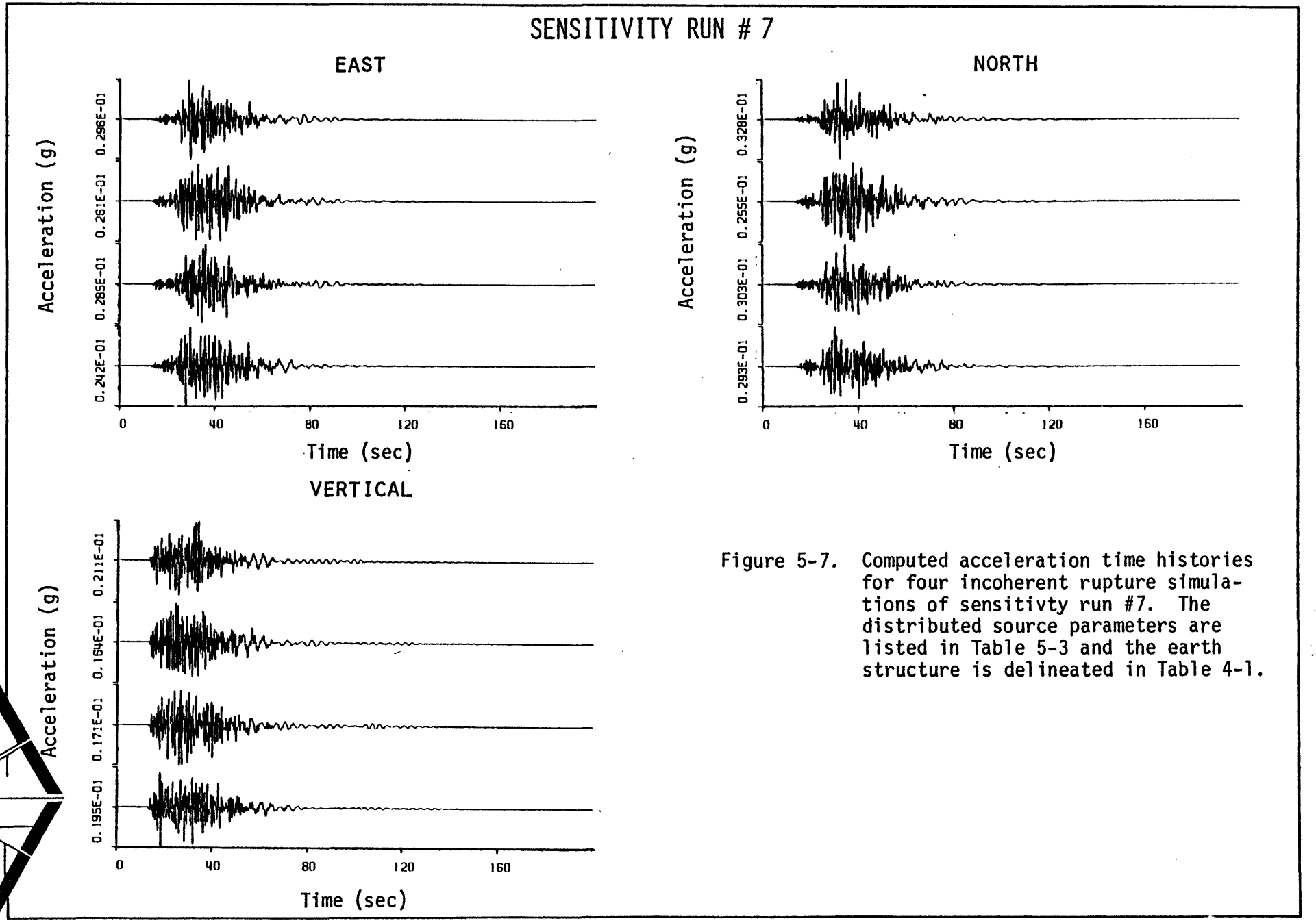

Figure 5-7. Computed acceleration time histories for four incoherent rupture simulations of sensitivty run #7. The distributed source parameters are listed in Table 5-3 and the earth structure is delineated in Table 4-1.

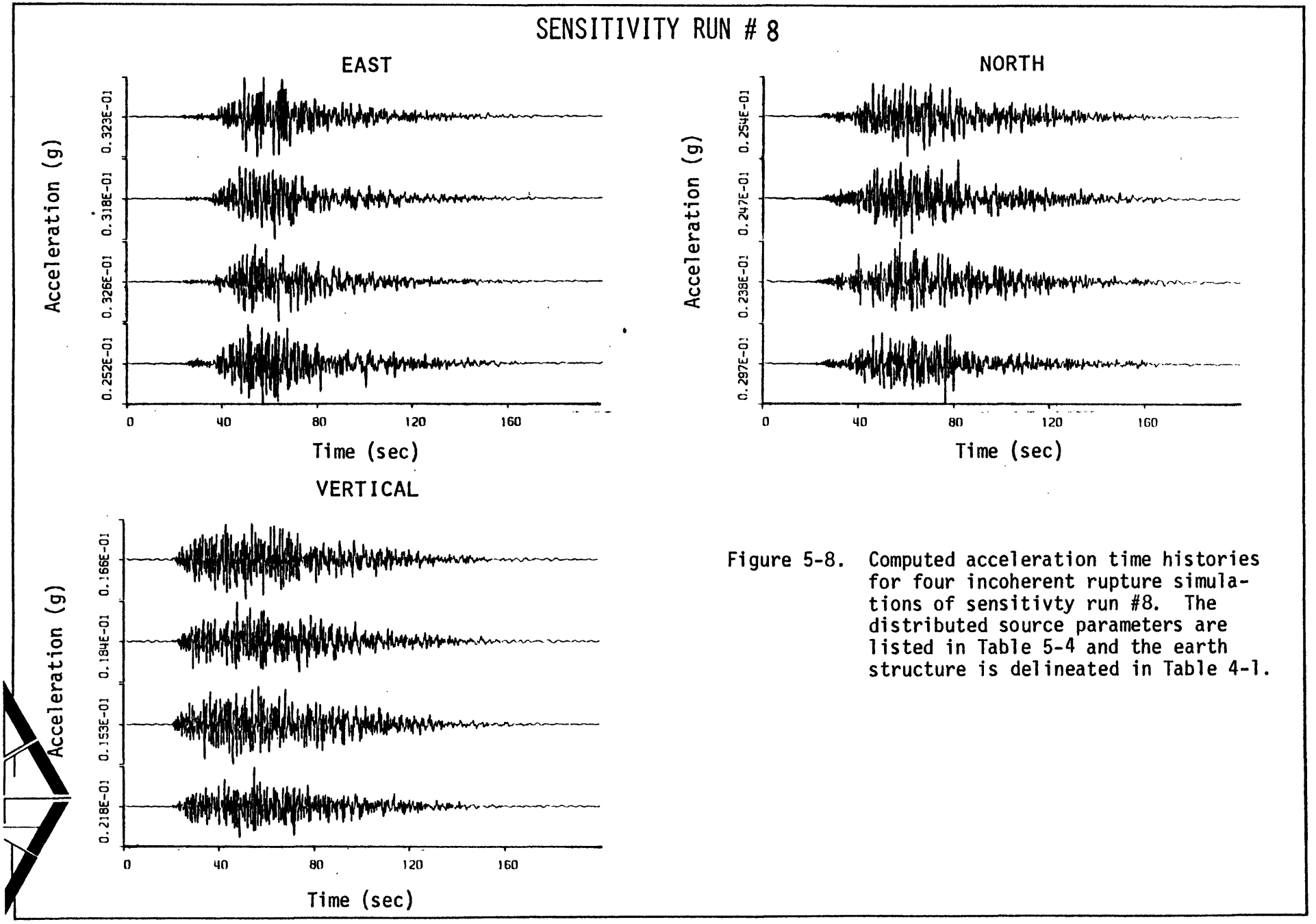

Figure 5-8. Computed acceleration time histories for four incoherent rupture simulations of sensitivty run #8. The distributed source parameters are listed in Table 5-4 and the earth structure is delineated in Table 4-1.

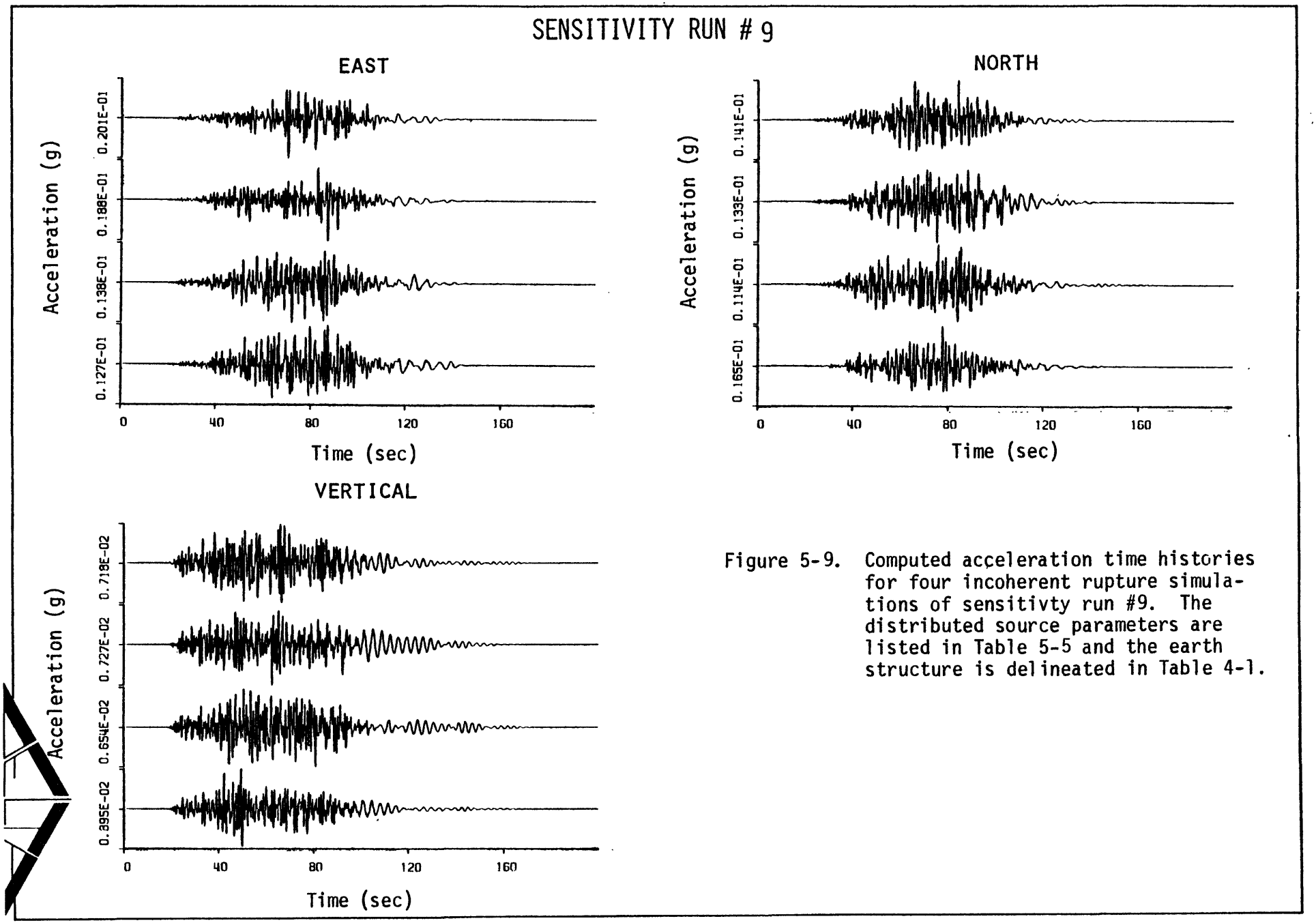

Figure 5-9. Computed acceleration time histories for four incoherent rupture simulations of sensitivty run #9. The distributed source parameters are listed in Table 5-5 and the earth structure is delineated in Table 4-1.

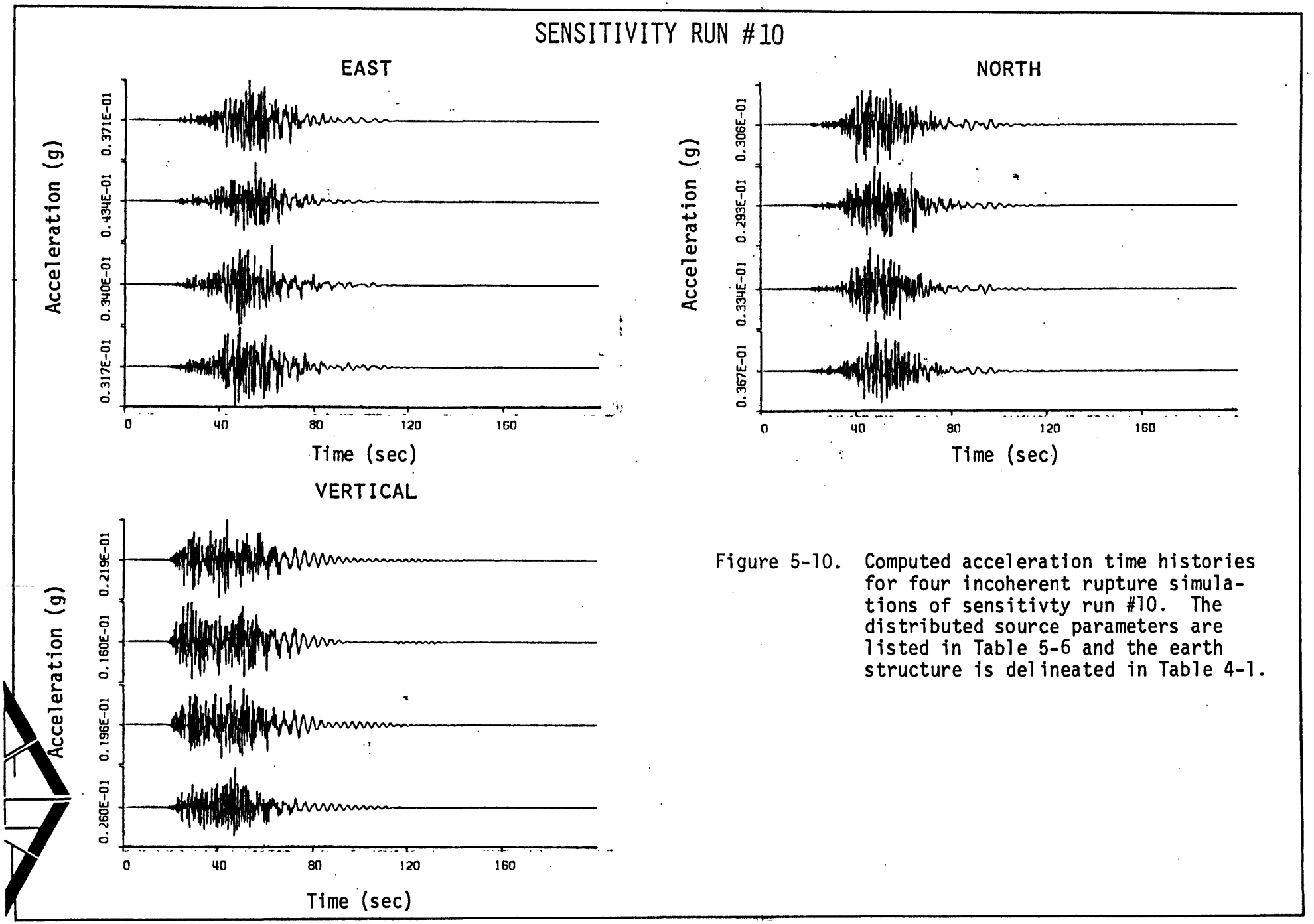

Figure 5-10. Computed acceleration time histories for four incoherent rupture simulations of sensitivty run #10. The distributed source parameters are listed in Table 5-6 and the earth structure is delineated in Table 4-1.

5.1 RUPTURE LENGTH

The sensitivity calculations in this section are used to ascertain the influences of rupture length on the computed ground motions at downtown Los Angeles. The ground motions from unilateral strike-slip earthquakes along the San Andreas Fault are compared for four different rupture lengths. The distributed source parameters for these four sensitivity calculations are listed in Table 5-1. The four different rupture lengths of 100, 175, 250 and 50 km correspond to earthquake magnitudes of approximately 7.5, 7.8, 8.0 and 7.2, respectively. The location of the epicenter varies between sensitivity calculations: for rupture lengths of 100 and 50 km (run numbers 1 and 4), the epicenter is positioned at the bend near Cajon Pass; for rupture lengths of 175 and 250 km (run numbers 2 and 3), the epicenter is positioned at a point near San Gorgonio (refer to Figure 4-3 for these locations along the San Andreas Fault).

The acceleration time histories computed for four incoherent rupture simulations of each of these four sensitivity calculations are shown in Figures 5-1 through 5-4, respectively. These calculated ground motions resemble recorded motions remarkably well. The duration of ground shaking increases as the rupture length increases. For example, a total duration of about 100 seconds is observed for the 100 km-long rupture used in Figure 5-1 while a total duration of about 140 seconds is observed for the 250 km-long rupture used in Figure 5-3. The duration of high-frequency shaking varies from 35, 50, 75 to 100 seconds as the rupture length varies from 50, 100, 175 to 250 km. The longer-period surface-waves trail behind the higher-frequency body-wave arrivals and exhibit characteristics of the Los Angeles basin earth structure. For the 250-km-long rupture in Figure 5-3, the body-wave duration is so long that the high frequency shaking is superimposed atop the surface waves. Another characteristic common to actual recordings is the larger amplitude of early arriving compressional waves in the vertical components relative to the horizontal components. Zero time corresponds to the time of rupture initiation at the hypocenter which accounts for the later first arrivals in Figures 5-2 and 5-3 due to the greater epicentral distance to downtown Los Angeles relative to the epicentral distances used in Figures 5-1 and 5-4.

The 2% damped pseudo-velocity response spectra associated with using these acceleration-time histories as forcing functions to a one-degree-of-freedom damped oscillator system are shown in Figures 5-11, 5-12 and 5-13 for the horizontal EAST, horizontal NORTH and vertical components, respectively. Also shown in each figure is a summary of the peak accelerations, velocity and displacement values for the four sensitivity calculations. The response spectral values at each period as well as the peak values correspond to the mean values of the four random rupture simulations for each sensitivity calculation.

The lower-frequency mean velocity and displacement peaks for the horizontal NORTH component in Figure 5-12 increase as the rupture length is increased (compare sensitivity calculations #4, 1, 2, 3 for the lengths of 50, 100, 175 and 250 km, respectively); the response spectral values at longer periods behave similarly. The low-frequency constituents for the other horizontal component and the vertical component are not as sensitive at long periods to the rupture length. Whereas the response spectral values are strongly influenced by the time domain peaks which tend to saturate with increased rupture length, the low-frequency Fourier spectral values (not shown) do, in fact, increase with rupture length due to the increased duration of ground shaking.

The peak acceleration values and corresponding low-period response spectra values appear to saturate (at this distance of 56 km from the fault) with increasing magnitude for magnitudes greater than 7.2, which is approximately the magnitude of the 50-km rupture in sensitivity calculation #4. However, some explanation is needed to guard against misinterpretation of these results, since these high-frequency constituents are strong functions of the Nyquist frequency and the material quality factors used in the calculations. The Nyquist frequency was constrained to 5 Hz in the calculations and although the most reliable estimates were used for the material quality factors, uncertainties do exist in these values that represent the material attenuation in the Los Angeles basin. Nevertheless, the concept of high-frequency saturation is intuitively satisfying. The probability of experiencing large ground accelerations is a function of the distance from the rupture zone as well as the likelihood of having the rupture focus energy at the receiver.

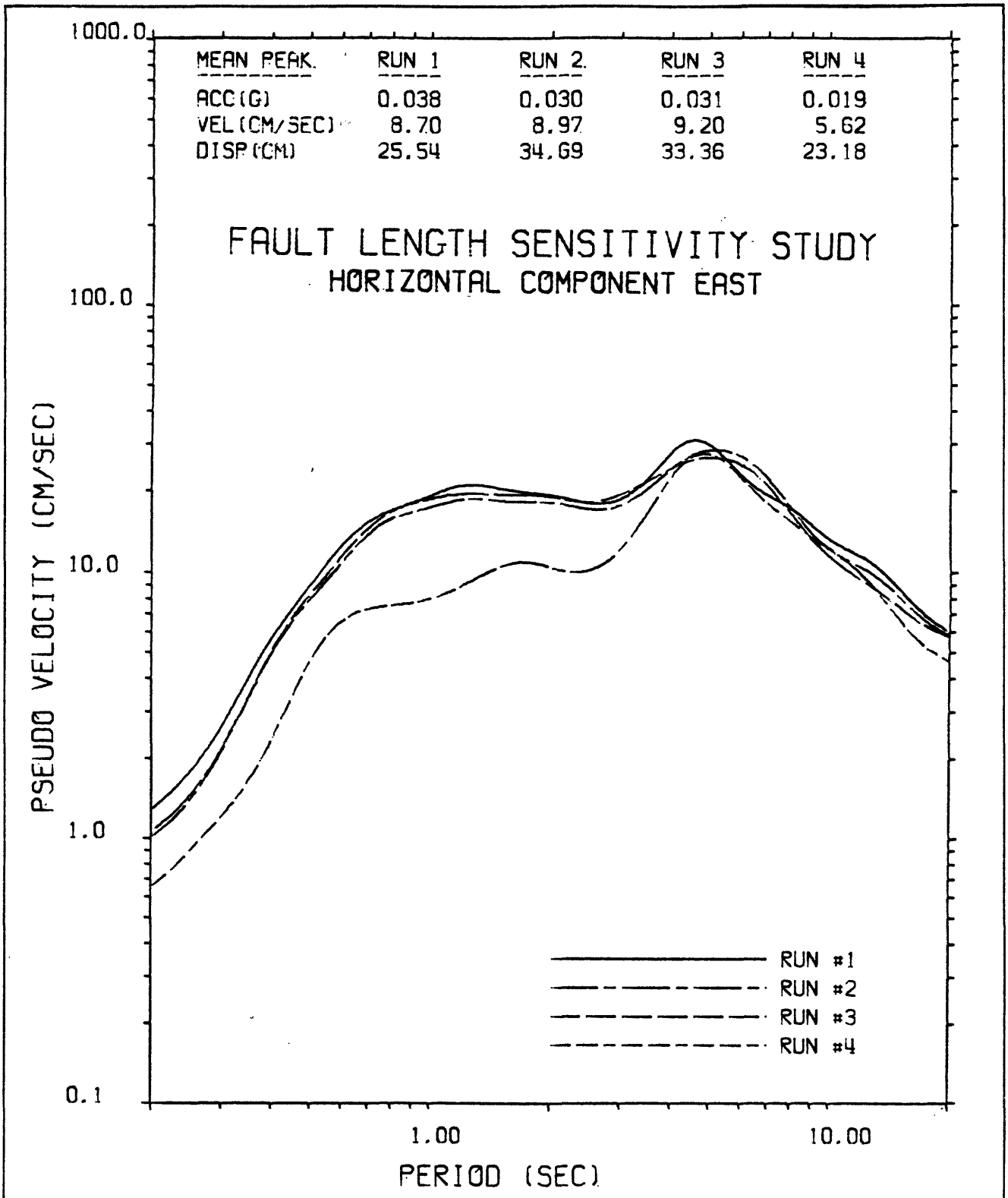

Figure 5-11. Effect of rupture length on the horizontal component EAST of ground motion at downtown Los Angeles. The distributed source parameters are listed in Table 5-1 for each sensitivity run. The pseudo-velocity 2% damped response spectral values at each period as well as the peak time domain values represent the mean values of four incoherent rupture simulations. Response spectral values are somewhat smoothed.

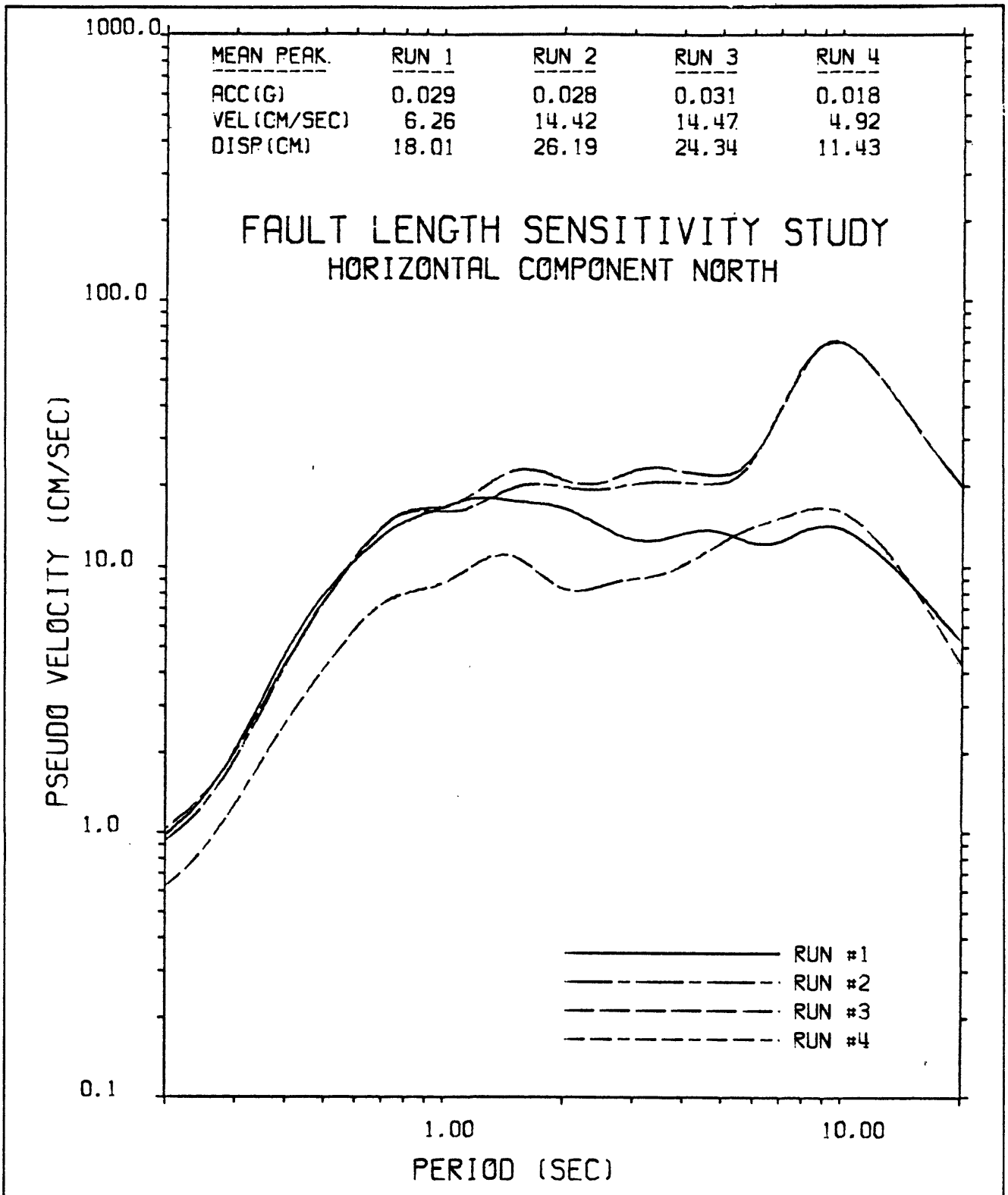

Figure 5-12. Effect of rupture length on the horizontal component NORTH of ground motion at downtown Los Angeles. The distributed source parameters are listed in Table 5-1 for each sensitivity run. The pseudo-velocity 2% damped response spectral values at each period as well as the peak time domain values represent the mean values of four incoherent rupture simulations. Response spectral values are somewhat smoothed.

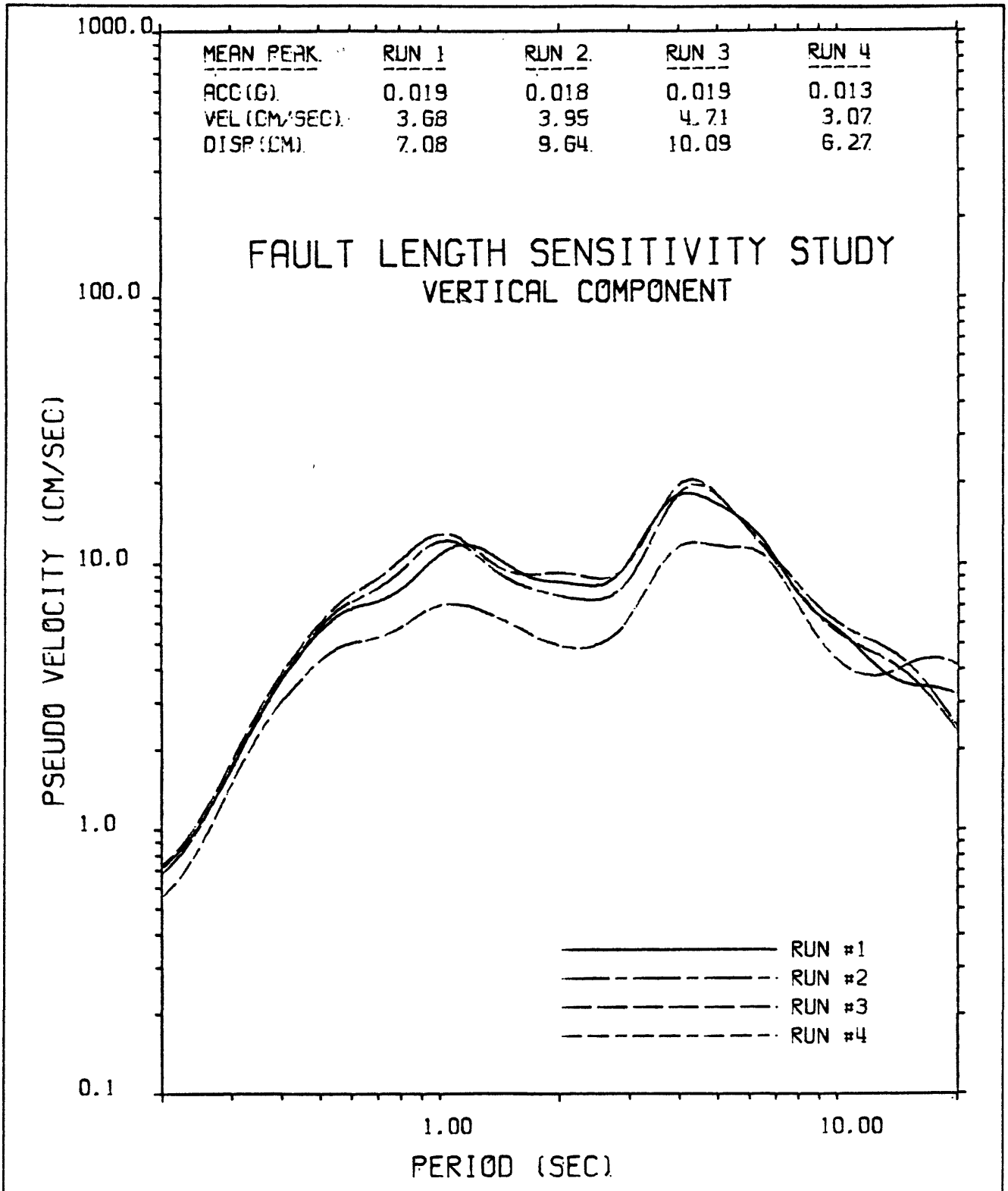

Figure 5-13. Effect of rupture length on the vertical component of ground motion at downtown Los Angeles. The distributed source parameters are listed in Table 5-1 for each sensitivity run. The pseudo-velocity 2% damped response spectral values at each period as well as the peak time domain values represent the mean values of four incoherent rupture simulations. Response spectral values are somewhat smoothed.

Therefore, once an earthquake has ruptured a sufficient distance along the closest zone of possible focussing, any further rupture merely produces ground accelerations within a given probability of exceedance. Any variation in peak ground acceleration once the rupture has reached its high-frequency saturation length are explained in terms of the incoherence of the incipient rupture. Even this latter phenomena explaining the variations in peak values is reproduced by the calculated time histories. For example, the relatively anomalous mean peak values of 0.038 g for the EAST component in the sensitivity calculation #1 is due to the isolated spike of 0.058 g in the fourth incoherent rupture simulation of this sensitivity calculation as shown in Figure 5-1.

5.2 FAULT TYPE

The sensitivity calculations in this section are used to ascertain the influences of fault type on the computed ground motions at downtown Los Angeles. The ground motions from a magnitude 7.5 unilateral strike-slip earthquake along the San Andreas Fault (between Cajon Pass and Palmdale) are compared to the ground motions for the same earthquake but with 45 degree oblique motions (i.e., equal contributions of strike-slip and vertical dip-slip motion). The distributed source parameters for these two sensitivity calculations (numbers 1 and 5) are listed in Table 5-2.

The acceleration time histories computed for four incoherent rupture simulations of each of these two sensitivity calculations are shown in Figures 5-1 and 5-5, respectively. The accelerograms in Figure 5-5 are similar to those in Figure 5-1, which were described in Section 5.1.

The comparisons of the 2% damped pseudo-velocity response spectra associated with these acceleration-time histories are shown in Figures 5-14, 5-15 and 5-16 in the same format as the response spectral comparisons in Section 5.1. Again, the response spectral values at each period represent the mean values of the four random rupture simulations as do the peak acceleration, velocity and displacement values at the top of each figure. The average of the two horizontal components is basically unaltered at all frequencies considered when using 45 degree oblique motion instead of pure strike-slip motion (e.g., average horizontal peak acceleration is 0.0335 g in both cases). The vertical components, however, are increased by up to 20 percent at high frequency and more substantially at lower frequencies as shown in Figure 5-16.

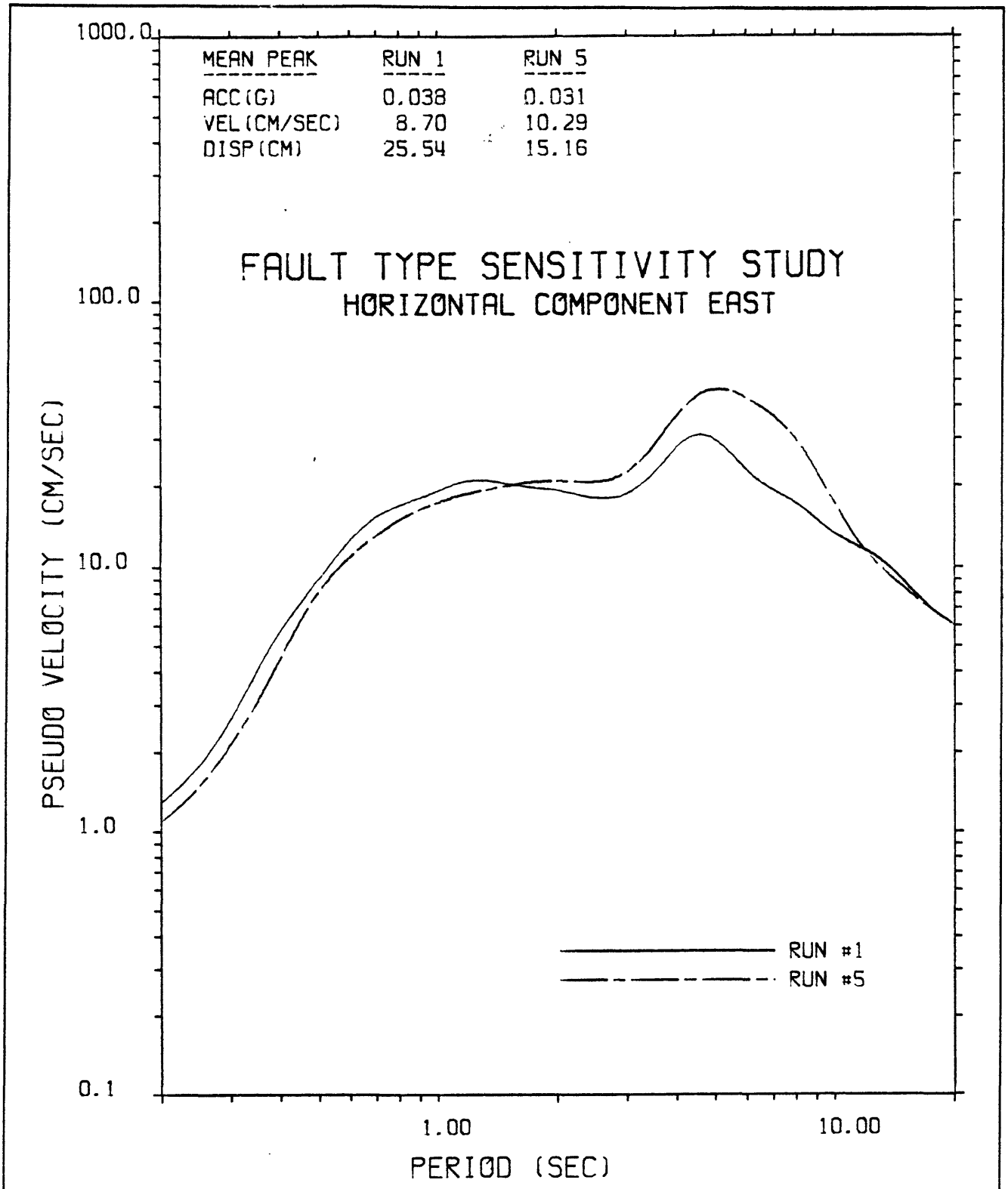

Figure 5-14. Effect of fault type on the horizontal component EAST of ground motion at downtown Los Angeles. The distributed source parameters are listed in Table 5-2 for each sensitivity run. The pseudo-velocity 2% damped response spectral values at each period as well as the peak time domain values represent the mean values of four incoherent rupture simulations. Response spectral values are somewhat smoothed.

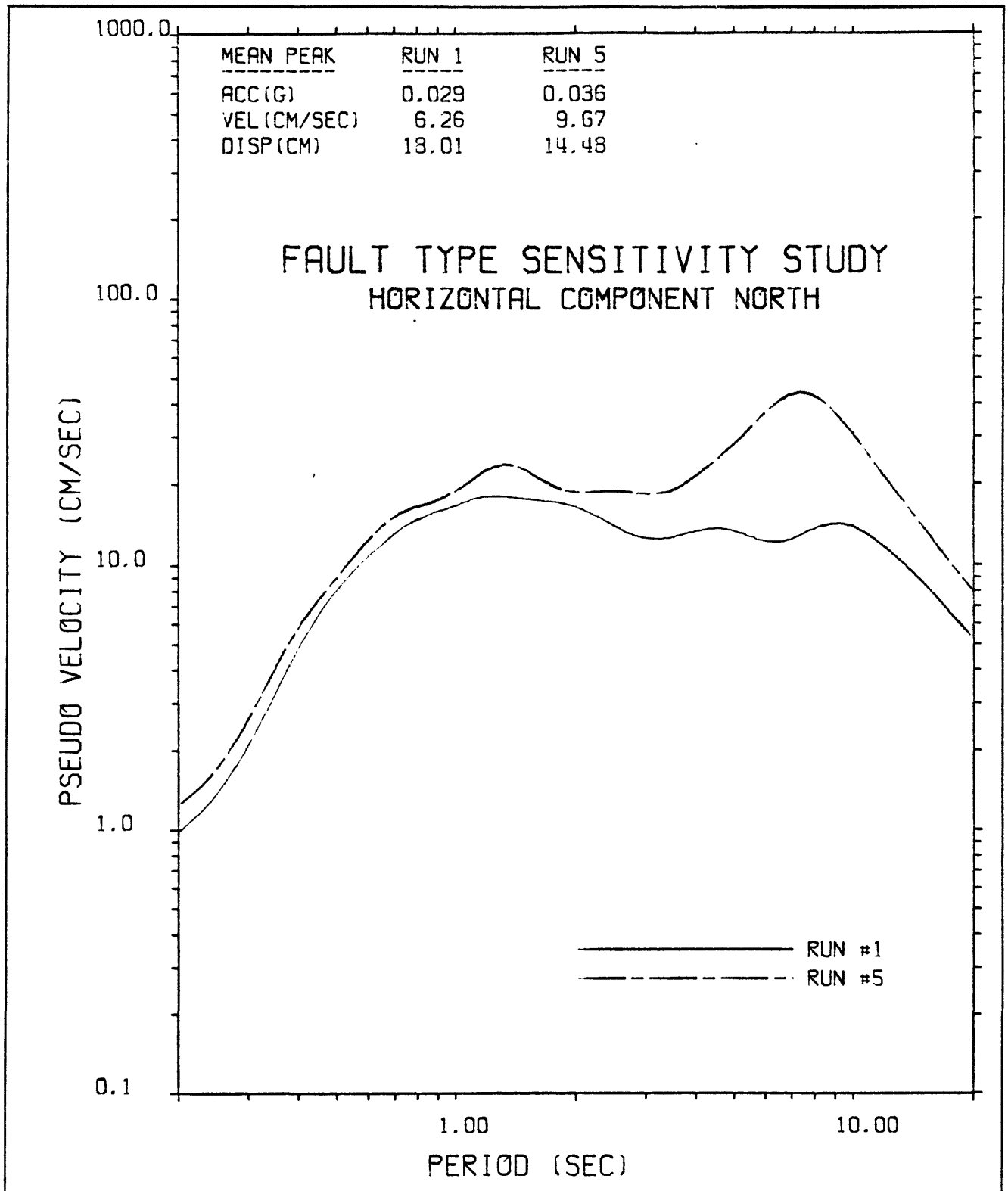

Figure 5-15. Effect of fault type on the horizontal component NORTH of ground motion at downtown Los Angeles. The distributed source parameters are listed in Table 5-2 for each sensitivity run. The pseudo-velocity 2% damped response spectral values at each period as well as the peak time domain values represent the mean values of four incoherent rupture simulations. Response spectral values are somewhat smoothed.

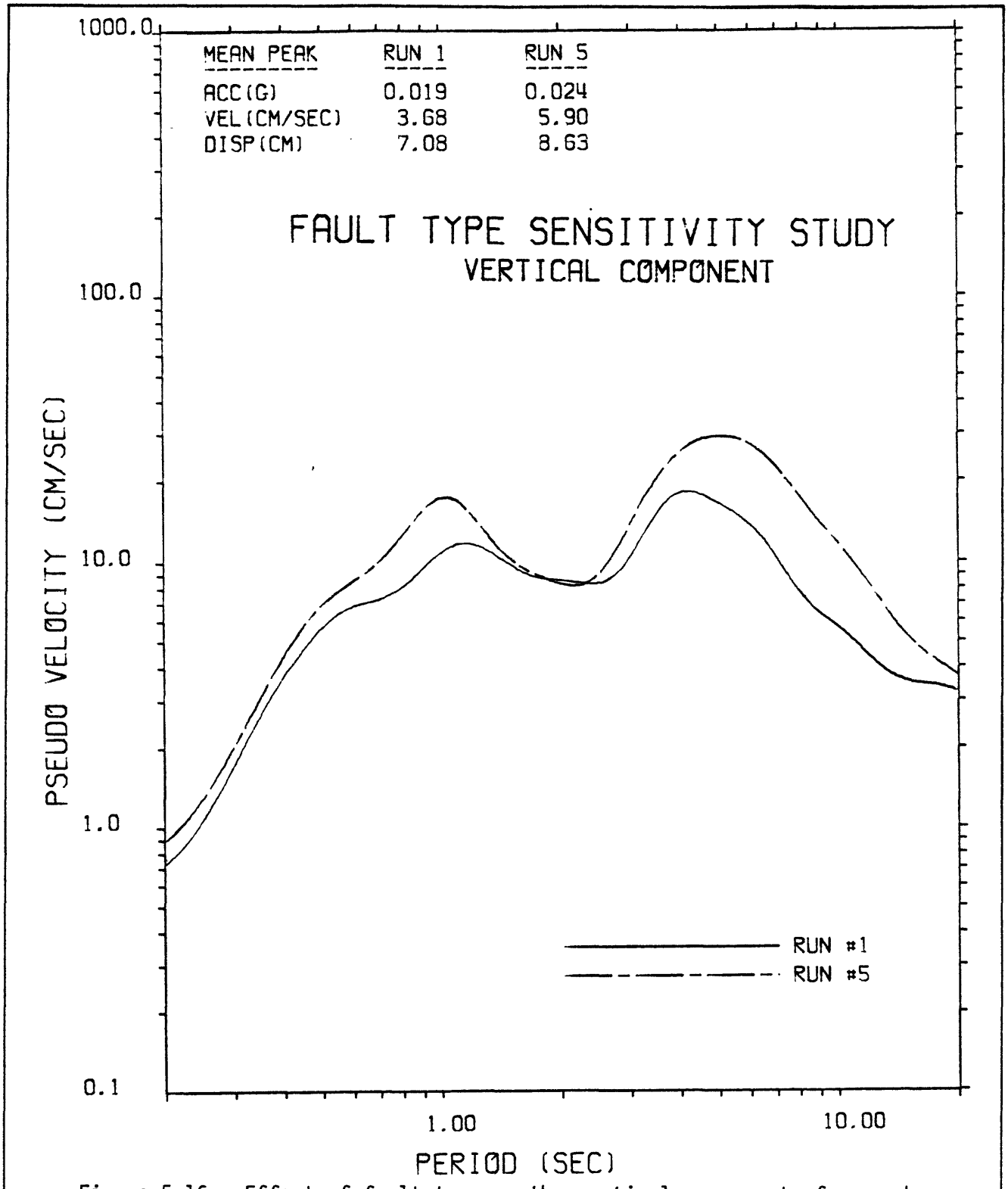

Figure 5-16. Effect of fault type on the vertical component of ground motion at downtown Los Angeles. The distributed source parameters are listed in Table 5-2 for each sensitivity run. The pseudo-velocity 2% damped response spectral values at each period as well as the peak time domain values represent the mean values of four incoherent rupture simulations. Response spectral values are somewhat smoothed.

5.3 RUPTURE DIRECTION

The sensitivity calculations in this section are used to ascertain the influences of rupture direction on the computed ground motions at downtown Los Angeles. The sensitivity to rupture direction is considered separately for earthquakes of different magnitudes. In the first sensitivity study, the ground motions from a magnitude 7.5 strike-slip earthquake along the San Andreas (between Cajon Pass and Palmdale) are compared for three different rupture directions (viz., unilateral rupture from southeast to northwest; unilateral rupture from northwest to southeast; and bilateral rupture in both directions from the midpoint). The distributed source parameters for these three sensitivity calculations (numbers 1, 6 and 7) are listed in Table 5-3.

The acceleration time histories computed for four incoherent rupture simulations of each of these three sensitivity calculations are shown in Figures 5-1, 5-6 and 5-7, respectively. The differences in first arrival times are associated with the different hypocentral distances of 96, 61 and 63 km for the three figures, respectively. The duration of the ground motion from the bilateral rupture in Figure 5-7 is similar to the duration for the 50-km-long rupture in Figure 5-4. The importance of the surface-waves relative to the body-waves is reduced in Figures 5-6 and 5-7 compared to Figure 5-1 and is probably associated with the smaller hypocentral distances.

The comparisons of the 2% damped pseudo-velocity response spectra associated with these acceleration time histories are shown in Figures 5-17, 5-18 and 5-19 in the same format as the response spectral comparisons in the previous two sections. Again, the response spectral values at each period represent the mean values of the four random rupture simulations as do the peak acceleration, velocity and displacement values at the top of each figure. Most of the rupture in sensitivity calculation #6 is focussed away from downtown Los Angeles, whereas, just the opposite is true for the orientation of the rupture in sensitivity calculation #1. This explains the lower amplitude of ground shaking for the northwest to southwest rupture direction for all three components at most

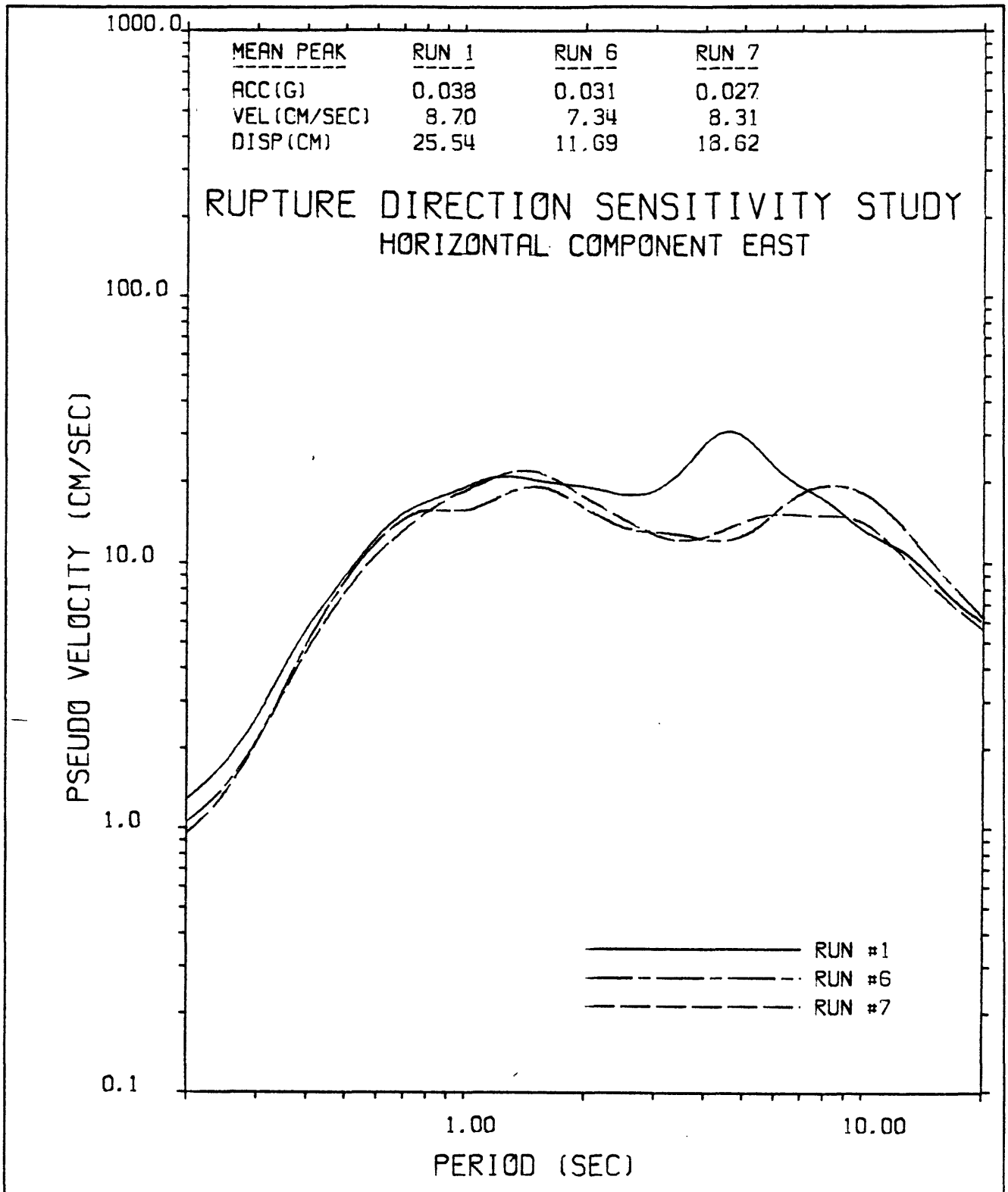

Figure 5-17. Effect of rupture direction on the horizontal component EAST of ground motion at downtown Los Angeles. The distributed source parameters are listed in Table 5-3 for each sensitivity run. The pseudo-velocity 2% damped response spectral values at each period as well as the peak time domain values represent the mean values of four incoherent rupture simulations. Response spectral values are somewhat smoothed.

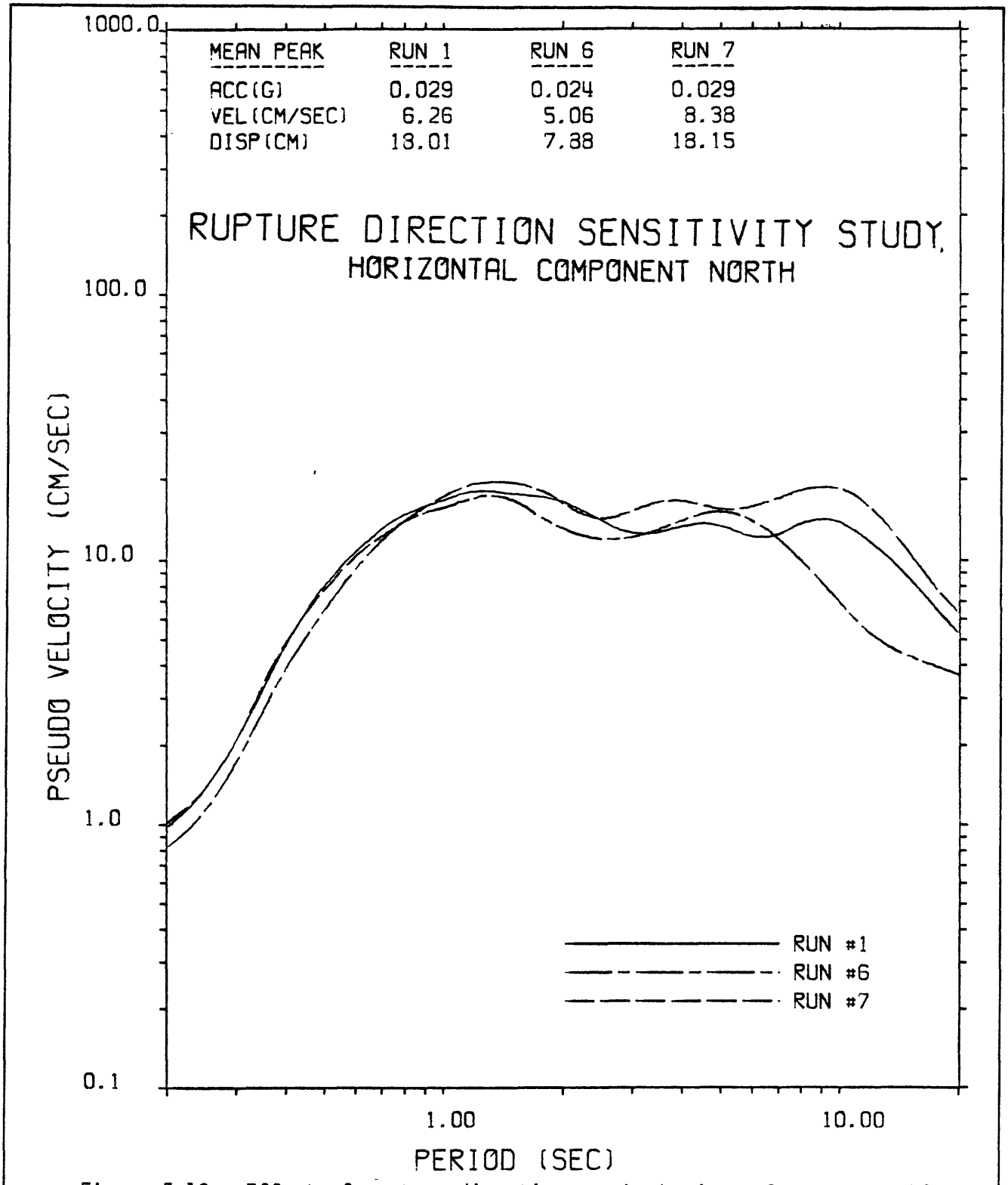

Figure 5-18. Effect of rupture direction on the horizontal component NORTH of ground motion at downtown Los Angeles. The distributed source parameters are listed in Table 5-3 for each sensitivity run. The pseudo-velocity 2% damped response spectral values at each period as well as the peak time domain values represent the mean values of four incoherent rupture simulations. Response spectral values are somewhat smoothed.

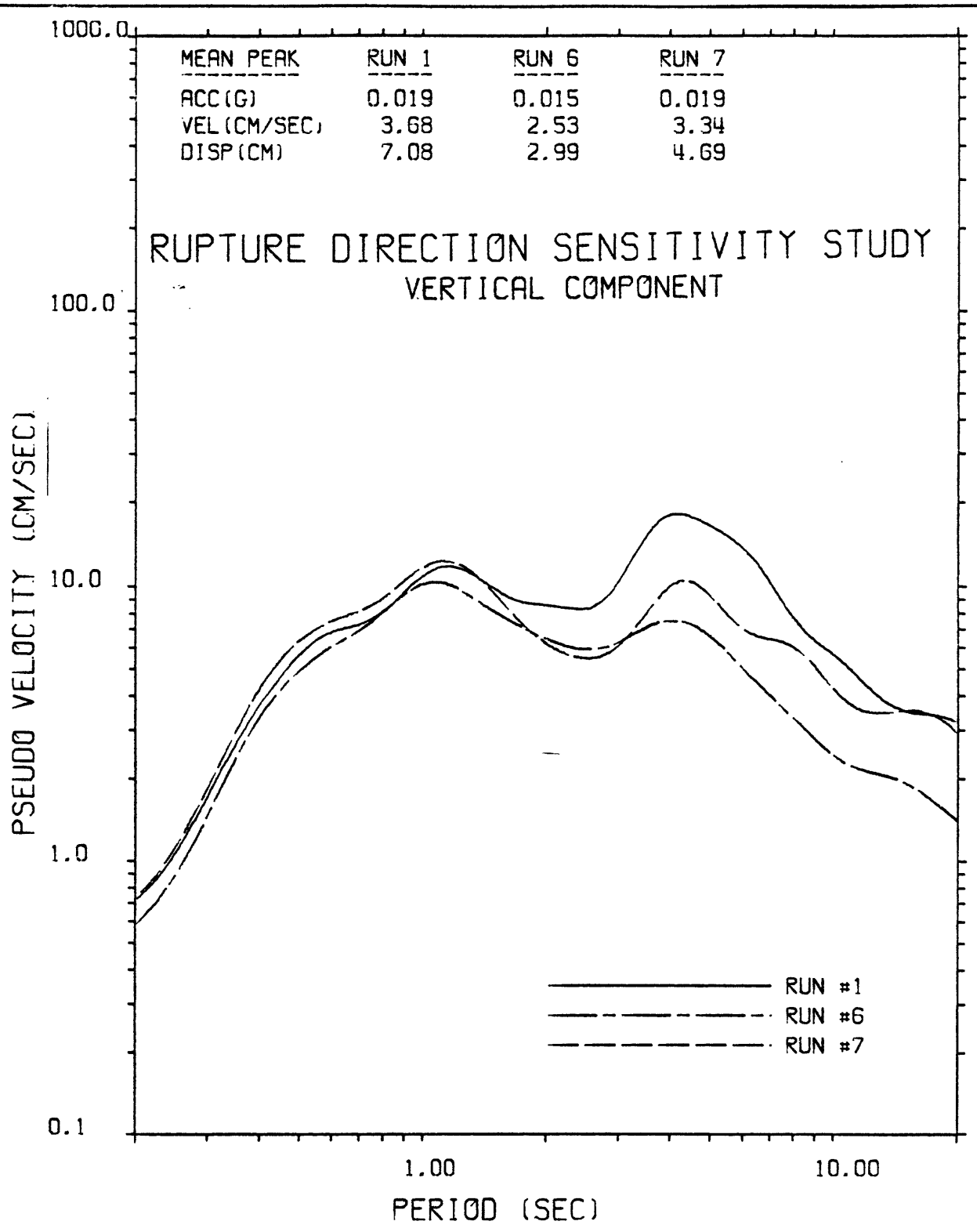

Figure 5-19. Effect of rupture direction on the vertical component of ground motion at downtown Los Angeles. The distributed source parameters are listed in Table 5-3 for each sensitivity run. The pseudo-velocity 2% damped response spectral values at each period as well as the peak time domain values represent the mean values of four incoherent rupture simulations. Response spectral values are somewhat smoothed.

frequencies. The same phenomenon but to a lesser degree, is responsible for the smaller reductions observed in the bilateral rupture.

In the second set of sensitivity studies, the ground motions from a magnitude 8.0 unilateral strike-slip earthquake along the San Andreas (between San Gorgonio and Tejon Pass) are compared for two different rupture directions (viz., southeast to northwest and northwest to southeast). The distributed rupture parameters for these two sensitivity calculations (numbers 3 and 8) are listed in Table 5-4. The rupture configuration in sensitivity calculation #8 is similar to the hypothesized configuration for the 1857 Fort Tejon earthquake.

The acceleration time histories computed for four incoherent rupture simulations of each of these two sensitivity calculations are shown in Figures 5-3 and 5-8, respectively. Again, the difference in first arrival times are associated with the different hypocentral distances of 165 and 105 km for the two figures, respectively. The duration is similar for the two rupture directions.

The comparisons of the 2% damped pseudo-velocity response spectra associated with these acceleration time histories are shown in Figures 5-20, 5-21 and 5-22 in the same format as the previous response spectral comparisons. The results are almost identical, which is further support for the high-frequency saturation with magnitude hypothesis of Section 5.1, since downtown Los Angeles received different lengths of similarly focussed rupture from the two rupture formations.

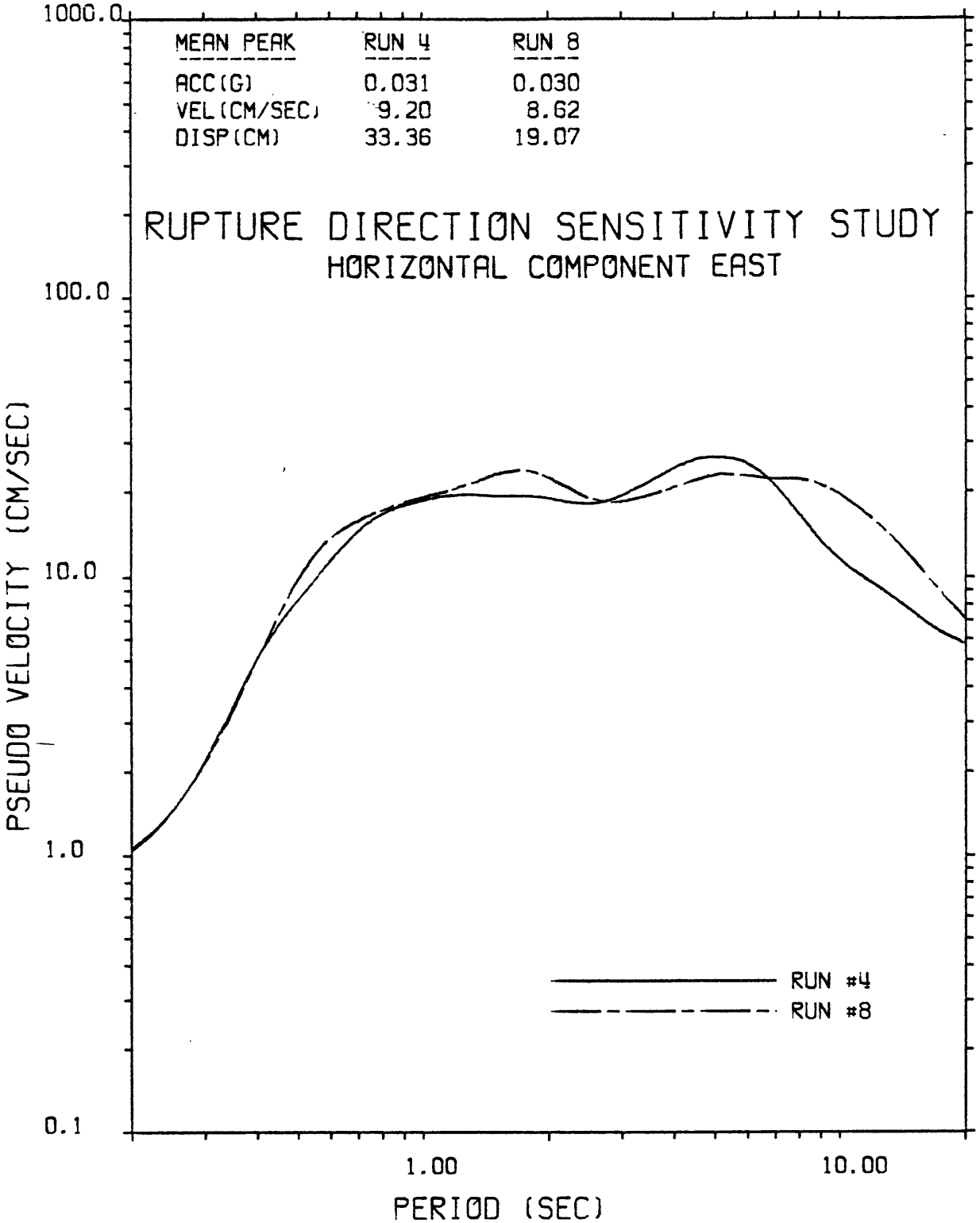

Figure 5-20. Effect of rupture direction on the horizontal component EAST of ground motion at downtown Los Angeles. The distributed source parameters are listed in Table 5-4 for each sensitivity run. The pseudo-velocity 2% damped response spectral values at each period as well as the peak time domain values represent the mean values of four incoherent rupture simulations. Response spectral values are somewhat smoothed.

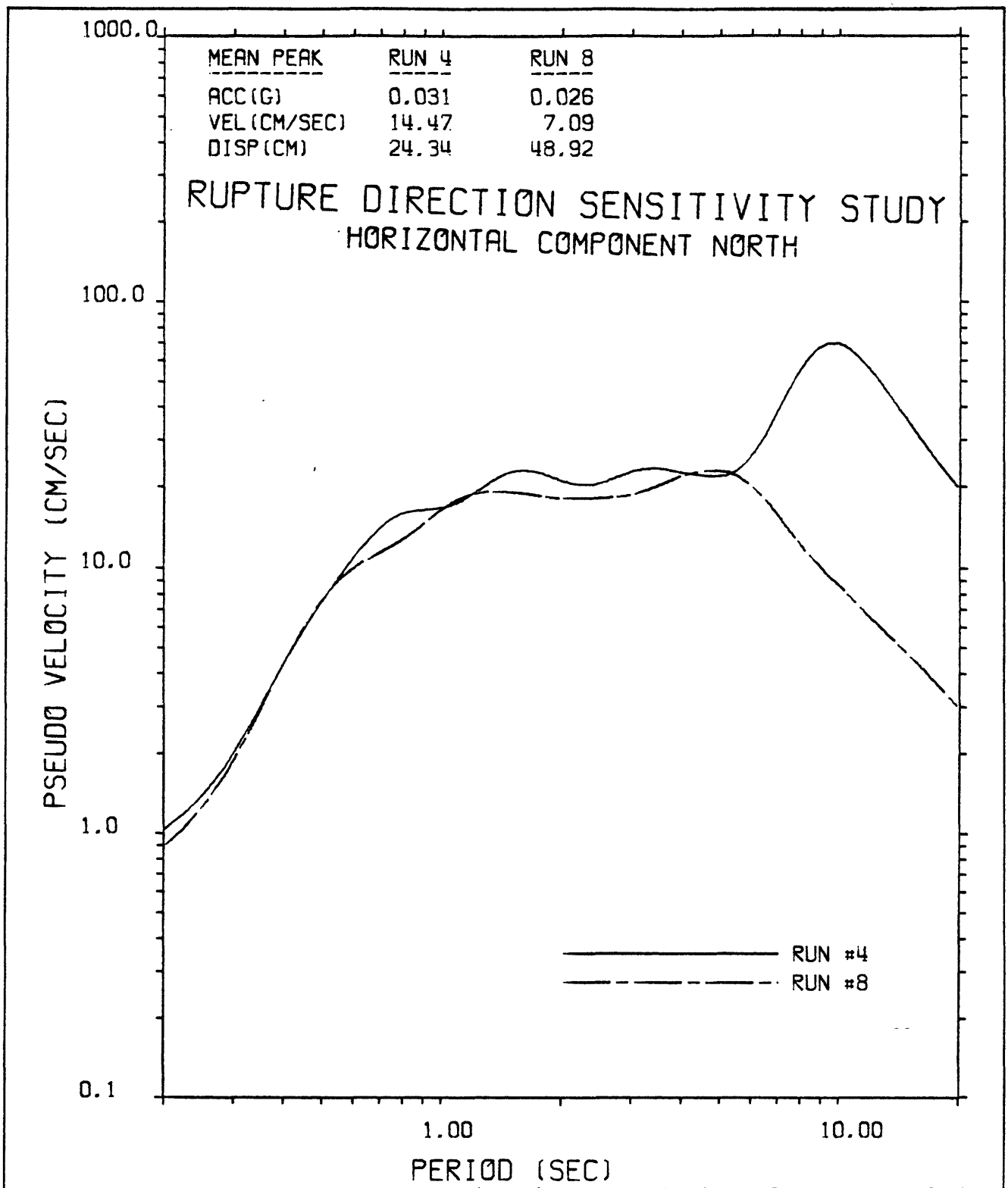

Figure 5-21. Effect of rupture direction on the horizontal component NORTH of ground motion at downtown Los Angeles. The distributed source parameters are listed in Table 5-4 for each sensitivity run. The pseudo-velocity 2% damped response spectral values at each period as well as the peak time domain values represent the mean values of four incoherent rupture simulations. Response spectral values are somewhat smoothed.

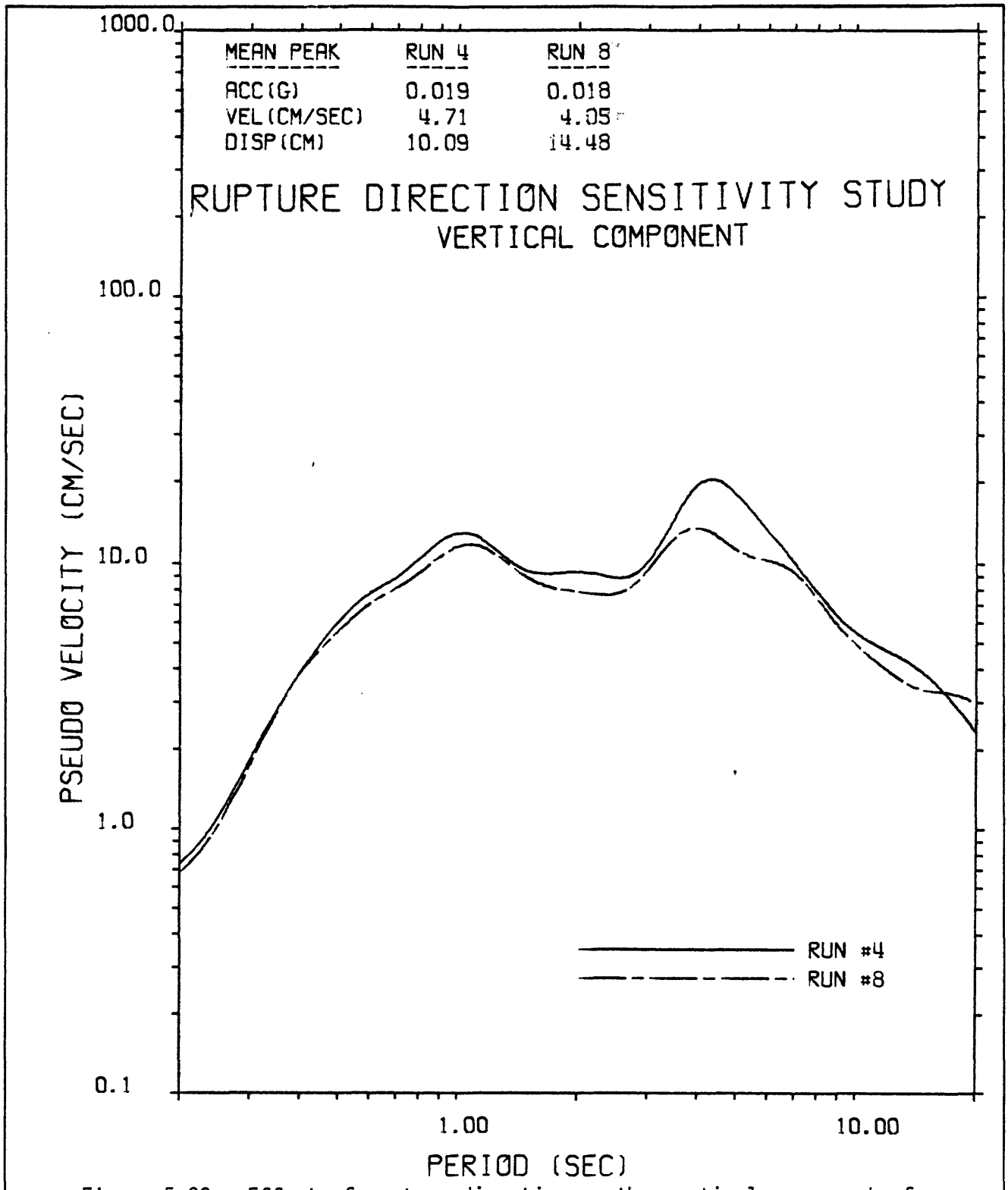

Figure 5-22. Effect of rupture direction on the vertical component of ground motion at downtown Los Angeles. The distributed source parameters are listed in Table 5-3 for each sensitivity run. The pseudo-velocity 2% damped response spectral values at each period as well as the peak time domain values represent the mean values of four incoherent simulations. Response spectral values are somewhat smoothed.

5.4 RUPTURE VELOCITY

The sensitivity calculations in this section are used to ascertain the influences of rupture velocity on the computed ground motions at downtown Los Angeles. The ground motions from a magnitude 7.5 unilateral strike-slip earthquake along the San Andreas Fault (between Bajon Pass and Palmdale) are compared for gross rupture velocities equal to 90 and 50 percent of the shear wave velocity in each subsurface layer. The distributed source parameters for these two sensitivity calculations (numbers 1 and 9) are listed in Table 5-5.

The acceleration time histories computed for four incoherent rupture simulations of each of these two sensitivity calculations are shown in Figures 5-1 and 5-9, respectively. As expected, the duration of ground shaking is much longer in Figure 5-9 since the propagating rupture front takes almost twice as long to travel from the hypocenter to any point on the rupture surface. However, the amplitude of ground shaking is reduced by about a factor of two since the increased spreading reduces the probabaility of constructive interference from adjacent points of rupture (i.e., the effect of focussing is reduced).

The comparisons of the 2% damped pseudo-velocity response spectra associated with these acceleration time histories are shown in Figures 5-23, 5-24 and 5-25 in the same format as the response spectra comparisons in the previous sections. The reduced effect of focussing associated with lowering the rupture velocity to 50 percent of the shear-wave velocity is seen to reduce the response spectral values at all periods for all three components. As shown in a previous work, the reduction is not linear, with less of a uniform trend observed when the rupture velocity is varied between 80 and 95 percent of the shear-wave velocity (DELTA, 1979).

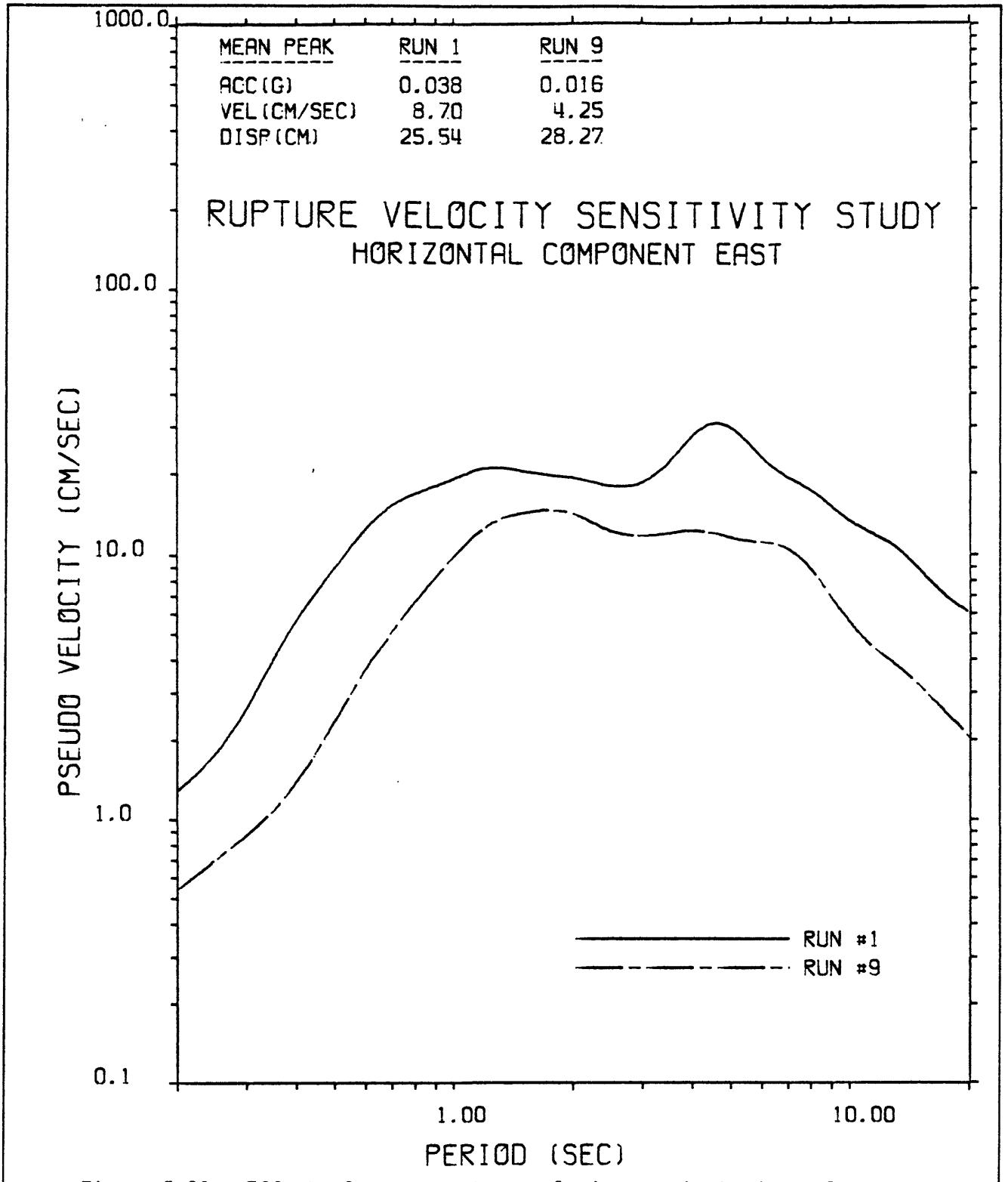

Figure 5-23. Effect of gross rupture velocity on the horizontal component EAST of ground motion at downtown Los Angeles. The distributed source parameters are listed in Table 5-5 for each sensitivity run. The pseudo-velocity 2% damped response spectral values at each period as well as the peak time domain values represent the mean values of four incoherent rupture simulations. Response spectral values are somewhat smoothed.

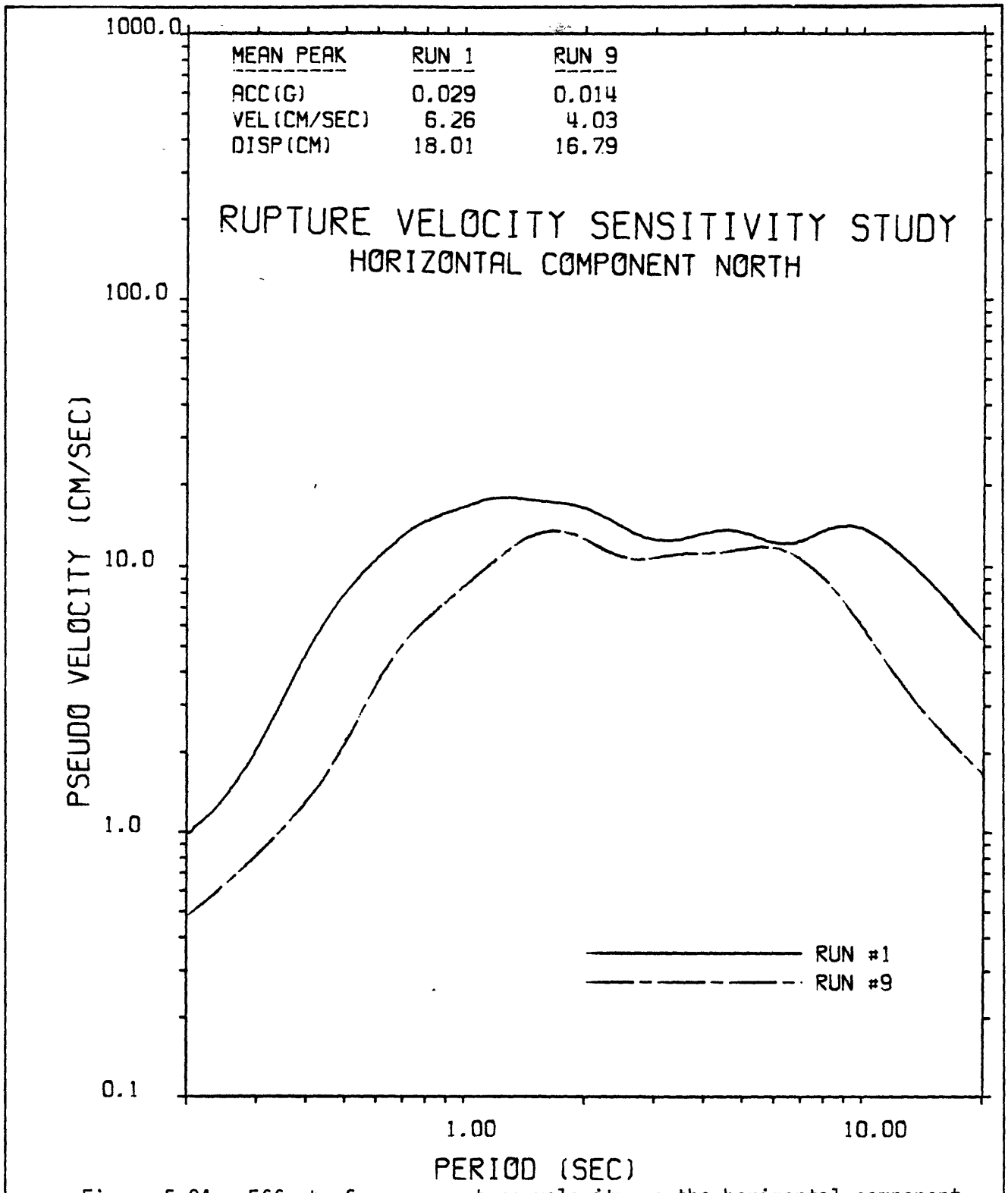

Figure 5-24. Effect of gross rupture velocity on the horizontal component NORTH of ground motion at downtown Los Angeles. The distributed source parameters are listed in Table 5-5 for each sensitivity run. The pseudo-velocity 2% damped response spectral values at each period as well as the peak time domain values represent the mean values of four incoherent rupture simulations. Response spectral values are somewhat smoothed.

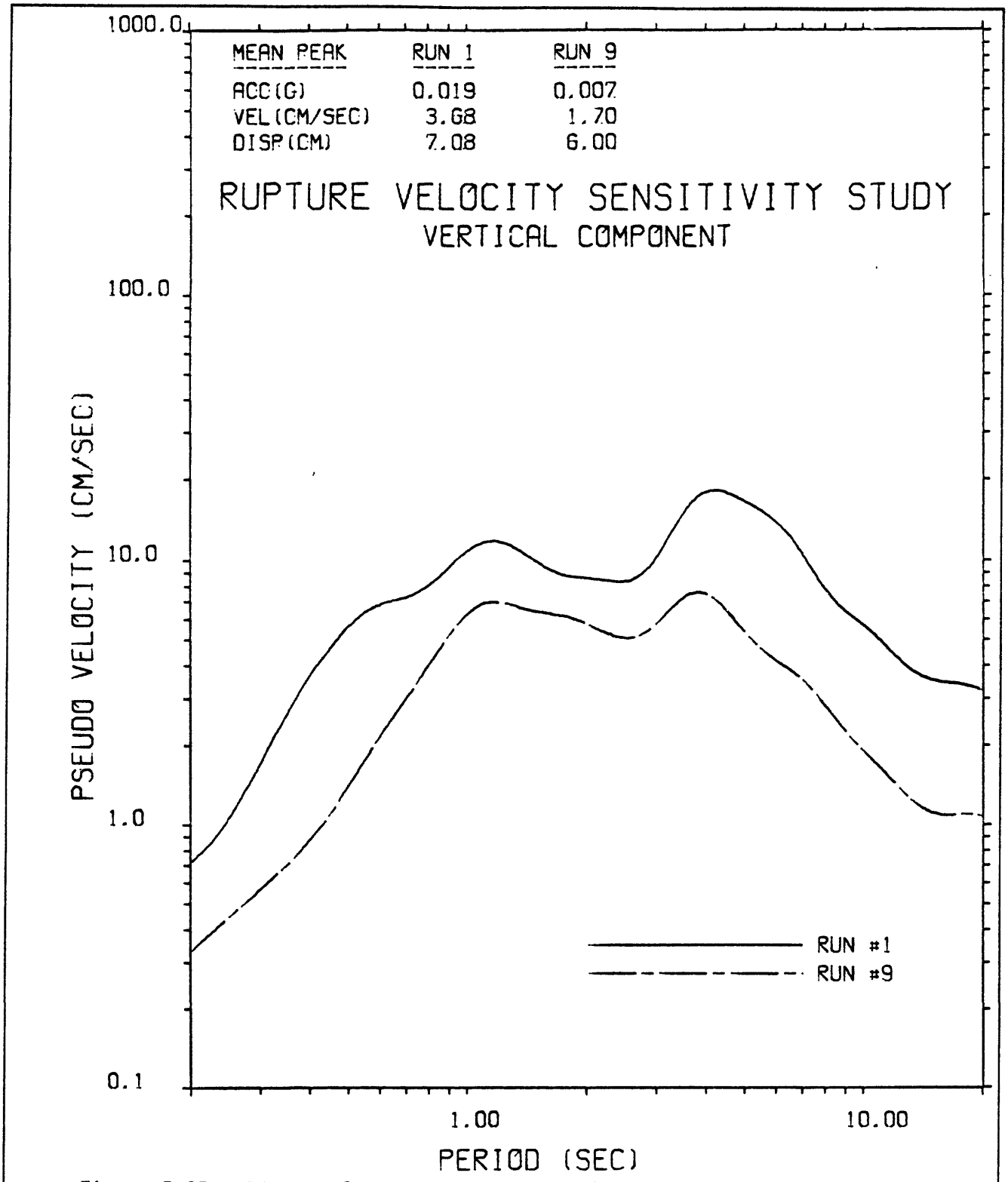

Figure 5-25. Effect of gross rupture velocity on the vertical component of ground motion at downtown Los Angeles. The distributed source parameters are listed in Table 5-5 for each sensitivity run. The pseudo-velocity 2% damped response spectral values at each period as well as the peak time domain values represent the mean values of four incoherent rupture simulations. Response spectral values are somewhat smoothed.

5.5 FAULT BOTTOM

The sensitivity calculations in this section are used to ascertain the influences of fault bottom on the computed ground motions at downtown Los Angeles. The ground motions from unilateral strike-slip earthquakes along the San Andreas Fault (between Cajon Pass and Palmdale) are compared for two different fault bottoms. The two fault bottoms extend to depths of 11.3 and 15 km and correspond to earthquake magnitudes of approximately 7.5 and 7.7, respectively. The rest of the distributed source parameters for these two sensitivity calculations (numbers 1 and 10) are listed in Table 5-6.

The acceleration time histories computed for four incoherent rupture simulations of each of these two sensitivity calculations are shown in Figures 5-1 and 5-10, respectively. The duration of ground shaking is quite similar, especially when considering the accelerograms on the same amplitude scales. The amplitude of ground shaking is about 10 percent higher for the deeper fault bottom. This is due to the increased energy released from the brittle rupture at depth and to the more efficient (i.e., higher quality factors) propagation paths from the deepest extent at 15 km to the surface receiver at downtown Los Angeles.

The comparisons of the 2% damped pseudo-velocity response spectra associated with these acceleration time histories are shown in Figures 5-26, 5-27 and 5-28 in the same format as the response spectral comparisons in the previous sections. A similar increase in the high frequency constituents of about 10 percent is observed for the deeper fault bottom; the higher velocity and displacement values are related to the larger magnitude.

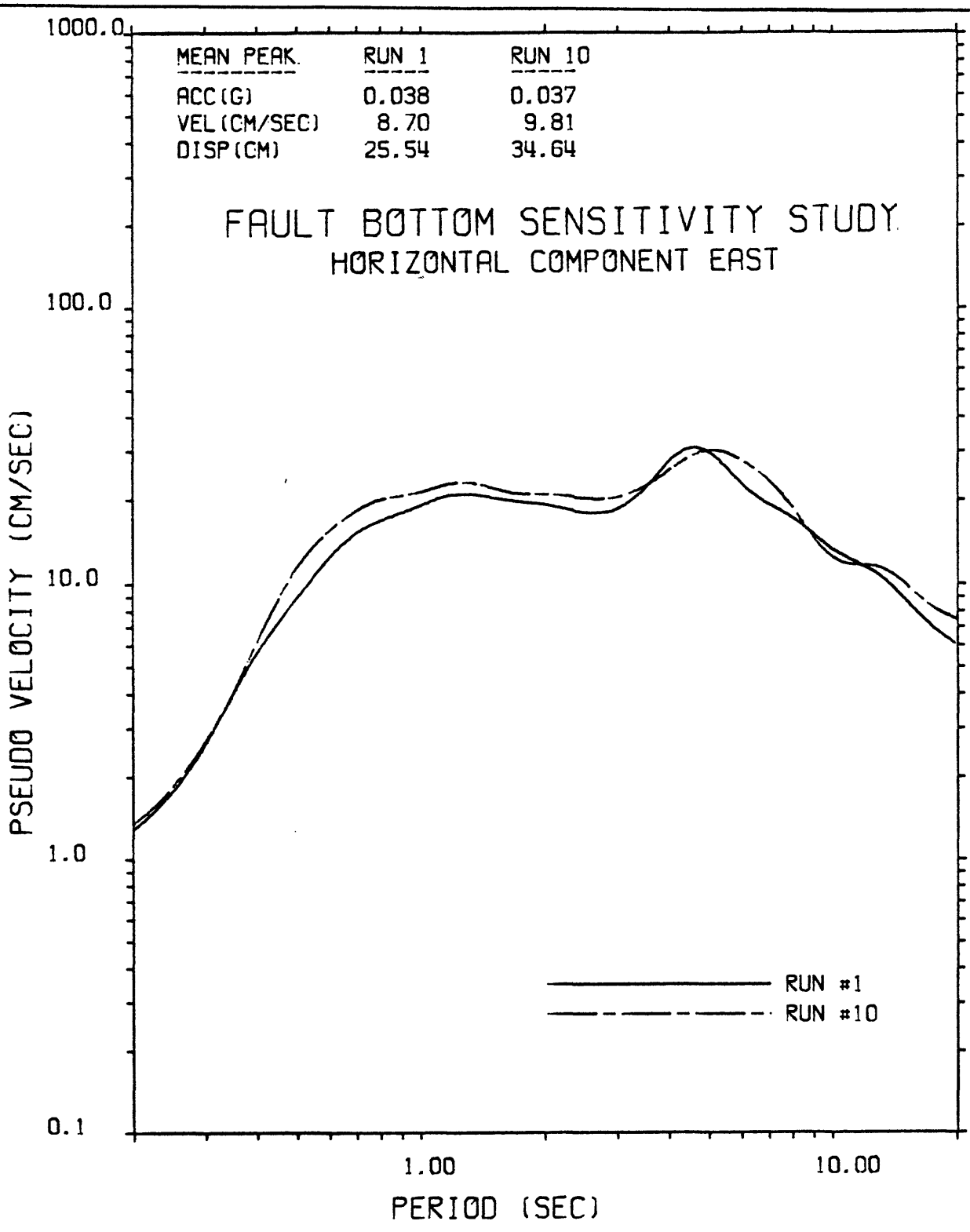

Figure 5-26. Effect of fault bottom velocity on the horizontal component EAST of ground motion at downtown Los Angeles. The distributed source parameters are listed in Table 5-6 for each sensitivity run. The pseudo-velocity 2% damped response spectral values at each period as well as the peak time domain values represent the mean values of four incoherent rupture simulations. Response spectral values are somewhat smoothed.

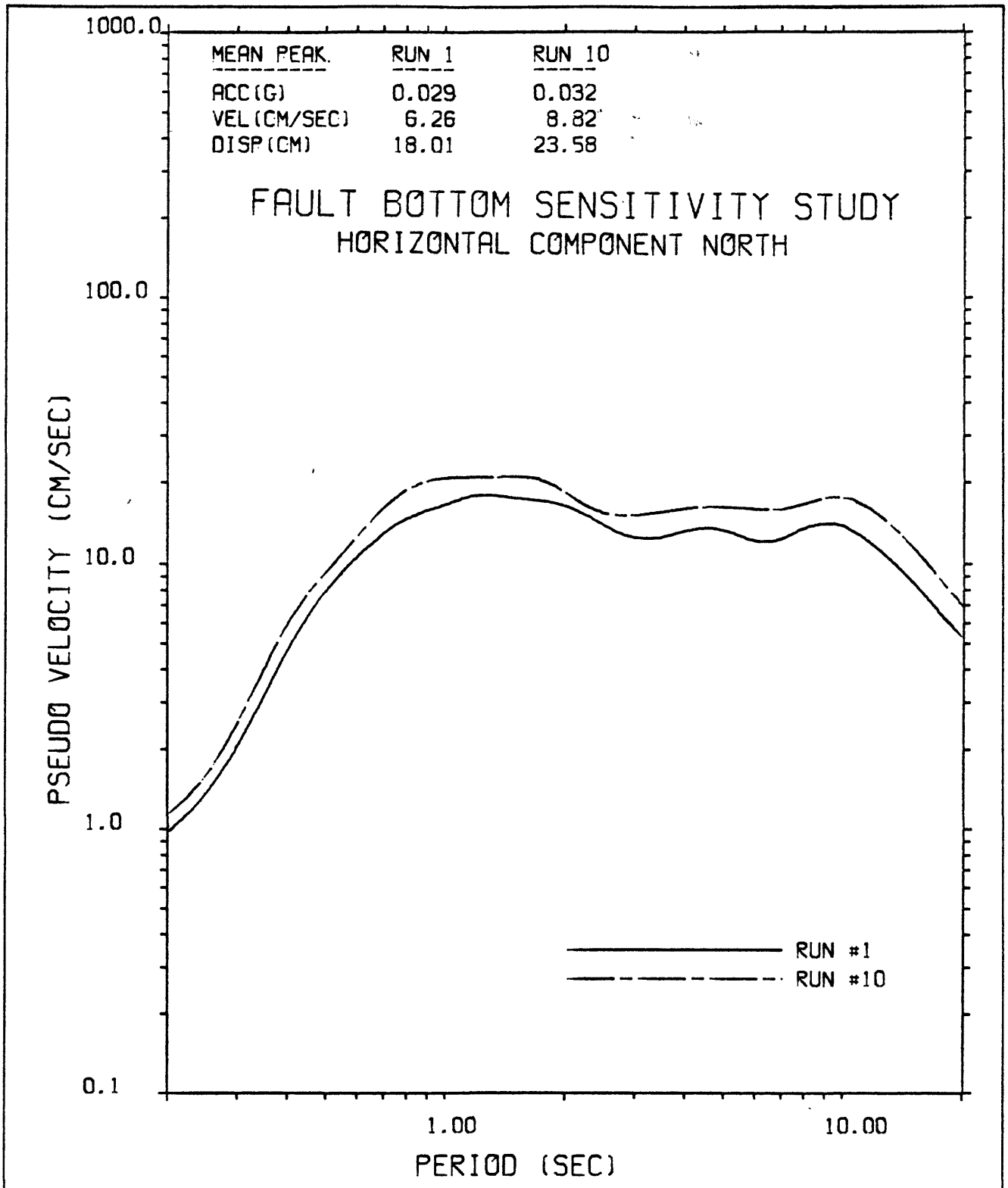

Figure 5-27. Effect of fault bottom velocity on the horizontal component NORTH of ground motion at downtown Los Angeles. The distributed source parameters are listed in Table 5-6 for each sensitivity run. The pseudo-velocity 2% damped response spectral values at each period as well as the peak time domain values represent the mean values of four incoherent rupture simulations. Response spectral values are somewhat smoothed.

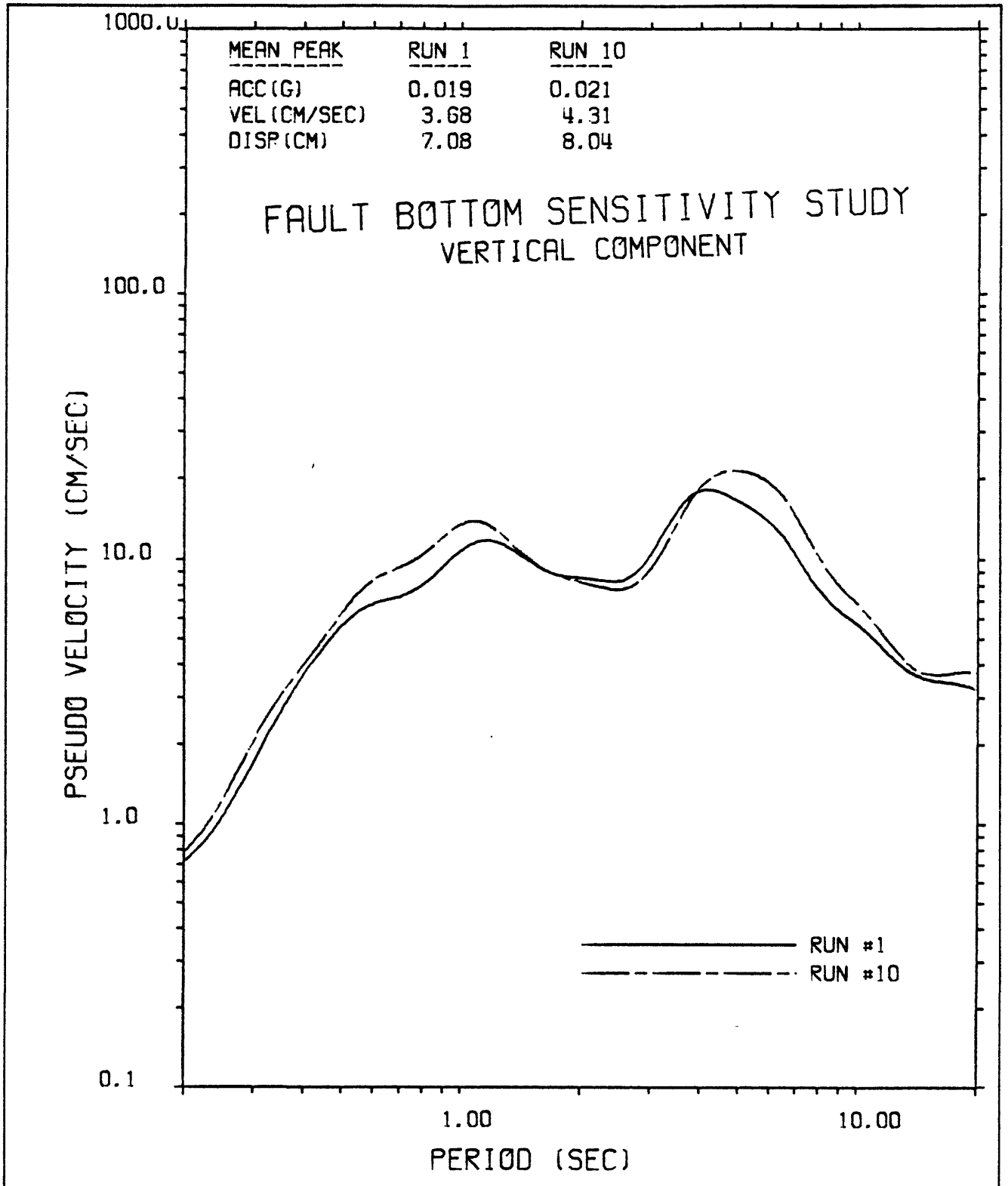

Figure 5-28. Effect of fault bottom velocity on the vertical component of ground motion at downtown Los Angeles. The distributed source parameters are listed in Tabel 5-6 for each sensitivity run. The pseudo-velocity 2% damped response spectral values at each period as well as the peak time domain values represent the mean values of four incoherent rupture simulations. Response spectral values are somewhat smoothed.

CHAPTER 6

SUMMARY AND CONCLUSIONS

The work presented in this report addresses the vulnerability of the Los Angeles basin to potential earthquake hazards from nearby faults. More specifically, this report attempts to predict the intensity and general character of ground motion from the most probable major earthquakes along these faults using sophisticated computer modeling methods. As discussed in Section 1.1, the faults believed to be most capable of supporting a major earthquake involving catastrophic ground shaking in the Los Angeles basin are the San Andreas Fault and the Newport-Inglewood Fault. The overwhelming advantage of using the semi-analytical computer model technique to simulate ground motions from major earthquakes along these faults is associated with the current inability to predict earthquake strong ground motion under specific geologic and tectonic conditions due to the scarcity of reliable strong motion recordings.

The methodology used in the computer modeling procedure is discussed in Section 3.1. Basically, the region of the fault that is postulated to undergo rupture is discretized so that a mathematical characterization of fault slippage may be spatially and temporally convolved with a discrete set of Green's functions. The Green's functions analytically account for the complete characterization of wave propagation over the entire frequency band of interest from every point of rupture to every receiver of interest in a viscoelastic layered representation of the earth. The methodology and validation of the procedure used to obtain these Green's functions is discussed in Sections 2.1 and 2.2, respectively. The model parameters characterizing the rupture configuration and the fault slippage at each point of rupture are included when evaluating the spatial integrals over the rupture surface.

Whereas the earthquake modeling procedure is highly sophisticated, the model parameterization is rather straightforward. Parameters of three types serve to define the earthquake model. The first set of

parameters are those defining the viscoelastic properties of the horizontally layered representation of the subsurface geologic environment. Each layer is characterized by shear and compressional wave velocities, density, layer thickness, and material quality factors for both shear and compressional waves. The second set of parameters are those defining the characterization of fault slippage at each point of rupture, leading to an idealized three-parameter slip function. The three parameters are the maximum (initial) slip velocity, final slip offset and duration of slip at a point. In addition, the rupture velocity must be specified to account for the propagating rupture along the fault surface. The third set of parameters are those defining the rupture extent including the geometry and orientation of the rupture surface with respect to all the receiver stations of interest as well as the hypocentral location. The earthquake modeling procedure has been validated against the most reliable and important strong motion recordings available from past Southern California earthquakes as discussed in Section 3.2. The maximum slip velocity, which is related to the dynamic stress drop, was found to be a constant equal to 800 cm/sec for all earthquakes modeled in the validation studies.

An average geologic structure for the Los Angeles basin is determined as a function of depth in Section 4.1. The compressional-wave velocities and layer thicknesses for the top five layers down to a depth of 15 km are assigned values based on two-way transit time velocity logs taken from oil wells (Teng, 1973). The compressional-wave velocity for the sixth layer down to a depth of 28.4 is determined indirectly from a refraction study by Roller and Healy (1963). The compressional-wave velocities for the remainder of the layers down to a depth of 70 km, as well as the underlying half-space, are assigned values based on travel-time data obtained from both natural and artificial events (Hadley and Kanamori, 1979). The shear-wave velocities in each layer are assigned values based on the Poisson's ratios as a function of depth for the Los Angeles basin (Kovach, 1974). The densities and material quality factors in each layer are assigned values based on generic formulae for Southern California geologic environments (DELTA, 1978, 1980b). Also discussed in Section 4.1 is the calculation of the Green's functions for this earth structure. The Green's

functions are evaluated at 1001 frequencies between 0 and 5 Hz for a mesh of nodes representing horizontal distances between 1 and 200 km and vertical depths between 0 and 15 km.

Finally, in Sections 4.2 and 4.3, the ground motions in the Los Angeles basin are calculated for several possible earthquakes along the San Andreas and Newport-Inglewood Faults, respectively. The results are presented in the form of maps describing values of peak acceleration, velocity and displacement at 22 receivers located throughout the Los Angeles basin. Of those rupture configurations considered along the San Andreas Fault, the largest ground motions overall were obtained for a magnitude approximately 7.5 earthquake (seismic moment of 1.025×10^{27} dyne-cm) rupturing from a locked portion of the fault near Cajon Pass to the Southern California Uplift region near Palmdale. However, the results seem to indicate that most regions of the Los Angeles basin are sufficiently far from this critical rupture to preclude catastrophic ground accelerations. The peak acceleration values of about 1/30 g for metropolitan Los Angeles (about 56 km from the San Andreas fault) are at least three times smaller than the corresponding values for cities closer to the fault; the peak acceleration values for the coastal communities (about 80 km from the San Andreas Fault) are an additional factor of two to three times smaller.

Similar to the computed earthquake ground motions, the high-frequency constituents of recorded ground motions experience strong attenuation as a function of the closest distance to the rupture zone for receivers further than about 10 km distance from the rupture zone. The western region of the Los Angeles basin is much closer to the Newport-Inglewood Fault than to the San Andreas Fault. In fact, much of the southern region of the Los Angeles basin including densely populated coastal communities such as Long Beach are within 10 km of the postulated rupture zone. It is not surprising, therefore that the ground motions computed for a major earthquake along the Newport-Inglewood Fault reach hazardous levels (peak ground accelerations in excess of 0.4 g) for regions near the line of postulated rupture focussing.

A word of caution must be expressed when interpreting these results in terms of earthquake hazards for the Los Angeles basin. The acceleration values are limited by the Nyquist frequency of 5 Hz chosen for the computation of the Green's functions. Furthermore, the peak acceleration values are strongly influenced by the material quality factors Q that characterize wave attenuation between source and receiver. Yet, the amplitude and, to a lesser degree, the frequency dependence of these quality factors is not well constrained. Therefore, the combination of limited Nyquist frequency and uncertainty in Q could translate into significant uncertainties in the computed peak ground accelerations for the Los Angeles basin from all the postulated earthquake ruptures.

The sensitivity of the calculated ground motions to particular model parameters is investigated in Chapter 5. Ground motions at downtown Los Angeles are calculated and compared for ten different earthquake ruptures along the San Andreas Fault. The comparisons are grouped into five types of sensitivity studies according to the model parameter that was varied (rupture length, fault type, rupture direction, rupture velocity and fault bottom). The acceleration time histories, the mean peak acceleration velocity and displacement values, and the mean pseudo-velocity response spectra are compared in each sensitivity study.

In the rupture length sensitivity study, the ground motions are compared from four ruptures of lengths 50, 100, 175 and 250 along the San Andreas Fault. The four lengths correspond to surface-wave magnitudes of approximately 7.2, 7.5, 7.8 and 8.0, respectively. The duration of computed ground acceleration increases from about 100 seconds to about 140 seconds as the rupture length increases from 100 to 250 km. The frequency content of the body-waves and surface-waves in the calculated accelerograms also resembles recorded motions from major earthquakes. The peak acceleration values at downtown Los Angeles are shown to saturate with increasing magnitude for surface-wave magnitudes greater than about 7.2 at this distance of 56 km from the fault.

In the fault type sensitivity study, the ground motions are compared for magnitude 7.5 earthquakes with strike-slip and 45-degree oblique motions. The average of the two horizontal components is basically unaltered at all frequencies between 0 and 5 Hz when using 45-degree dip-slip motion instead of pure strike-slip motion; the vertical components, however, are increased by up to 20 percent at high frequency and more substantially at low frequency.

In the two rupture direction sensitivity studies, three magnitude 7.5 earthquakes are compared with southeast to northwest, northwest to southeast and bilateral rupture directions and two magnitude 8.0 earthquakes are compared with southeast to northwest and northwest to southeast rupture directions. For the magnitude 7.5 earthquakes, when more rupture is focussed away from downtown Los Angeles, there is a corresponding reduction of high-frequency ground shaking. For the magnitude 8.0 earthquakes, the same reduction is not evidenced. This further supports the high-frequency saturation with magnitude hypothesis, since downtown Los Angeles receives different lengths of similarly focussed rupture from the two magnitude 8.0 earthquakes.

In the rupture velocity sensitivity study, the ground motions are compared for magnitude 7.5 earthquakes with gross rupture velocities of 90 and 50 percent of the shear-wave velocity in each layer. The duration of ground shaking is much longer for the slower propagating rupture because it takes almost twice as long to travel from the hypocenter to any point on the rupture surface. There is a corresponding reduction in amplitude of ground shaking by about a factor of two because the increased spreading of signal reduces the probability of constructive interference from adjacent points of rupture (i.e., effect of focussing is reduced).

In the fault bottom sensitivity study, the ground motions are compared for earthquakes with deepest extents of rupture equal to 11.3 and 15 km. The duration of ground shaking is quite similar, but the amplitudes are about 10 percent higher for the deeper fault bottom. This is due to the increased energy released from the brittle rupture at depth

and to the more efficient (i.e., higher quality factors) propagation paths from the deepest extent at 15 km to the surface receiver at downtown Los Angeles.

In conclusion, the computed ground motion maps in Chapter 4 illustrate the potential earthquake hazards for the Los Angeles basin as a function of distance and orientation from major earthquakes rupturing through critical regions with respect to the basin. The sensitivity studies in Chapter 5 further illustrate the potential earthquake hazards as a function of such model parameters as rupture length, fault type, rupture direction, rupture velocity and fault bottom. The results were necessarily band limited to a frequency of 5 Hz by the funds available under the present contract. The material quality facts have a significant effect on the results at and above this Nyquist frequency. Although the most reliable estimates were used for the material quality factors, uncertainties in their values would have to be resolved before attempting to investigate the earthquake hazards for the Los Angeles basin up to a frequency of 20 Hz.

CHAPTER 7

REFERENCES

Allen, C. R., P. St. Amand, C. F. Richter and J. M. Nordquist (1965). Relationship Between Seismicity and Geologic Structure in the Southern California Region, Bull. Seism. Soc. Am., 55, 753-797.

Apsel, R. J. (1979). Dynamic Green's Functions for Layered Media and Applications to Boundary-Value Problems, Ph.D. Thesis, University of California, San Diego, California, 349 pp.

Archuleta, R. J. and G. A. Frazier (1978). Three-Dimensional Numerical Simulations of Dynamic Faulting in a Half-Space, Bull. Seism. Soc. Am., 68, no. 3, pp. 573-598.

Blume, J. A. (1977). Strong Motion Records of the 1933 Long Beach Earthquake, LL 44 (draft).

Blume, J. A. (1978). Viscoelastic Parameters for the Long Beach Crustal Structure, provided by URS/John A. Blume & Associates, Engineers.

Boore, D. M. (1973). The Effect of Simple Topography on Seismic Waves: Implications for the Accelerations Recorded at Pacoima Dam, San Fernando Valley, California, Bull. Seism. Soc. Am., 63, pp. 1603-1609.

Bouchon, M. (1973). Effect of Topography on Surface Motion, Bull. Seism. Soc. Am., 63, pp. 615-632.

Cagniard, L. (1939). Reflexion et refraction des ondes seismigues progressives, Gautheir-Villars, Paris.

Castle, R. O., J. P. Church, M. R. Elliott, and J. C. Savage (1977). Preseismic and Coseismic Elevation Changes in the Epicentral Region of the Point Mugu Earthquake of February 21, 1973, Bull. Seism. Soc. Am., 67, 219-231.

Day, S. M. (1977). Finite Element Analysis of Seismic Scattering Problems, Ph.D. Thesis, University of California, San Diego, California, 149 pp.

Day, S. M. (1979). Three-Dimensional Finite Difference Simulation of Fault Dynamics, Systems, Science and Software Report SSS-R-80-4295.

deHoop, A. T. (1958). Representation Theorems for the Displacement in an Elastic Solid and Their Application to Elastodynamic Diffraction Theory, D.Sc. Thesis Technische Hogeschool, Delft.

deHoop, A. T. (1960). A Modification of Cagniard's Method for Solving Seismic Pulse Problems, Appl. Sci. Res., B8, 349-356

Del Mar Technical Associates (May 1978). Simulation of Earthquake Ground Motions for San Onofre Nuclear Generating Station, Unit 1: Final Report.

Del Mar Technical Associates (July 1979). Simulation of Earthquake Ground Motions for San Onofre Nuclear Generating Station, Unit 1: Supplement I.

Del Mar Technical Associates (August 1980). Simulation of Earthquake Ground Motions for San Onofre Nuclear Generating Station, Unit 1: Supplement II.

Del Mar Technical Associates (August 1980). Simulation of Earthquake Ground Motions for San Onofre Nuclear Generating Station, Unit 1: Supplement III.

Eaton, J. P., M. E. O'Neill and J. N. Murdock (1970). Aftershocks of the 1966 Parkfield Sequence, Bull. Seism. Soc. Am., 60, 1151-1197.

Frazier, G. A., and C. M. Petersen (1974). 3-D Stress Wave Code for the Illiac IV, Systems, Science and Software Report SSS-R-74-2103.

Gutenberg, B. (1944). Travel Times of Principal P and S Waves Over Small Distances in Southern California, Seism. Soc. Am. Bull., 34, 13-32.

Gutenberg, B. (1951). Revised Travel Times in Southern California, Seism. Soc. Am. Bull., 62, 427-439.

Gutenberg, B. (1952). Waves from Blasts Recorded in Southern California, Am. Geophys. Union Trans., 33, 427-431.

Gutenberg, B. (1955). Wave Velocities in the Earth's Crust, Geol. Soc. Am., Spec. Paper 62, 19-34.

Hadley, D. and H. Kanamori (1979). Seismic Structure of the Transverse Ranges, California, Geol. Soc. Am. Bull., 88, 1469-1478.

Harkrider, D. G. (1964). Surface Waves in Multilayered Elastic Media, Part I. Rayleigh and Love Waves from Buried Sources in a Multi-Layered Elastic Half-Space, Bull. Seism. Soc. Am., 54, 627-680.

Healy, J. H., W. W. Rubey, D. T. Griggs and C. B. Raleigh (1968). The Denver Earthquakes, Science, 161, 1301-1310.

Heaton, T. H. (1978). Generalized Ray Models of Strong Ground Motion, Ph.D. Thesis, California Institute of Technology, Pasadena, California, 292 pp.

Helmberger, D. V. (1968). The Crust-Mantle Transition in the Bering Sea, Bull. Seism. Soc. Am., 58, 179-214.

Kanamori, H. and D. Hadley (1975). Crustal Structure and Temporal Velocity Change in Southern California, Pure and Appl. Geophysics, 113, 257-280.

Kostrov, B. V. (1964). Self-Similar Problems of Propagating Shear Cracks, J. Appl. Math. Mech., 28, 1077-1087.

Kovach, R. L. (1974). Source Mechanisms for Wilmington Oil Field, California, Subsidence Earthquakes, Bull. Seism. Soc. Am., 64, 699-711.

Mooney, W. D. and G. A. McMechan (1979). Synthetic Seismogram Modeling for the Laterally Varying Structure in the Central Imperial Valley, U.S.G.S. (in press).

Olson, A. (1978). Synthesizing Ground Motion Using a Discrete Wave-Number Finite Element Representation, Abstr. in EOS, Trans. Am. Geophys. Union, 59, 1128, December 1978.

Prescott, W. H. and J. C. Savage (1976). Strain Accumulation on the San Andreas Fault Near Palmdale, California, J. Geophys. Res., 81, 4901-4908.

Press, F. (1956). Determination of Crustal Structure From Phase Velocity of Rayleigh Waves, 1, Geol. Soc. Am. Bull., 67, 1647-1658.

Press, F. (1960). Crustal Structure in the California-Nevada Region, J. Geophys. Res., 65, 1039-1051.

Richter, C. F. (1950). Velocities of P at Short Distances, Seism. Soc. Am. Bull., 40, 281-289.

Richter, C. F. (1958). Elementary Seismology, W. H. Freeman and Co., San Francisco.

Roller, J. C. and J. H. Healy (1963). Seismic-Refraction Measurements of Crustal Structure Between Santa Monica Bay and Lake Mead, J. Geophys. Res., 68, no. 20, 5837-5848.

Shor, G. G. (1955). Deep Reflections from Southern California Blasts, Am. Geophys. Union Trans., 36, 133-138.

Teng, T. L., C. R. Real and T. L. Henyey (1973). Microearthquakes and Water Flooding in Los Angeles, Bull. Seism. Soc. Am., 63, 859-875.

Thatcher, W. (1976). Episodic Strain Accumulation in Southern California, Science, 194, 691-695.

Trifunac, M. D. and J. N. Brune (1970). Complexity of Energy Release During the Imperial Valley, California Earthquake of 1940, Bull. Seism. Soc. Am., 60, 137-160.

Trifunac, M. D. (1974). A Three-Dimensional Dislocation Model for the San Fernando, California Earthquake of February 9, 1971. Bull. Seism. Soc. Am., 64, pp. 1393-1411.

Trifunac, M. D., and A. G. Brady (1975). On the Correlation of Seismic Intensity Scales with the Peaks of Recorded Ground Motion, Bull. Seism. Soc. Am., 64, 139-162.